Quantum Chemical Investigations of Structure, Bonding and EPR Parameters of Manganese Complexes relevant to Photosystem II

DISSERTATION

zur Erlangung des naturwissenschaftlichen Doktorgrades der

Julius-Maximilians-Universität Würzburg

vorgelegt von

Sandra Schinzel

aus Wertheim, Deutschland

WÜRZBURG 2009

Eingereicht am: _____

bei der Fakultät für Chemie und Pharmazie

1. Gutachter: _____

2. Gutachter: _____

der Dissertation

1. Prüfer: _____

2. Prüfer: _____

3. Prüfer: _____

des Öffentlichen Promotionskolloquiums

Tag des Öffentlichen Promotionskolloquiums: _____

Doktorurkunde ausgehändigt am: _____

Contents

Abbreviations

BP	**B**reit-**P**auli
BS	**B**roken **S**ymmetry
BS-DFT	**B**roken-**S**ymmetry **D**ensity **F**unctional **T**heory
CW EPR	**C**ontinous **W**ave **E**lectron **P**aramagnetic **R**esonance
DFT	**D**ensity **F**unctional **T**heory
ENDOR	**E**lectron **N**uclear **DO**uble **R**esonance
EPR	**E**lectron **P**aramagnetic **R**esonance
ESEEM	**E**lectron **S**pin **E**cho **E**nvelope **M**odulation
EXAFS	**E**xtended **X**-ray **A**bsorption **F**ine **S**tructure
HFC	**H**yper**F**ine **C**oupling
HF-EPR	**H**igh-**F**ield **E**lectron **P**aramagnetic **R**esonance
HS	**H**igh **S**pin
MO	**M**olecular **O**rbital
NO	**N**atural **O**rbital
NQC	**N**uclear **Q**uadrupole **C**oupling
OEC	**O**xygen-**E**volving **C**omplex
PO	**P**aired **O**rbital
PSII	**P**hoto**S**ystem II
SH	**S**pin **H**amiltonian
WOC	**W**ater-**O**xidizing **C**luster
XANES	**X**-ray **A**bsorption **N**ear **E**dge **S**tructure
XAS	**X**-ray **A**bsorption **S**pectroscopy
XRD	**X**-ray **D**iffraction **S**pectroscopy
ZFS	**Z**ero-**F**ield **S**plitting

Chapter 1

If there is magic on this planet, it is contained in water.

Loren Eiseley

Introduction

Oxygen powers a substantial part of life on earth. While the biological production of oxygen in plant photosynthesis by photosystem II (PSII) may be viewed as a waste byproduct, the oxygen produced contains a significant amount of the chemical energy generated.[1] The catalyst at which two water molecules are coupled in a four-electron oxidation to one O_2 molecule is known to be a tetranuclear manganese complex, known as the oxygen-evolving complex (OEC). Driven by four successive light excitations of the P_{680} chlorophyll dimer of PSII, four electrons are removed from the OEC, which passes through a cyclic sequence of five oxidation states $S_0 - S_4$.[2] While this so-called Kok cycle is focused exclusively on the accumulation of four oxidizing equivalents,[3-6] the removal of four protons has recently received increased attention, and an extended mechanism has been suggested.[7,8]

Obviously, the question of how nature utilizes light as its main energy source is of central importance for future renewable energy sources.[1] Not surprisingly, the structure, protein environment and function of the OEC have thus been at the focus of a tremendous amount of research over the past 25 years. The methodology applied ranges from

biochemical studies via X-ray diffraction,[9-13] X-ray absorption spectroscopies (especially EXAFS)[6,14], IR and optical spectroscopies[15-17] to electron paramagnetic resonance (EPR)[18,19] spectroscopy.

In particular, EPR spectroscopy is well-suited for studying the OEC, as it allows investigation of short-living paramagnetic species (at lifetimes down to 10^{-6} s or even less) and determination of their spin and oxidation states. The S_2 state is by far the best EPR-characterized state of the Kok cycle by EPR spectroscopy.[20-25] It can be characterized either by a signal centered at g = 2, arising from an S = 1/2 ground state of the manganese cluster (most probably in the $Mn^{III}Mn^{IV}Mn^{IV}Mn^{IV}$ valence state), or by a broad signal at g = 4.1, attributed to an S = 5/2 spin state. The appearance of two different spin states of an exchange-coupled cluster in the same sample is typical of spin frustration, giving rise to low-lying excited states. The multiline signal indicates an antiferromagnetically coupled mixed-valence manganese cluster, strongly resembling the multiline signal of dinuclear $Mn^{III}Mn^{IV}$ complexes.[26,27] Hyperfine coupling constants (HFC) have been accurately determined using ^{55}Mn-ENDOR spectroscopy,[24,25] revealing significant contribution from all four Mn ions and axial symmetry for each. Recently, Yeagle *et al*.[28,29] have employed multifrequency electron spin-echo envelope modulation (ESEEM) spectroscopy to determine the hyperfine and the nuclear quadrupolar coupling of one single ^{14}N nucleus coupled to the manganese cluster in the S_2 state. However, the spectra obtained are very complex and cannot be interpreted in detail without the aid of quantum chemical calculations. Calculation of molecular properties such as EPR parameters allows the close connection of theory and experiment and often leads to important conclusions about the geometric and electronic structure of the investigated system. Spectroscopic features often react extremely sensitively to subtle structural variations. Consequently, the calculation of spectroscopic properties is a sounds weird promising tool to give insight into the geometric and electronic structure of a system.

Quantum chemical studies[30-36] on models for the OEC have so far concentrated mainly on a) finding models that are consistent with the structural data obtained from XAS/EXAFS and X-ray crystallography or on b) trying to establish mechanistic aspects of the Kok cycle. We note that all of these studies have to be viewed as preliminary due to the incompleteness of the available structural information. Initially, almost all of these computations were based on high-spin “excited” states, thus eliminating the need to deal with the potentially complicated spin-coupling schemes present. However, multinuclear

complexes such as the tetranuclear manganese complex in PSII have energetically close-lying electronic levels and would, therefore, require a multi-determinant-based treatment for an accurate description of the real antiferromagnetic state. For large systems like multinuclear manganese complexes, this approach is currently too computationally expensive. Density-functional theory (DFT) is the method currently in use for the most complex problems, and the higher accuracy achievable, especially with modern functionals, is a key element in making the simulation of complex systems such as the OEC so promising. In particular the broken-symmetry density-functional theory (BS-DFT)[37,38] method is an suitable technique to overcome the problem of the normally required multi-determinant-based approach. However, broken-symmetry wavefunctions are not expected to represent the true wavefunction. Therefore, spin-projection techniques have to be applied to obtain the properties,[39,40] e.g. the g-tensor or the hyperfine coupling (HFC) constants of the system. In conclusion, a comparison of calculated with spectroscopic EPR data should give important insight into the structural environment of the OEC.

The goal of this thesis is to calculate EPR parameters for the S_2 state of the OEC using broken-symmetry density-functional methods (BS-DFT) for the first time, and to compare the calculated values with spectroscopic studies to validate different probable model systems for the OEC.

Objective of this Study

This thesis focuses on the calculation of EPR parameters of the tetranuclear manganese cluster in PSII using density-functional methods. This subject is perhaps the best possible example of a scientific field that is interdisciplinary, requiring an understanding of basic concepts of biology, quantum chemistry, and spectroscopy. Furthermore, careful validation studies of the used DFT methods on mono- and dinuclear manganese complexes are essential to find the most well-suited method on the calculation of the EPR parameters of the OEC. Therefore, this thesis is organized as follows.

After the introduction at hand, the background is described to understand the work in this thesis. Chapter 2 will briefly summarize the current knowledge of light driven oxidative water splitting in photosynthesis. Afterwards, a short treatment of density

functional theory (Chapter 3) and of the calculation of electron paramagnetic resonance parameters including presentation of spin-projection techniques (Chapter 4) will be given.

The application of modern DFT methods for calculating EPR parameters requires much experience. In particular, the calculation of hyperfine coupling constants exhibits many difficulties. Therefore, initial work was carried out to validate DFT methods for calculating g-tensors and hyperfine coupling constants (^{1}H, ^{17}O and ^{55}Mn) on simple inorganic mononuclear manganese complexes in the context of the OEC (Chapter 5). The focus is especially on the experimentally well-investigated $[Mn(H_2O)_6]^{2+}$ and $[Mn(H_2O)_6]^{3+}$ complexes.

Chapter 6 presents a validation study on a series of DFT exchange-correlation functionals for calculating EPR parameters of the divalent manganese coordination site of the saccharide-binding protein concanavalin A.[41] Besides the performance of different exchange-correlation functionals for the calculation of spin-density distributions as well as the g-tensor and HFCs, the point-dipole approximation in estimation proton positions on coordinated protein residues and water molecules from ENDOR data will be validated.

We then carry on to dinuclear systems in Chapter 7. Any investigation of EPR parameters for multinuclear complexes using spin-projection techniques must be preceded by a careful calibration of the available density functionals, since it is not possible to make a safe *a priori* prediction of how well a particular functional will perform. Therefore, we present in Chapter 7 a systematic study for the calculation of EPR parameters for $Mn^{III}Mn^{IV}$ complexes including biologically relevant complexes like manganese catalase. A main focus is the influence of the exchange-correlation functional on the computed spin-density distributions and spectroscopic parameters (g-tensors, ^{55}Mn, ^{14}N, and ^{1}H hyperfine coupling tensors, and Heisenberg exchange couplings). The broken-symmetry results for the ^{55}Mn HFC and the Heisenberg exchange coupling will be analyzed with respect to influences of the bridging and terminal ligand. Furthermore, the tensor orientations will be investigated as in simulations of EPR spectra it is often assumed that the tensor axes of all HFC tensors and of the g-tensor coincide. Additionally, the spin contamination of the BS-KS determinants will be analyzed using natural orbital occupations, paired-orbital overlaps, and an expansion into quasi-restricted determinants in the paired-orbital basis.

This thesis concludes in Chapter 8 with the calculation of EPR parameters of the S_2 state for the OEC. Different model systems created from the most recent experimental data (XRD and EXAFS) will be analyzed with respect to the structure and the most

probable spin-density distribution of the BS solutions. Spin-projection techniques will be applied to obtain the ^{55}Mn and ^{14}N HFC constants as well as ^{14}N and ^{55}Mn nuclear quadrupole couplings, enabling us for the first time to evaluate the quality of molecular model complexes for the OEC by direct comparison with experimental EPR, ENDOR and ESEEM data.

A number of general conclusions summarizing the work and outlook is provided in Chapter 9.

Chapter 2

If you have enough energy you can solve many of the top ten problems the world is facing such as water, food supplies, poverty and disease.

Richard E. Smalley, 2004.

The Oxygen-Evolving Complex of Photosystem II

2.1 Introduction

Photosynthesis is the most fundamental process for life on earth:[1-7]

$$H_2O + CO_2 \underset{\text{Respiration (catalyzed)}}{\overset{\text{Photosynthesis (catalyzed)}}{\rightleftharpoons}} 1/n\ (CH_2O)_n + {}^3O_2$$

This overall process is separated into two sets of reactions: the light and the dark reactions. Light energy is used as the driving force to oxidize water, reduce ferrodoxin, and provide a proton gradient that helps provide the energy for ATP production. In the dark, or carbon fixation reactions Fe-NADPH is used to reduce atmospheric CO_2 for incorporation into simple sugars. While the production of oxygen in plant photosynthesis by photosystem II (PSII) may be viewed as a waste byproduct, the oxygen produced contains a significant amount of the chemical energy generated,[8] and it is of course of fundamental importance in its own right, as it powers a substantial part of life on earth. The catalyst at which two water molecules are coupled in a four-electron oxidation to one

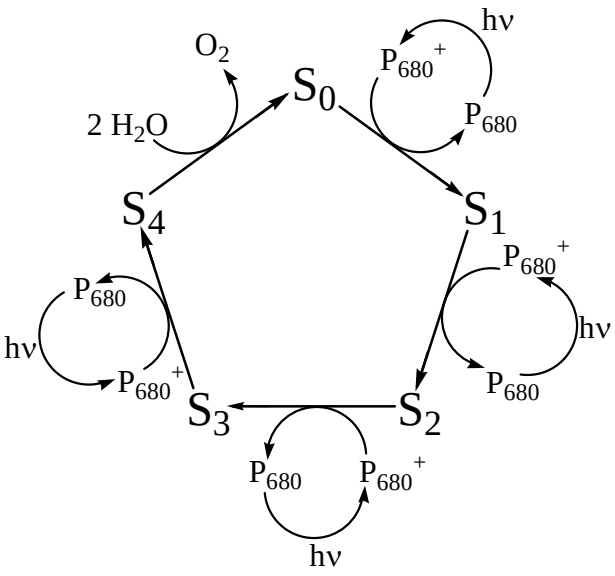

Figure 2.1. Kok cycle.

O_2 molecule is known to be a tetranuclear manganese complex, termed the oxygen-evolving complex (OEC) or water-oxidizing cluster (WOC). Driven by four successive light excitations of the P_{680} chlorophyll dimer of PSII, four electrons are removed from the OEC, which passes through a cyclic sequence of five oxidation states S_0 – S_4 (Kok cycle, Figure 2.1).[9] The most oxidized state (S_4) spontaneously decays (without further photoinduction) into the S_0 state, and dioxygen is released. The S_0 and S_1 states are dark-stable, and the S_2 and S_3 states decay in seconds regime towards the S_1 state. The Kok cycle focuses exclusively on the accumulation of four oxidizing equivalents.[10-13] Recently, the removal of four protons has received increased attention, and an extended mechanism has been suggested.[14,15]

In view of its importance, the PSII has received extensive studies from a wide range of approaches in the past several decades regarding its protein composition, function, and dynamic regulation. Several studies via X-ray diffraction,[6,16-19] X-ray absorption spectroscopies (in particular EXAFS)[13,20], IR and optical spectroscopies[21-23] to electron paramagnetic resonance (EPR)[24,25] spectroscopy have given the first hints to the structure of the OEC, but the precise molecular details of water oxidation catalyzed by the OEC remain unclear. Critical questions related to the process of photosynthetic water oxidation are: 1) What are the exact positions of manganese, calcium, and the bridging and terminal ligands? 2) How many water-derived ligands are coordinated to the tetranuclear manganese cluster and what are their protonation states? 3) What are the oxidation states and structural changes in the Mn complex as the OEC proceeds through the S-state cycle? 4) What is the mechanism to make dioxygen?

The focus of this chapter is on the elucidation of the structure of the OEC in PSII (section 2.2). After a short discussion of structural models obtained from crystallographic studies, including the spatial organization of the protein subunits and cofactors and the limitations due to radiation damage (section 2.2.1), results of X-ray absorption (XAS,

section 2.2.2) and electron paramagnetic resonance (EPR, section 2.2.3) studies will be reviewed. Finally, the function of the PSII (section 2.3) as well as quantum chemical studies (section 2.4) will be shortly discussed.

2.2 The Structure of the Oxygen-Evolving Complex

2.2.1 Crystallographic Studies

X-ray crystallography provides information about location, structure and protein environment of the Mn_4Ca^{2+} cluster of the PSII, which is a large protein complex located in the chloroplast thylakoid membranes of higher plants and algae and in the plasma membranes of cyanobacteria. However, no high-resolution crystal structure is yet available. Moreover, all these synchrotron experiments suffer from radiation damage,[26] which probably leads to modified positions of the metal atoms and a loss of water ligands. 80% of the manganese ions in the S_1 state have probably been photoreduced to Mn(II), and multinuclear oxo-bridges are damaged.[20] It is thus unlikely that an accurate structure of the cluster core has been obtained. Consequently, the structural data can only be seen as a useful starting guess for the correct structure.

Zouni *et al*. published the first successful crystal structure of PSII from *Synechococcus elongatus* at 3.8 Å resolution in 2001.[17] The structure gives insight into the spatial organisation of the protein subunits and cofactors and, most importantly, it reveals the position within the PSII of the four Mn ions. The four manganese atoms of the OEC are arranged in a 3+1 fashion. Three manganese ions were positioned to form the corners of an isosceles triangle, and a fourth manganese atom was placed near the centre of the triangle with inter-atomic distances about 3 Å. However, the low resolution (3.8 Å) was not sufficient and the subunits of the PSII were not completely assigned. Furthermore, positions for the Ca^{2+} as well as the bridging ligands were not proposed.

Kamiya *et al*. obtained a crystal structure from the thermophilic cyanobacterium, *Thermosynechococcus vulcanus*, at 3.7 Å resolution,[19] which suggests possible ligands for the metal cluster from the side chains of the D1 protein (Ala-344, Asp-170, Glu-333 or His-332, His-337, Asp-189 or His190, Tyr-73). All four Mn atoms are located roughly in the same plane and a Ca^{2+} ion was not included in the model.

The first reliable information about the protein environments of all major cofactors of PSII was provided by the crystal structure of the cyanobacterium *Thermosynechococcus*

elongates at 3.5 Å resolution.[18] PSII exists as a homodimer, in which the monomers are related by a noncrystallographic twofold axis perpendicular to the membrane plane. Ferreira's model consists of 19 polypeptide subunits and many cofactors (especially chlorophyll a and carotenoids). Figure 2.2a shows the cofactors involved in electron transfers perpendicular to the internal pseudo-C_2 axis, coordinated by the two subunits D1 and D2. Ferreira *et al*. proposed a cubane-like Mn_3CaO_4 cluster, in which each metal ion has three tri-μ-oxo bridges, linked to a fourth Mn atom by a mono-μ-oxo bridge. The Mn-Mn distances within the cubane-like cluster are 2.7 Å, and 3.4 Å for Mn-Ca^{2+} (typical for the oxo bridges proposed). The following amino acid residues are suggested to be directly ligated to the manganese ions: D1-Asp342, D1-Asp170, D1-Glu333, D1-Glu189, D1-His332, and CP43-Glu354. D1-Ala344 is considered as not directly coordinated to the calcium ion. In this XRD study, the calcium atom could be located for the first time.

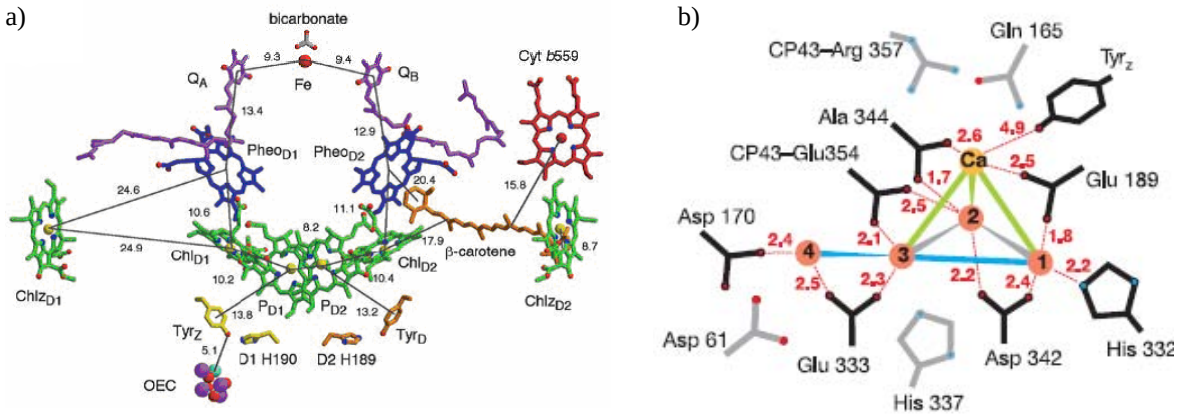

Figure 2.2. a) Arrangement of cofactors of the electron transfer chain shown perpendicular to the internal pseudo-C_2 axis. Full lines indicate center-to-center distances (Å between cofactors). Reproduced from ref. [18] with permission from The American Association for the Advancement of Science.
b) OEC with amino acid residues from 3.0 Å crystal structure. Distances [Å] between Mn (red) and Ca^{2+} (orange) are indicated by the connecting lines (grey: 2.7 Å; blue: 3.3 Å, green: 3.4 Å). Amino acids of the first coordination sphere are black, of the second grey. Reproduced from ref. [16] with permission from Nature Publishing Group.

In 2005, another crystal structure measured up to 3.0 Å was published by Loll *et al*. (Figure 2.2b).[16] This model provides a more complete description of the protein complex than the structure of Ferreira, including an additional protein subunit, but does not contain the bridging oxides between the metal centers. The positions of three Mn atoms differ from the ones obtained by Ferreira, but roughly agree with Zouni's structure.

Compared to Ferreira's 3.5 Å structure, the 3.0 Å structure finds the dangler manganese ion further away from the cubane-like cluster, suggesting a linkage of a single oxo bridge. All amino acid carboxylate ligands are in the structure by Loll modelled as bridging ligands, which is the second main difference of these two crystal structures.

2.2.2 X-ray Absorption Spectroscopy

X-ray absorption and emission spectroscopy (XAS and XES), as well as extended X-ray absorption fine structure studies (EXAFS), do not suffer from the radiation damage problem due to much shorter exposure times. These methods have been particularly useful in probing the electronic and geometric structures and, therefore, to decipher the mechanism of the water oxidation reaction.[13,27-30] EXAFS provides information about short-range electron scattering to give accurate bond lengths in the first and second coordination spheres. XAS spectroscopy has also been used to attempt the determination of the oxidation states of the Mn ions of the OEC.[4,31] The results of different XAS experiments are given in Table 2.1.

Table 2.1. Properties of the OEC (XAS data).

S state	*d(Mn-Mn)*	*d(Mn-O) or d(Mn-N)*	*d(Mn-Ca)*	*Mn oxidation states*[4,31]
S_0[32, 33]	two 2.7 Å one 2.85 Å one 3.3 Å			(a) II, III, III, III (b) II, III, IV, IV (c) III, III, III, IV
S_1[34-36]	two 2.7 Å one 2.8 Å one > 3.3 Å	first coordination shell 1.8–2.0 Å	one 3.3 – 3.5 Å	(a) III, III, III, III (b) III, IV, III, IV
S_2[37, 38]	two or three 2.7 Å one > 3.3 Å			(a) III, III, III, IV (b) III, IV, IV, IV
S_3[39]	one or two 2.8 Å, one or two 2.95 Å one 3.3–3.5 Å			(a) III, III, IV, IV (b) IV, IV, IV, IV

The $S_0 \rightarrow S_1$ transition involves only small changes in interatomic distances. A reduction of one 2.85 Å Mn-Mn distances could be observed[32,33] and Haumann *et al*. suggested a deprotonation of a μ-hydroxo bridge.[33] No EXAFS-detectable change in the coordination of Mn in the OEC could be observed for the $S_1 \rightarrow S_2$ transition.[38] The next

step in the Kok cycle ($S_2 \rightarrow S_3$) is accompanied by a significant change in the structure of the cluster,[36] due to changes in the Mn-Mn bridging mode (a new 2.7 Å Mn-Mn distance) and a possible formation of a third Mn-(μ-oxo)-Mn unit.[33]

XAS spectroscopy investigations[31] and studies of the stoichiometry of the reaction between the OEC and exogenous reductants[40] suggested the following most probable Mn oxidation state assignments: S_0 (II, III, IV, IV) or (III, III, III, IV), S_1 (III, III, IV, IV), S_2 (III, IV, IV, IV), S_3 (III, IV, IV, IV) or (IV,IV,IV,IV). At least three of the S-state transitions involve manganese oxidation, but it is still unclear if in the $S_2 \rightarrow S_3$ or, alternatively, in the $S_3 \rightarrow S_4$ transition the ligand sphere is oxidized.[41,42] The $S_3 \rightarrow S_4 => S_0$ transition, which is coupled to dioxygen formation, is poorly understood. Dau *et al*. have extended the classical Kok cycle, in which the sequence and interplay of electron and proton abstraction events at the donor side of PSII is described and a further intermediate state S_4' is assumed.[14,15]

2.2.3 EPR Spectroscopy

EPR spectroscopy is particularly well-suited for the study of these processes, as it allows to investigate short-lived paramagnetic species (at lifetimes down to 10^{-6} s or even below) and to determine spin and oxidation states. Britt *et al.*[24,43] and others (see ref. [25] and references therein and ref. [44]) used continous-wave electron paramagnetic resonance (CW EPR) spectroscopy to perform experiments on different S-states of photosystem II. However, CW EPR spectroscopy suffers from inherent resolution limitations. In particular, the ligand couplings are often not resolved. This may often be overcome by performing pulsed EPR experiments (ESEEM: electron spin echo envelope modulation, and ESE-ENDOR: electron spin echo-electron nuclear double resonance).[24] In the OEC, magnetic nuclei are naturally present (e.g. ^{55}Mn, ^{1}H, ^{14}N), but can also be introduced through incorporation of labelled amino acids, substrates, inhibitors, or cofactors (e.g. ^{2}H, ^{15}N, ^{13}C, ^{87}Sr).

Table 2.2 summarizes briefly some of the most important results of the $S_0 - S_3$ states, using PSII usually prepared from spinach.

Table 2.2. EPR spectroscopic data of the OEC.

S state	*g-factor*	*Signal feature*	*^{55}Mn HFC [MHz]*	*Multiplicity*
S_0[1, 45-49]	g = 2.0	24 – 26 multiline signals, 80 – 90 G spacing	[1] A_{iso}=247 (-23,-23,46); A_{iso}=220 (-30,-30,60); A_{iso}=347 (-27,-27,54); A_{iso}=217 (-23,-23,46)	1/2
S_1[50-52]	g = 4.8	$^{\parallel}$mode: broad signal (600 G wide)		1
	g = 12	$^{\parallel}$mode: ≥18 multiline signals		1
S_2[1, 2, 53-56]	g = 1.98	19 – 21 mulitline signals, 80 – 90 G spacing	[1] A_{iso}=245 (-10,-10,20); A_{iso}=205 (-20,-20,40); A_{iso}=295 (-15,-15,30); A_{iso}=193 (-18,-18,36)	1/2
	g = 4.1	broad signal (340 – 360 G wide)	[2-4] A_{iso}=245 (-13,-13,26); A_{iso}=200 (-20,-20,40); A_{iso}=297 (-14,-14,28); A_{iso}=217 (-17,-17,34)	5/2
S_3[57-59]	g = 6.7, g = 8 and g = 12	$^{\perp}$mode, broad signal $^{\parallel}$mode: broad signals (300 G, 200 G wide)	-	1

For the S_0 state a multiline signal is observed at g = 2.0, originating from an S = 1/2 ground state.[1,45-49] This S = 1/2 ground state probably results from the coupling within a Mn_4(II, III, IV, IV) or Mn_4(III, III, III, IV) cluster, in agreement with the above mentioned XAS data (Table 2.2). Furthermore, ^{55}Mn ENDOR measurements provided effective hyperfine coupling tensors for the four manganese atoms.[1]

The excited S = 1 spin state for S_1 (ground state S = 0)[60] provides a broad signal centered at g = 4.8, detected in parallel polarization mode.[50-52] Another signal appears at about g = 12 and shows 18 or more hyperfine lines, a feature characteristic of the Mn cluster.

The S_2 state is by far the best EPR-investigated state of the Kok cycle.[1,2,53-56] It can be characterized either by a signal centered at g = 2, arising from an S = 1/2 ground state, or by a broad signal at g = 4.1, attributed most probably to a S = 5/2 spin state. The appearance of two different spin states of an exchange-coupled cluster in the same sample is typical for spin frustration, giving rise to low-lying excited states. The multiline signal indicates an antiferromagnetically coupled mixed-valence manganese cluster. Initially, it was assumed that the g = 4.1 signal comes from an isolated Mn(IV) center.[61] However, this notion was refused.[62] ^{55}Mn ENDOR spectroscopy of dinuclear Mn_2(III,IV) model

complexes exhibited patterns strongly resembling to the multiline signal of the S_2 state.[63, 64] Based on ^{55}Mn ENDOR studies of the S_2 signal,[2] Britt *et al*. suggested a "3+1" model, named the "dangler model". In this model the fourth dangler Mn is linked to the $Mn_3Ca^{2+}O_4$ cubane via a mono-μ-oxo bridge.

Using conventional perpendicular mode, a broad signal at g = 6.7 could be observed for the S_3 state,[57-59] arising from an S = 1 spin state. Parallel-mode EPR reveals broad signala at g = 8 and g = 12.

Additionally, more advanced pulsed EPR/ESEEM and ENDOR studies have provided a substantial amount of information on ligand hyperfine couplings, either to ^{14}N in bound histidine (A_{iso}=7.3 MHz)[65,66] or in inhibitor ammonia or azide ligands,[24] to ^{2}H of substrate ligands derived from deuterated water (or of inhibitor acetate),[24] to ^{17}O in systems treated with labelled water,[67,68] or to ^{87}Sr in systems where Ca had been replaced by ^{87}Sr enriched strontium.[69]

Furthermore, EPR spectroscopy has been used to measure the dipolar distance between Tyr_Z and the OEC metal-oxo cluster, giving distances close to 8 Å,[70,71] which is in good agreement with the X-ray crystallographic models. The assumption, that Tyr_Z is the direct electron donor to the manganese cluster, was also confirmed by revealing several intermediate state signals involving an interaction of the Tyr_Z radical with the intact tetranuclear manganese cluster.[24]

2.3 The Function of Photosystem II

Three different types of reaction sequences occur during the overall process of plastoquinone (PQ) reduction with water as hydrogen donor in PSII: (1) light induced stable charge separation within the central D1 and D2 subunits producing the radical ion pair $P_{680}^{+}Q_A^{-}$, (2) oxidative water splitting leading to the formation of molecular oxygen and four protons energetically driven by P_{680}^{+}, (3) reduction driven by Q_A^{-} of plastoquinone to quinol under proton reception.[72] Only the second reaction sequence will be briefly reported here. The electron flow in PSII is shown in Figure 2.3.

P_{680} is a specific pigment complex containing chlorophylls (Chl_{D1}, Chl_{D2}, P_{D1}, P_{D2}). The cationic radical P_{680}^{+} is formed by singlet state excitation of P_{680}, forming an excited P_{680}* species. This excited chlorophyll center reduces a pheophytin molecule (Pheo) and is itself oxidized to P_{680}^{+}. With a reduction potential of +1.25 V, P_{680}^{+} is one of the

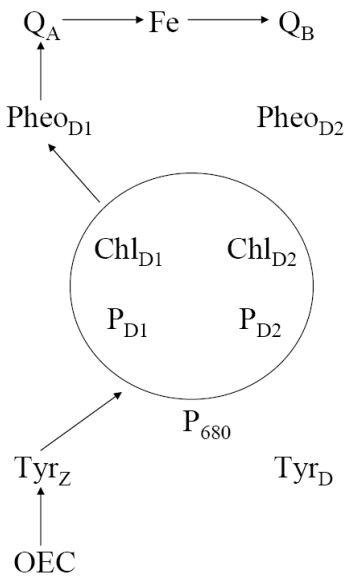

Figure 2.3. Schematic view of electron flow.

strongest oxidants in biology.[73] The electron coming from the oxidation of the OEC by P_{680}^+ continues to the second weakly bound quinone Q_B. After its reduction by two electrons, Q_B diffuses out into the membrane to continue the photosynthetic electron transfer chain at the cytochrome b_6f complex.

At the donor side of PSII, the stepwise oxidation of the OEC by P_{680}^+ (see Figure 2.1) is mediated by a redox-active tyrosine cofactor, Tyr_Z, having a reduction potential of 1.0 V.[74] The PSII contains[75] two redox active tyrosine cofactors (see Figure 2.2), Tyr_z in polypeptide D1 and Tyr_D in polypeptide D2. Both are localized symmetrically according to the P680 unit, but only Tyr_Z is involved in the Kok cycle. The protonation state of the phenolic OH group of Tyr_Z influences strongly the energetics of tyrosine oxidation, and, hence, the driving force of Tyr_Z oxidation by the cationic radical P_{680}^+ as well as the successive one-electron S state transitions oxidized by Tyr_Z. In order to achieve charge balance and to keep the oxidation potential of the OEC in the various S states, protons are released during the Kok cycle.[76] The kinetics of the coupling mode between electron transfer (ET) and proton transfer (PT) are still unclear.[77] Quantum mechanical studies are a promising tool to investigate the kinetics as well as to establish mechanistic aspects of the Kok cycle, including the effect of cofactors like calcium or chloride.

It is widely accepted that one calcium is required per OEC,[75] which probably binds one substrate water molecule[76,78] and might modify the redox potential by controlling the proton transfer.[34] Like calcium, it is hypothesized that chloride influences the proton-transfer from the OEC.[79] One chloride is bound to the OEC, probably to calcium or the dangler manganese atom,[80] but the position is still unclear. Recent studies[81,82] suggested that Cl^- is not a direct ligand to manganese.

2.4 Quantum Chemical Studies on the Photosystem II

Quantum chemical studies on models for the OEC have so far concentrated mainly on a) finding models that are consistent with the structural data obtained from XAS/EXAFS and X-ray crystallography or on b) trying to establish mechanistic aspects of the Kok cycle. We note that all of these studies have to be viewed as preliminary due to the incompleteness of structural information available. Siegbahn and coworkers[83-85] proposed a mechanism for oxygen evolution based on DFT calculations (B3LYP). The crystal structures of Ferreira and Loll, as well as EXAFS-based structures by Yano (see above) were used as starting points to calculate full mechanisms and energy diagrams, allowing conclusions on the mechanism. The effect of a chloride ligand, as well as the effects of substituting calcium with cadmium or strontium were investigated.[83-85]

Batista *et al*.[86-89] employed quantum mechanical/molecular mechanics (QM/MM) methods based on the X-ray structure of Ferreira *et al*. to carry out structure optimizations. The focus was entirely on the structure determination, no redox potentials, pK_a values, or transition states were computed. They presented for the first time a broken-symmetry solution for the OEC.[89] We will refer to this work in Chapter 8.

Except of the study from Batista and co-workers,[89] all of the computations were based on high-spin "excited" states, thus avoiding to have to deal with the potentially complicated spin-coupling schemes present. It was thus assumed that a) the structures are not much affected by the spin coupling between the different manganese centers and, b) mechanistic details also remain largely unaffected. While the first point may be a reasonable approximation, the latter appears more doubtful.

To the best of our knowledge, no explicit calculations of EPR parameters for the OEC have been reported. Within the work of this thesis, we will fill this gap (see Chapter 8).

Chapter 3

The underlying physical laws necessary for the mathematical theory of a large part of physics and the whole of chemistry are thus completely known, and the difficulty is only that the exact solution of these laws leads to equations much too complicated to be soluble.

P. A. M. Dirac, 1929

Density-Functional Theory

3.1 Introduction

The ultimate goal for transition metal systems is to obtain thermochemical data, molecular structures, frequencies, transition-state structures, and activation barriers, as well as assignments of EPR, NMR, photoelectron, or UV spectra, by quantum-chemical methods. All these problems can be covered by *ab initio* Hartree-Fock (HF) and post-HF methods, which include electron correlation. However, these methods are computationally quite demanding and the scaling with the size of the system is unfavourable.

Since the beginning of the 1980s the development of density functional theory (DFT) methods have brought chemical accuracy due to the development of GGA and hybrid functionals.[1,2] In combination with the unbroken progress in computer technology, this method is the most powerful tool in our days for a reasonable computational cost to study large systems such as transition metal complexes. The 1998 Nobel Prize to John Pople and Walter Kohn is the most evident documentation for the importance of computational methods in general and DFT in particular.

In this thesis, a main focus will be on exchange-coupled metal systems having energetically close lying electronic levels that would, therefore, require a multi-determinant based treatment for a correct description of the real antiferromagnetic state. For large systems like multinuclear manganese complexes, this approach is too expensive. Therefore, broken-symmetry density-functional theory (BS-DFT) is the most widely used possibility to overcome this problem.

This chapter shall give a short overview of elementary quantum chemical principles, which are necessary to understand DFT (section 3.2). Furthermore, basic concepts of DFT are reviewed in section 3.3 to understand the subsequent chapters of this thesis. For a deeper understanding of DFT, the books of Parr and Yang[3] and Koch and Holthausen[4] are recommended. Section 3.4 will briefly explain BS-DFT. The system of atomic units will be employed to all equations (electronic charge e = 1, electronic mass m_e = 1, Planck's constant $h = 2\pi$, $4\pi\varepsilon_0$=1, speed of light $c \approx 137.036$).

3.2 Elementary Quantum Chemistry

3.2.1 Schrödinger Equation

The time-independent, non-relativistic Schrödinger equation describes a molecular system consisting of N electrons and M nuclei:

$$\widehat{H}_{total}\Psi\left(\boldsymbol{r}_N, \boldsymbol{R}_M\right) = E_{total}\Psi\left(\boldsymbol{r}_N, \boldsymbol{R}_M\right). \tag{3.1}$$

The corresponding Hamilton operator $\widehat{H}$ is described by the position vectors $\boldsymbol{r}_N$ and $\boldsymbol{R}_M$ and acts on the wave function to return the energy E of the system as its eigenvalue:

$$\widehat{H}_{total} = -\sum_{i=1}^{N}\frac{1}{2}\nabla_i^2 - \sum_{A=1}^{M}\frac{1}{2m_A}\nabla_A^2 - \sum_{i=1}^{N}\sum_{A=1}^{M}\frac{Z_A}{r_{iA}} - \sum_{i=1}^{N}\sum_{j>i}^{N}\frac{1}{r_{ij}} + \sum_{A=1}^{M}\sum_{B>A}^{M}\frac{Z_A Z_B}{R_{AB}}. \tag{3.2}$$

The *Born-Oppenheimer* approximation simplifies the complicated Schrödinger equation. Due to the huge difference in mass between electrons and nuclei, the rapid movement of the electrons can be separated from the much slower movement of the

nuclei, assuming that the electrons follow the nuclei instantaneously during the motion of the latter.

The resulting electronic Hamiltonian can be written as

$$\widehat{H} = -\sum_{i=1}^{N}\frac{1}{2}\nabla_i^2 - \sum_{i=1}^{N}\sum_{A=1}^{M}\frac{Z_A}{r_{iA}} - \sum_{i=1}^{N}\sum_{j>i}^{N}\frac{1}{r_{ij}} = \widehat{T} + \widehat{V}_{Ne} + \widehat{V}_{ee}\ . \tag{3.3}$$

The nuclei are fixed in space, their kinetic energy is zero and the potential energy due to nucleus-nucleus repulsion is a constant. $\widehat{T}$ is the kinetic energy and $\widehat{V}_{ee}$ is the potential energy of the electrons. In DFT, the potential energy due to nucleus-electron attraction $\widehat{V}_{Ne}$ is often termed the external potential, and might include also external magnetic or electric fields.

3.2.2 Solutions for the Schrödinger Equation: The Hartree-Fock Approximation

Finding a solution for the non-relativistic, time-independent Schrödinger equation (3.1) is one of the crucial tasks of quantum chemistry. An exact solution can be obtained only for one-electron systems. Hartree introduced in 1927[5] one of first and simplest approximations to solve the Schrödinger equation for more than one electron. However, electrons are fermions with spin of 1/2 and hence the wavefunction must be antisymmetric. Therefore, Fock and Slater proposed in 1930[6,7] a variational ansatz for the total wavefunction that takes the form of a normalized so-called *Slater determinant*

$$\Psi_{SD}(r_1,...,r_N) = \frac{1}{\sqrt{N!}}\begin{vmatrix} \psi_1(r_1) & \cdots & \psi_N(r_1) \\ \vdots & \ddots & \vdots \\ \psi_1(r_N) & \cdots & \psi_N(r_N) \end{vmatrix}. \tag{3.4}$$

Here, the wavefunction fulfills the *antisymmetric* behaviour (*Pauli's exclusion principle*), and changes sign when any pair of one-electron coordinates is swapped. The one-electron wave functions $\psi_N(r_N)$ (*spin orbitals*) are composed of a *spatial orbital* $\phi(r)$ and one *spin function* $\sigma(s)$ (α or β):

$$\psi_N(r_N) = \phi(r)\sigma(s)\,. \tag{3.5}$$

The spin orbitals have to be orthonormal, the spatial orbitals are usually calculated under the constraint of them being orthonormal.

The electronic Hamiltonian for a many-electron system can be written in terms of one- and two-electron parts:

$$\hat{h}_i = -\frac{1}{2}\nabla_i^2 - \sum_A^M \frac{Z_A}{r_{iA}} \text{ and} \tag{3.6}$$

$$\hat{g}_{ij} = \frac{1}{r_{12}}. \tag{3.7}$$

From evaluating the energy as an expectation value of the Hamiltonian, we obtain

$$E = \left\langle \Psi_{SD} \middle| \hat{H} \middle| \Psi_{SD} \right\rangle = \sum_i^N \left(i \middle| \hat{h} \middle| i \right) + \frac{1}{2}\sum_i^N \sum_j^N \left(ii \middle| jj \right) - \left(ij \middle| ji \right). \tag{3.8}$$

The two-electron terms (*ii*|*jj*) and (*ij*|*ji*) are the so-called *Coulomb* and *exchange* integrals, respectively:

$$\left(ii \middle| jj \right) = \int\int |\psi_i(r_1)|^2 \frac{1}{r_{12}} |\psi_j(r_2)|^2 \, \mathrm{d}r_1 \mathrm{d}r_2 \text{ and} \tag{3.9}$$

$$\left(ij \middle| ji \right) = \int\int \psi_i(r_1)\psi_j^*(r_1)\frac{1}{r_{12}}\psi_j(r_2)\psi_i^*(r_2)\mathrm{d}r_1\mathrm{d}r_2. \tag{3.10}$$

Let us introduce the effective one-electron Fock operator $\hat{f}$

$$\hat{f} = -\frac{1}{2}\nabla_i^2 - \sum_A^M \frac{Z_A}{r_{iA}} + V_{HF}(r_i), \tag{3.11}$$

leading to the *Hartree-Fock* equations

$$\hat{f}\psi_i = \varepsilon_i \psi_i. \tag{3.12}$$

In eq. (3.12), the *Lagrangian multipliers* ε_i have the physical interpretation of *orbital energies*. The idea of the Hartree-Fock method is to put all electron-electron interactions, the local *Coulomb operator* $\hat{J}$ and the non-classical, non-local *exchange operator* $\hat{K}$, in the HF potential

$$V_{HF}(r_i) = \sum_j^N \left(\hat{J}_j(r_1) - \hat{K}_j(r_1) \right), \text{ with} \tag{3.13}$$

$$\hat{J}_j(r_1) = \int \left| \psi_j(r_2) \right|^2 \frac{1}{r_{12}} dr_2 \text{ and} \tag{3.14}$$

$$\hat{K}_j(r_1)\psi(r_1) = \int \psi_j(r_2)^* \frac{1}{r_{12}} \psi_i(r_2) dr_2 \psi_j(r_1) . \tag{3.15}$$

In eq. (3.8), the double summation and thus the term i = j is allowed and describes the Coulomb interaction of the charge distribution of one electron with itself. This *self interaction* has no physical sense. However, due to opposite sign of the exchange integral in the case i = j, this self-interaction is cancelled. Unfortunately, this self-interaction problem is not solved yet in DFT (see below).

Even though the Hartree-Fock approximation represents an immense simplification compared to the Schrödinger equation, the resulting equations are still too complicated to be solved exactly for most system of chemical interest. In the so-called LCAO method, we can take advantage of our chemical knowledge. A molecule orbital $\phi_i(r)$ can be expanded as a *Linear Combination of (approximate) Atomic Orbitals* $\chi_p(r)$

$$\phi_i(r) = \sum_{p=1}^N C_{pi} \chi_p(r) . \tag{3.16}$$

The atomic orbitals $\chi_p(r)$ are generally not the solutions to the atomic problem and are just the functions of the coordinates of a single electron, the so-called *basis functions*. In chemistry, Gaussian basis functions are widely used, only some present day calculations are performed with Slater type orbitals, plane waves or numerical basis functions. In solid-state physics, especially plane waves are of great importance.

Within the LCAO scheme, the energy has to be minimized with respect to the coefficients C_{pi} which specify the MOs. This leads to the *Roothaan-Hall equations*[8, 9]

$$\boldsymbol{FC} = \boldsymbol{SC\varepsilon}\,, \tag{3.17}$$

where $\boldsymbol{F}$ is the Fock matrix, $\boldsymbol{C}$ is a M×M square matrix of the coefficients C_{pi}, $\boldsymbol{S}$ is the overlap matrix, and $\boldsymbol{\varepsilon}$ is the diagonal matrix of SCF orbital energies.

The Fock matrix is defined from atomic orbitals. Initially, a set of orbitals is guessed to obtain an approximate Fock operator. The Fock operator can be diagonalized to obtain a new set of orbitals, which replace the old ones in constructing a new Fock operator, and so on. After a certain number of iterations, the orbitals do not change anymore from one iteration to the next, i.e. *convergence* is found. This procedure is called *self-consistent field* (SCF).

Furthermore, an exact or almost exact numerical solution for the HF equations is rather difficult to obtain except for atoms or diatomic molecules. The most powerful tool to obtain approximate solutions is the variation method based on the *variational principle*. It implies that the true ground state energy E_0 is always lower than the HF energy E_{HF} and can be applied to obtain the HF energy

$$E_{HF} = \min_{\Psi_{SD}\to N} E\left[\Psi_{SD}\right]. \tag{3.18}$$

In summary, the HF method is based on three approximations: a) the total electronic wave function is approximated by one single Slater determinant, b) the self-consistent field (SCF) method is used to find an appropriate set of spin orbitals $\psi_N(r_N)$ to describe the ground state of the system, and c) the electron correlation is neglected.

According to Löwdin,[10] the *correlation energy* is defined as

$$E_C^{HF} = E_0 - E_{HF}\,. \tag{3.19}$$

The correlation of electrons due to instantaneous repulsion is not covered in the HF potential and is often divided into *dynamical* and *non-dynamical* or *static* correlation. The *dynamical* correlation is a short range effect and comes from the actual motions of the individual electrons. So-called post-HF methods like Configuration Interaction (CI),

Perturbation Theory (e.g. Møller-Plesset) or Coupled-Cluster (CC) are appropriate to recover dynamical correlation.

For molecules having more than one ground state Slater determinant with comparable energies, the single-determinant approach fails because one ground state Slater determinant is not sufficient to describe the true ground state. This effect is called *non-dynamical* or *static* correlation. It can be important in open-shell systems like excited states or transition metals. This effect can usually be dealt by multiconfigurational SCF (MCSCF) techniques such as the complete active space SCF (CASSCF) scheme.

However, all these wavefunction-based methods become computationally expensive for large systems because the wave function for an N electron system depends on $3N$ coordinates ($4N$ if spin is included). Therefore, in density-functional theory (DFT) only the density, depending only on 3 coordinates independent on the size of the system, has to be determined to get the ground-state electronic energy. Furthermore, non-dynamical correlation in systems having energetically close lying electronic levels can also be treated in DFT using the so-called *broken-symmetry DFT* (BS-DFT, see below).

3.3 Density-Functional Theory

3.3.1 The Hohenberg-Kohn Theorem

The first Hohenberg-Kohn theorem[11] established that the ground state of an electronic system with N electrons is just a functional of the electronic density, which is defined by

$$\rho(r) = N \int ... \int \left|\Psi(r_1, r_2, ..., r_N)\right|^2 ds_1 dr_2 ... dr_N \ . \tag{3.20}$$

Given a known density $\rho(r)$, one could form the Hamilton operator, solve the Schrödinger equation, and determine the wave functions and energy eigenvalues, and, hence, all the properties of the system. Therefore, in DFT only three variables are needed for an N-electron system (or four if spin is included) compared to Hartree-Fock theory (see above).

The electronic energy can, therefore, be represented as a *functional* of the density

$$E[\rho] = V_{Ne}[\rho] + T[\rho] + V_{ee}[\rho] = \int \rho(r) v(r) dr + F[\rho], \tag{3.21}$$

where $T[\rho]$ is the kinetic energy and $V_{ee}[\rho]$ is the electron-electron interaction energy. The Hohenberg-Kohn functional $F[\rho]$ is a universal functional of ρ:

$$F[\rho] = T[\rho] + V_{ee}[\rho] = \left\langle \Psi \left| \hat{T} + \hat{V}_{ee} \right| \Psi \right\rangle, \tag{3.22}$$

where $V_{ee}[\rho]$ can be split into a well known classical Coulomb part $J[\rho]$ and a nonclassical term $E_{ncl}[\rho]$. This Hohenberg-Kohn functional could in principle give an exact solution of the Schrödinger equation. Nevertheless, no accurate Hohenberg-Kohn functional is known, and especially the kinetic energy functional is rather difficult to approximate.

The second Hohenberg-Kohn theorem introduces the variational principle in DFT (see also above). The approximate density $\tilde{\rho}$ determines $\tilde{\upsilon}$ and, hence, the corresponding wavefunction $\tilde{\Psi}$, which can be used in the usual variational principle

$$\left\langle \tilde{\Psi} \left| H \right| \tilde{\Psi} \right\rangle = \int \tilde{\rho}(r) \upsilon(r) dr + F\left[\tilde{\rho}\right] = E\left[\tilde{\rho}\right] \geq E[\rho]. \tag{3.23}$$

3.3.2 Kohn-Sham Theory

Kohn and Sham introduced in 1965[12] the so-called Kohn-Sham (KS) orbitals in such a way that the largest part of the kinetic energy can be computed simply to good accuracy *via* a non-interacting reference system.

Let us start with the separation of the Hohenberg-Kohn functional $F[\rho]$ from eq. (3.22) into the kinetic energy of a system with non-interacting electrons $T_S[\rho]$, the classical Coulomb repulsion $J[\rho]$, and the term $E_{xc}[\rho]$, which is by definition the exchange and correlation energy of an interacting system. It follows that the exchange-correlation energy is

$$E_{xc}[\rho] = T[\rho] - T_S[\rho] + V_{ee}[\rho] - J[\rho]. \tag{3.24}$$

Inserting $E_{xc}[\rho]$ into eq. (3.21) leads to the Kohn-Sham energy expression

$$E[\rho] = \int \rho(r) v(r) dr + T_S[\rho] + J[\rho] + E_{xc}[\rho]. \tag{3.25}$$

Let us consider the determinantal wavefunction for *N* non-interacting electrons in *N* Kohn-Sham (KS) orbitals ψ_i, which are almost always expanded in basis sets because the Kohn-Sham orbitals (unlike the density) assume a complicated shape. The sum of the squares of the occupied KS orbitals is the true density of the real system. The orbitals obey equations similar to the HF equations of the form

$$\left[-\frac{1}{2}\nabla^2 + \upsilon_s(r) \right] \psi_i = \varepsilon_i \psi_i, \tag{3.26}$$

with the Kohn-Sham operator

$$\hat{f}^{KS} = -\frac{1}{2}\nabla^2 + \upsilon_s(r). \tag{3.27}$$

Combining eqs. (3.26), and (3.27) leads to the *Kohn-Sham equations*

$$\left[-\frac{1}{2}\nabla^2 + \upsilon(r) + \int \frac{\rho(r')}{|r - r'|} dr' + \upsilon_{xc}(r) \right] \psi_i = \varepsilon_i \psi_i. \tag{3.28}$$

The functional derivative is the exchange-correlation potential υ_{xc} and describes the fact that every electron tries to both maximize the attraction from the nuclei, and minimize the repulsion from the other electrons:

$$\upsilon_{xc} = \frac{\delta E_{xc}[\rho]}{\delta \rho(r)}. \tag{3.29}$$

These equations give *in principle* the *exact density*, once the exact exchange-correlation functional $E_{xc}[\rho]$ has been determined. Compared to the Hohenberg-Kohn description, eq. (3.28) is much more approximate due to the exchange-correlation potential, which is only a functional of the density. Furthermore, not only the exchange in the HF sense, but also the correlation is included in this approach. Analogously to the HF equations, the KS equations can be solved iteratively.

3.3.3 Functionals

The exact exchange-correlation energy functional is not known, and approximations have to be used. There are four widely used approaches: 1) *Local density approximation* (LDA) with a dependence only of the density, 2) *Generalized gradient approximation* (GGA) applying the density and its gradients, 3) *Meta GGAs* using beside the density and its gradient also higher derivates of the density and the kinetic energy density, and 4) *Hybrids* including also exact exchange admixture. Furthermore, the proper Kohn-Sham local and multiplicative self-consistent treatment of hybrid functionals within the framework of the *optimized effective potential* (OEC) was recently reported.[13-17] Localized hybrid potentials have been obtained within the localized Hartree-Fock(CEDA approximation to the OEC method).[18-20]

In the LDA, the local density is treated like a uniform electron gas, assuming that the density varies very slowly. The main advantage of LDA is that the exact analytical form of the exchange energy functional for the uniform electron gas is known (Slater exchange)[21] and the correlation energy of a uniform electrons gas has already been determined by quantum Monte Carlo methods.[22] For utilizing these results in DFT, interpolations are necessary. The interpolation formula of Vosko, Wilk and Nusair (VWN)[23] is regarded as relatively exact, and was later updated by Perdew and Wang.[24]

However, bond lengths calculated by the LDA approximation are too short, except for hydrogen bondings which are too long. These facts limited the use of the LDA approximation in chemistry.

Both the density and its gradients are used in the GGA method. In 1986, the first gradient corrected functionals were determined (exchange by Becke,[25] and Perdew and Wang,[26] and correlation by Perdew[27]). The most utilized functionals are the exchange part of Becke[28], and the correlation part of Perdew[27] or Lee, Yang and Parr (LYP).[29] Due to the inclusion of dynamical correlation and the good results in thermochemistry, this method is quite popular in chemistry. In general, bond lengths can be quite reasonable, but barriers are underestimated due to the fact that GGAs are not self-interaction free.

Except TPSS,[21,24,30,31] meta GGAs are not widely used in chemistry because the introduction of higher derivates of the density and the kinetic energy density has not lead to major improvements.

Hybrid functionals contain both DFT exchange and Hartree-Fock type exchange calculated from the orbitals. One of the most popular hybrid exchange-correlation hybrid functionals is the B3LYP[32,33] functional with 20% exact exchange energy E_x^0 (b = 0.72, c = 0.81), generally leading to remarkably good results for thermochemistry and structures of transition metal compounds:

$$E_{xc}^{B3LYP} = aE_x^0 + (1-a)E_x^{Dirac} + b\Delta E_x^{B88} + (1-c)E_c^{VWN} + cE_c^{LYP}. \qquad (3.30)$$

The influence of exact-exchange admixture is for transition-metal complexes very important.[34-36] Exact-exchange admixture has usually three major effects on the spin-density distribution:[34-36] a) the metal-ligand bond becomes more ionic (self-interaction errors tend to render the bonds too covalent at LDA or GGA level),[35-40] and b) valence-shell spin polarization across covalent bonds is enhanced, leading often to larger spin contamination,[35] c) core-shell spin polarization at the metal center is also enhanced (improved). However, even hybrid functionals are not self-interaction free and have problems with long-range properties.

3.4 Broken-Symmetry Density-Functional Theory

In the Kohn-Sham formalism, DFT uses a fictitious single determinant reference to represent the density of the system. However, open-shell multiplets e.g. in multinuclear transition metal complexes, require a multideterminant wavefunction for a qualitatively correct picture. Indeed, using existing functionals, one typically encounters spin-contaminated BS determinants in calculations on open-shell multiplets. The basic idea of BS-DFT is to mimic a multiplet for a molecule with two spin centers A and B by a single determinantal BS solution, which has excess α spin on spin center A and excess β spin on spin center B, and, hence, the spin symmetry is broken.

Starting point is the following wave function

$$\psi_{BS}^{guess} = \left|(core)\varphi_A\overline{\varphi}_B\right|. \tag{3.31}$$

This determinant defines not yet the broken symmetry state, and it has three remarkable properties. Firstly, its energy E_{BS}^{guess} is always higher than the energy of the corresponding high-spin (HS) state, which can be easily described by a single determinant DFT approach, and possesses, therefore, little spin contamination. Secondly, the wavefunction defined by eq. (3.31) is a mixture of 50% of the high-spin wavefunction ψ_{HS} and of 50% of the wavefunction of the antiferromagnetic state ψ_{AF}. The third property of wavefunction (3.31) is important for our calculations on EPR parameters, because ψ_{BS}^{guess} exhibits the same charge density but a different spin-density than ψ_{AF}. Therefore, spin-projection techniques are needed to obtain the appropriate g-tensors and hyperfine coupling constants (see section 4.10).

To obtain from wavefunction ψ_{BS}^{guess} a wavefunction ψ_{BS}, which is able to describe the antiferromagnetic coupling properly, the variational principle has to be applied to re-optimize the orbitals.[41] The true broken-symmetry wavefunction ψ_{BS} is given by

$$\psi_{BS} = \left|(core')\varphi'_A\overline{\varphi'}_B\right|. \tag{3.32}$$

The non-orthongonal relaxed orbitals φ'_A and $\overline{\varphi}'_B$ are generally less localized than the orthogonal orbitals φ_A and $\overline{\varphi}_B$ from the intial guess. This additional flexibility allows to lower the energy of ψ_{BS}, which is not any more an equal mixture of ψ_{HS} and ψ_{AF}.

In order to obtain the coupling strengths of the two spin centers, the energies E_{BS} and E_{HS} can mapped onto the Heisenberg Hamiltonian to obtain the Heisenberg exchange coupling constant *J*. Different mapping schemes for dinuclear complexes will be presented in the subsequent section.

3.4.1 Mapping Schemes for Dinuclear Complexes

The Heisenberg exchange coupling constant *J* describes the magnetic coupling between localized spins in the Heisenberg-Dirac-van Vleck Hamiltonian

$$\hat{H}_{HDvV} = -2J\vec{S}_A\vec{S}_B, \tag{3.33}$$

where $\vec{S}_A$ and $\vec{S}_B$ are spin operators on centers A and B, respectively.

For weakly coupled molecular fragments between which the magnetic orbital overlap is small Noodleman[42] has defined *J* as

$$J = -\frac{E_{hs} - E_{bs}}{4S_AS_B}, \tag{3.34}$$

where E_{hs} and E_{BS} are the energies of the high-spin and broken-symmetry spin states, respectively, and S_A and S_B are the individual spins.

Implying a strong interaction limit, Alvarez *et al.*[43-45] proposed the following relationship

$$J = -\frac{E_{hs} - E_{bs}}{2\left(2S_AS_B + S_B\right)}. \tag{3.35}$$

These two treatments from Noodleman (small interaction limit) and Alvarez (strong interaction limit) can differ by a factor of two. For antiferromagnetically coupled manganese systems, the weak interaction case is certainly more realistic.

A more general formula, which treats the projections of Noodleman and Alvarez as special cases, is the suggestion of Yamaguchi and coworkers[46] to compute J as

$$J = -\frac{E_{hs} - E_{bs}}{\left\langle \vec{S}^2 \right\rangle_{hs} - \left\langle \vec{S}^2 \right\rangle_{bs}}, \tag{3.36}$$

where $\left\langle \vec{S}^2 \right\rangle_{hs}$ and $\left\langle \vec{S}^2 \right\rangle_{bs}$ are the computed total spin angular momentum expectation values for the high-spin and broken-symmetry spin states, respectively. This scheme is supposed to be independent of the bonding situation and hence usuable for any coupling strength.

3.4.2 Corresponding Orbital Transformation and Paired-Orbital Analysis

The SOMOs that are involved in the magnetic interaction are frequently not the highest occupied orbitals due to spin-polarization effects.[47] To properly identify the magnetic orbitals, Amos *et al*. have developed the so-called *corresponding orbital transformation* (COT).[48] The magnetically active orbitals may already be identified by computing the *natural orbitals* (NO's) of the system. Natural orbitals are defined by Löwdin[49] as the eigenfunctions of the spinless one-particle electron density matrix. These orthogonal NO's may be subsequently transformed to *paired orbitals* (PO's), where corresponding magnetic pairs are identified by their small finite (non-integer) overlap. For the transformed POs each occupied spin-up orbital has a spatial overlap unequal zero with at most one spin-down orbital. Three subsets of orbitals exist:

1) doubly occupied spin-up/spin-down pairs with a spatial overlap of nearly 1.00,
2) non-orthogonal singlet coupled magnetic pairs, and
3) unmatched spin-up orbitals (SOMOs).

Furthermore, based on this paired-orbital (PO) transformation,[48] it is possible to analyze the nature of the BS-KS wavefunction more closely. In particular, the origin of the spin contamination may be traced back to a limited number of PO pairs, following an expansion of the unrestricted wavefunction Ψ^U into quasi-restricted determinants in the PO basis:[50,51]

$$\Psi^U = C^0 D^0 + \sum_{i=1}^{k} C_i^1 D_i^1 + \sum_{i<j}^{k} C_{ij}^2 D_{ij}^2 + ... + C^k D^k \ . \tag{3.37}$$

C_i are the expansion coefficients, k is the number of corresponding orbitals, and D the set of restricted determinants obtained by substitutions of “occupied” by “virtual” PO’s.[50]

Chapter 4

There is an infinite number of wrong ways to get the right answer.

A. D. McLean

Calculation of Electron Paramagnetic Resonance Parameters

4.1 Introduction

Electron paramagnetic resonance (EPR) spectroscopy is a technique that probes certain properties and the environment of a paramagnetic center by characterizing the interaction of that center with an applied magnetic field. Any species containing one or more unpaired electrons can be investigated, including inorganic and organic free radicals, and systems that contain transition metal ions. Especially for analyzing bioinorganic open-shell sites, such as the oxygen-evolving complex (OEC), EPR spectroscopy is one of the most powerful tools. The spin and oxidation states, which are especially interesting for redox systems, as well as the coordination sphere of the metal center, can be determined. Therefore, important insights into molecular and electronic structure, into dynamics, and ultimately into the mechanism of electron-transfer systems in biology may be provided by modern EPR methods. However, the measured EPR spectra of biological systems are usually very complex, and quantum chemical calculations of EPR parameter of corresponding model systems are extremely valuable to correlate the spectra with the above-mentioned molecular properties.

First, basic backgrounds of EPR spectroscopy will be shortly presented (section 4.2). Some results presented in this thesis evolved from fruitful collaborations with spectroscopists. Thus, section 4.3 briefly reports widely used experimental techniques. Subsequently, the theory of the effective spin Hamiltonian, which provides the essential link between theory and experiment will be introduced (section 4.4). The concept of electron spin will be briefly recalled in section 4.5. From section 4.5 on, dimensionless atomic units will be applied. Section 4.6 summarizes the perturbation theory applied to magnetic resonance parameters which turns out to be the most systematic framework for property calculations. In this thesis, the focus will be on the calculation of g-tensors, hyperfine coupling (HFC), and nuclear quadrupole coupling (NQC) constants. Therefore, the theoretical formalism of these parameters will be shortly reviewed in sections 4.7, 4.8, and 4.9, respectively, following the fundamental textbooks on EPR theory.[1-4] Section 4.10 reports spin-projection techniques, which are required to obtain magnetic resonance parameters of multinuclear systems.

4.2 Basic Principles

EPR spectroscopy is based on the information that can be gained from the interaction of electromagnetic radiation with the magnetic moments of the electrons.[1-4] A free electron having the spin angular momentum $\vec{S}$ possesses a corresponding magnetic dipole moment of

$$\vec{\mu}_e = g_e \beta_e \vec{S}\,, \tag{4.1}$$

where g_e is the g-factor of a free electron (2.002319) and β_e Bohr's magneton. The free electron in vacuum has two eigenstates with respect to its spin: |+1/2> and |-1/2> (details about the properties of the spin are given in section 4.5). In the presence of an external magnetic field B_0 the electron can be aligned parallel or antiparallel to the field. Hence, the electron spin can flip by the absorption/emission of virtual magnetic photons and the energy separation ΔE between the spin states is given by

$$\Delta E = g_e \beta_e B_0\,. \tag{4.2}$$

In EPR spectroscopy, the electron spin transitions between different electron Zeeman levels are stimulated. The observables in an EPR experiment are the electronic *g-value*, the *line shape*, and the *multiplet structure* or *hyperfine structure*.

Generally, the *g-value g* can be measured with very high precision in EPR experiments. The more fundamental equation for the determination of the g-factor of an atom or molecule with an S = 1/2 state is:

$$h\upsilon = g\beta_e B_0 , \tag{4.3}$$

with υ is the irradiated microwave frequency. The theoretical background concerning the g-tensor will be presented in section 4.7.

An analysis of the *line shape* can e.g. determine rate constants of dynamic processes.

The *hyperfine structure* is probably most interesting for the chemist. The scalar and the dipolar coupling of the unpaired electron with magnetic nuclei lead to splitting of the electronic Zeeman level into hyperfine sublevels and thus to additional EPR transitions. This multiplet structure can often be resolved only insufficiently, in particular of large transition metal systems such as the OEC.

4.3 Experimental Techniques

The purpose of this section is to describe briefly the essential features of experimental techniques.[1-4]

EPR spectroscopy is a very sensitive spectroscopic technique and provides useful information about the environment and electronic geometry of systems containing unpaired electrons by characterizing the interaction of the paramagnetic center with an applied magnetic field. Transitions between electron spin states can be induced by on-resonant electromagnetic microwave radiation. Typically, the frequency is set to a fixed value (X-band 9.5 GHz, Q-Band 35 GHz, and W-Band 95 GHz), and the magnetic field is varied in search of resonance. This standard instrumentation is called continuous wave (CW) spectrometer. For many years, EPR spectroscopy was dominated by CW methods. Recently, pulse EPR techniques become the more and more important.

Most of the EPR experiments are still performed at X-band. However, in EPR spectroscopy samples are often run at more than one frequency. This helps to interpret the

spectral features because the effective spin Hamiltonian (see below) can be broken into a field dependent part (Zeeman terms) and a field independent part (e.g. zero-field terms). Especially, advances in high-field EPR (HF-EPR) spectroscopy offer new opportunities for the investigation of paramagnetic metal ion sites. Higher frequency data are of enormous value due to an increasing of the resolution of the g-anisotropy. Therefore, distinguishing spectra features due to g-anisotropy from those due to hyperfine and other interactions becomes possible.

Electron Nuclear Double Resonance (*ENDOR*) experiments rely on the interaction of nuclear and electron spins. Due to introducing additional selection rules, a resolution of the hyperfine signals of different nuclei becomes possible, e.g. ^{1}H, ^{2}H, ^{13}C, ^{14}N, and ^{55}Mn.

Another important method to study hyperfine signals is the so-called *ESEEM* (Electron Spin Echo Envelope Modulation) experiment. A significant feature of especially ESEEM spectroscopy of metal complexes is to obtain metal-ligand nuclei distances and angles. Especially the possibility to localize protons is an enormous advantage of these methods compared to XRD experiments.

ESEEM and ENDOR are complementary techniques. ESEEM is used to study the more distant weakly coupled nuclei with HFC constants less than about 10 MHz, and ENDOR is preferred for investigations of more strongly coupled closer nuclei having hyperfine values in the range of 2 – 40 MHz. Both techniques can be used to obtain quadrupole coupling constants. In recent years, there has been increased emphasis on pulsed ENDOR spectroscopy. Due to this method, the detection of nuclei coupled to the electron spin that might otherwise not be observed in CW experiments becomes possible. Furthermore, multidimensional ESEEM experimental techniques have emerged. This facilitates the assignment and analysis of ESEEM spectra for the purposes of structure determination.

However, spectral simulations using perturbation theory are usually carried out to obtain the EPR parameters. Not all EPR parameters are taken into account to simulate the spectra and, therefore, sometimes large approximations are assumed in the simulations (e.g. axial symmetry, neglecting the nuclear quadrupole coupling, sign of the EPR parameters, see also Chapter 8). Therefore, it should be noted that experimental data have often to be considered carefully.

Finally, some common classification of symmetry specifications used in solid-state EPR are given:

a) *Isotropic*: requires x, y and z to be degenerated, i.e. all three components of the EPR property are the same.
b) *Axial:* requires the presence of at least a threefold axis of rotation, which makes x and y degenerated, i.e. two principal values of the EPR tensor are equal but differ from the third one.
c) *Rhombic:* belongs to point groups where x, y and z are all singly degenerated, i.e. all three principal values are different.

4.4 Effective Spin Hamiltonian

The effective spin Hamiltonian $\hat{H}_{eff}$ relates theory and experiment. The spectra are analyzed in terms of this phenomenological energy expression for a limited number of degrees of freedom. It includes all magnetic interactions arising from the spin magnetic moments of electrons $\vec{S}$ and of nuclei $\vec{I}_N$, e.g.:

$$\hat{H}_{eff} = \vec{S}\mathbf{D}\vec{S} + \beta\vec{B}\mathbf{g}\vec{S} + \sum_N \vec{S}\mathbf{A}\vec{I}_N + \sum_{M<N} \vec{I}_M\mathbf{Q}\vec{I}_N \,. \tag{4.4}$$

The eigenvalues of the numerical parameters in eq. (4.4) correspond to the observed levels. The zero-field splitting (ZFS) **D** describes the interaction of the electron spins ($< 10^{-3}$ cm^{-1}). The g-tensor **g** parameterizes the interaction of the total electronic magnetic dipole moment and the external magnetic field $\vec{B}$ (0 – 10 cm^{-1}), the hyperfine coupling (HFC) tensor **A** the interaction of the total electronic spin with nuclear spins (< 1 cm^{-1}), and the quadrupole interaction **Q** the interaction of the nuclear quadrupole moment (spin $I > ½$) with the total electric field gradient at the nucleus (< 0.01 cm^{-1}).

4.5 Spin

The spin was first experimentally detected in the famous Stern and Gerlach experiment in 1921[5] and is a natural consequence of the Dirac equation which describes the relativistic motion of a single electron.[6] The Dirac equation contains a four-component relativistic wave function $\boldsymbol{\Psi}$

$$-\frac{\hbar}{i}\frac{\partial \boldsymbol{\Psi}}{\partial t} = \left(\frac{hc}{i}\nabla \boldsymbol{\alpha} + \boldsymbol{\beta} mc^2\right)\boldsymbol{\Psi}, \tag{4.5}$$

where m is the rest mass of the electron, c is the speed of light, and $\boldsymbol{\alpha}$ and $\boldsymbol{\beta}$ are 4×4 matrices.

The resulting four partial differential equations lead to two electronic and two positronic solutions. In chemistry, mainly two electronic solutions are of interest, leading to a two-component wavefunction. Within the first and second Pauli limit, the two component wave function can be furthermore reduced to a one-component equation. The resulting expression features the so-called *Breit-Pauli (BP) Hamiltonian*[1] which can be described for a many-electron molecule by

$$\widehat{H} = \widehat{H}_e + \widehat{H}_N + \widehat{H}_{eN}, \tag{4.6}$$

in which $\widehat{H}_e$ consists of 12 pure electronic contributions, the pure nucleus term $\widehat{H}_N$ comprises 4 contributions, and the electron-nucleus term $\widehat{H}_{eN}$ includes 6 terms. Details about the BP Hamiltonian are given in ref. [7]. The relevant contributions, which will be used in the framework of perturbation theory to calculate EPR parameters, will be given below.

The BP Hamiltonian provides, therefore, insight into electromagnetic behaviour by accounting explicitly for the appropriate terms. However, beside the spin operators, the BP Hamiltonian is also dependent on the electronic positions, electronic spins, nuclear positions and possible external electric fields, *etc*. These degrees of freedom can be averaged out and their effects on the additional variables are implicitly included in the *parameters* remaining in the so-called *effective spin Hamiltonian* (eq. (4.4)) which contains only *spin operators*.

4.6 Perturbation Theory applied to Magnetic Resonance Parameters

Magnetic properties can be defined within quantum mechanical perturbation theory as the derivative of the total energy of a molecule with respect to perturbation parameters arising from, e.g. external magnetic field, nuclear and electronic magnetic moments, relativistic effects, *etc*. In this section, it will first be shown how first-order derivatives of the energy of a molecule can be formulated and calculated. The general theory will then be applied to the calculation of EPR parameters.

The basic idea in magnetic resonance perturbation calculation of EPR parameters is to apply a perturbation V on top of the spin-free non-relativistic reference state:

$$\widehat{H}^{(0)} = -\sum_{i=1}^{N}\frac{1}{2}\nabla_i^2 - \sum_{i=1}^{N}\sum_{A=1}^{M}\frac{Z_A}{r_{iA}} - \sum_{i=1}^{N}\sum_{j>i}^{N}\frac{1}{r_{ij}}, \tag{4.7}$$

leading to the eigenvalue equation with the dimensionless ordering parameter λ

$$\widehat{H}\left|\Psi_i\right\rangle = \left(\widehat{H}^{(0)} + \lambda V\right)\left|\Psi_i\right\rangle = E_i\left|\Psi_i\right\rangle. \tag{4.8}$$

Employing the perturbation series expansion gives

$$E = E^{(0)} + E^{(1)}\lambda + E^{(2)}\lambda^2 + \ldots \text{ and} \tag{4.9}$$

$$\Psi = \Psi^{(0)} + \Psi^{(1)}\lambda + \Psi^{(2)}\lambda^2 + \ldots, \tag{4.10}$$

where $\psi^{(0)}$ is the solution of the unperturbed time-independent Schrödinger equation with the eigenvalue $E^{(0)}$ and the superscripts (n) denote the n^{th} order corrections.

Equations (4.9) and (4.10) can be substituted into eq. (4.8). After collecting the terms of same powers in λ, multiplying all equations by $\left\langle\Psi^0\right|$, and applying orthogonality relations, the following expressions for the n^{th} order energies are obtained in solving the unperturbed Schrödinger equation

$$E^{(0)} = \left\langle \Psi^{(0)} \middle| \widehat{H}^{(0)} \middle| \Psi^{(0)} \right\rangle, \tag{4.11}$$

$$E^{(1)} = \left\langle \Psi^{(0)} \middle| V \middle| \Psi^{(0)} \right\rangle, \tag{4.12}$$

$$E^{(2)} = \left\langle \Psi^{(0)} \middle| V \middle| \Psi^{(1)} \right\rangle. \tag{4.13}$$

The interested reader is referred to the textbooks of Szabo and Ostlund[8], Cramer,[9] and McWeeny.[3] Expanding $\left|\Psi^{(1)}\right\rangle$ in terms of eigenfunctions $\varphi^{(n)}$ of $\widehat{H}^{0}$ results in the typical 2nd order Rayleigh-Schrödinger expression

$$E^{(2)} = \sum_{n} \frac{\left\langle \varphi^{(0)} \middle| V \middle| \varphi^{(n)} \right\rangle \left\langle \varphi^{(n)} \middle| V \middle| \varphi^{(0)} \right\rangle}{E^{(0)} - E^{(n)}}. \tag{4.14}$$

Let us turn to the 2nd order perturbational treatment of EPR parameters. Expressions for the EPR parameters are obtained by combining, in the sense of perturbation theory, the terms of the Breit-Pauli Hamiltonian to various powers n in α^{2n}, in which α is the fine structure constant. That is suitable BP terms have to be chosen as perturbations to first or second order, such that the corresponding correction terms exhibit the same dependence on the magnetic field and electron or nuclear spins as the effective spin Hamiltonian term. The EPR parameters such as the g-tensor, hyperfine coupling, and the nuclear quadrupole coupling are then given as derivatives of the total molecular energy E:

$$\mathbf{g} = \frac{1}{\mu_B} \frac{\partial^2 E}{\partial \boldsymbol{B} \partial \boldsymbol{S}}\bigg|_{\boldsymbol{B}=0, \boldsymbol{S}=0} \tag{4.15}$$

$$\mathbf{A} = \frac{\partial^2 E}{\partial \boldsymbol{I}_N \partial \boldsymbol{S}}\bigg|_{\boldsymbol{I}_N=0, \boldsymbol{S}=0} \tag{4.16}$$

$$\mathbf{Q} = \frac{\partial^2 E}{\partial \boldsymbol{I}_M \partial \boldsymbol{I}_N}\bigg|_{\boldsymbol{I}_M=0, \boldsymbol{I}_N=0} \tag{4.17}$$

4.7 g-Tensor

The g-tensor describes the electronic Zeeman effect. Together with the zero-field splitting tensor, it serves as a convenient summary of the electronic transitions in EPR spectra. The observed energies and intensities correspond to the eigenstates obtained from the effective spin Hamiltonian (eq. 4.4). For not too heavy elements, the contributions to the g-tensor are quite small compared to the g-value of the free electron (g_e = 2.002319…), thus, the g-tensor will be provided as correction to g_e (in ppt, i.e. in units of 10^{-3})

$$\mathrm{g} = g_e 1 + \Delta\mathrm{g} \,. \tag{4.18}$$

Up to the level of the Breit-Pauli Hamiltonian, the electron-Zeeman effect consists of following contributions:[4,10-13]

$$\begin{aligned}\widehat{H} = \widehat{H}_{Zeeman}(S,B) + \widehat{H}_{RMC}(S,B) + \widehat{H}_{OZ}(B) \\ + \widehat{H}_{SO}(S) + \widehat{H}_{SO-GC}(S,B)\end{aligned} \,. \tag{4.19}$$

The first-order *electron-Zeeman interaction* is the most important contribution to the g-tensor arising from the interaction of the electronic spin $\boldsymbol{S}_i$ with the external magnetic field $\boldsymbol{B}$

$$\widehat{H}_{Zeeman}(S,B) = \frac{1}{2} g_e \sum_i \boldsymbol{S}_i \cdot \boldsymbol{B} \,. \tag{4.20}$$

The *spin-orbit operator* $\widehat{H}_{SO}(S)$ provides the largest contribution to the g-shift tensor and is of second-order. It consists of the *one-electron spin-orbit operator* $\widehat{H}_{SO(1e)}(S)$, the *two-electron spin-same-orbit operator* $\widehat{H}_{SSO(2e)}(S)$, and the *spin-other orbit term* $\widehat{H}_{SOO(2e)}(S)$:

$$\widehat{H}_{SO(1e)}(S) = \frac{1}{4}\alpha^2 g' \sum_{N,i} Z_N \frac{\boldsymbol{S}_i \cdot \boldsymbol{l}_{iN}}{\boldsymbol{r}_{iN}^3} \tag{4.21}$$

$$\widehat{H}_{SSO(2e)}(S) = \frac{1}{4}\alpha^2 g' \sum_{i,j} \frac{\boldsymbol{S}_i \cdot \boldsymbol{l}_{ij}}{\boldsymbol{r}_{ij}^3} \tag{4.22}$$

$$\widehat{H}_{SOO(2e)}(S) = -\alpha^2 \sum_{i,j} \frac{\boldsymbol{S}_i \cdot \boldsymbol{l}_{ij}}{\boldsymbol{r}_{ij}^3}, \tag{4.23}$$

where α is the fine structure constant, g' is the spin-orbit g'-factor (g' = $2g_e - 2$), and $\boldsymbol{l}$ are the angular momentum operators.

The *spin-orbit gauge-correction* $\widehat{H}_{SO-GC}(B,S)$ term results of the field-dependence of the origin of the magnetic vector potential to the choice of a computational coordinate system. Experiences with *ab initio* and DFT calculation indicate that the gauge dependence of the g-tensor is usually small.[4] Therefore, placing the gauge origin at the centroid of the electron charge is sufficient to obtain accurate results in small molecules. For larger systems, further approaches are widely used: GIAO (gauge-including atomic orbtals), IGLO (individual gauge origin for localized orbitals), and GIPAW (gauge-including projector-augmented waves.[4] The *spin-orbit gauge-correction* $\widehat{H}_{SO-GC}(B,S)$ term consists also of a one-electron $\widehat{H}_{SO-GC(1e)}(B,S)$ and a two-electron part $\widehat{H}_{SO-GC(2e)}(B,S)$:

$$\widehat{H}_{SO-GC(1e)}(B,S) = \frac{1}{8}\alpha^2 g' \sum_{N,j} Z_N \frac{\boldsymbol{S}_i \left(\boldsymbol{B}(\boldsymbol{r}_{iN} \cdot \boldsymbol{r}_{iO}) - \boldsymbol{r}_{iO}(\boldsymbol{r}_{iN} \cdot \boldsymbol{B}) \right)}{\boldsymbol{r}_{iN}^3} \tag{4.24}$$

$$\widehat{H}_{SO-GC(2e)}(B,S) = \frac{1}{8}\alpha^2 g' \sum_{N,j} Z_N \frac{\left(\boldsymbol{S}_i - 2\boldsymbol{S}_i \right) \left(\boldsymbol{B}(\boldsymbol{r}_{ij} \cdot \boldsymbol{r}_{iO}) - \boldsymbol{r}_{iO}(\boldsymbol{r}_{ij} \cdot \boldsymbol{B}) \right)}{\boldsymbol{r}_{ij}^3} \tag{4.25}$$

The *orbital-Zeeman* operator $\widehat{H}_{OZ}(B)$ describes the interaction between the external magnetic field $\boldsymbol{B}$ and the orbital magnetic moment $\boldsymbol{l}_{iO}$

$$\widehat{H}_{OZ}(B) = -\frac{1}{2} \sum_i \boldsymbol{l}_{iO} \cdot \boldsymbol{B}. \tag{4.26}$$

In the perturbation theory treatment of the g-tensor the external magnetic field, spin-orbit coupling and other relativistic terms are treated as perturbations.

Following expression results for the g-shift in the framework of double perturbation theory as a mixed second-order molecular property

$$\Delta g = \Delta g_{SO/OZ} + \Delta g_{RMC} + \Delta g_{GC} \,. \tag{4.27}$$

The „paramagnetic“ second-order spin-orbit/orbital Zeeman cross term, $\Delta g_{SO/OZ}$, dominates (except for extremely small Δg-values)[1]. The last two terms represent the “diamagnetic” first-order contributions and are rather small: Δg_{RMC} is the relativistic mass correction term and Δg_{GC} the one-electron part of the gauge correction term:[10-13]

$$\begin{aligned}\Delta g_{SO/OZ,uv} = \frac{1}{S}\Bigg[& \sum_{k}^{occ(\alpha)} \sum_{a}^{virt(\alpha)} \frac{\left\langle \psi_k^\alpha \middle| \widehat{H}_{SO,u} \middle| \psi_a^\alpha \right\rangle \left\langle \psi_a^\alpha \middle| \widehat{H}_{OZ,v} \middle| \psi_k^\alpha \right\rangle}{\varepsilon_k^\alpha - \varepsilon_a^\alpha} \\ & - \sum_{k}^{occ(\beta)} \sum_{a}^{virt(\beta)} \frac{\left\langle \psi_k^\beta \middle| \widehat{H}_{SO,u} \middle| \psi_a^\beta \right\rangle \left\langle \psi_a^\beta \middle| \widehat{H}_{OZ,v} \middle| \psi_k^\beta \right\rangle}{\varepsilon_k^\beta - \varepsilon_a^\beta} \Bigg]\end{aligned} \tag{4.28}$$

$$\Delta g_{RMC,uv} = \frac{1}{S}\delta_{uv}\left[\sum_{k}^{occ(\alpha)} \left\langle \psi_k^\alpha \middle| \widehat{H}_{RMC,uv} \middle| \psi_k^\alpha \right\rangle - \sum_{k}^{occ(\beta)} \left\langle \psi_k^\beta \middle| \widehat{H}_{RMC,uv} \middle| \psi_k^\beta \right\rangle \right] \tag{4.29}$$

$$\Delta g_{SO-GC,uv} = \frac{1}{S}\left[\sum_{k}^{occ(\alpha)} \left\langle \psi_k^\alpha \middle| \widehat{H}_{SO-GC,uv} \middle| \psi_k^\alpha \right\rangle - \sum_{k}^{occ(\beta)} \left\langle \psi_k^\beta \middle| \widehat{H}_{SO-GC,uv} \middle| \psi_k^\beta \right\rangle \right] \tag{4.30}$$

Here *S* is the effective spin quantum number allowing the application of the equations to the high-spin systems. $\psi_k^{\alpha/\beta}$ and $\psi_a^{\alpha/\beta}$ are unperturbed occupied and virtual α/β Kohn-Sham molecular orbitals, ε_k and ε_a are the corresponding eigenvalues.

Using hybrid functionals in DFT calculations, the orbital-Zeeman operator $\widehat{H}_{OZ}$ can be substituted by the so-called *Fock operator F'*:

$$F_v' = \frac{\boldsymbol{l}_v}{r^3} - \frac{2}{\alpha} a_0 \sum_{k=1}^{n/2} K_{k,v}' \,, \tag{4.31}$$

where ($\boldsymbol{l}_v/r^3$) is the paramagnetic nuclear-spin electron-orbit (PSO) operator, $K'_{k,v}$ is a component of the response exchange operator, and a_0 is the weight of HF exchange depending on the specific hybrid functional used.[14-16] GGA or LDA functionals lead to an uncoupled DFT (UDFT) treatment for this second-order term ($a_0 = 0$).

4.8 Hyperfine Coupling Constant

The hyperfine coupling parameter describes the interaction of unpaired electrons with magnetic nuclei (see eq. (4.4)). In the second-order perturbation theory treatment the perturbing Hamiltonian $\hat{V}$ consists of terms depending on the nuclear spin moment I and the effective electronic spin S:

$$\hat{V} = \hat{H}_{FC}(S,I) + \hat{H}_{dip}(S,I) + \hat{H}_{HC-SO}(S,I) + \hat{H}_{PSO}(I) + \hat{H}_{SO}(S), \qquad (4.32)$$

where $\hat{H}_{FC}(S,I)$ is the *Fermi-contact* operator, $\hat{H}_{dip}(S,I)$ is the *spin-dipolar* operator, $\hat{H}_{HC-SO}(S,I)$ is the *one-electron spin-orbit hyperfine correction* term, and $\hat{H}_{PSO}(I)$ and $\hat{H}_{SO}(S)$ are the *two-electron hyperfine correction* terms. The explicit expressions for the terms are given in ref. [7]. Here, we summarize only the resulting terms.

In the usual nonrelativistic first-order approximation, isotropic hyperfine splittings A_{iso} correspond to the Fermi-contact term A_{FC}, which is the dominant part for light-atom systems.

$$A_{FC} = \frac{4\pi}{3}\beta_e\beta_N g_e g_N \langle S_Z \rangle^{-1} \sum_{u,v} P_{u,v}^{\alpha-\beta} \langle \psi_u | \delta(\boldsymbol{R}_N) | \psi_v \rangle \ . \qquad (4.33)$$

Here β_e is the Bohr magneton, β_N the nuclear magneton, g_N is the g-value of nucleus N, $\langle S_Z \rangle$ is the expectation value of the z-component of the total electronic spin, $P_{u,v}^{\alpha-\beta}$ is the spin density matrix, and the summation runs over all occupied molecular orbitals. The components T_{ij}(N) of the resulting anisotropic tensor are given by

$$T_{ij}(N) = \frac{1}{2}\beta_e\beta_N g_e g_N \langle S_Z \rangle^{-1} \sum_{u,v} P_{\mu,\nu}^{a-\beta} \left\langle \psi_\mu \left| \mathbf{r}_N^{-5} \left(\mathbf{r}_N^2 \delta_{ij} - 3\mathbf{r}_{N,i}\mathbf{r}_{N,j} \right) \right| \psi_\nu \right\rangle, \qquad (4.34)$$

where $\boldsymbol{r}_N = r - R_N$ (R_N is the position vector of nucleus N).

The first-order contribution comes from the spin-orbit hyperfine correction operators (S is the effective spin quantum number)

$$\widehat{H}_{HC-SO,uv} = \frac{1}{S}\left[\sum_{k}^{occ(\alpha)} \left\langle \psi_k^{\alpha} \middle| H_{HC-SO,uv} \middle| \psi_k^{\alpha} \right\rangle - \sum_{k}^{occ(\beta)} \left\langle \psi_k^{\beta} \middle| H_{HC-SO,uv} \middle| \psi_k^{\beta} \right\rangle \right] \quad (4.35)$$

The second-order perturbation treatment of refs. [14, 15] is used to compute spin-orbit (SO) corrections to the hyperfine tensor (in this thesis, the corrections are only relevant for the metal HFC). At the coupled-perturbed Kohn-Sham level, the dominant SO correction term arises as a second-order cross term between the one- and two-electron SO Hamiltonian H_{SO} and the paramagnetic nuclear-spin electron-orbit (PSO) operator

$$\begin{aligned}\widehat{H}_{SO,uv} = \frac{1}{S}\Bigg[& \sum_{k}^{occ(\alpha)} \sum_{a}^{virt(\alpha)} \frac{\left\langle \psi_k^{\alpha} \middle| \widehat{H}_{SO,u} \middle| \psi_a^{\alpha} \right\rangle \left\langle \psi_a^{\alpha} \middle| \widehat{H}_{PSO,v} \middle| \psi_k^{\alpha} \right\rangle}{\varepsilon_k^{\alpha} - \varepsilon_a^{\alpha}} \\ & - \sum_{k}^{occ(\beta)} \sum_{a}^{virt(\beta)} \frac{\left\langle \psi_k^{\beta} \middle| H_{SO,u} \middle| \psi_a^{\beta} \right\rangle \left\langle \psi_a^{\beta} \middle| \widehat{H}_{PSO,v} \middle| \psi_k^{\beta} \right\rangle}{\varepsilon_k^{\beta} - \varepsilon_a^{\beta}} \Bigg]\end{aligned} \quad (4.36)$$

4.9 Nuclear Quadrupole Coupling Constant

The last term in eq. (4.4) describes the nuclear quadrupole interaction. For nuclei with $I > ½$, their nonspherical charge distribution interacts with the electric field gradient used at the nucleus. This interaction is parameterized by the nuclear quadrupole coupling tensor **Q**. **Q** is traceless and can be expressed as

$$\vec{I}\mathbf{Q}\vec{I} = \frac{e^2 q_{zz} Q}{4I(2I-1)}\left[\left(3I_z^2 - I\left(I+1\right)^2\right) + \eta\left(I_x^2 - I_y^2\right)\right], \quad (4.37)$$

where e^2q_{zz} is the electric field gradient at the nucleus along the principal z axis, and η is the asymmetry parameter defined by

$$\eta = \left|\frac{q_{xx} - q_{yy}}{q_{zz}}\right|. \quad (4.38)$$

4.10 Spin-Projection Techniques

In Chapter 3, the broken-symmetry DFT (BS-DFT) was introduced, which is in our days the only suitable method to treat large multinuclear transition metal complexes. The electron density of the broken-symmetry (BS) solution agrees very well with the electron density of the real antiferromagnetic (AF) state.[17] The NQC parameters involve the total electron density rather than the spin density and are thus expected to be described well already by the BS calculation without spin projection, in contrast to the g-tensor and the HFC parameters. The BS spin densities differ from the "real" AF state. Therefore, spin-projection techniques are needed to obtain the appropriate g-tensors and hyperfine coupling constants.[18,19] In this section, we will start with spin-projection techniques for dinuclear $Mn^{III}Mn^{IV}$ complexes (4.10.1). Finally, section 4.10.2 shows the spin-projection techniques used for tetranuclear $Mn^{III}Mn^{IV}Mn^{IV}Mn^{IV}$ complexes, which is the underlying oxidation state distribution in the S_2 state of the Kok cycle.

4.10.1 Dinuclear $Mn^{III}Mn^{IV}$ Complexes

For the evaluation of the g-tensor, two separate DFT calculations are carried out, from which the g-tensor of the high spin state (g_{hs}) and the g-tensor of the broken-symmetry doublet configuration (g_{bs}) are obtained. Spin-projection schemes give access to the g-tensor site values $\boldsymbol{g}_i$ of the exchange coupled $Mn^{III}Mn^{IV}$ complex ($M_S^{hs} = S_A + S_B$, $M_S^{bs} = S_A - S_B$; S_A and S_B are the spin on center A and B, respectively)[20]

$$\boldsymbol{g}_1 = \frac{1}{2S_1}\left[g_{hs} M_S^{hs} + g_{bs} M_S^{bs} \right] \text{ and} \tag{4.39}$$

$$\boldsymbol{g}_2 = \frac{1}{2S_2}\left[g_{hs} M_S^{hs} - g_{BS} M_S^{bs} \right]. \tag{4.40}$$

Following this approach, the effective g-tensor g is given by[19]

$$g = c_1\mathbf{g}_1 + c_2\mathbf{g}_2 + \frac{c_1 c_2}{5J}(\mathbf{g}_1 - \mathbf{g}_2)[(3c_1 + 1)\cdot\mathbf{D}_1 - (3c_2 + 1)\cdot\mathbf{D}_2]. \tag{4.41}$$

In eq. (4.41) the spin projection coefficients are

$$c_i = \frac{\mathrm{S}(\mathrm{S}+1) + \mathrm{S}_\mathrm{i}(S_i+1) - S_j(S_j+1)}{2S(S+1)}. \tag{4.42}$$

For dinuclear $Mn^{III}Mn^{IV}$ complexes the spin projection coefficients are $c_1 = 2$ (Mn^{III}, d^4) and $c_2 = -1$ (Mn^{IV}, d^3). In view of the large exchange coupling (J > 100 cm^{-1}) and relatively small zero-field splitting (< 5 cm^{-1}),[19,21] the ZFS contributions may be neglected[22] and eq. (4.41) can be reduced to

$$g = c_1\mathbf{g}_1 + c_2\mathbf{g}_2 . \tag{4.43}$$

The effective hyperfine site values A_i^{eff} of the antiferromagnetic state can be calculated from the respective HFCs of the BS state A_i^{bs} by conversion into hyperfine site values and multiplication with the spin projection coefficients c_i:

$$A_i^{eff} = c_i \frac{A_i^{bs} M_S^{bs}}{\pm S_i} \tag{4.44}$$

Due to vector coupling, the hyperfine site values A_i^{eff} for a dinuclear $Mn^{III}Mn^{IV}$ complex are given as[19]

$$A_1^{eff} = c_1\mathbf{a}_1 - \frac{\mathbf{a}_1}{5J} c_1c_2[(3c_1+1)\cdot\mathbf{D}_1 - (3c_2+1)\cdot\mathbf{D}_2] \text{ and} \tag{4.45}$$

$$A_2^{eff} = c_2\mathbf{a}_2 - \frac{\mathbf{a}_2}{5J} c_1c_2[(3c_1+1)\cdot\mathbf{D}_1 - (3c_2+1)\cdot\mathbf{D}_2]. \tag{4.46}$$

Neglecting again the ZFS contributions, eqs. (4.45) and (4.46) can be simplified to

$$A_1^{eff} = c_1\mathbf{a}_1 \text{ and} \tag{4.47}$$

$$A_2^{eff} = c_2\mathbf{a}_2 , \tag{4.48}$$

where $\mathbf{a}_\mathrm{i}$ are the local HFC tensors.

4.10.2 Tetranuclear $Mn^{III}Mn^{IV}Mn^{IV}Mn^{IV}$ Complexes

With growing numbers of nuclei, the spin-projection equations become rapidly more complicated. Fortunately, the methodology analogous to that presented above for dinuclear $Mn^{III}Mn^{IV}$ complexes can in principle be applied to the tetranuclear manganese clusters which are studied in this thesis and have an oxidation state assignment of (III)(IV)(IV)(IV) with a S = 1/2 spin ground state.

A system with *n* paramagnetic ions may be described by the effective spin Hamiltonian

$$\hat{H}_{eff} = \sum_{i=1}^{n} \beta \vec{B} \mathbf{g}_i \vec{S}_i + \sum_{i=1}^{n} \vec{S}_i \mathbf{a}_i \vec{I}_i + \sum_{i=1}^{n} \vec{S}_i \mathbf{d}_i \vec{S}_i + \sum_{i=1}^{n} \vec{I}_i \mathbf{p}_i \vec{I}_i - \sum_{i<j}^{n} J_{ij} \vec{S}_i \vec{S}_j \,, \qquad (4.49)$$

where $\vec{S}_i$ is the electronic spin operator of ion *i*, and $\vec{B}$ is the external magnetic field. The local HFC tensor $\mathbf{a}_i$ ("site value") parameterizes the interaction of $\vec{S}_i$ with the nuclear spin operator of ion *i*, $\vec{I}$. The local g-tensor $\mathbf{g}_i$ of ion *i* parameterizes the interaction of its electronic spin with the external field $\vec{B}$, and the local tensors $\mathbf{d}_i$ express the zero-field splitting (ZFS) of ions *i*. Local NQC tensors $\mathbf{p}_i$ interact with the nuclear magnetic moments. Finally, J_{ij} represents the isotropic Heisenberg exchange interaction between the paramagnetic centers *i* and *j*. For brevity, we have not included the nuclear Zeeman term nor the HFC or NQC terms for ligand nuclei. To be able to relate directly to the experimental spectra for a spin-coupled multinuclear cluster as the OEC, one has to account for the coupled spin states. This requires going to a spin-coupled representation, using the vector spin-coupling model.[20,23-25] We may thus write the spin Hamiltonian of the OEC in terms of effective, coupled tensors (the NQC has been neglected here),

$$\hat{H}_{eff} = \beta \vec{B} \mathbf{g} \tilde{\vec{S}} + \sum_{i=1}^{n} \tilde{\vec{S}} \mathbf{A}_i \vec{I}_i + \tilde{\vec{S}} \mathbf{D} \tilde{\vec{S}} \,, \qquad (4.50)$$

parameterizing interactions between effective spins, $\tilde{\vec{S}}$ (*i* runs over the four coupled manganese centers). The effective tensors may in turn be related to the isolated (site) tensors of eq. (4.49) by spin projection. For an S = 1/2 ground state, the last, ZFS-related

term vanishes. We are mainly interested here in the effective HFC tensors $\mathbf{A}_i$ (g-tensors will be analyzed in detail elsewhere). In general, they may be related to the local site tensors by

$$\mathbf{A}_i = \boldsymbol{\rho}_i \mathbf{a}_i \,, \tag{4.51}$$

where $\boldsymbol{\rho}_i$ is a spin projection matrix. It depends on the spin at site *i*, on the exchange couplings of the exchange multiplet, and on the local ZFS tensors. For dinuclear $Mn^{III}Mn^{IV}$ complexes, previous studies have assumed the exchange interaction to be the dominant coupling mechanism between the ions, and the ZFS to be negligible. Then the ZFS terms drop out of the spin projection matrices, which reduce to scalars. Here we will adopt this assumption, which has typically been made implicitly also in spectra simulations for the OEC. In case of a dinuclear complex the "scalar approximation" leads to the simple spin projection coefficients

$$\mathbf{A}_i = c_i \mathbf{a}_i \,, \tag{4.52}$$

where

$$c_i = \frac{\mathrm{S}(\mathrm{S}+1) + \mathrm{S}_i(S_i+1) - S_j(S_j+1)}{2S(S+1)} \,. \tag{4.53}$$

For the Mn^{III} site, $c_1 = +2$, and for the Mn^{IV} site, $c_2 = -1$.[22,26,27] For the spin-coupled S = 1/2 states of an $Mn^{III}Mn^{IV}Mn^{IV}Mn^{IV}$ cluster (see Chapter 8), we have always one site with $M_S = +2$ (Mn^{III} site), one with $M_S = +3/2$, and two with $M_S = -3/2$ (this is borne out also by computed spin densities of BS states). A full treatment including ZFS terms, and without any approximations, quickly becomes very complicated. There are indications from spectra simulations,[28-30] that at least for the isotropic Mn HFCs of the S_2 state of the OEC, the ZFS contributions may indeed be neglected to a first approximation. With this assumption, extension of eq. (4.52) to the tetranuclear system leads to the same spin projection coefficients as in the dinuclear case.[20] The restriction that the coefficients have to add up to +1 to obtain an S = 1/2 state leads to a spin-projection coefficient $c = +1$ for the $M_S = +3/2$ site. This agrees qualitatively with the (non-integer) coefficients obtained in simulations (see, e.g., ref. [30]).

While this may hold to a good approximation for the isotropic Mn HFCs (and will be used also for the ^{14}N ligand HFCs), the neglect of ZFS contributions is a more doubtful

assumption for the Mn HFC anisotropies. If the local ZFS is nonnegligible, and if the intrinsic $\mathbf{d}_i$ tensors are not all coaxial, there may be ZFS-mediated anisotropy transfer between the sites for the effective HFC tensors. While we will provide full spin-projected HFC tensors in the Tables in Chapter 8 (with the same scalar coefficients as used for the isotropic values), we expect them to be less reliable than the isotropic HFCs. Moreover, we regard also reported anisotropies from spectra simulations to be somewhat doubtful. We will thus base our discussions mainly on the isotropic HFCs. The spin projection scheme described above is applied directly to the local HFCs computed for the BS states, without involvement of contributions from the HS state. More sophisticated spin-projection procedures involving local ZFS tensors are currently evaluated but are outside the scope of this thesis.

Chapter 5

To see the world for a moment as something rich and strange is the private reward of many a discovery.

Edward M. Purcell, 1952.

Electron Paramagnetic Resonance Parameters of Simple Inorganic Mononuclear Manganese Complexes

5.1 Introduction

Manganese ions embedded at the core of metalloprotein play crucial roles in the redox processes to sustain life. One of the most important multinuclear manganese complexes, the oxygen-evolving complex (OEC), was already introduced in Chapter 2. Enzymes like the superoxide dismutase of prokaryotes and of the organelles of eukaryotes and the catalase of lactobacilli are also prominent manganese containing enzymes.[1] Manganese is of great importance for redox reactions due to its stability in biological systems in several oxidation states, Mn(II), Mn(III) and Mn(IV). Furthermore, the bonds to the ligands are often not very strong.[2] Besides the redox properties, the function as a Lewis acid is the second important role in enzymes.[3]

Furthermore, divalent manganese ions behave as spherical polarizable ions due to their half-filled $3d^5$ shell and are typically six-coordinated and octahedral. They possess a radius of approximately 0.75 Å, somewhat larger than that of magnesium (0.65 Å), smaller than that of calcium (0.99 Å), and almost equals to that of zinc (0.74 Å).[3] In view of the similar sizes, Mn(II) can be used as a spin probe to substitute these metals.[4]

Therefore, these complexes become paramagnetic and can be studied by EPR spectroscopy.[2]

The history of EPR applications started with the study of Mn(II) complexes by Zavoisky.[5] Since then there have been numerous EPR studies on manganese complexes in diverse materials, but also in biological systems. However, most manganese complexes are high-spin systems and have, consequently, a complicated magnetism, leading to complex EPR spectra. Therefore, the calculation of EPR parameters of appropriate model systems is needed to analyze and interpret the spectra in detail. Modern relativistic density functional methods for the calculation of EPR parameters furnish a good foundation to rationalize and even to predict the central parameters underlying the EPR spectra. This approach bears the potential of becoming an indispensable tool in the investigation of paramagnetic species in biological systems.

Our goal here is to validate density functional methods for the calculation of EPR parameters (g-tensor, ^{1}H, ^{17}O and ^{55}Mn hyperfine coupling constants) for the experimentally well-investigated $[Mn(H_2O)_6]^{2+}$ complex (section 5.3). Subsequently, the ^{55}Mn HFC constants of $[Mn(H_2O)_6]^{3+}$ are compared with experimental data (section 5.4). The best DFT method will be used to compare the ^{55}Mn HFCs for a variety of simple inorganic manganese complexes (section 5.5). This will be done in useful complexes in the context of the OEC of PSII.

5.2 Computational Details

All structure optimizations were carried out with the Turbomole 5.8 and Turbomole 5.9.1[6] code at BP86[7,8] DFT level with TZVP basis sets[9] using unrestricted Kohn-Sham wavefunctions.

Subsequently, unrestricted Kohn-Sham single-point calculations were also performed with Turbomole 5.9.1[6] using a 9s7p4d basis set for manganese (specifically designed for hyperfine calculations[10,11,27,28]) and flexible IGLO-III[12,13] basis sets for the ligand atoms. For $[Mn(H_2O)_6]^{2+}$ the following DFT exchange-correlation functionals were compared: the GGA functionals a) BP86[7,8] and b) BLYP[14,15], the hybrid functionals c) B3LYP[14,15] with 20% exact exchange and d) BHLYP[14,16] with 50% exact exchange, as well as the user-defined hybrid functionals e) B-60LYP with 60% exact exchange (40% E_X^{Slater} and 40% ΔE_x^{B88} and E_c^{LYP}), f) B-70LYP with 70% exact exchange (30%

E_X^{Slater} and 30% ΔE_x^{B88} and E_c^{LYP}), g) B-80LYP with 80% exact exchange (20% E_X^{Slater} and 20% ΔE_x^{B88} and E_c^{LYP}), h) B-90LYP with 90% exact exchange (10% E_X^{Slater} and 10% ΔE_x^{B88} and E_c^{LYP}) and i) B-95LYP with 95% exact exchange (5% E_X^{Slater} and 5% ΔE_x^{B88} and E_c^{LYP}). For $[Mn(H_2O)_6]^{3+}$ only three DFT functionals were compared: BP86, B3LYP and BHLYP. For all other complexes, unrestricted Kohn-Sham single-point calculations were performed only on BHLYP level.

The unrestricted Kohn-Sham orbitals were transferred to the MAG-Respect property package[17] by suitable interface routines. The atomic mean-field approximation (AMFI)[18,19] has been used to compute the matrix elements of the Breit-Pauli spin-orbit (SO) operator. In g-tensor calculations, a common gauge at the metal center was employed.

5.3 The $[Mn(H_2O)_6]^{2+}$ Complex

The $[Mn(H_2O)_6]^{2+}$ complex is spectroscopically the best characterized simple inorganic divalent manganese complex. We will start with an analysis of the spin-density distribution (section 5.3.1). Subsequently, results of the g-tensor are discussed (section 5.3.2). The g-tensor is, as expected for an octahedral complex, very close to the g-value of a free electron. Finally, our computed hyperfine coupling constants will be compared to ^{55}Mn, ^{1}H and ^{17}O ENDOR data, section 5.3.3, 5.3.4, and 5.3.5, respectively.

The optimized structure of the investigated complex is octahedral and exhibits Mn-O distances of 2.21 Å (exp.:[20] 2.20 Å).

5.3.1 Spin-Density Analysis

A correct description of the spin-density distribution is mandatory for the calculation of EPR parameters. Table 5.1 provides Mulliken atomic spin densities for $[Mn(H_2O)_6]^{2+}$ obtained with different functionals. The spin-density distribution in transition-metal complexes is generally influenced by the following effects:[10,11,21] a) the metal-ligand bond is described too covalent at LDA or GGA level due to self-interaction errors,[11,21-25] and b) valence-shell spin polarization across covalent bonds is enhanced, leading often to larger spin contamination,[11] c) core-shell spin polarization at the metal center is also enhanced (improved). While the latter effect is important for the metal hyperfine

coupling[11] (see below), the two former trends may counteract each other:[23,26] the increased ionicity may actually decrease the tendency towards valence-shell spin polarization. This seems to be the case here. The enhanced bond ionicity is reflected in an increase of spin density at the metal center and less spin density on the ligand atoms (Table 5.1).

We observe a manganese spin density which is close to the expected spin value of 5 for a d^5 Mn(II) ion. The ligand atoms possess positive spin-density contributions, occurring from spin delocalization effects.

Even with large exact-exchange admixtures, derivation of $<S^2>$ form 8.75 of the Kohn-Sham wavefunction is small.

Table 5.1. Mulliken atomic spin densities and $<S^2>$ of $[Mn(H_2O)_6]^{2+}$.

	Mn	*O*	*H*	$<S^2>$
BLYP	4.878	0.010	0.005	8.752
B3LYP	4.912	0.006	0.004	8.752
BHLYP	4.928	0.006	0.003	8.752
B-60LYP	4.928	0.007	0.002	8.752
B-70LYP	4.927	0.008	0.002	8.752
B-80LYP	4.925	0.008	0.002	8.752
B-90LYP	4.923	0.009	0.002	8.752
B-95LYP	4.922	0.009	0.002	8.752

5.3.2 The g-Tensor

Table 5.2 compares computed g-shift tensors for $[Mn(H_2O)_6]^{2+}$ with experimental data. For all functionals, a nearly isotropic g-tensor close to the g-value of 2.002319 of a free electron is obtained, which is an expected situation for a high spin d^5 Mn^{2+} complex. Our calculations reproduce the measured g-value of 2.00.[27] The dependence on the used functional is negligible.

Table 5.2. g-Shift components (in ppt) and absolute g-values of $[Mn(H_2O)_6]^{2+}$.[a]

	Δg_{iso}	Δg_{11}	Δg_{22}	Δg_{33}
BLYP	0.1 (2.0024)	0.1 (2.0024)	0.1 (2.0024)	0.1 (2.0024)
B3LYP	-0.2 (2.0021)	-0.2 (2.0021)	-0.2 (2.0021)	-0.2 (2.0021)
BHLYP	-0.4 (2.0019)	-0.4 (2.0019)	-0.4 (2.0019)	-0.4 (2.0019)
B-60LYP	-0.4 (2.0019)	-0.4 (2.0019)	-0.4 (2.0019)	-0.4 (2.0019)
B-70LYP	-0.4 (2.0019)	-0.4 (2.0019)	-0.4 (2.0019)	-0.4 (2.0019)
B-80LYP	-0.5 (2.0018)	-0.5 (2.0018)	-0.5 (2.0018)	-0.5 (2.0018)
B-90LYP	-0.5 (2.0018)	-0.5 (2.0018)	-0.5 (2.0018)	-0.5 (2.0018)
B-95LYP	-0.5 (2.0018)	-0.5 (2.0018)	-0.5 (2.0018)	-0.5 (2.0018)
exp.[b]	2.00			

[a]Absolute g-values in parentheses. [b]From frozen solution measurements (35 GHz) of $[Mn(H_2O)_6]^{2+}$.[27]

5.3.3 ^{55}Mn Hyperfine Coupling Constant

Isotropic ^{55}Mn hyperfine data[28] for $[Mn(H_2O)_6]^{2+}$ are compared to our computations in Table 5.3. Due to an enhancement of (overall negative) core-shell spin polarization contributions to the spin density at the nucleus[11,29] and due to generally more spin density on manganese (see section 5.3.1), the isotropic coupling constant A_{iso} in such systems depends appreciably on exact-exchange admixture. Increasing the exact-exchange admixture thus renders the couplings more negative and improves agreement with the experimental data[28] (Table 5.3). As expected for an octahedral complex, the HFC anisotropy is zero, reflecting the isotropic spin-density distribution in a high-spin d^5 Mn^{2+} system.

Table 5.3. Computed and experimental ^{55}Mn HFC tensors (in MHz) of $[Mn(H_2O)_6]^{2+}$.

	First-order				A^{SO}	*Total* **A***-tensor*	
	A_{FC}	T_{11}	T_{22}	T_{33}	A_{PC}	A_{iso}	$<S^2>$
BLYP	-137.9	0.0	0.0	0.0	-2.9	-140.8	8.752
B3LYP	-168.0	0.0	0.0	0.0	-2.6	-170.6	8.752
BHLYP	-206.0	0.0	0.0	0.0	-2.1	-208.1	8.752
B-60LYP	-217.4	0.0	0.0	0.0	-1.9	-219.3	8.752
B-70LYP	-228.4	-0.1	0.0	0.1	-1.7	-230.1	8.752
B-80LYP	-239.1	-0.1	0.0	0.1	-1.6	-240.6	8.752
B-90LYP	-249.4	-0.1	0.0	0.1	-1.4	-250.8	8.752
B-95LYP	-254.4	-0.1	0.0	0.1	-1.3	-255.7	8.752
exp.[b]						-245	
Kaupp[c]						-199	
Neese[d]						-164	

[a] A_{iso} is the total isotropic value, T_i represent the traceless part of the full **A** tensor, A_{FC} and A_{PC} denote the isotropic first-order Fermi-contact and second-order pseudo-contact (spin-orbit) contributions to the full total **A** tensor, respectively. [b]Single crystal EPR study from ref. [28]. [c]DFT calculations with MAG-ReSpect (B3PW91, (15s11p6d)/[9s7p4d] for Mn, BII for ligand atoms) from ref. [30]. [d]DFT calculations with ORCA (BP86, [CP(PPP)] for Mn, TZ for ligand atoms) from ref. [31].

SO contributions have previously been found very important already for *3d* metals.[26,30,31] For $[Mn(H_2O)_6]^{2+}$, SO contributions are rather small compared to the isotropic nonrelativistic Fermi-contact term A_{FC}.

Reproducing the experimental value of -245 MHz[28] requires an exact-exchange admixture between 80 and 90%. However, it is desirable to employ a functional with such a high amount of exact-exchange admixture, because increasing the exact-exchange admixture suffers mostly from spin contamination effects. Therefore, we analyze the B3LYP and BHLYP results to define an empirical *scaling factor F*, which can be used to multiply the calculated isotropic value A_{iso} of a given value to predict the experimental HFC constant. This factor can then be used for predicting HFC constants in systems for which no experimental data exist. In the case of B3LYP, the scaling factor F is given by 1.46, and for BHLYP by 1.19. We will return to this empirical scaling factor in Chapter 7 in the discussion of hyperfine coupling constants for dinuclear manganese complexes.

5.3.4 ^{1}H Hyperfine Coupling Constants.

The calculated ^{1}H HFCs agree excellently with experimental data (Table 5.4). However, our calculations were carried out in gas phase. Therefore, no environmental effects are included and the results have to be validated carefully. As already observed for the ^{55}Mn HFCs, the isotropic hyperfine coupling is extremely dependent on the used functional. An exact-exchange admixture of more than 70% provides excellent agreement with experimental data. The nearly axial anisotropic part does not depend on the amount of exact-exchange admixture, and we can reproduce very precisely the experimental values.

Table 5.4. Computed and experimental ^{1}H HFC tensors (in MHz) of $[Mn(H_2O)_6]^{2+}$.

	A_{iso}	A_{FC}	T_{11}	T_{22}	T_{33}
BLYP	1.8	1.8	-3.4	-3.0	6.4
B3LYP	1.4	1.4	-3.4	-3.1	6.5
BHLYP	1.1	1.1	-3.4	-3.1	6.5
B-60LYP	1.0	1.0	-3.4	-3.1	6.5
B-70LYP	0.9	0.9	-3.4	-3.1	6.5
B-80LYP	0.9	0.9	-3.4	-3.1	6.5
B-90LYP	0.8	0.8	-3.4	-3.1	6.5
B-95LYP	0.8	0.8	-3.4	-3.1	6.5
exp.[a]	0.8	0.8	-3.4	-3.4	6.8

[a]Frozen solution ENDOR measuement from ref. [34].

5.3.5 ^{17}O Hyperfine Coupling Constants

Different DFT methods were validated on the Mn^{2+} hexaquo complex, for which high-field ENDOR data are available (Table 5.5).[32] The sign of the experimentally determined ^{17}O A_{iso} could be confirmed, but the calculations show a notable deviation from axiality. The absolute value of the isotropic coupling is slightly overestimated in the DFT calculations and shows the best agreement with experiment at relatively large exact exchange-admixture (> 50%). The anisotropic part does not depend much on the functional and is already reproduced well with the GGA functional BLYP.

Table 5.5. Computed and experimental ^{17}O HFC tensors (in MHz) of $[Mn(H_2O)_6]^{2+}$

	A_{iso}	A_{FC}	T_{11}	T_{22}/T_{33}	½ (T_{22} + T_{33})
BLYP	-12.5	-12.5	-2.1	0.3 / 1.9	1.1
B3LYP	-10.8	-10.8	-2.2	0.5 / 1.7	1.1
BHLYP	-10.1	-10.1	-2.2	0.6 / 1.6	1.1
B-60LYP	-9.8	-9.8	-2.3	0.7 / 1.6	1.2
B-70LYP	-9.6	-9.6	-2.3	0.7 / 1.6	1.2
B-80LYP	-9.5	-9.5	-2.3	0.7 / 1.6	1.2
B-90LYP	-9.3	-9.3	-2.3	0.7 / 1.6	1.2
B-95LYP	-9.3	-9.3	-2.3	0.7 / 1.6	1.2
Neese[a]	-11.3	-11.3	-2.2	0.5 / 1.7	1.1
exp.[b]	-7.5	-7.5	-2.0	1.0 / 1.0	1.0

[a]DFT calculations with ORCA (B3LYP, [CP(PPP)] for Mn, EPR-II for ligand atoms).[32] [b]Frozen solution 95 GHz ENDOR study of ref. [32].

5.4 The $[Mn(H_2O)_6]^{3+}$ complex

The manganese(III) ion is ubiquitious among biological systems, especially important in the OEC of PSII. Therefore, experience in calculating hyperfine couplings (HFC) for Mn(III) systems is required to predict HFCs of Mn(III) in more complex systems. The $[Mn(H_2O)_6]^{3+}$ complex is spectroscopically well characterized by high-field EPR (HF-EPR) spectroscopy. In general, Mn(III) complexes are high-spin systems, having an S = 2 electronic spin state, which can interact with the I = 5/2 nuclear spin. The influence of different DFT levels on EPR parameters was already carefully analyzed in 5.3. Here we focus only on the results for three commonly used functionals (BP86, B3LYP, and BHLYP), and we will discuss the differences compared to the divalent hexaaqua complex.

The $[Mn(H_2O)_6]^{3+}$ complex exhibits due its d^4 configuration a Jahn-Teller distortion, resulting in a distortion from octahedral geometry (d(Mn-O_{ax}) = 2.19 Å, d(Mn-O_{eq}) = 1.99 Å).

Table 5.6 provides the Mulliken atomic spin densities. As in $[Mn(H_2O)_6]^{2+}$, a higher amount of exact-exchange admixture leads to more spin-density on the metal atom. Spin delocalisation occurs towards the axial oxygen atoms, and spin polarization to the equatorial oxygen atoms.

Table 5.6. Mulliken atomic spin densities and $<S^2>$ of $[Mn(H_2O)_6]^{3+}$.

	Mn	O_{ax}	O_{eq}	H_{ax}	H_{eq}	$<S^2>$
BP86	3.928	0.051	-0.008	0.004	-0.001	6.021
B3LYP	3.946	0.041	-0.010	0.003	0.000	6.020
BHLYP	3.996	0.028	-0.015	0.002	0.000	6.017

The calculated g-tensor is nearly axial (see Table 5.7) and differs more strongly from the g-value of a free electron (2.0023) than $[Mn(H_2O)_6]^{2+}$. All g-shift components are negative. The dependence on the used functional is appreciable. The B3LYP functional can reproduce the best the experimental value.

Table 5.7. g-Shift components (in ppt) and absolute g-values of $[Mn(H_2O)_6]^{3+}$.[a]

	Δg_{iso}	Δg_{11}	Δg_{22}	Δg_{33}
BP86	-52 (1.9971)	-120 (1.9903)	-23 (2.0000)	-13 (2.0010)
B3LYP	-78 (1.9945)	-161 (1.9862)	-41 (1.9982)	-31 (1.9992)
BHLYP	-113 (1.9910)	-224 (1.9799)	-64 (1.9959)	-52 (1.9971)
exp.[b]	-75 (1.9948)	-179 (1.9844)	-23 (2.000)	-23 (2.000)

[a]Absolute g-values in parentheses. [b]From high-field single crystal EPR measurements.[33]

Let us turn to the metal hyperfine coupling constant (Table 5.8). Again, the discrepancy between experimental and calculated values for the isotropic part is not negligible. Therefore, we can define a scaling factor *F* (BP86: 1.51, B3LYP: 1.48, BHLYP: 1.24), which is for the used functional similar to those obtained for the divalent complex $[Mn(H_2O)_6]^{2+}$ (see section 5.3.3). All functional provide the anisotropic part excellently and their results differ only slightly.

Table 5.8. Computed and experimental ^{55}Mn HFC tensors (in MHz) of $[Mn(H_2O)_6]^{3+}$.

	First-order				A^{SO}	*Total* ***A****-tensor*	
	A_{iso}	T_1	T_2	T_3	A_{FC}	A_{PC}	$\langle S^2 \rangle$
BP86	-150.6	-33.5	-28.2	61.8	-142.0	-8.5	6.021
B3LYP	-152.6	-34.4	-29.7	64.1	-142.9	-9.7	6.020
BHLYP	-182.6	-35.8	-29.8	65.6	-171.4	-11.3	6.017
exp.[a]	-226.9	-33.9	-33.9	67.7			

[a]From high-field single crystal EPR measurements.[33]

5.5 Other Mononuclear Manganese Complexes

In this last section of Chapter 5, ^{55}Mn HFCs and ^{17}O HFCs of a series of mononuclear Mn(III) and Mn(IV) complexes are given (Table 5.9 and 5.10). Most of the analogous divalent manganese complexes with anionic ligands are not stable in gas phase calculations. The chosen complexes might be probable elements for the tetranuclear manganese cluster in PSII. The results should serve as reference data for subsequent discussions and only some tendencies are discussed here.

Due to their d^4 configuration leading to a Jahn-Teller distortion, all Mn(III) complexes show large anisotropies. The fivefold coordinated Mn(IV) complexes provide larger anisotropic HFCs than the sixfold coordinated ones.

For all sixfold coordinated complexes, the Mn(IV) complex exhibits a less negative value than the corresponding Mn(III) complex. In the case of fivefold coordinated complexes, it is the Mn(III) complex which has a less negative HFC than the Mn(IV) complex.

Except for $[Mn(H_2O)_5(OH)]^{3+}$, A_{iso} increases with stronger coordination. For Mn(III), a higher coordination number is accompanied with a more negative isotropic HFC, whereas for Mn(IV), a higher coordination number renders the HFC less negative.

Table 5.9. Computed and experimental ^{55}Mn HFC tensors (in MHz) (BHLYP results).

	A_{iso}*	A_{iso}	T_1	T_2	T_3	A_{FC}	A_{PC}	$\rho^{\alpha-\beta}$	$<S^2>$
$[Mn(H_2O)_6]^{3+}$	-219.2	-182.7	-35.9	-29.8	65.8	-171.4	-11.3	3.996	6.018
$[Mn(H_2O)_5(OH)]^{2+}$	-281.2	-234.3	-60.3	28.6	31.7	-226.4	-7.9	4.208	6.150
trans-$[Mn(H_2O)_4(OH)_2]^{+}$	-274.9	-229.1	-63.2	30.2	33.0	-220.6	-8.6	4.028	6.045
$[Mn(H_2O)_5(O)]^{+}$	-416.0	-346.7	-54.3	26.7	27.6	-342.3	-4.4	4.410	6.414
$[Mn(H_2O)_5]^{3+}$	-200.6	-167.2	-37.3	-26.6	64.0	-156.6	-10.7	3.995	6.020
$[Mn(H_2O)_4(OH)]^{2+}$	-251.6	-209.7	-43.4	6.3	37.2	-203.2	-6.5	4.392	6.333
$[Mn(H_2O)_6]^{4+}$	-200.2	-166.8	-0.1	0.0	0.0	-147.8	-19.0	3.217	3.821
$[Mn(H_2O)_5(OH)]^{3+}$	-189.4	-157.8	-10.2	-6.7	16.9	-138.5	-19.3	3.688	4.309
trans-$[Mn(H_2O)_4(OH)_2]^{2+}$	-233.2	-194.3	-3.7	0.8	2.8	-174.6	-19.7	3.020	3.819
cis-$[Mn(H_2O)_4(OH)_2]^{2+}$	-242.5	-202.1	-7.0	-3.3	10.3	-174.2	-13.7	3.573	4.108
$[Mn(H_2O)_5(O)]^{2+}$	-386.3	-321.9	-8.4	-6.2	14.6	-303.2	-18.7	3.275	4.169
$[Mn(H_2O)_5]^{4+}$	-236.0	-196.7	-48.6	23.8	24.7	-179.4	-17.3	3.700	4.256
$[Mn(H_2O)_4(OH)]^{3+}$	-288.4	-240.3	-27.9	-19.4	47.3	-226.0	-14.3	3.761	4.420

[a] A_{iso}* represents the scaled hyperfine coupling constant (BHLYP result of A_{iso} mulitplyied by a scaling factor of 1.2 determined in investigations on $[Mn(H_2O)_6]^{2+}$ and $[Mn(H_2O)_6]^{3+}$). $\rho^{\alpha-\beta}$ is the Mulliken spin density of the manganese atom.

Finally, Table 5.10 provides ^{17}O hyperfine data. The validation study on the Mn^{2+} hexaquo complex showed an overestimation of the absolute value of ^{17}O A_{iso} (exp.:[32] -7.4 MHz, BHLYP: -10.1 MHz). Therefore, the absolute value of the calculated ^{17}O hyperfine data is expected to be also overestimated for all complexes. Furthermore, it is difficult to see any tendencies.

Table 5.10. Computed and experimental ^{17}O HFC tensors (in MHz) (BHLYP results).

		A_{iso}	T_1	T_2	T_3	$\rho^{\alpha-\beta}$
$[Mn(H_2O)_6]^{2+}$		-10.1	-2.2	0.6	1.6	-10.1
$[Mn(H_2O)_6]^{3+}$	O_{ax}	-18.9	-3.7	0.8	2.9	0.029
	O_{eq}	1.4	-1.7	0.3	1.3	-0.015
$[Mn(H_2O)_5(OH)]^{2+}$	O_{OH}	-5.7	-15.5	-9.0	24.6	-0.255
	O_{ax}	-2.5	-1.3	-0.2	1.5	-0.008
	O_{eq}	-10.7	-3.6	0.6	1.8	0.006
trans-$[Mn(H_2O)_4(OH)_2]^{+}$	$O_{OH\ ax}$	-3.6	-6.4	-0.4	6.8	-0.032
	$O_{H2O\ eq}$	-7.9	-2.5	0.8	1.7	0.003
$[Mn(H_2O)_5(O)]^{+}$	O_O	-5.6	-24.5	-24.3	48.7	-0.451
	O_{ax}	-7.7	-1.9	0.5	1.5	0.002
	O_{eq}	-11.2	-2.2	0.5	1.6	-0.001
$[Mn(H_2O)_6]^{4+}$		9.7	-6.9	0.6	6.3	-0.030
$[Mn(H_2O)_5(OH)]^{3+}$	O_{OH}	-19.5	-39.7	-31.6	71.2	-0.636
	O_{ax}	-20.6	-3.6	-0.2	3.8	0.023
	O_{eq}	6.1	-3.5	0.7	2.9	-0.028
trans-$[Mn(H_2O)_4(OH)_2]^{2+}$	$O_{OH\ ax}$	-14.5	-17.0	1.8	15.3	0.058
	$O_{H2O\ eq}$	5.9	-2.2	-0.3	2.5	-0.042
cis-$[Mn(H_2O)_4(OH)_2]^{2+}$	O_{OH}	-12.2	-23.0	-14.9	39.0	-0.330
	$O_{OH\ trans}$	9.0	-2.3	0.2	2.1	-0.002
	$O_{H2O\ ax}$	-0.3	-2.5	-0.6	3.1	-0.041
$[Mn(H_2O)_5(O)]^{2+}$	O_O	-25.6	-42.2	-41.2	83.4	-0.208
	O_{ax}	-14.3	-2.8	0.6	2.2	0.006
	O_{eq}	0.1	-1.2	0.3	0.9	-0.022

[a] A_{iso} is the total isotropic value, T_i represent the traceless part of the full **A** tensor. $\rho^{\alpha-\beta}$ is the Mulliken spin density of the oxygen atom.

5.6 Conclusions

Hyperfine coupling constants and g-tensors were calculated for simple mononuclear complexes to evaluate the performance of different DFT exchange-correlation potentials for the calculation of spin-density distribution and metal/ligand hyperfine parameters. We found that spin contamination is no problem even with larger exact-exchange admixture.

For $[Mn(H_2O)_6]^{2+}$ isotropic hyperfine couplings of manganese and hydrogen are well reproduced with respect to experiment, when the hybrid functional includes about 80% exact-exchange admixture. For the ^{55}Mn HFC, a scaling factor *F* was defined, which is used to multiply the calculated isotropic shift to obtain the best possible correspondence to the experimental value (for B3LYP 1.46, for BHLYP 1.19). The ^{55}Mn HFC is isotropic and spin-orbit contributions to the metal hyperfine tensor have been found to be small, consistent with the high-spin d^5 electronic characteristics. Anisotropic ^{1}H HFCs are relatively insensitive with respect to the exact-exchange admixture. The absolute value of the isotropic ^{17}O coupling is overestimated in our calculations and a large amount of exact exchange-admixture (> 50%) is needed to obtain reasonable results. Comparable to ^{1}H HFCs, the anisotropic part of the ^{17}O HFC does not depend strongly on the functional and can be reproduced with a GGA functional.

For the trivalent complex $[Mn(H_2O)_6]^{3+}$, the calculated g-tensor is approximately axial and differs significantly from the g-value of a free electron than $[Mn(H_2O)_6]^{2+}$. All g-shift components are negative and the dependence on the used functional is appreciable. The B3LYP functional shows the best performance in regard of the experimental value. We can also define a scaling factor *F* (BP86: 1.51, B3LYP: 1.48, BHLYP: 1.24), which is for the used functional similar to those obtained for the divalent complex $[Mn(H_2O)_6]^{2+}$. All functionals provide the anisotropic part in good accuracy.

Finally, ^{55}Mn HFCs and ^{17}O HFCs of a series of mononuclear Mn(III) and Mn(IV) complexes are given, which should serve as reference data for further work in this thesis.

Chapter 6

We can sum up by saying that as the result of discoveries in the field of enzyme chemistry some questions have been answered and many questions have arisen. We live in an expanding universe in more senses than that of the astronomers.

James B. Sumner, 1946.

Structure and Electron Paramagnetic Resonance Parameters of the Manganese Site of Concanavalin A

6.1 Introduction

The saccharide-binding protein concanavalin A belongs to the large and ubiquitous plant lectin family.[1,2] The importance of these proteins is the ability to bind saccharides. Each member of the plant haemagglutinin has a unique saccharide specificity. However, many details of the biological role of these proteins are still unclear.[2] The metalloprotein concanavalin A of the Jack bean was the first saccharide-binding protein that has been characterized crystallographically.[3,4] It exhibits two metal ion binding sites, a transition-metal-binding site S1, which binds Mn^{2+}, Co^{2+}, Ni^{2+}, Zn^{2+} or Cd^{2+}, and a calcium-binding site S2, coordinating Ca^{2+}or Cd^{2+}.[5] The metal ions are responsible for stabilizing the binding site and for fixing the positions of amino acids that interact with sugar ligands.[6]

Recently, the crystal structure of concanavalin A (Mn^{2+} on S1, Ca^{2+} on S2) and its bound water at 100 K was solved to an ultrahigh resolution (0.94 Å) based on synchrotron data.[7] The Mn^{2+} ion is surrounded by three carbonyl oxygen atoms, one nitrogen atom of histidine, and two water molecules in a slightly distorted octahedral coordination arrangement (Scheme 6.1). The Mn-O bond lengths in the plane containing

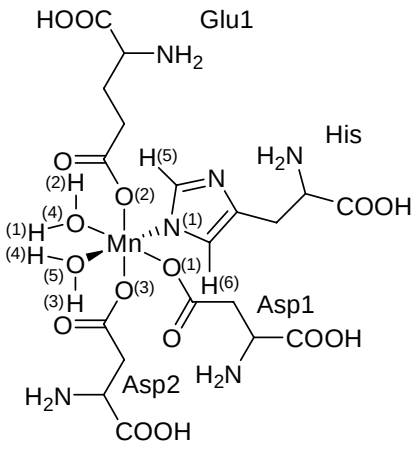

Scheme 6.1. A model of the Mn^{2+}-binding site S1, truncated after the first amino acid.

the coordinating atoms of Asp1, Glu, Asp2, and $H_2O(4)$ are nearly equal, whereas the bond lengths to His and $H_2O(5)$ are significantly longer.

The first EPR study (35 GHz) on concanavalin A was reported in 1974, in which the Mn^{2+} spectrum of a single crystal was interpreted in terms of a spin Hamiltonian with an isotropic g-tensor (g = 2.0009), a nearly isotropic ^{55}Mn hyperfine tensor ($A_{\|}$ = 264.3 MHz, $A_{\perp}$ = 256.2 MHz), and an axial zero-field splitting (ZFS) (D = 0.02 cm^{-1}).[8,9]

Recently, Goldfarb *et al*. have investigated the frozen solution and the single crystal of concanavalin A by W-band (95 GHz) pulsed EPR and ^1H electron-nuclear double resonance spectroscopic techniques (ENDOR).[10] HF-EPR and ^1H HF-ENDOR offer new opportunities for the investigation of paramagnetic transition metal complexes. In particular, for Mn^{2+} (S = 5/2, I = 1/2) it is better to measure the central transition $|-½,m> \rightarrow |½,m>$, thereby obtaining better resolution and a higher sensitivity. Contrary to X-ray crystallography, which is by far the most established and effective method for determining the three-dimensional structure of proteins, ENDOR measurements on single crystals can provide information on the location of protons, when the metal center is paramagnetic.[11,12] Frozen solution results,[10] from which the water proton positions could not be assigned uniquely, were refined in a single crystal study, and the atomic coordinates of the protons were calculated (within the point-dipole approximation).[12]

Our goal here is to confirm by quantum chemical calculations this type of structure determination by ENDOR, and to analyze the interrelations between electronic structure and EPR/ENDOR parameters for an experimentally well-investigated biological manganese site. To our knowledge, there exist no theoretical studies on concanavalin A. Moreover, we use this well-defined biological system to evaluate the dependence of electronic structure and EPR parameters on a series of DFT exchange-correlation functionals. The yet unknown ^{17}O hyperfine couplings will be predicted. We want to identify the most suitable DFT methods to be applied also to computational studies on more complicated or less well characterized biological Mn sites.

6.2 Computational Details

Initial coordinates have been taken from the 0.94 Å resolution synchrotron data, deposited in the Protein Data Bank (PDB entry 1NLS; cf. Figure 6.1).[7] Keeping the heavy-atom positions fixed, the hydrogen positions were then optimized, except for those of the two water molecules, for which optimized distances (0.976 Å) and angles (106.5°) for a coordinated water molecule in the $[Mn(H_2O)_6]^{2+}$ complex were applied (Model "dist. X-ray"). The optimization was carried out with the Turbomole 5.8[13] code at B3LYP[14,15] DFT level with SVP basis sets[16] using unrestricted Kohn-Sham wavefunctions. Attempts of a full structure optimization resulted in a breakdown of the coordination sphere (one ligand was expelled), indicating that constraints due to the protein environment have to be taken into account (in particular, there are bridges between different amino acids that are probably structurally relevant but not included in the computational model used for optimization). When keeping the heavy-atom positions fixed, the smaller computational model (Figure 6.1) and a more extended model corresponding to the atoms shown in Scheme 6.1 provided virtually identical spin-density distributions and EPR parameters. We will therefore in the following concentrate on the smaller model. In addition to the structure derived from the X-ray data, we investigated also a model, in which the metal-ligand distances were adjusted to reproduce the Mn-H distances from ENDOR data[10] (Model "dist. ENDOR"), while keeping angles and bond lengths within the ligands fixed to the same values as in the first model.

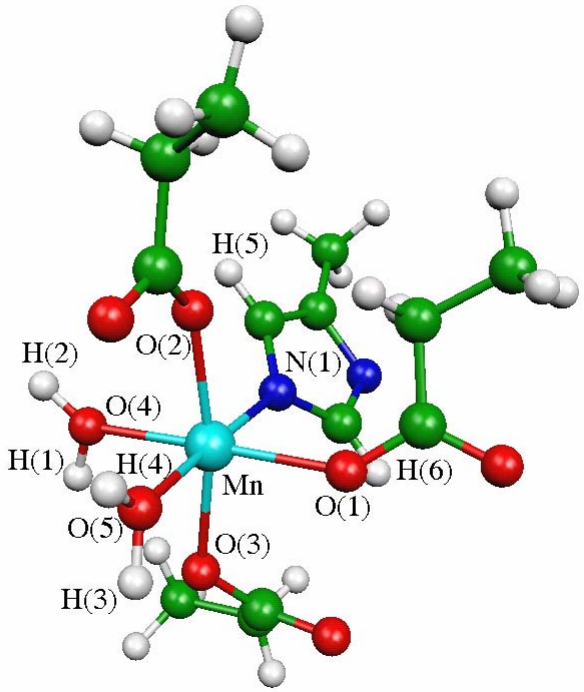

Figure 6.1. Structure and atom labels of concanavalin A.

Unrestricted Kohn-Sham single-point calculations were performed with Gaussian03[17] using a 9s7p4d basis set for manganese (specifically designed for hyperfine calculations[18,19]) and flexible IGLO-III[20,21] basis sets for the ligand atoms.

The following DFT exchange-correlation functionals were compared: the GGA functionals a) BP86[22,23] and b) BLYP[14,15], the hybrid functionals c) B3LYP[14,15] with 20% exact exchange and d) BHLYP[14,24] with 50% exact exchange, as well as the user-defined hybrid functionals e) B-60LYP with 60% exact exchange (40% E_x^{Slater} and 40% ΔE_x^{B88} and E_c^{LYP}) and f) B-70LYP with 70% exact exchange (30% E_x^{Slater} and 30% ΔE_x^{B88} and E_c^{LYP}).

The unrestricted Kohn-Sham orbitals were transferred to the MAG-Respect property package[25] by suitable interface routines. The atomic mean-field approximation (AMFI)[26,27] has been used to compute the matrix elements of the spin-orbit (SO) operator. In g-tensor calculations, a common gauge at the metal center was employed. Differences between calculations with the IGLO-III basis and IGLO-II-based results are very small for ^{1}H HFC (< 0.1 MHz), suggesting that the ligand basis set is essentially converged. The Fermi-contact contributions to the ^{55}Mn HFC change by 2 MHz, suggesting that there is a very slight shift of spin density. We will exclusively report the IGLO-III-based results.

The dielectric constant of a protein is not very high ($\varepsilon \approx 4$). Therefore, solvent effects were evaluated by Kohn-Sham single point calculations using the polarizable continuum model (PCM) and the BHLYP functional in chloroform ($\varepsilon = 4.9$). The ^{1}H HFC differs only slightly between gas phase and solvent calculations (< 0.1 MHz). A small influence is observed for the Fermi-contact term A_{FC} for the ^{55}Mn HFC (gas phase: -196.0 MHz, $CHCl_3$: -199.8 MHz). In the following only the gas phase calculations will be discussed.

6.3 Results and Discussions

Goldfarb *et al*. have carried out several W-band (95 GHz) pulsed EPR and electron-nuclear double resonance (ENDOR) studies on concanavalin A in frozen solution and in a single crystal.[10,28-30] ^{1}H ENDOR indicated all protons to have axially symmetric hyperfine tensors. The two imidazole protons, situated 3.56 Å from Mn^{2+}, are magnetically equivalent, but the four water protons are magnetically inequivalent, situated at distances between 2.67 and 3.24 Å.

6.3.1 Spin-Density Analysis

As the computed EPR/ENDOR parameters depend decisively on the quality of the spin-density distribution, Table 6.1 provides Mulliken atomic spin densities (atomic spin densities from natural population analyses are very similar) obtained with different functionals, and spin-density isosurface plots with a subset of three functionals are shown in Figure 6.2.

Table 6.1. Mulliken atomic spin densities and $<S^2>$ expectation values in the concanavalin A model.

	Mn	*O(1)*	*O(2)*	*O(3)*	*O(4)*	*O(5)*	*N(1)*
BP86	4.901	0.014	-0.006	-0.003	-0.027	-0.019	-0.035
BLYP	4.786	0.031	0.006	0.012	-0.020	-0.009	-0.017
B3LYP	4.905	0.014	0.003	0.002	-0.007	-0.005	-0.015
BHLYP	4.929	0.009	0.004	0.002	-0.001	0.000	-0.008
B-60LYP	4.930	0.009	0.005	0.003	0.000	0.001	-0.006
B-70LYP	4.920	0.012	0.006	0.002	0.002	0.003	-0.002

	H(1)	*H(2)*	*H(3)*	*H(4)*	*H(5)*	*H(6)*	$<S^2>$
BP86	0.043	0.034	0.022	0.016	-0.001	0.001	8.758
BLYP	0.055	0.047	0.026	0.017	0.000	0.001	8.760
B3LYP	0.018	0.015	0.012	0.009	0.000	0.001	8.754
BHLYP	0.009	0.007	0.006	0.005	0.000	0.000	8.753
B-60LYP	0.007	0.006	0.005	0.004	0.000	0.000	8.753
B-70LYP	0.006	0.005	0.005	0.004	0.000	0.000	8.753

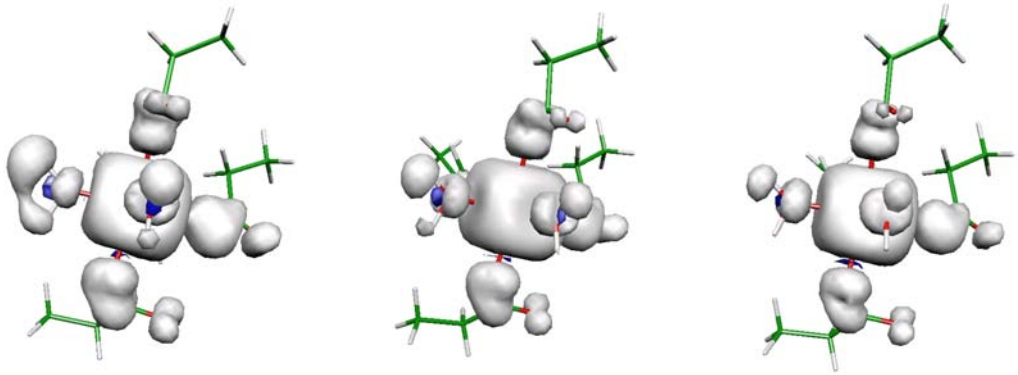

BP86 B3LYP BHLYP

Figure 6.2. Spin-density distribution. Isosurfaces ±0.0005 a.u.

Spin contamination of the Kohn-Sham wavefunction is small, even with large exact-exchange admixtures (cf. $<S^2>$ expectation values in Table 6.1). In fact, the spin contamination decreases even somewhat with more exact exchange, which is probably indirectly due to the enhanced ionicity of the metal-ligand bonds. Exact-exchange admixture has usually three effects on the spin-density distribution in transition-metal complexes:[18,19,31] a) the metal-ligand bond becomes more ionic (self-interaction errors tend to render the bonds too covalent at LDA or GGA level)[19,31-35], and b) valence-shell spin polarization across covalent bonds is enhanced, leading often to larger spin contamination,[19] c) core-shell spin polarization at the metal center is also enhanced (improved). While the latter effect is important for the metal hyperfine coupling[19] (see below), the two former trends may counteract each other:[33,36] the increased ionicity may actually decrease the tendency towards valence-shell spin polarization. This seems to be the case here. The enhanced bond ionicity is reflected in an increase of spin density at the metal center and less spin density on the ligand atoms (Table 6.1, Figure 6.2).

Independent on the functional and on details of the spin-density distribution, an assignment to an electronic structure of a high-spin Mn^{2+} (d^5) system is obtained at all computational levels. The manganese spin density is close to the formally expected five unpaired spins (Table 6.1). The coordinated histidine nitrogen atom exhibits negative spin density due to spin polarization. At BP86 level, negative spin density is found also for four oxygen atoms in the first coordination sphere. This is reduced to just one oxygen atom at BHLYP level (Table 6.1). Above 50% exact exchange, only the negative spin density on nitrogen remains. Thus, in contrast to many other cases,[18,19,33] obviously spin polarization becomes less important here with more exact exchange, due to less delocalization of spin density upon the ligands. Delocalized positive spin density is found particularly at the water and imidazole protons.

6.3.2 The g-Tensor

An isotropic g-tensor with g_{iso} = 2.0009+/-0.0004 (the uncertainty may also be considered as an upper limit for the g-anisotropy) was measured (EPR study at 35 GHz).[9] This is the expected situation for a high spin d^5 Mn^{2+} complex. Our calculations (Table 6.2) confirm the very small g-shifts and extremely small anisotropy. Larger exact-exchange admixture reduces g_{iso} somewhat and thereby improves agreement with experiment.

Table 6.2. g-Shift components (in ppt) and absolute g-values of the concanavalin A model.[a]

	Δg_{iso}	Δg_{11}	Δg_{22}	Δg_{33}
BP86	0.1 (2.0024)	0.0 (2.0023)	0.0 (2.0023)	0.2 (2.0025)
BLYP	0.1 (2.0024)	-0.1 (2.0022)	0.0 (2.0023)	0.3 (2.0026)
B3LYP	-0.2 (2.0021)	-0.3 (2.0020)	-0.2 (2.0021)	-0.2 (2.0021)
BHLYP	-0.4 (2.0019)	-0.5 (2.0018)	-0.4 (2.0019)	-0.4 (2.0019)
B-60LYP	-0.5 (2.0018)	-0.5 (2.0018)	-0.5 (2.0018)	-0.4 (2.0019)
B-70LYP	-0.5 (2.0018)	-0.5 (2.0018)	-0.5 (2.0018)	-0.4 (2.0019)
exp.[b]	-1.4±0.4 (2.0009±0.0004)			

[a]Absolute g-values in parentheses. [b]From 35 GHz EPR measurements on a single crystal of Mn^{2+}, Ca^{2+}-concanavalin A.[9]

6.3.3 ^{55}Mn Hyperfine Coupling Constant

Isotropic ^{55}Mn hyperfine data are available from Q- and W-band EPR studies[9,10] and are compared to our computations in Table 6.3 (HFC anisotropy is available from Q-band single-crystal measurements[8,9]). The isotropic coupling constant A_{iso} in such systems depends appreciably on exact-exchange admixture, due to an enhancement of (overall negative) core-shell spin polarization contributions to the spin density at the nucleus[19,37] (and due to generally more spin density on manganese, see above). This renders the couplings more negative and improves agreement with the experimental data[9,10] (Table 6.3). The negative sign of A_{iso} has been confirmed experimentally.[30,38] The extremely small HFC anisotropy found[8,9] is also confirmed by the calculations. It reflects the rather isotropic spin-density distribution in a high-spin Mn^{2+} system.

Table 6.3 provides also spin-orbit (SO) corrections to the hyperfine tensor. SO contributions have previously been found very important already for *3d* metals.[36,39,40] Here they are rather small compared to the isotropic nonrelativistic A_{FC}, again in agreement with the d^5 configuration (for an O_h symmetrical high-spin d^5 system with $^6A_{1g}$ ground state, SO effects would vanish exactly).

Table 6.3. Computed and experimental ^{55}Mn HFC tensors (in MHz).[a]

	First-order			A_{SO}	*Total* ***A****-tensor*	
	A_{FC}	T_{11}	T_{22}	T_{33}	A_{PC}	A_{iso}	$\langle S^2 \rangle$
BP86	-140.2	-1.2	-0.3	1.5	-3.1	-143.3	8.758
BLYP	-122.0	-2.1	0.0	2.2	-3.1	-125.1	8.760
B3LYP	-155.6	-0.5	-0.2	0.7	-2.7	-158.3	8.754
BHLYP	-196.0	-0.6	0.0	0.6	-2.2	-198.2	8.753
B-60LYP	-208.1	-0.7	0.0	0.6	-2.0	-210.1	8.753
B-70LYP	-224.6	-0.9	0.1	0.7	-1.8	-226.3	8.753
exp.[b]		-2.7	-2.7	5.4		-258.9	
exp.[c]						-262.5	

[a] A_{iso} is the total isotropic value, T_i represent the traceless part of the full **A** tensor, A_{FC} and A_{PC} denote the isotropic first-order Fermi-contact and second-order pseudo-contact (spin-orbit) contributions to the full total **A** tensor, respectively. [b] From 35 GHz EPR measurements on a single crystal of Mn^{2+}, Ca^{2+}-concanavalin A.[9] [c] From 95 GHz ENDOR.[30]

6.3.4 ^{1}H Hyperfine Coupling Constants.

The ^{1}H HFCs were computed for two different structures (Table 6.4): a) after DFT optimization of the hydrogen positions (except for the water protons, for which standard water structure parameters were used; cf. Computational Details), and b) after elongation of the Mn-L distances to reproduce hydrogen positions deduced from ENDOR spectra[10] (cf. Computational Details). Experiments indicate approximately axial symmetry for the proton HFC tensors. This is confirmed by the calculations. SO corrections are negligible for the proton HFC tensors and are thus not provided in the Table.

Table 6.4. Computed and experimental ^{1}H HFC tensors (in MHz).

			A_{iso}	A_{FC}	T_{11} /T_{22}	T_{33}	A' [a]
H(1)	dist. X-ray[b]	BP86	3.7	3.7	-3.2 / -3.1	6.3	
	2.89 Å	BLYP	4.4	4.4	-3.2 / -3.2	6.3	
		B3LYP	2.4	2.4	-3.3 / -3.2	6.4	
		BHLYP	1.6	1.6	-3.3 / -3.1	6.5	6.4
		B-60LYP	1.5	1.5	-3.3 / -3.1	6.5	
		B-70LYP	1.4	1.4	-3.3 / -3.1	6.5	
	dist. ENDOR[c]	BP86	1.6	1.6	-4.0 / -3.8	7.9	
	2.67 Å	BLYP	1.7	1.7	-4.1 / -3.8	7.8	
		B3LYP	0.9	0.9	-4.2 / -3.9	8.0	
		BHLYP	0.5	0.5	-4.2 / -3.9	8.1	8.1
		B-60LYP	0.4	0.4	-4.2 / -3.9	8.1	
		B-70LYP	0.4	0.4	-4.2 / -3.9	8.1	
		exp.[d]	0.1		-4.2	8.2	
		exp.[e]	0.1		-4.0	8.0	
H(2)	dist. X-ray[b]	BP86	2.3	2.3	-3.3 / -3.3	6.6	
	2.85 Å	BLYP	2.7	2.7	-3.3 / -3.3	6.6	
		B3LYP	1.7	1.7	-3.4 / -3.3	6.7	
		BHLYP	1.2	1.2	-3.5 / -3.3	6.8	6.8
		B-60LYP	1.1	1.1	-3.5 / -3.3	6.8	
		B-70LYP	1.0	1.0	-3.5 / -3.3	6.8	
	dist. ENDOR[c]	BP86	5.0	5.0	-3.0 / -2.8	5.8	
	2.99 Å	BLYP	5.5	5.5	-3.0 / -2.9	5.8	
		B3LYP	3.4	3.4	-3.0 / -2.9	5.9	
		BHLYP	2.6	2.6	-3.0 / -2.9	5.9	5.9
		B-60LYP	2.4	2.4	-3.0 / -2.9	5.9	
		B-70LYP	2.3	2.3	-3.0 / -2.9	5.9	
		exp.[d]	0.1		-3.0	6.0	
		exp.[e]	0.8		-3.5	7.0	

			A_{iso}	A_{FC}	T_{11} /T_{22}	T_{33}	A' [a]
H(3)	dist. X-ray[b]	BP86	2.2	2.2	-3.0 / -2.9	5.9	
	2.97 Å	BLYP	2.5	2.5	-3.0 / -2.9	5.9	
		B3LYP	1.6	1.6	-3.0 / -2.9	6.0	
		BHLYP	1.2	1.2	-3.1 / -2.9	6.0	5.9
		B-60LYP	1.1	1.1	-3.1 / -2.9	6.0	
		B-70LYP	1.0	1.0	-3.1 / -2.9	6.0	
	dist. ENDOR[c]	BP86	0.2	0.2	-3.8 / -3.4	7.2	
	2.76 Å	BLYP	0.2	0.2	-3.8 / -3.4	7.1	
		B3LYP	0.1	0.1	-3.9 / -3.5	7.3	
		BHLYP	-0.1	-0.1	-3.9 / -3.5	7.4	7.4
		B-60LYP	-0.1	-0.1	-3.9 / -3.5	7.4	
		B-70LYP	-0.1	-0.1	-3.9 / -3.5	7.4	
		exp.[d]	0.0		-3.75	7.5	
		exp.[e]	0.4		-3.9	7.8	
H(4)	dist. X-ray[b]	BP86	1.5	1.5	-3.1 / -3.0	6.0	
	2.93 Å	BLYP	1.7	1.7	-3.1 / -2.9	6.0	
		B3LYP	1.2	1.2	-3.2 / -3.0	6.2	
		BHLYP	0.9	0.9	-3.2 / -3.0	6.2	6.3
		B-60LYP	0.9	0.9	-3.2 / -3.0	6.2	
		B-70LYP	0.8	0.8	-3.2 / -3.0	6.2	
	dist. ENDOR[c]	BP86	2.4	2.4	-2.3 / -2.2	4.5	
	3.24 Å	BLYP	2.7	2.7	-2.3 / -2.2	4.6	
		B3LYP	2.0	2.0	-2.4 / -2.3	4.7	
		BHLYP	1.6	1.6	-2.4 / -2.3	4.7	4.6
		B-60LYP	1.5	1.5	-2.4 / -2.3	4.7	
		B-70LYP	1.5	1.5	-2.4 / -2.3	4.7	
		exp.[d]	0.6		-2.7	5.4	
		exp.[e]	0.4		-2.5	5.0	
H(5)	dist. X-ray[b]	BP86	0.2	0.2	-2.0 / -1.9	3.8	
	3.39 Å	BLYP	0.2	0.2	-2.0 / -1.8	3.8	
		B3LYP	0.1	0.1	-2.0 / -1.9	3.9	
		BHLYP	0.1	0.1	-2.0 / -1.9	3.9	4.1
		B-60LYP	0.1	0.1	-2.0 / -1.9	4.0	
		B-70LYP	0.1	0.1	-2.0 / -1.9	4.0	
	dist. ENDOR[c]	BP86	0.1	0.1	-1.7 / -1.6	3.3	
	3.56 Å	BLYP	0.1	0.1	-1.7 / -1.6	3.3	
		B3LYP	0.1	0.1	-1.7 / -1.7	3.4	
		BHLYP	0.0	0.0	-1.8 / -1.7	3.4	3.5
		B-60LYP	0.0	0.0	-1.8 / -1.7	3.4	
		B-70LYP	0.0	0.0	-1.8 / -1.7	3.4	
		exp.[d]	0.0		-1.75	3.6	
		exp.[e]	0.1		-1.94	3.9	

			A_{iso}	A_{FC}	T_{11} /T_{22}	T_{33}	A' [a]
H(6)	dist. X-ray[b]	BP86	0.0	0.0	-2.0 / -1.8	3.8	
	3.39 Å	BLYP	0.0	0.0	-1.9 / -1.8	3.8	
		B3LYP	0.0	0.0	-2.0 / -1.9	3.9	
		BHLYP	0.0	0.0	-2.0 / -1.9	3.9	4.1
		B-60LYP	0.0	0.0	-2.0 / -1.9	3.9	
		B-70LYP	-0.1	-0.1	-2.0 / -1.9	3.9	
	dist. ENDOR[c]	BP86	0.0	0.0	-1.7 / -1.6	3.3	
	3.56 Å	BLYP	0.0	0.0	-1.7 / -1.6	3.3	
		B3LYP	0.0	0.0	-1.7 / -1.7	3.4	
		BHLYP	0.0	0.0	-1.7 / -1.7	3.4	3.5
		B-60LYP	0.0	0.0	-1.7 / -1.7	3.4	
		B-70LYP	0.0	0.0	-1.7 / -1.7	3.4	
		exp.[d]	0.0		-1.75	3.6	
		exp.[e]	0.1		-1.99	4.0	

[a]Anisotropic term A' derived from the point-dipole approximation: $A' = \frac{g_e \beta_e g_N \beta_N}{hr^3} \rho(3\cos^2\delta - 1)$ [MHz], where g_e and g_N are the electron and nuclear g-values, ρ ist the spin density at the manganese atom, δ is the angle between the applied field and the direction of the hydrogen bond, and r is the distance Mn-H in Å. [b]H-Mn distance with optmized imidazole proton positions (see Computational Details). [c]Mn-L bond lengths adjusted to reproduce ENDOR Mn-H distances (see Computational Details). [d]From 95 GHz ENDOR; accuracy ±0.1 MHz.[10] [e]From 95 GHz ENDOR; accuracy ±0.04 MHz.[12]

Starting with the anisotropic parts of the six ^{1}H HFC tensors studied, we see very little dependence on the functional and rather good agreement with experiment, including the trends for the different H_2O proton locations. This suggests that the anisotropic tensor components are dominated by the direct dipolar interaction with the metal-centered spin density. Then the point-dipolar approximation should work well, as does seem to be the case (see Table 6.4). Indeed, agreement between ENDOR-derived and computed Mn-H distances is essentially perfect for water protons H(1)-H(3), whereas estimates based on ENDOR appear to overestimate the remaining distances by about 0.2 Å.

Turning to the more difficult A_{iso} of the water protons, we see that the diminishing spin delocalization onto the ligands with increasing exact-exchange admixture reduces the isotropic hyperfine couplings and thereby brings the computations into better agreement with experiment. Changes above 50% exact exchange tend to be small. For H(4), use of the larger ENDOR-derived Mn-H distance would interestingly lead to a much larger A_{iso} (Mulliken spin densities on H(4) are also consistently about twice the value for the optimized structure, for all functionals). It is clear, however, that in this case

the shorter, optimized distance and the lower A_{iso} values are to be preferred. The optimized distance agrees also better with ^{2}D ENDOR measurements on a concanavalin A preparation with deuterated ligands (d(Mn-D) = 3.08 Å).[10]

The two histidine protons H(5) and H(6) exhibit an almost purely dipolar tensor,[10] as is confirmed by the computations (so is the magnetic equivalence of the two protons). Here the dipolar tensor depends very slightly more on the functional than for H(1)-H(4). The optimized Mn-H(5) and Mn-H(6) distances agree much better with crystallographic data[12] (Mn-H(5) = 3.41 Å, Mn-H(6) = 3.44 Å) than the larger ENDOR-derived values.

6.3.5 ^{17}O Hyperfine Coupling Constants

To predict the ^{17}O hyperfine interaction of the water ligands and the coordinated amino acids, different DFT methods were first validated on the Mn^{2+} hexaquo complex, for which high-field ENDOR data are available (see section 5.3.5).[41]

Following these results for $[Mn(H_2O)_6]^{2+}$, Table 6.5 compares the ^{17}O HFCs for the two different concanavalin A structures (cf. Computational Details) for the BP86 and B-60LYP functionals. As already observed for the Mn^{2+} aquo complex, there is not much variation for the different components of the hyperfine coupling tensor of the oxygen atoms of the amino acid ligands O(1), O(2) and O(3) with different functionals, even though the Mulliken spin densities have different signs for O(2) and O(3) for the different functionals (negative for BP86, positive for B-60LYP, see Table 6.1). The choice of the model (X-ray vs. ENDOR-based distances, cf. above) also affects the hyperfine couplings of the amino-acid oxygen atoms very little.

In contrast to O(1)-O(3), the exchange-correlation functional influences the HFCs much more for the water oxygen atoms O(4) and O(5), in particular for the isotropic value. Here the substantial differences between the X-ray- and ENDOR-derived Mn-O distances also lead to appreciable variations in the computed HFC tensors.

Table 6.5 provides also results for nitrogen atom N(1) of the imidazole ligand. In spite of a strong influence of exact-exchange admixture on the Mulliken spin density (cf. Table 6.1), even the isotropic nitrogen hyperfine coupling constant is affected very little.

Table 6.5. Computed and experimental ^{14}N and ^{17}O HFC tensors (in MHz) in the concanavalin A model.

L	*d(Mn-L)*		A_{iso}	A_{FC}	T_{11}	T_{22}	T_{33}
O(1)	dist. X-ray[a]	BP86	-8.7	-8.7	-3.3	1.3	2.0
	2.15 Å	B-60LYP	-8.8	-8.8	-2.7	1.1	1.6
	dist. ENDOR[b]	BP86	-7.8	-7.8	-3.7	1.4	2.3
	2.15 Å	B-60LYP	-8.0	-8.0	-2.6	1.1	1.5
O(2)	dist. X-ray[a]	BP86	-9.2	-9.2	-2.5	1.0	1.5
	2.17 Å	B-60LYP	-9.3	-9.3	-2.6	1.2	1.4
	dist. ENDOR[b]	BP86	-8.7	-8.7	-2.5	1.0	1.5
	2.17 Å	B-60LYP	-8.9	-8.9	-2.6	1.2	1.4
O(3)	dist. X-ray[a]	BP86	-7.5	-7.5	-1.8	0.4	1.4
	2.19 Å	B-60LYP	-7.9	-7.9	-2.1	0.7	1.3
	dist. ENDOR[b]	BP86	-6.1	-6.1	-1.6	0.3	1.3
	2.15 Å	B-60LYP	-7.1	-7.1	-1.9	0.6	1.3
O(4)	dist. X-ray[a]	BP86	-22.8	-22.8	-1.1	0.0	1.0
	2.18 Å	B-60LYP	-12.5	-12.5	-2.0	0.6	1.4
	dist. ENDOR[b]	BP86	-21.2	-21.2	-1.0	0.0	1.1
	2.16 Å	B-60LYP	-11.7	-11.7	-2.0	0.6	1.4
O(5)	dist. X-ray[a]	BP86	-14.7	-14.7	-1.4	0.3	1.1
	2.26 Å	B-60LYP	-10.3	-10.3	-2.0	0.7	1.3
	dist. ENDOR[b]	BP86	-11.6	-11.6	-1.4	0.5	0.9
	2.41 Å	B-60LYP	-7.9	-7.9	-1.8	0.7	1.1
N(1)	dist. X-ray[a]	BP86	4.0	4.0	-0.7	-0.6	1.4
	2.23 Å	B-60LYP	3.9	3.9	-0.7	-0.6	1.3
	dist. ENDOR[b]	BP86	4.1	4.1	-0.7	-0.6	1.3
	2.44 Å	B-60LYP	3.6	3.6	-0.6	-0.5	1.1

[a]H-Mn distance with optmized imidazole proton positions (see Computational Details). [b]Mn-L bond lengths adjusted to reproduce ENDOR Mn-H distances (see Computational Details).

6.4 Conclusions

We have used the structurally and EPR/ENDOR-spectroscopically well characterized manganese site in the saccharide-binding protein concanavalin A to evaluate a) the performance of different DFT exchange-correlation potentials for the calculation of spin-density distribution and metal/ligand hyperfine parameters in biological manganese sites, and b) the validity of the point-dipole approximation in estimating proton positions on coordinated protein residues and water molecules from ENDOR data.

Isotropic hyperfine couplings on both metal and the ligand protons are best reproduced when the hybrid functional exhibits about 50% or more exact-exchange admixture. This is consistent with previous results for both very early 3*d* metal centers (e.g. V^{IV} complexes[42,43]) and very late metals (e.g. for Cu(II) systems[36]). Notably, spin contamination is no problem with larger exact-exchange admixture but even diminishes, due to decreased metal-ligand covalency. Spin-orbit contributions to the metal hyperfine tensor have been found to be small, consistent with the high-spin d^5 electronic characteristics.

Anisotropic ^{1}H HFCs are relatively insensitive to the exact-exchange admixture, demonstrating that they are dominated by the large metal-centered spin density. This helps to justify the point-dipole approximation used to estimate hydrogen-atom positions from dipolar HFCs determined in ENDOR spectra. The ENDOR-derived distances agree well with optimized Mn-H distances for water protons H(1)-H(3) but overestimate the experimental and computed values by about 0.2 Å for the remaining protons. The ^{17}O HFCs for the oxygen atoms directly bonded to the manganese center in concanavalin A were predicted based on prior method validation for the $[Mn(H_2{}^{17}O)_6]^{2+}$ complex.

Chapter 7

The world of the (nuclear) spins is a true paradise for theoretical and experimental physicists.

Richard R. Ernst, 1992.

Validation of Broken-Symmetry Density Functional Methods for the Calculation of Electron Paramagnetic Resonance Parameters of Dinuclear Mixed-Valence $Mn^{III}Mn^{IV}$ Complexes

7.1 Introduction

In this chapter we will turn to dinuclear manganese complexes. A main challenge for spin-coupled multinuclear transition-metal systems are their energetically close-lying electronic levels. To describe correctly the antiferromagnetic couplings present in ground and excited states, very accurate calculations would require a multi-determinant based treatment. For the systems of interest, their size typically prohibits such a multideterminantal treatment so far. This holds in particular for the OEC. A cost-efficient approximate alternative of wide-spread use are broken-symmetry density functional theory (BS-DFT)[1,2] techniques (see section 3.4), where single-determinantal unrestricted Kohn-Sham (KS) wavefunctions are appropriately spin-projected[3,4] to simulate energy levels and spin-density distributions of the true antiferromagnetically coupled states. The main area of application of BS-DFT has been in the computation of Heisenberg exchange coupling constants that describe the spin couplings of the system. Yet, EPR parameters like hyperfine coupling constants (HFCs) or electronic g-tensors have also been in the

focus of interest early on[5] (see also ref. [6]). Recently, Sinnecker *et al*.[7,8] have carried out BS-DFT based EPR parameter calculations (for g-tensors, and ^{55}Mn, ^{14}N and ^{1}H HFCs) for the dinuclear $Mn^{III}Mn^{IV}$ complexes $[(dtne)Mn(\mu\text{-}O)_2(\mu\text{-}OAc)Mn]^{2+}$, and for a model of the superoxidized state of dimanganese catalase (**Mn-cat**).

Here we extend these important studies to a larger set of mixed-valence dinuclear $Mn^{III}Mn^{IV}$ complexes with different bridging and terminal ligand sets, and to a wider selection of functionals, with the aim to validate BS-DFT approaches to be applied to the OEC. In particular, we are interested in examining the effect of exact-exchange (EXX) admixture in hybrid exchange-correlation functionals. This point has not yet been addressed in detail for BS-DFT calculations of EPR parameters but is deemed crucial for accurate predictions. Calculations on mononuclear Mn complexes suggest, for example,[9] that Mn HFCs and certain ligand HFCs require substantially larger EXX admixture than provided by standard hybrid functionals like B3LYP. As we will also provide results for Heisenberg exchange coupling constants, we note in passing, in addition to the abovementioned work of Sinnecker and Neese, BS-DFT studies on the exchange couplings of dinuclear $Mn^{III}Mn^{IV}$[10] and $Mn^{IV}Mn^{IV}$[11] complexes (the vast literature on BS-DFT calculations of exchange couplings of di- and multinuclear transition-metal complexes in general is outside the scope of this introduction; some references will be given later in the paper). We will compare different functionals and different spin-projection schemes[2,12] in this context and will study the influence of bridging and terminal ligand sets.

7.2 Computational Details

Structure optimizations and KS wavefunction computations were done with the Turbomole code (revision 5.8 and revision 5.9.1, the latter locally modified to allow the use of custom-made hybrid functionals).[13] For catalase, initial coordinates have been taken from crystallographic studies of ref. [14]. To construct the model **Mn-cat**,[8] histidine residues have been substituted by methyl imidazole and glutamates by acetate. Structure optimizations were done at B3LYP/SVP level,[15,16,17] using unrestricted KS wavefunctions. Structures of both BS and HS solutions have been fully optimized.

Subsequent unrestricted KS single-point calculations used a 9s7p4d all-electron manganese basis set (designed for hyperfine calculations[15,17-19]) and flexible

IGLO-II[20,21] basis sets for the ligand atoms. Different exchange-correlation functionals were compared: a) the BLYP[15,16] GGA functional, the hybrid functionals b) B3LYP[15,16] with 20% exact exchange and c) BHLYP[15,22] with 50% exact exchange, as well as the custom-made hybrid functionals d) B-XXLYP with XX = 60, 70, 80, 90% exact exchange (100-XX% E_x^{Slater}, 100-XX% ΔE_x^{B88}, and E_c^{LYP}). Mulliken spin densities were used to characterize the broken-symmetry and high-spin states.

The unrestricted KS orbitals were transferred to the MAG-Respect property package[23] by suitable interface routines. The atomic mean-field approximation (AMFI)[24,25] has been used to compute the matrix elements of the Breit-Pauli spin-orbit (SO) operator for g-tensors and SO corrections to the Mn hyperfine tensors.

The paired-orbital analyses were done with the UHF decomposition code of Zilberberg *et al.*[26,27] based on a Gaussian03[28] single-point calculation at B3LYP[15,16] DFT level with the extended basis set described above.

7.3 Model Systems

Figure 7.1 shows the labels of the core atoms (Mn, O) of the investigated model systems $[LMn(\mu\text{-}O)MnL]^{3+}$ (**1-(μ-O)**, L^- = *N*,*N*-bis(2-pyridylmethyl)-*N*'-salicyliden-1,2-diaminoethane), $[(bipy)_2Mn(\mu\text{-}O)_2Mn(bipy)_2]^{3+}$ (**2-(μ-O)$_2$**, bipy = 2,2'-bipyridine), $[(phen)_2Mn(\mu\text{-}O)_2Mn(phen)_2]^{3+}$ (**3-(μ-O)$_2$**, phen = 1,10-phenanthroline), $[(dtne)Mn(\mu\text{-}O)_2(\mu\text{-}OAc)Mn]^{2+}$ (**4-(μ-O)$_2$(μ-OAc)**, dtne = 1,2-bis(1,4,7-triazacyclonon-1-yl)ethane), $[(tacn)Mn_2(\mu\text{-}O)_2(\mu\text{-}OAc)(tacn)]^{2+}$ (**5-(μ-O)$_2$(μ-OAc)**, tacn = 1,4,7-triazacyclononane), $[(tacn)Mn(\mu\text{-}O)(\mu\text{-}OAc)_2Mn(tacn)]^{3+}$ (**6-(μ-O)(μ-OAc)$_2$**), and **Mn-cat** (a previously studied model[8] for the superoxidized state of dimanganese catalase). The two systems **4-(μ-O)$_2$(μ-OAc)**[7] and **Mn-cat**[8] are those investigated in previous computational studies by Sinnecker and Neese.

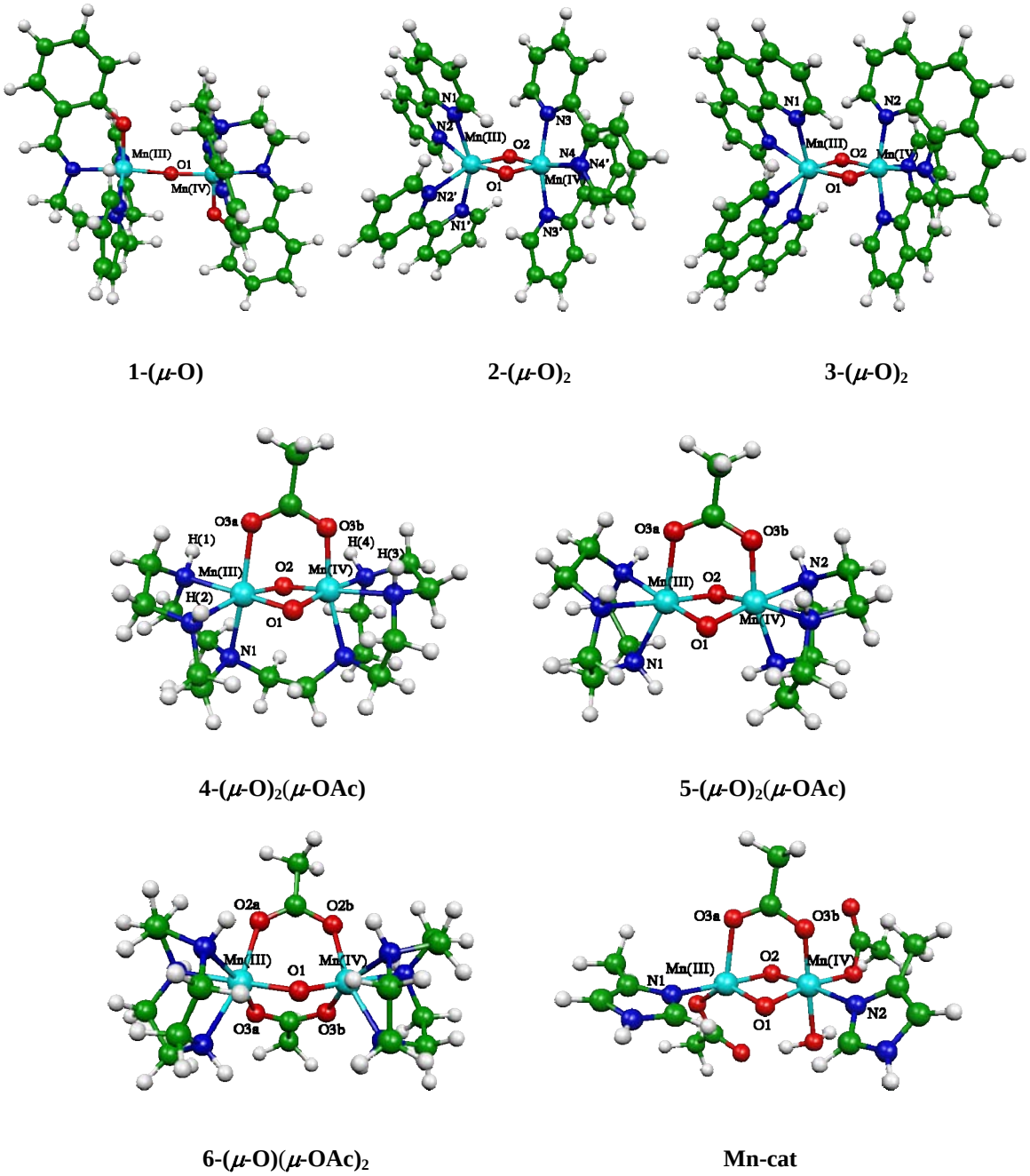

1-(μ-O) **2-(μ-O)$_2$** **3-(μ-O)$_2$**

4-(μ-O)$_2$(μ-OAc) **5-(μ-O)$_2$(μ-OAc)**

6-(μ-O)(μ-OAc)$_2$ **Mn-cat**

Figure 7.1. Structures and atom labels of model systems **1** – **6** and **Mn-cat**.

7.4 Results and Discussion

For all seven dinuclear $Mn^{III}Mn^{IV}$ complexes (Figure 7.1), we will compare the results of structure optimization in the HS and BS state (section 7.4.1). After a discussion of the Mulliken spin density (section 7.4.2), a paired-orbital analysis of the spin contamination follows (section 7.4.3) For each parameter (Heisenberg exchange coupling, g-tensors, ^{55}Mn, ^{14}N and ^{1}H HFC constants) the dependence on exact-exchange admixture will be discussed (sections 7.4.4 – 7.4.9). The influence of terminal ligand size and of the bridging ligand sets will be studied for Heisenberg exchange couplings and for the ^{55}Mn HFC constants.

7.4.1 Structures

For the OEC, one usually assumes[29-32] that the differences between the optimization in the HS and the BS state are rather small (but cf. refs. [7,8]). Distances of the optimized HS and BS states are shown in Table 7.1.

The comparison of central distances of the optimized HS and BS states with experimental data indicates first of all the distinctly different coordination environment of the two Mn centers in all cases, consistent with localized ("trapped") mixed-valent complexes (**Mn-cat** is not analyzed, as no experimental data for the superoxidized state are available). Generally, the distorted octahedral Mn^{III} ion exhibits larger distances to the ligand atoms than the Mn^{IV} center.

The optimized BS structure (S = 1/2) exhibits generally better agreement with the experimental X-ray data than the optimized HS structure (S = 7/2). The by far largest differences between BS and HS structure (Table 7.1) are found for **1-(μ-O)**, where the single (μ-O) bridge provides relatively high flexibility of the core region. Here the HS calculation gives significantly larger Mn-Mn and Mn^{III}-O1 distances than the BS optimization. In the other cases, the differences tend to be below 0.03 Å. The deviations of the BS results from experiment are less than 0.05 Å for Mn-Mn distances and less than 0.07 Å for Mn-O distances. The largest discrepancy is again found for **1-(μ-O)**. Comparison with experiment for **5-(μ-O)$_2$(μ-OAc)** should be made only after averaging the two sides in the computations, as the reported experimental C_2 symmetry is due to statistical disorder.[38] This is a common problem in the structural characterization of such trapped mixed-valence systems.[38]

Table 7.1. Comparison of optimized interatomic distances (in Å) for HS and BS states to experimental data.[a]

		Mn-Mn	*Mn^{III}-O1*	*Mn^{III}-O2a*	*Mn^{III}-O3a*	*Mn^{IV}-O1*	*Mn^{IV}-O2b*	*Mn^{IV}-O3b*
	HS	3.668	1.929	-	-	1.743	-	-
1-(μ-O)	BS	3.569	1.861	-	-	1.739	-	-
	Exp.[b]	3.524	1.797	-	-	1.727	-	-
	HS	2.761	1.898	1.899	-	1.779	1.779	-
2-(μ-O)$_2$	BS	2.761	1.883	1.894	-	1.772	1.767	-
	Exp.[c]	2.716	1.853	1.856	-	1.784	1.784	-
	HS	2.754	1.897	1.897	-	1.777	1.777	-
3-(μ-O)$_2$	BS	2.755	1.886	1.885	-	1.767	1.767	-
	Exp.[d]	2.748	1.802	1.802	-	1.798	1.798	-
4-(μ-O)$_2$	HS	2.639	1.867	1.88	2.191	1.783	1.772	1.919
(μ-OAc)	BS	2.611	1.859	1.862	2.192	1.778	1.768	1.923
	Exp.[e]	2.55	1.83	1.83	2.14	1.78	1.78	1.97
5-(μ-O)$_2$	HS	2.663	1.883	1.878	2.224	1.784	1.785	1.92
(μ-OAc)	BS	2.645	1.873	1.866	2.224	1.778	1.779	1.922
	Exp.[f]	2.588	1.817	1.808	2.079	1.817	1.808	2.079
6-(μ-O)	HS	3.198	1.867	2.111	2.058	1.772	1.906	1.915
(μ-OAc)$_2$	BS	3.210	1.843	2.116	2.061	1.759	1.908	1.917
	Exp.[g]	3.230	1.826	1.999	1.948	1.814	1.951	2.000

[a]B3LYP/SVP optimized structures. See Figure 7.1 for the different complexes and labels. [b]X-ray data taken from ref. [33]. [c]X-ray data taken from ref. [34]. [d]X-ray data taken from ref. [35]. [e]X-ray data taken from ref. [36]. [f]X-ray data taken from ref. [37]. The C_2 symmetrical structure is due to statistical disorder. [g]X-ray data taken from ref. [38].

Based on the BS optimizations, we note the following points: Clearly different Mn-Mn distances occur for the different cores. The largest Mn-Mn distance is obtained for the mono-μ-oxo bridged core due to its almost linear arrangement. The di-μ-oxo bridged complexes **2-(μ-O)$_2$** and **3-(μ-O)$_2$** exhibit Mn-Mn distances of 2.76 Å with very similar, planar central units. That is, bipy and phen ligands provide very similar frameworks for the central bridge. Even smaller model complexes $[(dab)_2Mn(\mu\text{-}O)_2Mn(dab)_2]^{3+}$ and $[(NH_3)_4Mn(\mu\text{-}O)_2Mn(NH_3)_4]^{3+}$ differ in the core region by less than 0.02 Å from the larger systems (see Appendix A). The di-μ-oxo-mono-μ-acetato bridged complexes **4-(μ-O)$_2$(μ-OAc)** and **5-(μ-O)$_2$(μ-OAc)** have even lower Mn-Mn distances (Table 7.1). In contrast, a significantly larger distance is obtained for the mono-μ-oxo-di-μ-acetato bridged complex **6-(μ-O)(μ-OAc)$_2$**.

Table 7.2 provides the BS-optimized core distances for $Mn^{III}Mn^{IV}$ complexes with similar terminal ligand sets (one tacn and sometimes additionally one water ligand) but different bridges. For the modified model systems, similar trends are found as for the experimentally studied complexes, indicating the importance of the bridging ligands and the limited influence of the terminal ligands.

Table 7.2. Influence of the bridge on interatomic distances (in Å) in tacn model complexes.

		Mn-Mn	*Mn^{III}-O1a*	*Mn^{III}-O2a*	*Mn^{III}-O3a*	*Mn^{IV}-O1b*	*Mn^{IV}-O2b*	*Mn^{IV}-O3b*
$[(tacn)(H_2O)Mn(\mu\text{-}O)Mn(H_2O)(tacn)]^{5+}$	BS	3.835	2.113	-	-	1.730	-	-
$[(tacn)(H_2O)Mn(\mu\text{-}O)_2Mn(tacn)]^{3+}$	BS	2.713	1.872	1.866	-	1.778	1.778	-
$[(tacn)Mn(\mu\text{-}O)(\mu\text{-}OOAc)Mn(tacn)]^{4+}$	BS	3.422	1.958	1.934	-	1.709	1.908	-
$[(tacn)Mn_2(\mu\text{-}O)_2(\mu\text{-}OAc)(tacn)]^{2+}$	BS	2.645	1.873	1.866	2.224	1.778	1.779	1.922
(5-(μ-O)$_2$(μ-OAc))	Exp.[a]	2.588	1.817	1.808	2.079	1.817	1.808	2.079
$[(tacn)Mn(\mu\text{-}O)(\mu\text{-}OAc)_2Mn(tacn)]^{3+}$	BS	3.210	1.843	2.116	2.061	1.759	1.908	1.917
(6-(μ-O)(μ-OAc)$_2$)	Exp.[b]	3.230	1.826	1.999	1.948	1.814	1.951	2.000

[a]X-ray data were taken from ref. [37]. Comparison with experiment is difficult due to statistical disorder and effective C_2 symmetry (see above). [b]X-ray data were taken from ref. [38].

7.4.2 Mulliken Spin Densities

Mulliken atomic spin densities (Table 7.3) provide a simple check of the unrestricted KS wavefunction obtained, regarding both the oxidation states of the individual Mn centers and the spin-coupling pattern. For all systems, the HS state is well represented by a ferromagnetic coupling between an Mn^{III} and an Mn^{IV} center. The BS state exhibits the expected antiferromagnetic coupling. The S^2 expectation values of the HS solutions are close to the nominal value for an S = 7/2 state, whereas the broken-symmetry nature of the BS solution is apparent from the fact that values around 3.7-4.0 are found (at the given computational level) instead of the 0.75 expected for a pure S = 1/2 state (see PO analysis below). The spin densities on the Mn^{III} center are close to the ideal d^4 configuration (the somewhat lower value for the HS state in **1-(μ-O)** reflects the larger delocalization across the linear bridge in this case). More notable deviations from the ideal d^3 configuration for the Mn^{IV} center are seen for the BS states of the first three

complexes (and again for the HS state of **1-(μ-O)**). Interestingly, the spin density on the Mn^{IV} center depends notably on the bridging ligand, reflecting the more pronounced covalency of the Mn^{IV}-O bonds and an associated larger spin polarization. Acetate bridges tend to diminish this effect and provide somewhat larger absolute spin densities on the Mn^{IV} centers. In the BS states, spin polarization of the bridge oxygen atoms is particularly pronounced for the single bridge in **1-(μ-O)** but is also large for the di-μ-oxo bridges and still notable for the other oxo bridges. Slightly positive spin density on the bridging acetate oxygen atoms points more to spin delocalization than to spin polarization. Interestingly, the HS state of **1-(μ-O)** exhibits large positive spin density on the bridging oxygen, in accordance with substantial spin delocalization (this is made possible by the parallel orientation of the unpaired spins). Smaller positive spin densities are visible on the other oxo bridges in the HS states. Curiously, in the HS states small negative spin densities are found on bridging acetate oxygen atoms.

Table 7.3. Mulliken atomic spin densities and $<S^2>$ expectation values of HS and BS states.[a]

		Mn^{III}	*Mn^{IV}*	*O1*	*O2a*	*O3a*	*O2b*	*O3b*	*$<S^2>$*
1-(μ-O)	HS	3.58	2.34	0.46	-	-	-	-	15.75
	BS	3.82	-2.55	-0.29	-	-	-	-	3.72
2-(μ-O)$_2$	HS	3.95	2.89	0.09	-	-	-	-	15.86
	BS	3.95	-2.69	-0.21	-0.21	-	-	-	3.77
3-(μ-O)$_2$	HS	3.96	2.89	0.09	0.09	-	-	-	15.88
	BS	3.95	-2.69	-0.21	-0.21	-	-	-	3.77
4-(μ-O)$_2$(μ-OAc)	HS	3.88	2.88	0.13	0.16	0.06	-	-0.03	15.85
	BS	3.86	-2.71	-0.15	-0.16	0.02	-	0.05	3.74
5-(μ-O)$_2$(μ-OAc)	HS	3.92	2.88	0.14	0.12	0.06	-	-0.03	15.85
	BS	3.88	-2.74	-0.16	-0.14	0.02	-	0.04	3.76
6-(μ-O)(μ-OAc)$_2$	HS	4.00	3.05	0.13	0.03	0.02	-0.02	-0.02	15.88
	BS	3.93	-2.94	-0.18	0.01	-0.01	0.03	0.03	3.81
Mn-cat	HS	3.87	2.93	0.16	0.03	0.05	-	-0.03	15.85
	BS	3.89	-2.78	-0.09	-0.13	0.02	-	0.05	3.77

[a]B3LYP single-point calculation with 9s7p4d basis for Mn and IGLO-II basis for the ligand atoms.

The influence of exact-exchange admixture on the atomic spin densities of the BS state of **2-(μ-O)$_2$** is studied in Table 7.4. As found also for mononuclear complexes,[18,19,39] larger exact exchange admixture enhances the spin density on the Mn centers, due to the more ionic metal-ligand bonding, and partly due to increased spin polarization. GGA functionals tend to overestimate metal-ligand covalency, and this is compensated by some exact exchange. However, for very large admixtures (> 50%), a counteracting effect is visible, that leads to a slight decrease of the spin density on the Mn^{III} center, likely due to the effects of spin polarization. The spin densities on the bridging oxygen atoms depend in a striking manner on the functional: starting from appreciably negative values at GGA level, they go through zero between 50% and 60% exact exchange and then turn significantly positive at 70-80% exact exchange. As enhanced spin polarization with more exact exchange would be expected to lead to overall more negative values, apparently the more ionic Mn-O bonding at larger exact exchange counteracts this effect. At 90% exact exchange, pronounced symmetry breaking renders the two oxygen atoms strongly nonequivalent, indicating this KS wavefunction to be unphysical.

Table 7.4. Dependence of Mulliken atomic spin densities and $\langle S^2 \rangle$ expectation values of the BS state of **2-(μ-O)$_2$** on the amount of exact-exchange admixture.

	Mn^{III}	Mn^{IV}	*O1*	*O2*	$\langle S^2 \rangle$
BLYP	3.60	-2.36	-0.195	-0.204	3.39
B3LYP	3.95	-2.69	-0.208	-0.213	3.77
BHLYP	4.09	-3.17	-0.047	-0.043	4.00
B60LYP	4.07	-3.40	0.071	0.083	4.11
B70LYP	4.03	-3.63	0.207	0.234	4.25
B80LYP	3.98	-3.79	0.303	0.373	4.39
B90LYP	4.00	-3.81	0.006	0.710	4.58

7.4.3 Paired-Orbital Analysis of Spin Contamination in the BS State

The S^2 expectation value tends to be near 3.75 for all systems at B3LYP level (cf. Table 7.3), lower at GGA level and higher at larger exact-exchange admixture (Table 7.4). This value may be analyzed within the formalism of an expansion of the BS determinant into quasirestricted determinants in the basis of the PO's (see section 3.4.2).[26,27,40] The magnetic NO's for **2-(μ-O)$_2$** obtained at B3LYP level are shown in Figure 7.2 and look similar also for other functionals (not shown). The occupation numbers of the NOs (see Table 7.5 for **2-(μ-O)$_2$**) give generally the expected picture of seven magnetic orbitals: this includes the "true" SOMO of the S = 1/2 system (occupation 1.00) and three pairs of corresponding orbitals, indicated by complementary deviations of the NO occupation numbers from 1.0. These deviations may be translated[28] into overlaps of the corresponding PO's, also shown in Table 7.5 (numbers in parentheses). As has been discussed in refs. [26,27,40], all spin contamination (i.e. deviation of $\langle S^2 \rangle$ from the nominal value of 0.75 for S = 1/2) may be traced back to those active pairs. Indeed, three magnetic pairs with small overlap should give rise to an increase of $\langle S^2 \rangle$ by three units.[26,27] This situation is almost ideally represented by the B3LYP results (cf. Tables 7.3, 7.4). The BLYP GGA calculations are known to overestimate delocalization. This may be seen from the larger overlaps of ca. 0.4 for the three corresponding magnetic PO's (or from the larger deviations of the NO occupation numbers from 1.0, Table 7.5). The B3LYP PO overlaps are close to 0.2 and the BHLYP ones close to 0.1. While the larger overlap for BLYP decreases the spin contamination compared to the B3LYP results, the small overlap for BHLYP enhances it. Moreover, the spin polarization of formally inactive NO's/PO's increases with increasing exact-exchange admixture. This is visible in Table 7.5 from the deviations of formally doubly occupied NO's 190, 191, and 192 from 2.0 (and from the non-zero occupations of the corresponding NO's 200, 201, and 202). Further analyses based on the PO-based expansion into quasirestricted determinants in eq. (3.37)[26,27] are provided in Table A5 in Appendix A. The spin contamination of the BS-KS determinant arises from single, double and triple substitutions of the leading restricted determinant of the expansion (some contributions arise also from the spin polarization of the formally doubly occupied set – POs 190, 191, 192).

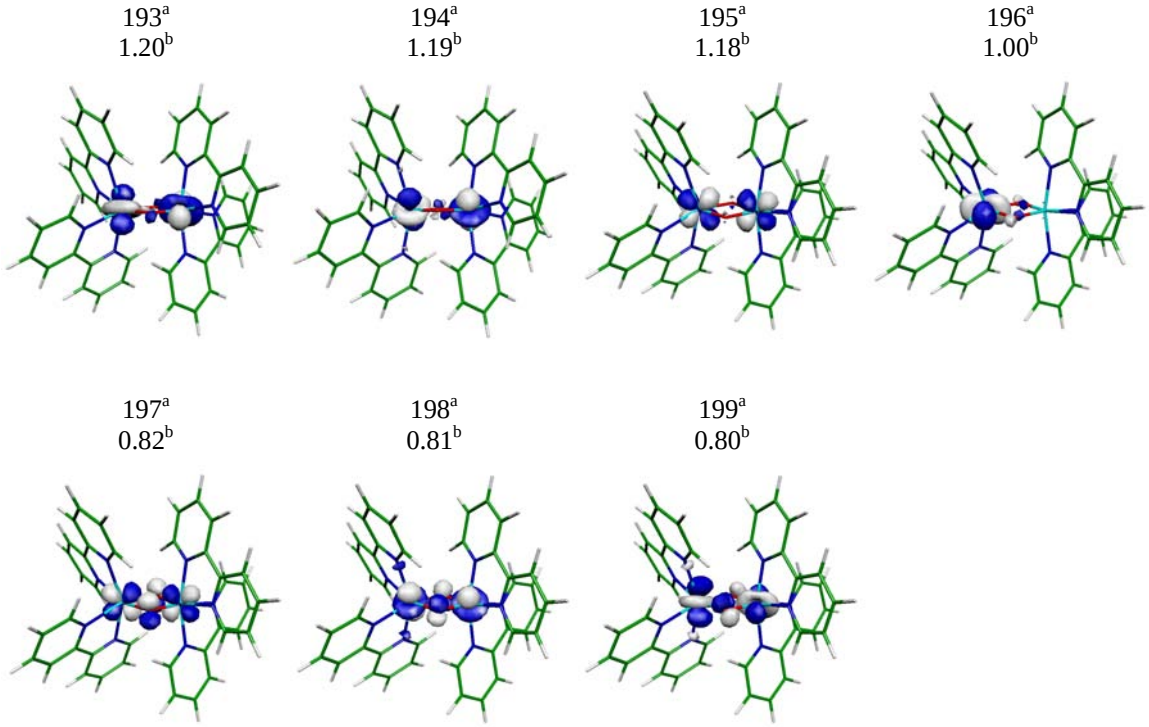

Figure 7.2. Active (magnetic) NO's for **2-(μ-O)$_2$** (B3LYP results; +/-0.05 a.u. isosurfaces). [a]Orbital number. [b]NO occupation.

Table 7.5. Dependence of NO occupation numbers and PO overlaps for **2-(μ-O)$_2$** on the functional.[a]

NO number	*BLYP*	*B3LYP*	*BHLYP*
190	2.00000	2.00000	1.98821 (0. 98821)
191	2.00000	1.98705 (0. 98705)	1.98057 (0.98057)
192	1.98357 (0.98357)	1.95115 (0. 95115)	1.96595 (0. 96595)
193	1.46588 (0.46588)	1.20303 (0. 20303)	1.11833 (0. 11833)
194	1.40930 (0. 40930)	1.19258 (0. 19258)	1.10617 (0. 10617)
195	1.34338 (0. 34338)	1.18020 (0. 18020)	1.10483 (0. 10483)
196	1.00000 (SOMO)	1.00000 (SOMO)	1.00000 (SOMO)
197	0.65662 (0. 34338)	0.81980 (0. 18020)	0.89517 (0. 10483)
198	0.59070 (0. 40930)	0.80742 (0. 19258)	0.89383 (0. 10617)
199	0.53412 (0.46588)	0.79697 (0. 20303)	0.88167 (0. 11833)
200	0.01643 (0.98357)	0.03885 (0. 95115)	0.03405 (0. 96595)
201	0.00000	0.01295 (0. 98705)	0.01943 (0. 98057)
202	0.00000	0.00000	0.01179 (0. 98821)

[a]See Figure 7.2 for the seven magnetic NOs 193-199.

7.4.4 Exchange Coupling Constants

As knowledge of spin-coupling patterns in multinuclear systems is essential for an understanding of the spectroscopic properties, we have also computed the Heisenberg exchange couplings, using the above mentioned spin projection schemes of Noodleman *et al*. and Yamaguchi *et al*. (see section 3.4.1). The vast literature[41-51] on broken-symmetry DFT calculations of exchange couplings for multinuclear transition metal complexes cannot be described here in detail. The small energy differences involved, the intrinsically multideterminantal nature of the lower-spin states, and the necessity of mapping the electronic structure onto the Heisenberg spin Hamiltonian, make this a challenge for quantum chemistry. BS-DFT with standard hybrid functionals like B3LYP tends to work surprisingly well when spin projection is used.[11] This is confirmed for the present title systems. Figure 7.3 illustrates for the example of **2-(μ-O)$_2$** the large dependence of *J* on exact-exchange admixture in the functional, and the good performance of B3LYP (likely related to the physically well-defined structure of the BS-KS determinant at this level, see above). The Noodleman[2] and the Yamaguchi[12] mapping schemes perform similarly, confirming the weak interaction between the spins for the complexes studied here. The pure GGA BLYP functional exhibits larger spin delocalization[52] and thus more negative *J* values. In contrast, larger exact-exchange admixture overcorrects and gives too low absolute values for *J*. The unprojected BS-DFT formula of Ruiz *et al*.[42,44,53] (eq. (3.35)) gives generally lower values (see Table A6 in Appendix A) and provides poorer agreement with experiment when used with B3LYP (but reasonable agreement with BLYP).

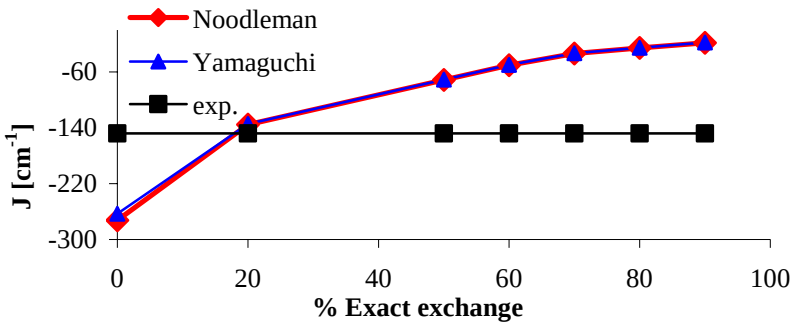

Figure 7.3. Dependence of the Heisenberg exchange coupling constant *J* on the amount of exact-exchange admixture for **2-(μ-O)$_2$**. Experimental *J* value taken from ref. [35].

B3LYP results for the entire series of complexes are provided in Table 7.6. Differences between data obtained with the moderate-basis SVP and those with extended basis sets are very small. Obviously, the energy differences between HS and BS states are not very basis-set dependent.[11] In all cases, the Noodleman (eq. (3.34)) and Yamaguchi (eq. (3.36)) projection schemes provide very similar results. For complexes with di-μ-oxo or di-μ-oxo-μ-carboxylato cores, agreement with experiment is excellent (for **Mn-cat** no truly reliable estimate is available). For the remaining two compounds **1-(μ-O)** and **6-(μ-O)(μ-OAc)$_2$**, the calculations underestimate the experimental absolute values by factors 3-4. Presumably,[11] OAc bridges give rise to some spin delocalization between the centers in the HS state, thus partly invalidating the basis for the spin projection. In case of **1-(μ-O)**, the question of the accuracy of the structure optimization may come into play (cf. Table 7.1). The calculated distances are especially for the HS state much larger than distances derived from X-ray experiments (Mn-Mn: HS: 3.67 Å; X-ray:[33] 3.52 Å). Computation of *J* for the X-ray structure of **1-(μ-O)**[33] gives -185 cm^{-1}, i.e. a value closer to experiment.

The di-μ-oxo bridged complexes exhibit larger antiferromagnetic coupling than the di-μ-oxo-μ-carboxylato bridged ones, in spite of the longer Mn-Mn distances (Table 7.6). The magnetic interactions are more efficient in the planar di-μ-oxo structures than in a tilted Mn_2O_2 core,[47] as present in the (μ-O)$_2$(μ-OAc) bridged systems. In general, O^{2-} is a strong donor, leading to strong Mn-oxo π interactions, which are responsible for the strong super-exchange-mediated[48,54] antiferromagnetic interactions.

Table 7.6. Heisenberg exchange coupling constants *J* (in cm^{-1}).[a]

	Noodleman		**Yamaguchi**		**Exp.**
	SVP	*9s7p4d/II*	*SVP*	*9s7p4d/II*	
1-(μ-O)	-138	-135	-136	-134	-353[b]
2-(μ-O)$_2$	-141	-136	-140	-134	-148[c]
3-(μ-O)$_2$	-142	-136	-141	-135	-148[c]
4-(μ-O)$_2$(μ-OAc)	-127	-120	-125	-119	-110[d]
5-(μ-O)$_2$(μ-OAc)	-117	-109	-117	-108	-110[e]
6-(μ-O)(μ-OAc)$_2$	-15	-12	-15	-12	-40[f]
Mn-cat	-79	-73	-78	-72	<-175[g]

[a]B3LYP results with either SVP basis for all atoms or with 9s7p4d for Mn and IGLO-II for N,O,H,C. [b]Experimental value taken from ref. [33]. [c]Experimental value taken from ref. [35]. [d]Experimental value taken from ref. [36]. [e]Experimental value taken from ref. [37]. [f]Experimental value taken from ref. [38]. [g]A lower bound of -175 cm^{-1} has been estimated.[55]

To evaluate the influence of the terminal ligand sets, we have computed *J* for smaller models of **3-(μ-O)$_2$**, where the phen ligands had been replaced by simpler ligands. Even for the simplest model $[(NH_3)_4Mn(\mu\text{-}O)_2Mn(NH_3)_4]^{3+}$, -132 cm^{-1} are obtained (Noodleman projection, SVP basis), in good agreement with experiment (see Table A7 in Appendix A).

In the opposite type of computational experiment, we have kept the terminal ligand framework similar (tacn and H_2O; see also above) and changed the bridges. As expected,[47] this has a larger effect on *J* (see Table 7.7). The influence of the bridge depends on the various superexchange pathways provided by the bridging oxo and acetato ligands.[7,8] Overall, smaller Mn-Mn distances and a planar Mn_2O_2 core give rise to larger antiferromagnetic couplings. These effects work into opposite directions for $[(tacn)(H_2O)Mn(\mu\text{-}O)_2Mn(tacn)]^{3+}$ and $[(tacn)Mn(\mu\text{-}O)_2(\mu\text{-}OAc)Mn(tacn)]^{2+}$, leading to rather similar couplings. Complexes with a di-μ-oxo bridge have *J* couplings in the range of -110 to -150 cm^{-1} (Tables 7.6, 7.7). A similar range is covered by di-μ-oxo-μ-carboxylato bridged complexes (-108 to -127 cm^{-1}). Small antiferromagnetic coupling is computed for **6-(μ-O)(μ-OAc)$_2$**. Small ferromagnetic coupling is obtained for $[(tacn)Mn(\mu\text{-}O)(\mu\text{-}OAc)Mn(tacn)]^{4+}$ (Table 7.7). Due to the OAc bridge, a delocalization of the unpaired electrons in the high-spin state occurs,[11] reducing the antiferromagnetic coupling. This effect can also be observed in complexes $[(tacn)Mn(\mu\text{-}O)_2(\mu\text{-}OAc)Mn(tacn)]^{2+}$ and $[(tacn)Mn(\mu\text{-}O)(\mu\text{-}OAc)_2Mn(tacn)]^{3+}$. The more μ-carboxylato bridges, the lower is the antiferromagnetic coupling. The spin-density distributions of these complexes are given in Figure 7.4.

Table 7.7. Dependence of *J* (in cm^{-1}) on bridging ligand set.[a]

	Noodleman	**Yamaguchi**	**Exp.**
$[(tacn)(H_2O)Mn(\mu\text{-}O)Mn(H_2O)(tacn)]^{5+}$	-23	-23	-
$[(tacn)(H_2O)Mn(\mu\text{-}O)_2Mn(tacn)]^{3+}$	-106	-105	-
$[(tacn)Mn(\mu\text{-}O)(\mu\text{-}OAc)Mn(tacn)]^{4+}$	44	43	-
$[(tacn)Mn(\mu\text{-}O)_2(\mu\text{-}OAc)Mn(tacn)]^{2+}$	-109	-108	-110[b]
$[(tacn)Mn(\mu\text{-}O)(\mu\text{-}OAc)_2Mn(tacn)]^{3+}$	-12	-12	-40[c]

[a]B3LYP calculations with 9s7p4d basis for Mn and IGLO-II for N,O,H,C. [b] Experimental value taken from ref. [37]. [c]Experimental value taken from ref. [38].

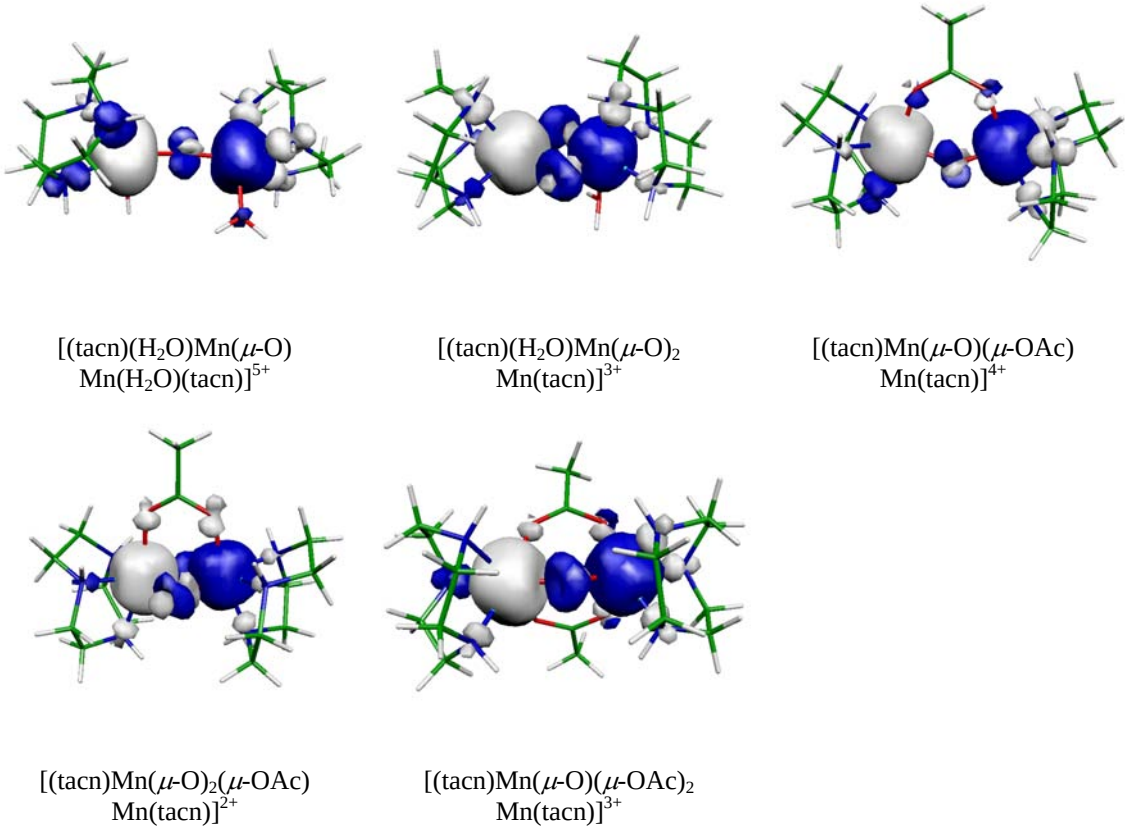

Figure 7.4. Spin-density isosurfaces (±0.005 a.u) for tacn complexes with different bridging ligands.

7.4.5 g-Tensors

Computed effective g-tensors, eq. (4.43), tend to agree reasonably well with experiment (Table 7.8). The g-anisotropy is generally small for all title complexes, and the isotropic g-value is close to free-electron value. Dependence on the functional is small, and for **2-(μ-O)$_2$** even the BLYP GGA functional provides reasonable results for g_{iso}. At very large exact-exchange admixtures, agreement with experiment may be improved further (see also results for **Mn-cat** in Figure A1 in Appendix A). Comparing our B3LYP results with those of Sinnecker *et al*. for **4-(μ-O)$_2$(μ-OAc)**[7] and **Mn-cat**,[8] we see some moderate discrepancies (data not shown) in that their overall effective g-shift components are all somewhat below g_e, whereas in our calculations g_{22} and g_{33} are above g_e and g_{11} is below (Table 7.8). This brings their data closer to experiment for **4-(μ-O)$_2$(μ-OAc)**[7] (in fact, most of the complexes in Table 7.8, whereas our positive g_{22} and g_{33} values agree better for **Mn-cat**). Differences between the two sets of calculations could arise from a) different spin-orbit operators (atomic-meanfield operators in this work

vs. semi-empirical operators in refs. [7,8]), b) different structures (we used optimized structures individually for HS and BS states, whereas Sinnecker and Neese used the HS structures for both calculations), c) general differences between the optimized structures and basis sets used, or d) the gauge origin of the magnetic vector potential (placed at the center of charge density in our calculations). Yet, our evaluations of all of these points did not reveal the origin: Our use of the same semi-empirical spin-orbit operators used by Sinnecker *et al*. actually increased g_{22} and g_{33} further in all cases, and the dependencies on structures, basis-sets or gauge origin turned out to be too small to account for the differences. We therefore have currently no good explanation for the (moderate) discrepancies in the computed effective g-tensors, in particular as hyperfine couplings computed from the same Kohn-Sham wavefunctions agree very well.

Overall, the g-tensors for different systems tend in any case to be too similar to have much diagnostic value for structural details. g-Tensor orientations will be discussed further below together with those of the ^{55}Mn hyperfine tensors.

Table 7.8. g-Shift components (in ppt) and absolute g-values.[a]

		Δg_{iso}	Δg_{11}	Δg_{22}	Δg_{33}
1-(μ-O)	B3LYP	-1.7 (2.001)	-14.7 (1.988)	0.5 (2.003)	9.1 (2.011)
	exp.[b]	7.3 (1.995)	20.3 (1.982)	5.3 (1.997)	-3.7 (2.006)
2-(μ-O)$_2$	B3LYP	3.2 (1.9991)	14.5 (1.9878)	-1.7 (2.0040)	-3.2 (2.0055)
	exp.[c]	11.0 (1.9913)	20.6 (1.9817)	9.1 (1.9932)	3.3 (1.9990)
3-(μ-O)$_2$	B3LYP	2.9 (1.9994)	14.2 (1.9881)	-2.2 (2.0045)	-3.3 (2.0056)
	exp.[d]	11 (1.992)	20 (1.982)	8 (1.994)	3 (1.999)
4-(μ-O)$_2$(μ-OAc)	B3LYP	1.0 (2.0013)	11.5 (1.9908)	-3.4 (2.0057)	-5.2 (2.0075)
	exp.[c]	8.1 (1.9942)	18.5 (1.9838)	4.9 (1.9974)	1.0 (2.0013)
5-(μ-O)$_2$(μ-OAc)	B3LYP	0.9 (2.0014)	11.0 (1.9913)	-3.2 (2.0055)	-5.1 (2.0074)
	exp.[c]	6.3 (1.9960)	17.2 (1.9851)	1.8 (2.0005)	-0.2 (2.0025)
Mn-cat	B3LYP	-1.0 (2.0033)	10.0 (1.9923)	-3.5 (2.0058)	-9.6 (2.0119)
	exp.[c]	3.5 (1.9988)	14.7 (1.9876)	-1.7 (2.0040)	-2.5 (2.0048)
6-(μ-O)(μ-OAc)$_2$	B3LYP	1.3 (2.0010)	5.4 (1.9969)	1.7 (2.0006)	-3.1 (2.0054)

[a]Effective g-tensor. Absolute g-values in parentheses. [b]X-band EPR studies from ref. [33]. [c]High-field EPR studies from ref. [56]. [d]Mulitfrequency EPR studies from ref. [57].

7.4.6 ^{55}Mn Hyperfine Coupling Tensors

The ^{55}Mn hyperfine couplings exhibit much more sensitivity to bonding and structural details. Isotropic HFCs of transition metal nuclei are known to depend also sensitively on the exchange-correlation functional employed.[18] This includes manganese HFCs and has recently been confirmed for the mononuclear manganese binding site of concanavalin A (see Chapter 6).[9] Table 7.9 evaluates the ^{55}Mn tensors for **2-(μ-O)$_2$** with different functionals. Tensors after spin projection and isotropic site values are provided (eqs. (4.47, 4.48)).

Table 7.9. Dependence of ^{55}Mn hyperfine tensors (in MHz) for **2-(μ-O)$_2$** on exchange-correlation functional.[a]

	Mn^{III}							**Mn^{IV}**						
	a_{iso} *(site)*	A_{iso}	T_1 T_2 T_3	A_{FC}	A_1^{dip} A_2^{dip} A_3^{dip}	A_{PC}	$A_1^{dip,2}$ $A_2^{dip,2}$ $A_3^{dip,2}$	a_{iso} *(site)*	A_{iso}	T_1 T_2 T_3	A_{FC}	A_1^{dip} A_2^{dip} A_3^{dip}	A_{PC}	$A_1^{dip,2}$ $A_2^{dip,2}$ $A_3^{dip,2}$
			-48		-50		3			-2		-1		-1
BLYP	-133	-265	-37	-251	-39	-14	1	-122	122	1	114	1	8	-1
			85		89		-4			1		0		2
			-53		-57		4			-6		-7		1
B3LYP	-158	-316	-45	-302	-48	-14	3	-150	150	0	139	0	11	0
			98		105		-7			5		7		-2
			-55		-60		5			-6		-8		2
BHLYP	-181	-361	-47	-346	-51	-15	4	-174	174	-1	160	-2	14	1
			102		111		-10			7		10		-3
			-57		-63		6			-7		-10		3
B60LYP	-188	-376	-48	-360	-53	-16	5	-179	179	-4	165	-5	14	1
			105		117		-11			11		15		-4
			-61		-68		7			-10		-14		4
B70LYP	-198	-395	-51	-377	-57	-18	5	-183	183	-7	170	-9	13	2
			111		124		-13			17		22		-6
			-65		-73		8			-15		-19		5
B80LYP	-209	-417	-52	-398	-59	-19	7	-190	190	-8	177	-1	13	2
			117		132		-15			23		29		-7
			-88		-98		11			-41		-51		10
B90LYP	-220	-440	-26	-421	-30	-19	4	-252	252	14	239	19	13	-5
			114		129		-15			27		31		-4
			-25							-8				
Exp.[b]	-227	-454	-48					-218	218	-3				
			78							14				

[a]Site values obtained with extended basis set (see Computational Details). a_{iso}*(site)* is the intrinsic site isotropic hyperfine coupling constant. A_{iso} is the total isotropic value, T_i represent the traceless part of the full **A** tensor, A_{FC} and A_{PC} denote the isotropic first-order Fermi-contact and second-order pseudo-contact (spin-orbit) contributions to the full total **A** tensor, respectively. A_i^{dip} and $A_i^{dip,2}$ denote, respectively, the first-order nonrelativistic and second-order spin-orbit anisotropic tensors. [b]HF-EPR studies from ref. [56].

Due to the distorted coordination of high-spin d^4, Mn^{III} exhibits appreciable HFC anisotropy (and a nearly axial tensor). An almost isotropic HFC is found for the high-spin d^3 Mn^{IV} center. The dependence on the functional is as found before,[9] for both Mn centers: The isotropic Fermi-contact term A_{FC} becomes more negative with increasing EXX admixture, due to the enhancement of (overall negative) core-shell spin polarization contributions to the spin density at the nucleus.[18,19,39] Agreement with experiment is thus improved even up to rather large admixtures of exact exchange. SO contributions are on the order of about 5-10% of the nonrelativistic values. This is less than for some complexes of other 3*d* transition metals,[58-60] yet nonnegligible.[7,8] The HFC anisotropy of the Mn^{III} ions depends less on the functional. It is already reproduced reasonably well at B3LYP level and tends to be overshot somewhat at higher EXX admixtures. Notably, at EXX admixtures above 60%, the HFC anisotropies of the Mn^{IV} centers start to increase notably. This is likely an unphysical artefact of the increased spin contamination[18,19] (cf. S^2 expectation values in Table 7.4 and PO analysis above). Another observation in this context is the faster increase of the a_{iso} site values with exact exchange for the Mn^{IV} compared to the Mn^{III} centers (Table 7.9). We note in passing, that the differences between the BLYP GGA functional and the B3LYP hybrid functional are clearcut and consistent with the abovementioned dependence on EXX admixture. Somewhat more similar results obtained by Sinnecker *et al*. with BP86 vs. B3LYP functionals[7] may be attributed to compensating effects of exchange and correlation contributions to the functional (see ref. [18]).

In the long run, improved exchange-correlation functionals will be needed that allow optimum agreement with experiment for a wide range of spectroscopic parameters with one given functional. A possible route towards this goal are local hybrid functionals with position-dependent EXX admixture.[61-65] For the moment, we are content with more approximate short-term solutions. As the exchange couplings (see above) and several ligand HFCs (see below) are reproduced well with B3LYP, it would be desirable to be able to scale the computed A_{iso} at this level, as suggested recently,[7] to provide essentially quantitative predictions for the entire tensor. This requires that the errors due to incorrect description of the core-shell spin polarization are systematic and apply similarly to both Mn^{III} and Mn^{IV} centers, as well as to different coordination environments. The latter is clearly the case, as the B3LYP results for A_{iso} in **2-(μ-O)$_2$** have to be scaled by 1.44 for Mn^{III} and by 1.45 for Mn^{IV} (Table 7.9) to agree with experiment.

Table 7.10. ^{55}Mn hyperfine coupling tensors (in MHz).[a]

		Mn^{III}						Mn^{IV}					
		a_{iso} *(site)*	A_{iso}	A_{iso}*	T_1 T_2 T_3	A_{FC}	A_{PC}	a_{iso} *(site)*	A_{iso}	A_{iso}*	T_1 T_2 T_3	A_{FC}	A_{PC}
	Calc.	-114	-228	-331	-83 -21 104	-214	-14	-125	125	181	-13 0 12	113	12
1-(μ-O)	Exp.[b]	|191|	|381|		|99| |9| |108|			|183|	|183|		|3| |3| |6|		
	Calc.	-158	-316	-458	-53 -45 98	-302	-14	-150	150	218	-6 0 5	139	11
2-(μ-O)$_2$	Exp.[c]	-227	-454		-25 -48 78			-218	218		-3 -8 14		
	Calc.	-156	-311	-451	-52 -46 98	-297	-14	-150	150	218	-7 0 7	138	12
3-(μ-O)$_2$	Exp.[d]	-226	-451		-28 -50 78			-221	221		-8 -6 11		
	Calc.	-137	-274	-397	-54 -52 106	-261	-13	-149	149	216	-6 -2 7	138	11
4-(μ-O)$_2$(μ-OAc)	Exp.[c]	-195	-389		-17 -81 92			-207	207		-14 6 14		
	Calc.	-133	-266	-386	-52 -51 104	-253	-13	-150	150	218	-6 0 6	139	11
5-(μ-O)$_2$(μ-OAc)	Exp.[c]	-193	-386		-25 -73 92			-213	213		-14 8 11		
	Calc.	-134	-267	-387	-92 0 91	-254	-13	-160	160	232	-5 0 6	148	12
Mn-cat	Exp.[c]	-189	-378		-34 -48 78			-238	238		-6 -14 17		
6-(μ-O)(μ-OAc)$_2$	Calc.	-141	-282	-410	-112 25 86	-268	-14	-133	133	193	-10 -5 15	122	11

[a]B3LYP results. See footnote a of Table 7.9. A_{iso}* is obtained after scaling A_{iso} by 1.45. [b]X-band EPR data taken from ref. [33]. [c]HF-EPR data taken from ref. [56]. [d]Mulitfrequency EPR data taken from ref. [57].

The validity of the former condition for a range of the present dinuclear systems is explored in Table 7.10. Spin-projected B3LYP results are compared to ^{55}Mn HFC tensors from several EPR studies.[33,36,56] The behavior is as delineated above for **2-(μ-O)$_2$**: significant anisotropy for Mn^{III} centers, essentially isotropic HFCs for Mn^{IV} centers.

Scaling the total computed A_{iso} by a factor of ca. 1.45 provides excellent agreement with experiment (A_{iso}*, Table 7.10), independent of terminal and bridging ligand sets. Similar scaling factors were found from a somewhat more limited set of complexes by Sinnecker *et al*..[7,8] The anisotropies of the Mn^{III} centers are generally reproduced more or less reasonably without scaling. The small anisotropies of the Mn^{IV} centers are less well reproduced.

Turning our magnifying glass on the a_{iso} site values (Table 7.10), we see that the relative magnitudes for the Mn^{III} vs. Mn^{IV} centers are in most cases reproduced, but not always: for **1-(μ-O)** and **4-(μ-O)$_2$(μ-OAc)**, experiment would suggest slightly larger absolute values for the Mn^{III} center, whereas the calculations give the opposite behavior (but the differences are tiny). The switch from larger absolute a_{iso} site values for Mn^{III} in **2-(μ-O)$_2$** and **3-(μ-O)$_2$** to larger values for Mn^{IV} in **5-(μ-O)$_2$(μ-OAc)** and **Mn-cat** is well reproduced. The latter two cases are the most clearcut ones. These results show that overall the intrinsic isotropic site values for Mn^{III} and Mn^{IV} are surprisingly similar and translate into rather different projected A_{iso} values due to the factor two in the Mn^{III} projection. This will have to be kept in mind in studies on, e.g., the OEC.

Table 7.11. Dependence of ^{55}Mn hyperfine tensors (in MHz) of (μ-O)$_2$ bridged complexes on terminal ligand set.[a]

	Mn^{III}						**Mn^{IV}**					
	a_{iso} *(site)*	A_{iso}	A_{iso}*	T_1 T_2 T_3	A_{FC}	A_{PC}	a_{iso} *(site)*	A_{iso}	A_{iso}*	T_1 T_2 T_3	A_{FC}	A_{PC}
$[(NH_3)_4Mn(\mu\text{-}O)_2Mn(NH_3)_4]^{3+}$	-144	-288	-417	-54 -46 99	-275	-13	-153	153	222	-5 0 4	142	11
$[(dab)_2Mn(\mu\text{-}O)_2Mn(dab)_2]^{3+}$	-145	-290	-421	-54 -46 100	-277	-13	-153	153	222	-4 -3 7	141	12
$[(bipy)_2Mn(\mu\text{-}O)_2Mnbipy)_2]^{3+}$	-158	-316	-454	-53 -45 98	-302	-14	-150	150	218	-6 0 5	139	11
$[(phen)_2Mn(\mu\text{-}O)_2Mn(phen)_2]^{3+}$	-156	-311	-450	-52 -46 98	-297	-14	-150	150	218	-7 0 7	139	11
Exp.[b]	-226	-451		-28 -50 78			-221	221		-8 -6 11		

[a]B3LYP results. See footnote a of Table 7.10. [b]Mulitfrequency EPR data of $[(phen)_2Mn(\mu\text{-}O)_2Mn(phen)_2]^{3+}$ taken from ref. [57].

In Table 7.11, the ^{55}Mn HFC tensors are provided for **3-(μ-O)$_2$** and for models in which the phen ligands have been replaced by smaller units. Even for the smallest model system $[(NH_3)_4Mn(\mu\text{-}O)_2Mn(NH_3)_4]^{3+}$, the isotropic ^{55}Mn HFC of the Mn^{IV} center is essentially the same as for the full system with phen ligands. In case of NH_3 or dab ligands, the value for the Mn^{III} center is 7% too small in absolute value compared to the phen complex (note the switch in relative magnitude of the Mn^{III} and Mn^{IV} a_{iso} site values). Slight structural differences for the dab complex and the bipy and phen complex might explain this deviation (see Table A1 in Appendix A). For NH_3, its nonaromatic nature and different donor character come into play. The bipy complex is an almost perfect model of phen in this context. These findings suggest that similar simplifications of the terminal ligand sets may be cautiously applied to models of the OEC, where full modelling of the protein and cofactor environment is computationally demanding.

Table 7.12. Dependence of ^{55}Mn hyperfine tensors (in MHz) of tacn-based complexes on bridging ligand set.[a]

	Mn^{III}						**Mn^{IV}**					
	a_{iso} *(site)*	A_{iso}	A_{iso}*	T_1 T_2 T_3	A_{FC}	A_{PC}	a_{iso} *(site)*	A_{iso}	A_{iso}*	T_1 T_2 T_3	A_{FC}	A_{PC}
[(tacn)(H_2O)Mn(μ-O) Mn(H_2O)(tacn)]$^{5+}$	-110	-219	-318	-66 -6 72	-207	-12	-45	45	65	-35 -11 45	29	16
[(tacn)(H_2O)Mn^{III}(μ-O)$_2$ Mn^{IV}(tacn)]$^{3+}$	-99	-198	-287	-56 -47 102	-185	-13	-145	145	210	-9 -4 14	133	11
[(tacn)Mn(μ-O)(μ-OAc) Mn(tacn)]$^{4+}$	-104	-208	-302	-86 -2 88	-195	-13	-40	40	58	-29 -17 46	24	16
[(tacn)Mn(μ-O)$_2$(μ-OAc) Mn(tacn)]$^{2+}$	-133	-266	-386	-52 -51 104	-253	-13	-150	150	218	-6 0 6	139	11
[(tacn)Mn(μ-O)(μ-OAc)$_2$ Mn(tacn)]$^{3+}$	-141	-282	-409	-112 25 86	-268	-14	-133	133	193	-10 -5 15	122	11

[a]B3LYP results. See footnote a of Table 7.9.

Table 7.12 keeps the terminal ligand set more or less constant (tacn, and possibly terminal H_2O) and varies the bridges. At first sight surprisingly, [(tacn)(H_2O)Mn(μ-O) Mn(H_2O)(tacn)]$^{5+}$ and [(tacn)Mn(μ-O)(μ-OAc) Mn(tacn)]$^{4+}$ exhibit unusually small A_{iso} for the Mn^{IV} center. This can be traced back clearly to a five-coordination at this center, suggesting a diagnostic value of the Mn HFC in this context. This is interesting for the

OEC, as the coordination number of the different centers is currently far from settled. The other variations of the Mn^{IV} HFC are much smaller, with the (μ-O)(μ-OAc)$_2$ bridged system having the lowest A_{iso}. Stronger ligation appears to lead to larger HFCs. This agrees with results for mononuclear complexes. For example, at the same computational level we obtain A_{iso} of -147.8 MHz for $[Mn(H_2O)_6]^{4+}$, -227.6 MHz for $[Mn(H_2O)_5(OH)]^{3+}$, and -303.3 MHz for $[Mn(H_2O)_5(O)]^{2+}$. On the Mn^{III} side, the observed variations in Table 7.12 are smaller but suggest the largest A_{iso} for the triply bridged systems and the lowest value for the (μ-O)$_2$ bridged system. The mono-μ-O and (μ-O)(μ-OAc) bridged systems feature five-fold coordination for the Mn^{III} center and are therefore more difficult to compare with. Interestingly, however, the Mn^{III} HFCs appear to be changed less when going from six- to five-fold coordination. Insight from mononuclear complexes would suggest a similar trend as for Mn^{IV}, namely increasing A_{iso} with stronger coordination: $[Mn(H_2O)_6]^{3+}$: -171.4 MHz , compared to $[Mn(H_2O)_5(OH)]^{2+}$: -226.4 MHz, as well as $[Mn(H_2O)_5]^{3+}$: -135.6 MHz, compared to $[Mn(H_2O)_4(OH)]^{2+}$: -158.0 MHz.

7.4.7 Orientation of g- and ^{55}Mn Hyperfine Tensors

The orientation of the g- and hyperfine tensors with respect to the molecular framework and, in particular, with respect to each other, is crucial in the simulation of the EPR spectra. Often assumptions about coaxiality or of axial symmetry of tensors are made to reduce the degrees of freedom in a simulation. The known ability of modern DFT methods to typically provide the tensor orientations reliably is thus of interest to validate or invalidate these assumptions. The orientations of the computed HS, BS, and site g-tensors and of the A-tensors relative to the effective g-tensor have thus evaluated (see Table 7.13 for two complexes).

Figure 7.5 shows the orientations for **2-(μ-O)$_2$** (orientations for **4-(μ-O)$_2$(μ-OAc)** are given in Figure A3 in Appendix A). The computed g-tensor orientation for **2-(μ-O)$_2$** agrees with the experimental assignment.[36] The g_{11} vector lies perpendicular to the Mn_2O_2 plane. The g_{22}-axis is parallel to the Mn-Mn connection line, and the g_{33} axis parallel to the connection between the bridging oxygen atoms. The Euler angles between the principal axes of the HS and BS g-tensors are small, between 11.7° and 17.8°, as expected for a planar Mn_2O_2 core. Spin projection results in an effective g-tensor

orientation intermediate between those of g_{hs} and g_{bs} (slightly closer to g_{hs}, due to the larger weight of the HS tensor after spin projection; eqs. (4.39)-(4.43)). As expected, the orientation of the site g-tensor of the distorted Mn^{III} center ($\mathbf{g}_1$) dominates the effective g-tensor orientation, as indicated by the smaller absolute values of the Euler angles relative to the effective g-tensor.

Table 7.13. Euler angles (in degree) relative to the effective g-tensor principal axis system.

	g	g_{11}		g_{22}		g_{33}	
2-(μ-O)$_2$	$\mathbf{g}_{HS}$	g_{11}	4.8	g_{22}	5.6	g_{33}	7.4
	$\mathbf{g}_{BS}$	g_{11}	-5.7	g_{22}	-5.7	g_{33}	-10.4
	$\mathbf{g}_1$ [Mn^{III}]	g_{11}	3.4	g_{22}	3.9	g_{33}	5.2
	$\mathbf{g}_2$ [Mn^{IV}]	g_{11}	-5.8	g_{22}	-7.9	g_{33}	-10.3
	A [Mn^{III}]	A_3	-0.7	A_1	-35.5	A_2	35.6
	A [Mn^{IV}]	A_3	32.8	A_2	-7.0	A_1	33.7
4-(μ-O)$_2$(μ-OAc)	$\mathbf{g}_{HS}$	g_{11}	6.1	g_{22}	12.0	g_{33}	12.0
	$\mathbf{g}_{BS}$	g_{11}	-8.6	g_{22}	-16.9	g_{33}	-16.9
	$\mathbf{g}_1$ [Mn^{III}]	g_{11}	4.3	g_{22}	8.5	g_{33}	8.5
	$\mathbf{g}_2$ [Mn^{IV}]	g_{11}	-8.6	g_{22}	-16.5	g_{33}	-16.5
	A [Mn^{III}]	A_1	41.9	A_3	-8.2	A_2	40.1
	A [Mn^{IV}]	A_3	4.2	A_2	-1.2	A_1	-1.9

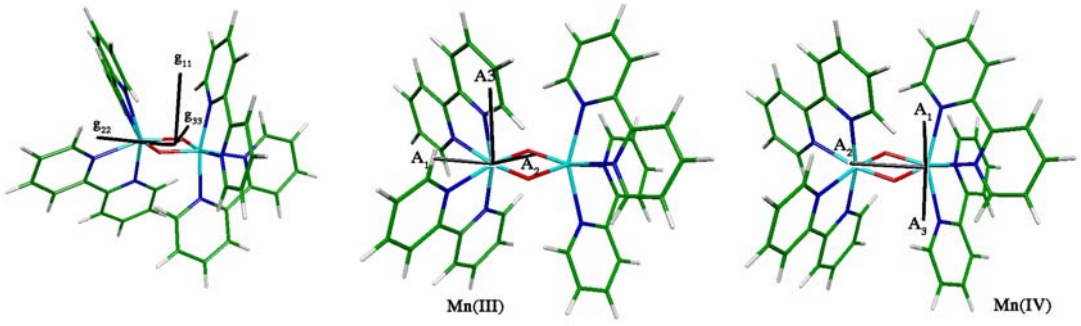

Figure 7.5. Orientation of g-tensor and manganese hyperfine tensors for **2-(μ-O)$_2$** (B3LYP results).

The often assumed covariance between HFC and g-tensors is clearly not fulfilled for **2-(μ-O)$_2$** (Figure 7.5, Table 7.13): While A_3 of the Mn^{III} HFC tensors coincides with g_{11}, the A_2 and A_1 orientations are rotated significantly relative to g_{22} and g_{33}, respectively. The HFC tensor orientation of the Mn^{IV} center is also not covariant to **g** or the Mn^{III} HFC

tensor (A_2 is covariant with g_{22}). But this is of lesser importance, due to the small HFC anisotropy on this center (see above).

For the di-μ-oxo-μ-carboxylato bridged complex **4-(μ-O)$_2$(μ-OAc)** with its non-planar core, g-tensor orientations are similar as for **2-(μ-O)$_2$**: g_{22} is again parallel to the Mn-Mn connection line, g_{33} parallel to the O-O connection line, and g_{11} perpendicular to the g_{22}-g_{33} plane (which now does not contain all four atoms of the core). Yet, the differences between the orientations of g_{hs} and g_{bs} are more pronounced (Table 7.13). Again, $\mathbf{g}_1$ dominates the effective g-tensor orientation. As for **2-(μ-O)$_2$**, we find the Mn^{III} A-tensor not to be covariant with the g-tensor, as shown by the large Euler angles for A_1 *vs*. g_{11} and A_2 *vs*. g_{33}. The Mn^{IV} HFC tensor orientation is close to that of the g-tensor but again likely to be less important for spectra simulations.

7.4.8 ^{14}N hyperfine coupling and nuclear quadrupole coupling tensors

Nitrogen donor ligands are present in several of the model systems studied, including catalase, and also in the OEC. In catalase, histidine imidazole nitrogens are coordinated to the two manganese centers (cf. Figure 7.1), and in the OEC a histidine is known to coordinate to one of the manganese centers.[66,67] Nitrogen HFCs and (given the quadrupolar nature of the ^{14}N nucleus) nuclear quadrupole coupling tensors are thus spectroscopic parameters with potential value for structure elucidation.

Table 7.14 evaluates the dependence of the parameters for the two distinguishable ligand nitrogen atoms for **Mn-cat** on exchange-correlation functional. Increased EXX admixture makes the isotropic ^{14}N HFC of N1 (bound to the Mn^{III} center) more negative. For the N2 atom bound to the Mn^{IV} center, the BLYP GGA functional gives a positive value, whereas increasing EXX admixture moves A_{iso} first towards small positive values (e.g. BHLYP, B60LYP) before turning it increasingly negative. No sign information is available from experiment, but the good agreement of the B3LYP results with both the absolute value of A_{iso} and with the nuclear quadrupole coupling and asymmetry (Table 7.14) suggests this level (and the positive sign of A_{iso}) to be more reliable than large EXX admixtures above 60%. Only one nitrogen atom was seen[68] in the ESEEM experiment, and its assignment[69] to N2-Mn^{IV} is consistent with our calculations and with those of Sinnecker *et al*..[8] The larger ^{14}N HFC of N1 is outside the range detectable by ESEEM but might be detected by ENDOR spectroscopy. For both N1 and N2, the calculations

suggest small hyperfine anisotropy, with somewhat larger dependence on the functional on the Mn^{IV} side (N2). For both nuclei, the nuclear quadrupole couplings increase with EXX admixture. Already BLYP and B3LYP perform almost identically compared to experiment. The asymmetry parameter behaves differently on the two nuclei. Again, the B3LYP results agree well with experiment.

Table 7.14. Dependence of nitrogen HFC and nuclear quadrupole coupling tensors (in MHz) on exact-exchange admixture.[a]

	N(1)-Mn^{III}								**N(2)-Mn^{IV}**							
	a_{iso} *(site)*	A_{iso}	T_1	T_2	T_3	$\|e^2qQ\|$	$\|\eta\|$	$\rho^{\alpha-\beta}$	a_{iso} *(site)*	A_{iso}	T_1	T_2	T_3	$\|e^2qQ\|$	$\|\eta\|$	$\rho^{\alpha-\beta}$
BLYP	-2.3	-4.5	-0.7	-0.5	1.2	2.55	0.56	-0.036	-2.8	2.8	-0.4	0.1	0.2	2.59	0.53	0.031
B3LYP	-2.4	-4.7	-0.8	-0.5	1.3	2.63	0.53	-0.038	-2.7	2.7	-0.5	0.2	0.3	2.64	0.51	0.032
BHLYP	-2.4	-4.7	-0.9	-0.5	1.4	2.75	0.52	-0.037	-1.1	1.1	-0.7	0.3	0.5	2.79	0.48	0.027
B60LYP	-2.6	-5.2	-0.9	-0.5	1.4	2.74	0.53	-0.038	0.2	-0.2	-0.9	0.4	0.5	2.90	0.46	0.022
B70LYP	-3.1	-6.1	-0.9	-0.4	1.4	2.70	0.56	-0.039	2.7	-2.7	-1.3	0.6	0.7	3.09	0.42	0.011
B80LYP	-3.6	-7.2	-0.9	-0.4	1.3	2.63	0.61	-0.041	6.8	-6.8	-1.8	0.8	0.9	3.37	0.36	-0.007
B90LYP	-3.9	-7.7	-0.9	-0.4	1.3	2.59	0.65	-0.042	8.6	-8.6	-2.0	0.9	1.1	3.52	0.34	-0.017
Exp.[b]									|2.45	|2.45|				2.34	0.51	

[a]HFC data spin-projected. $|e^2QC|$ denotes the electric quadrupole coupling and $|\eta|$ the asymmetry parameter. $\rho^{\alpha-\beta}$ is the Mulliken spin density at nitrogen. [b]ESEEM data for catalase from ref. [68].

The second dinuclear system, for which the ^{14}N HFCs have previously been computed is **4-(μ-O)$_2$(μ-OAc)**[7] (cf. Table 7.15). Our results for N1 (ligand to Mn^{III} along Jahn-Teller axis) agree well with those of Sinnecker and Neese and with experiment. In the closely related **5-(μ-O)$_2$(μ-OAc)**, ESEEM has provided a second, smaller splitting assigned to N2 (equatorial ligand to Mn^{IV}; cf. Figure 7.1 for atom labels). This relatively small splitting is underestimated somewhat by the computations. Notably, however, the smaller nuclear quadrupole coupling on N2 is better reproduced than the larger one on N1, which is overestimated. The asymmetry parameter is too low. Possible error sources are inaccuracies in the computed Mn-N distances along the Jahn-Teller axes of the Mn^{III} centers. The hyperfine tensors of these nitrogen nuclei at the Mn^{III} centers have all nearly axial symmetry and are highly anisotropic, which is rather difficult to observe with either ESEEM or ENDOR.[69]

Table 7.15 shows only results for those nitrogen atoms, for which an experimental assignment is available (see Table A9 in Appendix A for the remaining nitrogen nuclei). In addition to **Mn-cat**, **4-(μ-O)$_2$(μ-OAc)**, and **5-(μ-O)$_2$(μ-OAc)** discussed above, experimental data are also available for **2-(μ-O)$_2$** and **3-(μ-O)$_2$**. Agreement with experiment is similar as for the other complexes. Taking **2-(μ-O)$_2$** as an example, all ligating nitrogen atoms may be differentiated, based on the computed nitrogen HFCs and nuclear quadrupole tensors. The nitrogen atoms on the Jahn-Teller axes of the Mn^{III} center (N1, N1') exhibit particularly large A_{iso}, whereas the equatorial N2 and N2' have small values (0.6 MHz). The four nitrogen atoms bonded to Mn^{IV} exhibit similar, intermediate values (N3, N3': 2.5 MHz, N4, N4': 1.9 MHz). These results suggest that similar evaluations may help in structure elucidation also in more complex cases, provided nitrogen parameters are available from ESEEM and/or ENDOR.

Table 7.15. ^{14}N Hyperfine and nuclear quadrupole couplings (in MHz).[a]

			a_{iso} *(site)*	A_{iso}	T_1	T_2	T_3	$\lvert e^2qQ\rvert$	$\lvert\eta\rvert$	$\rho^{\alpha\text{-}\beta}$
2-(μ-O)$_2$	Mn^{III}	N1	7.3	14.6	-2.0	-1.7	3.7	3.83	0.07	0.027
	Exp.[b]		6.8	13.5						
	Exp.[c]		4.8	9.5				2.9		
	Mn^{IV}	N2	-2.5	2.5	-0.5	0.0	0.5	2.28	0.30	0.044
	Exp.[d]		-2.8	2.8				2.3		
3-(μ-O)$_2$	Mn^{III}	N1	6.4	12.8	-1.9	-1.7	3.6	3.81	0.07	0.026
	Exp.[c]		4.9	9.7				3.0		
4-(μ-O)$_2$ (μ-OAc)	Mn^{III}	N1	5.4	10.8	-2.4	-2.2	4.5	5.45	0.09	0.041
	Exp.[c]		4.9	9.7				3.0		
5-(μ-O)$_2$ μ-OAc)	Mn^{III}	N1	5.9	11.7	-2.2	-2.1	4.4	4.89	0.15	0.044
	Exp.[c]		4.8	9.6				2.20		
	Mn^{IV}	N2	-1.7	1.7	-0.1	0.0	0.1	2.36	0.27	0.039
	Exp.[e]		-2.9	2.9				2.5	0.6	
Catalase	Mn^{IV}	N2	-2.7	2.7	-0.5	0.2	0.3	-2.64	0.51	0.032
	Exp.[f]			(|2.88|)				(2.29)	(0.58)	

[a]B3LYP results. Cf. footnote a to Table 7.14. [b]ENDOR data taken from ref. [70]. [c]ENDOR data taken from ref. [36]. [d]ENDOR data taken from ref. [71]. [e]ESEEM data taken from ref. [36]. [d]ESEEM data taken from ref. [69].

7.4.9 ^{1}H Hyperfine Coupling Tensors

We finally want to evaluate the dependence of the ligand proton HFCs on the functional. For this, we have chosen **4-(μ-O)$_2$(μ-OAc)**, which had been studied previously by Sinnecker and Neese at BP86 and B3LYP levels.[7] Only the hydrogen atoms directly attached to the nitrogen nuclei in the first coordination sphere of the manganese atoms were experimentally accessible.[36] Moreover, H(1) *vs.* H(2) and H(3) *vs.* H(4) are in a too similar environment (cf. Figure 7.1) and could not be distinguished experimentally. They have been averaged computationally. Our B3LYP results (Table 7.16) are similar to those of Sinnecker *et al.*,[7] small differences likely arising from the different basis sets employed. As found already for mononuclear Mn complexes like the divalent site in concanavalin A or simple aqua complexes,[9] the isotropic HFC decreases somewhat with increasing EXX admixture. Yet, even at very high admixtures, the absolute value at the Mn^{III} site is still overestimated compared to experiment. In the case of the Mn^{IV} site, the values for H(3) and H(4) start to diverge for large EXX admixtures, suggesting artificial symmetry breaking due to unphysical spin contamination (see above). The HFC anisotropies are already reproduced well at B3LYP level (somewhat better than with BLYP) and cannot be improved significantly by enhanced EXX admixture.

Table 7.16. Dependence of hydrogen HFC tensors (in MHz) on exact-exchange admixture for **4-(μ-O)$_2$(μ-OAc)**.[a]

	a_{iso} *(site)*	A_{iso}	T_1	T_2	T_3	$\rho^{\alpha-\beta}$	a_{iso} *(site)*	A_{iso}	T_1	T_2	T_3	$\rho^{\alpha-\beta}$
	H(1)/H(2))-Mn^{III}						**H(3)/H(4)-Mn^{IV}**					
BLYP	2.8	5.3	-7.5	-6.2	13.5	0.005	3.0	-3.0	-6.1	2.6	3.6	-0.005
B3LYP	2.5	4.4	-8.4	-6.8	14.8	0.005	2.9	-2.9	-7.1	3.0	4.1	-0.005
BHLYP	2.4	4.6	-8.6	-6.9	15.5	0.005	2.8	-2.8	-8.2	3.5	4.7	-0.005
B60LYP	2.3	4.5	-8.6	-7.0	15.6	0.005	2.7	-2.7	-8.6	3.7	4.9	-0.005
B70LYP	2.3	4.5	-8.7	-7.0	15.7	0.005	2.5	-2.5	-8.9	3.9	5.1	-0.004
B80LYP	2.3	4.5	-8.7	-7.0	15.7	0.005	2.0	-2.0	-9.5	4.2	5.4	-0.004
B90LYP	2.3	4.4	-8.8	-7.0	15.8	0.005	1.5	-1.5	-9.9	4.3	5.6	-0.002
Sinnecker[b]	2.6	5.1	-8.1	-6.4	14.5		2.9	-2.9	-6.9	2.9	4.0	
Exp.[c]	2.6	+3.1	-8.7	-8.0	+16.7		1.5	-1.5	-7.2	+2.8	+4.4	

[a]HFC data spin-projected. $\rho^{\alpha-\beta}$ is the Mulliken spin density at hydrogen. [b]DFT study using ORCA (B3LYP//B3LYP) from ref. [7]. [c]Experimental data for [MnMn(μ-O)$_2$(μ-OAc)(CH$_3$)$_4$DTNE](BPh)$_4$.[36]

7.5 Conclusions

The detailed interpretation of EPR spectra for di- and multinuclear manganese complexes, like the oxygen-evolving complex of photosystem II, could be improved considerably if we may assist the experimentalists by reliable quantum chemical calculations and analyses. Building on important recent computational work by Sinnecker *et al.* on a synthetically available dinuclear model complex and on a model for dimanganese catalase, we have provided here a systematic study of various EPR parameters of a wider set of dinuclear $Mn^{III}Mn^{IV}$ complexes, using broken-symmetry DFT approaches. A main focus has been the evaluation of the influence of exact-exchange admixture in hybrid functionals on the computed spin-density distributions and spectroscopic parameters.

Spin-projected g-tensors are generally almost isotropic and exhibit only relatively small deviations from the free-electron value. While the g-tensors are reproduced well by the standard B3LYP functional, their diagnostic value remains low at this point. Computations on the ^{55}Mn hyperfine tensors confirm that a) the isotropic hyperfine couplings are underestimated by standard functionals, but b) this systematic error may be remedied to a good approximation by an empirical scaling factor (about 1.45 at B3LYP level). The hyperfine anisotropies are reproduced well already by standard functionals. The same holds for the ligand ^{14}N and ^{1}H hyperfine tensors. Ongoing work in our lab concentrates on finding suitable spin-projection schemes also for bridging ligand sets. We find the Mn^{III} hyperfine tensors not to be generally covariant to the g-tensors. This information is of importance for spectra simulations and will possibly affect also simulation results for the OEC.

The spin contamination of the BS-KS determinants has been analyzed using natural orbital occupations, paired-orbital overlaps, and an expansion into quasi-restricted determinants in the paired-orbital basis. It turns out, that the S^2 expectation values near 3.75 obtained at B3LYP level are well in line with the expected seven active orbitals, which include the truly unpaired “SOMO” and three pairs of corresponding magnetic orbitals. The lower $<S^2>$ for the BLYP functional arises from larger overlap between the PO’s, in line with an overestimation of delocalization by GGA functionals. The increased $<S^2>$ at higher exact-exchange admixtures arises partly from an increased active PO space, related to spin polarization of nominally doubly occupied orbitals. This additional spin contamination and the partly deteriorated results for other quantities restrict

somewhat the amount of exact exchange one may use to improve the isotropic ^{55}Mn HFCs. Fortunately, the insufficiently negative intrinsic isotropic Mn HFCs at B3LYP level may be corrected easily by scaling. In the long run, improved generations of functionals are desirable that allow a well-balanced description of core- and valence-shell spin polarization. Standard hybrid functionals like B3LYP with about 20% exact exchange may thus be used with predictive power also for more complicated systems like the oxygen-evolving complex of photosystem II, which will be presented in the following chapter.

Chapter 8

The pleasing aspect of this particular model is that it brings together different subfields of our central science. We are separated, split asunder – organic, inorganic, physical, biological, analytical chemists – by the very largesse of our creation. The variety of molecules we create, and the methods we use to study them breed jargon and specialization. Yet underneath the seeming complexity there must be a deep unity.

Roald Hoffmann, 1981

On the Structure of the Oxygen-Evolving Complex of Photosystem II: Density Functional Calculations on Electron Paramagnetic Resonance Parameters of the S_2 State

8.1 Introduction

In this chapter we will turn to the ultimately goal of this thesis: the oxygen-evolving complex (OEC) of photosystem II (PSII). The biological context as well as important crystallographic, XAS, EPR and quantum chemical studies are reviewed in Chapter 2.

We have limited this study on the S_2 state, that is by far best EPR-characterized state of the Kok cycle.[1-9] It exhibits either the so-called multiline signal at g = 2, arising from an S = 1/2 ground state, probably with a $Mn^{III}Mn^{IV}{}_3$ distribution of oxidation states, or a broad signal at g = 4.1, attributable most likely to an S = 5/2 spin state with the same Mn oxdidation states. The multiline signal indicates an antiferromagnetically coupled mixed-valence manganese cluster, strongly resembling the multiline signal of synthetic or biological dinuclear $Mn^{III}Mn^{IV}$ complexes.[10-12] Hyperfine coupling constants (HFCs) have been extracted by ^{55}Mn-ENDOR spectroscopy, revealing significant contributions from all four Mn ions. A variety of simulations derived from the EPR and ENDOR of the multiline signal of different samples are available,[5-7] which were used in attempts to

extract information about the ground state and its spin-coupling patterns. Recently, multifrequency ESEEM spectroscopy has been used to determine the ^{14}N HFC and nuclear quadrupolar coupling (NQC) of a histidine protein residue bound to the manganese cluster.[13,14]

EPR, ENDOR or ESEEM studies should benefit greatly from support by quantum-chemical calculations, which may provide structural information as well as insight into the nature of ground and excited states of the Kok cycle. Yet, so far no computational studies of EPR parameters for the OEC are available (calculations on dinuclear model complexes have been performed,[15-17] see also Chapter 7). The quantum-chemical studies on the OEC to date focused mainly on a) finding models that fit the structural parameters obtained from X-ray diffraction and XAS/EXAFS (see above) or on b) studying some mechanistic aspects of O-O bond formation on models.[18-25] All of these studies suffer from the incomplete structural information available currently from experiment.

Here we provide the first explicit quantum-chemical study of EPR parameters (^{55}Mn and ^{14}N HFCs and NQCs) for a substantial variety of model complexes of the S_2 state of the OEC, with the aim to compare different structural models suggested in the literature explicitly with experiment. Due to the complicated spin-coupling patterns of the formally $S = 1/2$ ground spin state of the S_2 state, a fully appropriate quantum-chemical treatment would require sophisticated multiconfigurational wavefunctions incorporating both dynamical and nondynamical electron correlation effects to a large extent. This is currently out of the question for a system of the complexity of the OEC. A possible alternative is to construct so-called broken-symmetry (BS) states within unrestricted Kohn-Sham density functional theory (DFT), followed by appropriate spin projection procedures.[15-17,26,27] Except for a very recent paper, in which the lowest BS state of a given position along the Kok cycle was considered for one model,[25] previous DFT calculations on the OEC were always done for high-spin states, as these are easier to compute. This precludes of course access to spin-density distributions or reliable EPR parameters. We have now been able to construct a wide variety of BS solutions for different models of the S_2 state. After spin projection, this provides access to hyperfine and nuclear quadrupole couplings, enabling us for the first time to evaluate the quality of molecular model complexes for the OEC by direct comparison with experimental EPR, ENDOR and ESEEM data.

This chapter is organized as follows. Section 8.2 describes the preparation of the structural models for the S_2 state based on the most reliable spectroscopic studies. Section 8.3 reports the computational details. The results of the structural features of the S_2 state with energetical considerations of the different broken-symmetry states are given in sections 8.4.1 and 8.4.2. Finally, the EPR parameters for the S_2 state are discussed in sections 8.4.3 and 8.4.4. Section 8.5 summarizes and concludes.

8.2 Model Systems for the Oxygen-Evolving Complex

X-ray crystallography has provided important information about the location and protein environment of the Mn_4Ca^{2+} cluster, with determinations down to 3.5 Å[28] and 3.0 Å[29] resoving most cofactors and most of the amino acid residues. Essentially all models suggested during the past 5 years include some information on the most likely protein ligation environment from these works. Yet, as discussed in the introduction, radiation damage (photodeduction of the cluster) prevents a clear picture of the positions of the manganese atoms and ligands.

8.2.1 Models Ferreira^{+1} and Ferreira-2^{+1}

In our screening, we have included one model used previously by Sproviero *et al.*[30] in DFT-based QM/MM studies, which is essentially based on the London X.-ray structure data[28,29] but used also distances from isotropic EXAFS spectra as constraints in structure optimization.[31] This model cluster bears one positive charge and will in the following be termed **Ferreira^{+1}** (Figure 8.1). It features a heterocubane-like Mn_3CaO_4 cluster with μ_3-oxo bridges. One of these bridges is actually of μ_4-type, as it connects also to the remaining dangler Mn atom (Mn_A, Figure 8.1). The amino acid residues suggested by the 3.5-Å resolution structure[28]

Ferreira^{+1}

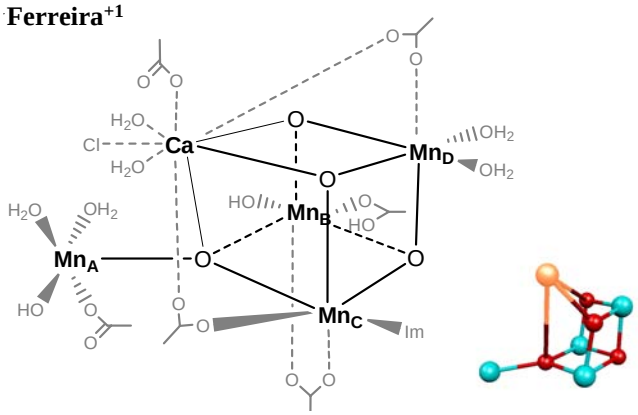

Figure 8.1. Core and structure for **Ferreira^{+1}**.

(D1-Asp342, D1-Asp170, D1-Glu333, D1-Glu189, CP43-Glu354, and D1-Ala344) have been modelled here by acetic acid or acetate (note the bridging mode of some of the acetates), and the D1-His332 residue at Mn_C by an imidazole ligand. The same has been done for all other models. We have not attempted to model the further protein environment by QM/MM methods at this point (as done, e.g. in ref. [30]), as this seems premature in view of the very limited structural information available at the moment. A main difference to the QM/MM-based model[30] is therefore in particular the environment of the Ca ion. To complete the coordination of the Mn ions to a coordination number of 5 for the dangler Mn_A and 6 for the other Mn ions, water and hydroxide ligands have been added. On Mn_B we had originally added one water ligand. During the optimization (see below for details), a proton from this ligand was transferred to the acetate ligand on Mn_B. Ca^{2+} often prefers 6-8 fold coordination. Seven ligands were chosen for the model. Two of the water ligands bound to Ca^{2+} and Mn_A have been considered to be involved in the O-O bond formation.[32,33] The position of the chloride ion known to be essential for the function of the OEC is still under discussion. Recent studies[34,35] suggested that Cl^- is not a direct ligand to manganese, and it has only been included in the model **Ferreira**$^{+1}$. To study the influence of the coordination number of the dangler manganese atom Mn_A, a modfied model **Ferreira-2**$^{+1}$ has been constructed, in which an additional water ligand has been added to Mn_A, providing sixfold coordination for all manganese atoms.

8.2.2 Model Dau^{+1}

Dau^{+1}

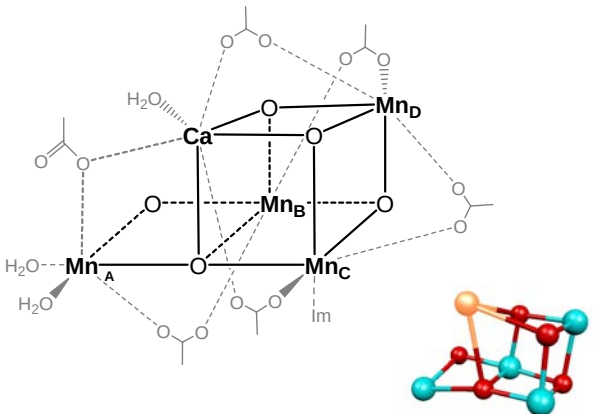

Figure 8.2. Core and structure for **Dau**$^{+1}$.

Most models suggested during the past years are primarily based on distances from EXAFS, augmented by a ligand sphere taken from the X-ray diffraction studies. We have adapted to the S_2 state an interesting structural model suggested by Dau *et al.* for the S_1 state.[36] It will be termed **Dau**$^{+1}$ (Figure 8.2) and is based on the EXAFS structure data of Dau and

Haumann,[37-39] augmented by amino acid residues from the Berlin X-ray structure.[29] The dangler Mn_A is linked to Mn_B by a di-μ-oxo-μ-acetato bridge, but it is sixfold coordinated and also linked to Mn_C. The Ca^{2+} atom is integrated into the cuboidal core, and only one carboxylato ligand is in a terminal position. Model **Dau^{+1}** is thus rather compact, and only three water molecules have been added. No chloride ion has been included.

8.2.3 Models Yano

A very powerful technique applied recently to the OEC is polarized high-resolution EXAFS on oriented PS-II membranes or single crystals. It provides additional information beyond the mere distances obtained from standard EXAFS. Based on such studies, Yano *et al*. have suggested three related yet distinct core structures of the OEC.[31,40] We have combined the cores of ref. [31] with ligation environments deduced from the 3.0 Å[28] and 3.5 Å[29] resolution X-ray structures. The construction of the models was done prior to the appearance of ref. [40]. The ligand spheres of our models are thus very similar but not identical to those of ref. [40]. The exact structural data depend of course also on the DFT optimizations (see below). Structures I, IIa, and III from ref. [31] give rise to our three (neutral) models **Yano-I^0**, **Yano-II^0** and **Yano-III^0**, respectively (Figure 8.3). All three models appear noticeably more open than the models discussed so far. Only **Yano-III^0** may be interpreted loosely as derived from a Mn_3CaO_4 heterocubane. Generally, the five-coordinate dangler Mn_A is connected to Mn_B by a di-μ-oxo-μ-acetato bridge. Mn_B is coordinated by one μ-oxo bridge to Mn_C and by one μ-oxo bridge to Ca^{2+} and Mn_D. Ca^{2+} is noticeably outside the cube. As in **Ferreira^{+1}** (see above and Figure 8.1), seven amino acid residues are directly coordinated. Only one or two carboxylato ligands are bound terminally. Thus, only four water-derived ligands are needed to complete the coordination (compared to eight in **Ferreira^{+1}**). No chloride ions have been included. Polarized EXAFS data on oriented membranes render model **Yano-I^0** less likely than **Yano-II^0** or **Yano-III^0**,[41-43] but we were interested nevertheless in examining its behavior during the structure optimizations (see below). Models **Yano-II^0** and **Yano-III^0** differ mainly in the position of the μ_3-oxo bridge: it points towards Ca^{2+} in **Yano-II^0**, whereas it is it is on the other side of the Mn3 plane in **Yano-III^0** (Figure 8.3). A positively charged model **Yano-II$^+$** has been obtained by protonating the terminal

carboxylato ligand on Mn_A. A model close to **Yano-II$^+$** has recently been studied by quantum chemical calculations.[44,45] It differs mainly by having one less water ligand on Ca.

Finally, two modifications of **Yano-II^0** were investigated to study the influence of the coordination number of the manganese atoms: a) in **Yano-II-A6^0** a water molecule was moved from Ca^{2+} to Mn_A, to make all manganese atoms sixfold coordinated; b) in **Yano-II-D5^0** the water molecule from Mn_D was moved to Mn_A, keeping Mn_D five-coordinate.

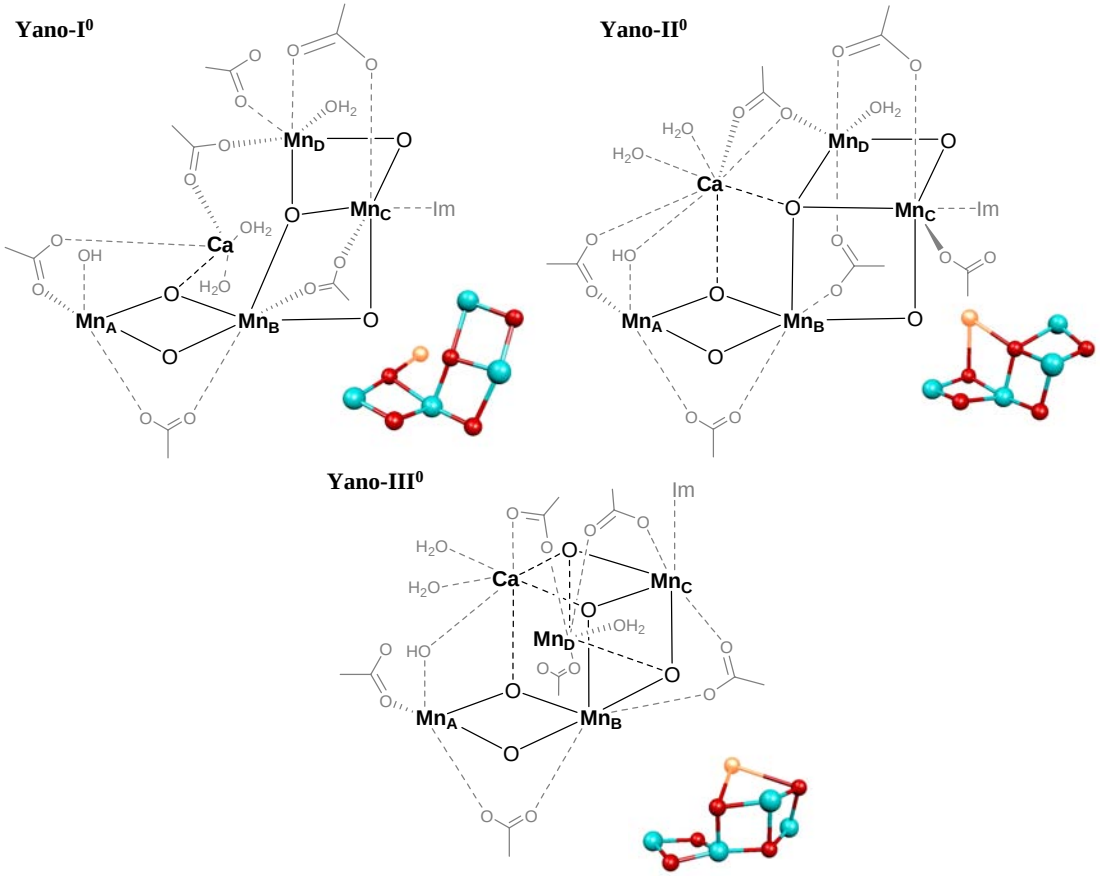

Figure 8.3. Core and structures for models **Yano**.

8.3 Computational Details

Structure optimizations and KS wavefunction computations were done with the Turbomole 5.9.1 code.[46] Based on the initial coordinates obtained as described above, the structure optimizations employed the B3LYP[47,48] hybrid functional with SVP basis sets[49] and unrestricted Kohn-Sham wavefunctions. We have been able to construct various different BS states for all models, in addition to the HS state. With suitable initial guess wavefunctions, the states remained stable, as confirmed by Mulliken spin density analyses (see below). It has thus been possible to optimize these different states all separately. While most of the structures remained relatively close to the starting coordinates, large reorganization during optimization was found for **Yano-I^{0}**, and **Ferreira^{+1}** also deviates nonnegligibly both from the X-ray structure data and from the QM/MM optimized structure (see below).

At these optimized structures, unrestricted Kohn-Sham single-point calculations for the calculations of HFC tensors were performed with Gaussian03[50] using a 9s7p4d basis set for manganese (specifically designed for hyperfine calculations[49,51,52]) and flexible IGLO-II[53,54] basis sets for the ligand atoms. We will denote this level by B3LYP/II//B3LYP/SVP. Previous computational studies on both mononuclear[55] and dinuclear[15-17] Mn complexes have indicated that B3LYP calculations provide reasonable agreement with experiment for the Mn HFC anisotropies and for the ligand EPR parameters (see also previous Chapters). Isotropic transition-metal hyperfine couplings are typically underestimated in absolute value at this level, due to an insufficient description of core-shell spin polarization.[51,52] Fortunately, the deviations for the isotropic Mn HFCs turned out to be systematic[15-17,55] and may be corrected by scaling the computed results with a factor of 1.45.[17]

The unrestricted Kohn-Sham orbitals were transferred to the MAG-Respect property package[56] by suitable interface routines to compute the HFC and NQC parameters. The atomic mean-field approximation (AMFI)[57,58] has been used to compute the matrix elements of the Breit-Pauli SO operator for the SO corrections to the Mn HFC tensors. Mulliken spin-density analyses were used to verify convergence to the proper BS and HS states. The BS states were in some cases further analyzed by transformation of the Kohn-Sham wavefunction to a basis of natural orbitals and subsequently to paired (corresponding) orbitals.[59-61] These calculations were based on the Gaussian03 program.[50]

8.4 Results and Discussion

For all of the models of the S_2 state described above, we will first discuss structures (section 8.4.1), relative energies and spin-density distributions of HS and different BS states (section 8.4.2). Subsequently, the ^{55}Mn HFC and the ^{55}Mn NQC parameters (section 8.4.3) as well as the ^{14}N HFC constants and the ^{14}N NQC parameters will be analyzed (section 8.4.4).

8.4.1 Structures and Energies

In computations on the OEC, it has usually been assumed[62-65] that the differences between the structures optimized in the HS and the BS states are small, and that a discussion of the more easily accessible HS structures is sufficient. However, in case of dinuclear $Mn^{III}Mn^{IV}$ complexes, some differences between HS and BS structures have been identified.[15-17] Given the potential dependence of EPR parameters even on moderate structural changes, an evaluation of the differences between HS and BS structures has been performed. For all states, the calculations converged generally to a $Mn^{III}(Mn^{IV})_3$ configuration, thereby confirming the most widely accepted[5,9,33,66,67] distribution of Mn oxidation states for the S_2 state of the OEC (as found also in previous quantum-chemical studies[30]). Yet, we find the distribution of the oxidation states to differ between the models (see below).

These oxidation states allow three different BS states to be constructed for a formal S = 1/2 situation. They are shown for the example of model **Yano-II^0** in Figure 8.4, together with isosurface plots of the computed spin densities of HS and BS states. For this model, the Mn^{III} d^4 center is generally found to be located at Mn_D (indicated by italics in our notation) as confirmed by Mulliken spin densities (see below). Note that to achieve a formal S = 1/2 state, the Mn^{III} ion has to exhibit M_S = +2, two of the Mn^{IV} centers M_S = -3/2 (indicated by a bar above the atom label) and one of them M_s = +3/2. Spin-density isosurface plots (Figures B4-B8 in Appendix B) confirm that we have been able to construct such BS Kohn-Sham wavefunctions for all possible combinations of spin alignments and investigated model complexes.

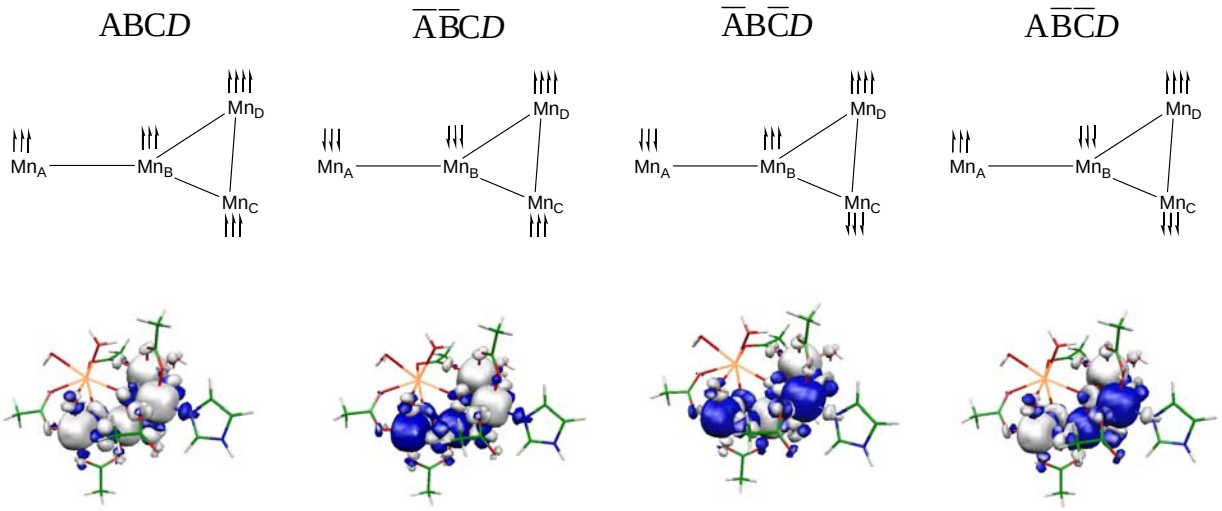

Figure 8.4. Spin configurations and spin-density distributions for HS and BS states of model **Yano-II^0** (isosurfaces ±0.003 a.u.). B3LYP/II//B3LYP/SVP results. See text for the notation of the spin configurations.

The optimized structures of the HS and BS states for this model are compared in Table 8.1 to the original data of the model obtained by simulating polarized-EXAFS data[31] (note that the EXAFS data pertain to the dark-stable S_1 state). Table 8.1 provides also the relative energies of the spin configurations. For all states, the Mn-Mn bond lengths are essentially consistent with the original values (with deviations of maximally 0.2 Å), indicating that the cluster has changed relatively little during quantum-chemical optimization. The inferior agreement for the Ca-Mn distances may reflect the flexibility of the Ca coordination environment (see above). The calculated Mn_C-N_{Im} bond lengths are are in good agreement (0.02 Å too long) with the X-ray diffraction results. Structural differences between the different spin configurations are below 0.05 Å in the distances. While the BS states are clearly below the HS state, they differ by less than 2 kJ/mol among each other at the given computational level. Small energy differences between the different BS states are found mostly also for the other models (see Tables B1-B8 in Appendix B). This is consistent with EPR spin-relaxation results, which indicate the lowest excited state to be only 30-40 cm^{-1} (ca. 0.3– 0.5 kJ/mol) above the ground spin state.[68-72] The energy separation depends on the S_2 state preparation, leading to the observed range of values. Of course the exact values for the computed energy differences between the different BS and HS states should not be overinterpreted in view of various possible errors sources. Yet in most cases at least a qualitatively reasonable picture is obtained (Tables B1-B8 in Appendix B).

Table 8.1. Distances (in Å) and relative stabilities (in kJ mol^{-1}) of the HS and different BS states for model **Yano-II^{0}**.

	ABC*D* (HS)	$\overline{A}\overline{B}CD$	$\overline{A}B\overline{C}D$	$A\overline{B}\overline{C}D$	model[a]
Mn_A-Mn_B	2.701	2.702	2.702	2.703	2.721
Mn_A-Mn_C	4.821	4.825	4.835	4.820	4.956
Mn_A-Mn_D	5.341	5.338	5.312	5.297	5.495
Mn_B-Mn_C	2.776	2.776	2.785	2.774	2.700
Mn_B-Mn_D	3.448	3.435	3.424	3.404	3.285
Mn_C-Mn_D	2.833	2.833	2.818	2.817	2.804
Ca-Mn_A	3.145	3.147	3.147	3.144	3.607
Ca-Mn_B	3.605	3.606	3.653	3.640	3.398
Ca-Mn_C	4.663	4.677	4.730	4.710	4.364
Ca-Mn_D	3.673	3.683	3.709	3.689	3.395
Mn_C-N_{Im}	2.034	2.032	2.035	2.031	2.015[b]
ΔE_{rel}[c]	14.8	0.0	0.5	2.1	-
$\langle S^2 \rangle$[c]	48.96	6.98	6.94	6.95	-

[a]EXAFS-based model structure IIa of ref. [31]. [b]X-ray data.[28] [c]B3LYP/II//B3LYP/SVP results for relative energies and spin contamination.

Given the relatively minor structural differences between the different spin states, we compare in Table 8.2 optimized structure parameters to the corresponding starting structures only for the lowest-energy computed BS state of each model. Full details for all spin states are provided in Tables B1-B8 in Appendix B. The largest relaxation of the structure with respect to the starting coordinates is found for models **Ferreira^{+1}** and **Yano-I^{0}**. In case of the former, this is understandable, as a) the original distances derived from X-ray diffraction suffer from the abovementioned radiation damage problems and limited resolution, and b) the QM/MM optimization[30] may reflect constraints introduced by the QM/MM model, which are not present in our optimizations. In particular, distances to Mn_A and to the calcium atom are longer in our optimizations, i.e. Mn_A has become more distant from the $CaMn_3O_4$ cluster core, and we cannot reproduce a ca. 3.3 Å Mn-Mn distance suggested by EXAFS (the necessary three distances in the 2.7-2.8 Å range are found, however). The fact that our computations pertain to the S_2 state and the X-ray and EXAFS data to the S_1 state may be of only

Table 8.2. Comparison of optimized Mn-Mn and Ca-Mn distances (in Å) with starting structures of the underlying models.

	Ferreira^{+1} $A\bar{B}\bar{C}D$	QM/MM optimized[a]	R-QM/MM[b]	X-ray data[c]	**Dau**$^{+1}$ $AB\bar{C}\bar{D}$
Mn_A-Mn_B	3.728	3.55	3.68	3.226	2.888
Mn_A-Mn_C	3.760	3.29	3.34	3.245	4.133
Mn_A-Mn_D	5.403	-	-	5.124	5.173
Mn_B-Mn_C	2.763	2.86	2.77	2.722	2.904
Mn_B-Mn_D	2.797	2.77	2.63	2.677	2.783
Mn_C-Mn_D	2.834	2.78	2.74	2.657	2.752
Ca-Mn_A	5.084	-	-	3.951	3.481
Ca-Mn_B	5.315	4.00	3.88	3.371	3.273
Ca-Mn_C	3.981	3.78	3.29	3.393	3.319
Ca-Mn_D	3.906	-	-	3.344	3.277
Mn_C-N_{Im}	2.082	-	-	2.015	2.088

	Yano-I^{0} $\bar{A}\bar{B}CD$	EXAFS-based[d]	**Yano-II**^{0} $\bar{A}\bar{B}CD$	EXAFS-based[e]	**Yano-III**^{0} $A\bar{B}\bar{C}D$	EXAFS-based[f]
Mn_A-Mn_B	2.716	2.729	2.702	2.721	2.718	2.721
Mn_A-Mn_C	5.002	4.738	4.825	4.956	5.154	4.970
Mn_A-Mn_D	5.229	4.936	5.338	5.495	5.481	5.456
Mn_B-Mn_C	2.710	2.703	2.776	2.700	2.788	2.720
Mn_B-Mn_D	4.176	3.260	3.435	3.285	3.677	3.251
Mn_C-Mn_D	2.835	2.809	2.833	2.804	2.826	2.804
Ca-Mn_A	3.305	5.039	3.147	3.607	3.730	4.375
Ca-Mn_B	3.394	3.397	3.606	3.398	3.363	3.732
Ca-Mn_C	4.283	4.942	4.677	4.364	3.384	3.401
Ca-Mn_D	3.240	3.400	3.683	3.395	3.408	3.403
Mn_C-N_{Im}	2.053	-	2.032	-	2.117	-

[a]Results of QM/MM optimizations[30] of the S_2 state based on X-ray data.[28] [b]Results of refined (R)-QM/MM optimizations[20] of the S_1 state based on X-ray data.[28] [c]X-ray data of ref. [28]. [d]Model structure I based on polarized-EXAFS data.[31] [e]Model structure IIa based on polarized-EXAFS data.[31] [f]Model structure III based on polarized-EXAFS data.[31]

moderate importance, as QM/MM calculations and EXAFS experiments indicate the structures of these two states to be very similar.[30,73]

In case of **Yano-I^0**, it is the Mn_A-Mn_C, Mn_A-Mn_D, Mn_B-Mn_D, and Ca-Mn_A distances that deviate most. In the originally suggested model structure, a μ_3-oxo bridge connects Mn_A, Mn_B and Mn_C, and Mn_B, Mn_C and Mn_D are in different planes.[31] After optimization, the μ_3-oxo bridge becomes a μ_2-oxo bridge connecting only Mn_A and Mn_B, and Mn_B, Mn_C and Mn_D are located in one plane. The ca. 3.3 Å Mn-Mn distance is missing also in this optimized structure (the Mn_B-Mn_D distance has increased to about 4.2 Å). The model has thus opened up and flattened during optimization.

No comparison to a starting model is possible for **Dau^{+1}**, as the structure was built from a qualitatively analogous model for the S_1 state, without a detailed structural basis from experiment. After optimization, the cluster appears to be too compact, however, with two Mn-Mn distances below 2.8 Å and two near 2.9 Å (Table 8.2). In fact, the optimized structure disagrees with the assumed presence of only two Mn-Mn distances below 2.9 Å and of one distance of 3.7 Å, on which the proposed model was based.[36] We note also that this is the only model where the computations gave a very slight preference to a high-spin ground state (cf. Table B3 in Appendix B). However, in view of the very small energy differences (see above), this should not be overrated.

For models **Yano-II^0** and **Yano-III^0**, changes in the structural parameters compared to the starting values are less pronounced, indicating better conservation of the general core. **Yano-II^0** performs better than **Yano-III^0** in this context, as one Mn-Mn- distance near 2.7 Å, two near 2.8 Å and one near 3.4 Å are obtained after optimization (in **Yano-III^0** the longer distance has increased to 3.68 Å). Somewhat larger rearrangements are found in the Ca coordination sphere. Similar results, in particular the better conservation of the core, have also been observed in recent DFT optimizations of the HS state for the two models, with slightly different ligand distributions.[45] We note in passing that a comparison of relative energies of all the **Yano** models (which have identical net composition, see above) would suggest the lowest overall energy for **Yano-I^0** (Table B9 in Appendix B). But this should not be overinterpreted, as again the protein environment might well shift the relative stabilities within the computed energy range.

The different topology of the various models is apparent from the distances (Table 8.2): **Ferreira^{+1}** is clearly a 3+1 dangler model, **Dau^{+1}** is more compact, and the EXAFS-based **Yano** models appear more open and feature the longer Mn-Mn distance (nominally near 3.3 Å) between Mn_B and Mn_D (see also Figures 8.1 – 8.3).

8.4.2 Spin-Density and Oxidation-State Distribution and their Dependence on Coordination Number

One usually assumes that the oxidation state changes in the OEC are largely manganese-based (note, however, that resonant inelastic X-ray scattering data have been interpreted in terms of strong covalency and delocalization of, e.g., the SOMO in the S_2 state[74]). The S_2 state (S = 1/2) is now essentially accepted to feature a $Mn^{III}(Mn^{IV})_3$ localized mixed-valence distribution of oxidation states.[33,66,67] This assignment is supported by a number of XAS, X-ray emission spectroscopy (XES), and EPR experiments,[7,33] and it is confirmed generally by our computations (as well as by earlier calculations[30,45]). Yet, the different models provide different positions of the unique Mn^{III} ion, as indicated by the Mulliken spin-density distributions (given in detail in Table 8.4 further below).

The original model **Ferreira**$^{+1}$, which has five-coordinate Mn_A, exhibits the Mn^{III} center on this very dangler atom (for all optimized HS and BS states, and also in previous QM/MM studies[30]). In **Ferreira-2**$^{+1}$, we therefore added a water molecule to Mn_A, to make all Mn atoms six-coordinate (see section above on construction of model systems). This moves the Mn^{III} site to Mn_B, confirming a dependence of the oxidation-state distribution of this model on coordination number, consistent with recent computational results for the S_1 state.[30] Model **Dau**$^{+1}$ agrees with **Ferreira**$^{+1}$ in having the Mn^{III} site on Mn_A for all HS and BS states. In the remaining, EXAFS-based models, the Mn^{III} site is on Mn_D (again independent of spin configuration), in spite of Mn_D being six-coordinate and Mn_A five-coordinate in **Yano-I**^{0}, **Yano-II**^{0}, and **Yano-III**^{0}. This is also not altered when making Mn_D six-coordinate by either moving a water molecule from Ca to Mn_A (**Yano-II-A6**^{0}) or from Mn_D to Mn_A (**Yano-II-D5**^{0}), cf. Table 8.4 below (we note that both of these water transfers lowers the energy somewhat, cf. Table B8 in Appendix B).

In practically all cases, initial guess wavefunctions with different oxidation-state distributions (i.e. not just different spin configurations for identical oxidation states) converged back to the most stable situations just discussed. For the example **Ferreira-2**$^{+1}$, we have attempted to force also all other distributions. This was not possible with the B3LYP functional but only in single-point calculations at the HS structure with the BHLYP functional, which incorporates 50% exact-exchange admixture (see Table 8.3). Most of the converged SCF energies are far above those with Mn_B being the d^4 ion, except for BS states $A\mathrm{B}\overline{\mathrm{C}}\overline{\mathrm{D}}$ and $\overline{\mathrm{A}}\mathrm{B}\overline{\mathrm{C}}D$. States with Mn_C as Mn^{III} position are

generally unsuitable. But even in those two cases mentioned, absolute spin density values significantly above 3 on other than the indicated nominal Mn^{III} centers indicate these electronic situations to be unstable, or at least significantly delocalized. This suggests that, while different spin-coupling patterns are close in energy, a given model complex exhibits clear preferences for a particular oxidation-state distribution (depending on coordination numbers and structure, cf. above). Previous quantum chemical calculations indicated also a strong dependence of the oxidation-state patterns on the choice of model and in particular on coordination numbers.[30,45] Experimental work based on simulations of EPR and ENDOR spectra, combined with a variety of constraints from other sides, favored Mn_A and Mn_D as the Mn^{III} site.[9]

Table 8.3. Mulliken spin-densities and relative stabilities[a] of different HS and BS states for **Ferreira-2**$^{+1}$.[b]

	$\rho^{\alpha-\beta}\,Mn_A$	$\rho^{\alpha-\beta}\,Mn_B$	$\rho^{\alpha-\beta}\,Mn_C$	$\rho^{\alpha-\beta}\,Mn_D$	E_{rel} [a]
$AB\bar{C}\bar{D}$	3.10	*3.96*	-3.15	-3.21	4.0
$\bar{A}B\bar{C}D$	-3.09	*3.98*	3.15	-3.23	0.0
$\bar{A}B\bar{C}D$	-3.07	*3.96*	-3.18	3.26	2.7
$AB\bar{C}\bar{D}$	*3.42*	3.96	-3.18	-3.26	6.7
$A\bar{B}C\bar{D}$	*3.78*	-3.24	3.47	-3.28	229.9
$A\bar{B}\bar{C}D$	*3.83*	-3.07	-3.09	3.32	256.1
$A\bar{B}C\bar{D}$	3.37	-3.95	*3.80*	-3.29	175.6
$\bar{A}BC\bar{D}$	-3.05	3.54	*3.78*	-3.17	185.0
$\bar{A}\bar{B}CD$	-3.08	-3.34	*3.82*	3.22	206.1
$A\bar{B}\bar{C}D$	3.15	-4.00	-3.30	*3.73*	143.2
$\bar{A}B\bar{C}D$	-3.14	3.96	-3.15	*3.47*	5.7
$\bar{A}\bar{B}CD$	-3.04	-3.55	3.28	3.80	234.8

[a]Energy in kJ mol^{-1} relative to spin configuration $\bar{A}B\bar{C}D$. [b]BHLYP/II single-point calculations at the optimized B3LYP/SVP HS structure.

We note finally that the S^2 expectation values of the HS states are generally only slightly above the nominal value of 48.75 for an S = 13/2 state (Table 8.1, Tables B1-B8 in Appendix B). The computed S^2 values for the BS states at the given computational level (B3LYP/II//B3LYP/SVP) are in all cases in a narrow range between 6.80 and 6.95, i.e. somewhat more than 6 above the nominal value for an S = 1/2 state. This may be understood straightforwardly from occupation numbers of natural orbitals (NOs) and a paired-orbital (PO) analysis[59-61] (as done previously for dinuclear $Mn^{III}Mn^{IV}$

complexes[17]): the NO occupations (shown for **Yano-II-D5^0** in Table B10 in Appendix B) identify clearly the nominally expected 13 magnetic orbitals (the NOs for all three different BS states of **Yano-II-D5^0** are plotted in Figures B1-B3 in Appendix B. PO transformation[59] groups these into a) one singly occupied orbital with no partner and b) six pairs of corresponding POs. An expansion of the unrestricted Kohn-Sham determinant into restricted determinants in the PO basis[60,61] shows that it is mainly these six weakly-overlapping pairs that account for a spin contamination of the BS determinant by about 6. An S^2 expectation value of 6.75 would thus be consistent with this general bonding picture, and this is exceeded only slightly by the calculations.

8.4.3 ^{55}Mn EPR Parameters

In Table 8.4 we evaluate the ^{55}Mn HFCs for all different energetically close-lying BS states of all models investigated. Direct comparison with experiment should be made for the values A_{iso}*, which are empirically scaled by 1.45 (see Computational Details).[17] We note that spin-orbit corrections to the isotropic HFCs (A_{PC}) are nonnegligible, in the range of 5-10% of the nonrelativistic Fermi-contact term (A_{FC}), a typical magnitude for Mn HFCs.[15-17,55] Scaled site values a_{iso}* are also given to see how the spin densities of Mn^{III} and Mn^{IV} centers (see above) correlate with the intrinsic hyperfine values.

Three different sets of experimental HFC tensors obtained in different simulations of EPR and ENDOR spectra are also given.[5-7] Before discussing in detail the isotropic HFCs, we mention that Table 8.4 provides also spin-projected hyperfine anisotropies (unscaled). We have to remember that these are likely to be less reliable both in the simulations of experimental data and in the computations than the isotropic HFCs (see Theory Section). In our computations, the Mn^{III} center in each model clearly exhibits the largest HFC anisotropy, as would be expected from the structural distortions of high-spin d^4 complexes, and as was found also for dinuclear complexes.[15-17] Yet this is not obvious from the simulation results for the OEC: here the anisotropies of all centers appear to be in the same order of magnitude. Of course appreciable assumptions have gone into the spectra simulations (as well as into the spin projection of the computed HFC tensors, see Theory Section), which may render the anisotropies less reliable: Except for the work of Charlot *et al.*,[7] axially symmetric HFC tensors have been assumed. The g-tensor has also usually been assumed to possess axial symmetry. None of

these assumptions is borne out by the computations, which give generally rhombic HFC and g-tensors (a detailed investigation of g-tensors is currently under work). It has furthermore been assumed that the tensor axes of all HFC tensors and of the g-tensor coincide. This is also not accurate, as found already for dinuclear $Mn^{III}Mn^{IV}$ complexes.[17] Finally, ^{55}Mn NQCs are in most cases assumed to be negligible. This has been questioned in ref. [5]. While we have neglected ZFS contributions in our current spin projections of the HFCs and thereby may have missed some ZFS-mediated anisotropy transfer between the sites, we feel that the computed anisotropies may actually be more realistic than those obtained from the spectra simulations. This remains to be confirmed in future work with more refined spin projections.

The isotropic HFCs should in any case be more reliable and will be used for comparison. The differences between the three sets of experimentally derived data[5-7] reflect not only the different way the simulations were done but also partly aspects of sample preparation. We regard these data (Table 8.4) thus for the moment as a range to compare with. Notably, all three sets feature one HFC near 300 MHz, likely attributable to the Mn^{III} site (see above). Two of the sets have two HFCs near 200 MHz and one near 250 MHz,[5, 6] whereas the data of Charlot *et al*.[7] feature two HFCs near 250 MHz and only one near 200 MHz. Neither sign information nor any assignment of the HFCs to specific Mn centers can be derived with certainty experimentally.

Before comparing the various different models, let us first have a closer look at model **Yano-II^0** as an example of the information and insights provided by the extensive data set in Table 8.4: for all BS states, the site value a_{iso}* of the Mn^{III} site Mn_D is in the same range of absolute values as those of the Mn^{IV} sites, in spite of the larger Mulliken spin density. In fact, a_{iso}* for the Mn^{IV} site Mn_B of the $\overline{A}B\overline{C}D$ configuration is even slightly larger than the value for the Mn^{III} site Mn_D. It is the spin projection that leads to much larger projected values A_{iso}*. This has been observed also for dinuclear $Mn^{III}Mn^{IV}$ complexes[15-17] and seems largely true for all models (see below). Turning thus to the projected values, we see that the different BS states have similar but clearly not identical absolute values. For example, the $\overline{A}B\overline{C}D$ configuration of **Yano-II^0** exhibits the overall largest HFCs, and the lowest-energy configuration $\overline{A}\overline{B}CD$ features the smallest ones, notably also for the Mn^{III} site Mn_D. It appears that a spin-down configuration on Mn_C renders the HFC on the Mn^{III} center Mn_D more negative. The spin alignment on Mn_B, which is more remote from Mn_D (ca. 3.4 Å compared to ca. 2.8 Å) in this model has a

Table 8.4. Computed ^{55}Mn hyperfine tensors (in MHz) for different model systems and broken-symmetry states compared to EPR/ENDOR simulation results.[a]

	BS state (ΔE)[b]		a_{iso}* *(site)*	A_{iso}*	A_{iso}	T_1	T_2	T_3	A_{FC}	A_{PC}	$\rho^{\alpha-\beta}$
Ferreira^{+1}	$AB\bar{C}\bar{D}$	A	-83	-165	-114	-66	-38	104	-100	-14	3.90
	(8.6)	B	-233	233	161	-10	-2	13	148	12	2.90
		C	-192	192	132	-7	-2	9	121	12	-2.94
		D	-186	186	128	-19	3	17	117	11	-2.96
	$A\bar{B}C\bar{D}$	A	-82	-164	-113	-67	-37	104	-99	-14	3.89
	(5.4)	B	-191	191	131	-10	-5	15	119	12	-2.86
		C	-241	241	167	-5	-3	8	154	12	2.94
		D	-191	191	132	-20	3	17	121	11	-2.96
	$A\bar{B}\bar{C}D$	A	-79	-158	-109	-65	-36	101	-96	-14	3.90
	(0.0)	B	-204	204	141	-9	-1	11	129	12	-2.85
		C	-216	216	149	-6	0	6	137	12	-2.91
		D	-232	232	160	-16	-6	22	149	11	2.95
Ferreira2^{+1}	$AB\bar{C}\bar{D}$	A	-204	204	141	8	1	-8	130	11	2.98
	(7.9)	B	-174	-348	-240	-73	-44	117	-227	-14	3.85
		C	-185	185	128	-8	0	8	116	12	-2.99
		D	-176	176	122	-19	1	18	110	12	-3.02
	$\bar{A}BC\bar{D}$	A	-212	212	146	-9	1	8	134	12	-2.86
	(0.0)	B	-163	-325	-224	-64	-48	113	-211	-14	3.87
		C	-231	231	159	12	-2	-10	148	11	2.94
		D	-229	229	158	-23	4	19	146	12	-2.98
	$\bar{A}B\bar{C}D$	A	-210	210	145	-10	2	7	133	12	-2.83
	(23.7)	B	-111	-221	-153	-69	-46	115	-139	-14	3.85
		C	-228	228	157	-3	-1	4	146	12	-2.90
		D	-200	200	138	18	1	-19	126	11	2.97
Dau^{+1}	$AB\bar{C}\bar{D}$	A	-173	-346	-239	-68	-41	109	-224	-14	3.90
	(0.0)	B	-221	221	153	-11	1	10	141	12	2.90
		C	-205	205	141	-3	-1	4	130	12	-2.94
		D	-195	195	135	-6	-1	7	123	12	-2.96
	$A\bar{B}C\bar{D}$	A	-194	-388	-268	-76	-39	115	-252	-16	3.89
	(10.2)	B	-205	205	142	-10	-2	12	130	11	-2.86
		C	-225	225	155	-8	1	8	144	12	2.94
		D	-215	215	148	-5	-2	7	136	12	-2.96
	$A\bar{B}\bar{C}D$	A	-188	-376	-259	-70	-48	117	-244	-15	3.90
	(11.5)	B	-204	204	141	-14	-1	15	129	12	-2.85
		C	-221	221	153	-8	1	7	141	12	-2.91
		D	-247	247	170	-6	2	4	159	12	2.95
Yano-I^{0}	$\bar{A}\bar{B}CD$	A	-167	167	115	-9	-3	12	104	12	-2.97
	(1.7)	B	-192	192	132	-12	-8	20	121	12	-2.87
		C	-222	222	153	-9	-1	10	141	12	2.88
		D	-189	-377	-260	-103	-4	107	-246	-14	3.88
	$\bar{A}B\bar{C}D$	A	-206	206	142	-14	-2	15	130	12	-2.97
	(0.0)	B	-244	244	169	-29	12	17	157	12	2.89
		C	-229	229	158	-8	-1	9	147	12	-2.85
		D	-207	-413	-285	-112	2	110	-271	-14	3.85
	$A\bar{B}\bar{C}D$	A	-205	205	142	-16	2	14	130	12	2.96
	(2.9)	B	-207	207	143	-24	-2	26	131	12	-2.82
		C	-194	194	134	-7	1	6	122	12	-2.87
		D	-205	-409	-282	-112	0	112	-268	-14	3.85

	BS state (ΔE)[b]		a_{iso}* *(site)*	A_{iso}*	A_{iso}	T_1	T_2	T_3	A_{FC}	A_{PC}	$\rho^{\alpha-\beta}$
Yano-II^0	$\overline{A}\overline{B}CD$	A	-164	164	113	-5	-1	6	102	12	-2.99
	(0.0)	B	-201	201	139	-12	-4	16	127	12	-2.95
		C	-219	219	151	-11	-1	12	139	12	3.02
		D	-226	-451	-311	-124	43	81	-297	-14	3.91
	$\overline{A}B\overline{C}D$	A	-207	207	143	-7	2	5	131	12	-2.96
	(0.5)	B	-259	259	179	-21	10	11	167	12	2.92
		C	-242	242	167	-17	4	13	155	12	-2.95
		D	-252	-503	-347	-131	58	73	-333	-14	3.89
	$A\overline{B}\overline{C}D$	A	-208	208	143	-5	-2	7	131	12	2.96
	(2.1)	B	-204	204	140	-17	0	17	129	12	-2.91
		C	-189	189	130	-12	-1	13	119	12	-3.00
		D	-254	-507	-350	-130	58	72	-336	-14	3.87
Yano-II^{+1}	$\overline{A}\overline{B}CD$	A	-169	169	117	-10	-2	12	105	12	-2.85
	(1.7)	B	-202	202	139	-13	-1	14	128	12	-2.84
		C	-223	223	154	-11	0	11	142	12	2.97
		D	-225	-450	-310	-125	34	91	-296	-14	3.87
	$\overline{A}B\overline{C}D$	A	-203	203	140	-8	0	8	128	12	-2.87
	(7.8)	B	-251	251	173	-20	6	14	162	12	2.79
		C	-239	239	164	-16	3	12	153	12	-2.86
		D	-236	-491	-339	-134	56	78	-325	-14	3.86
	$A\overline{B}\overline{C}D$	A	-200	200	138	-8	0	8	126	12	2.94
	(0.0)	B	-210	210	145	-14	-2	16	133	12	-2.90
		C	-187	187	129	-11	-1	12	117	12	-3.00
		D	-252	-504	-348	-132	53	79	-334	-14	3.87
Yano-II -A6^0	$\overline{A}\overline{B}CD$	A	-176	176	121	-4	0	4	110	12	-2.96
	(0.0)	B	-199	199	137	-13	-3	16	126	12	-2.95
		C	-216	216	149	-11	-1	12	137	12	2.99
		D	-226	-452	-312	-125	43	82	-298	-14	3.89
	$\overline{A}B\overline{C}D$	A	-219	219	151	-6	0	6	139	12	-2.95
	(0.9)	B	-260	260	179	-19	8	11	168	12	2.92
		C	-240	240	165	-16	4	12	154	12	-2.94
		D	-251	-502	-346	-132	57	75	-332	-14	3.88
	$A\overline{B}\overline{C}D$	A	-220	220	152	-6	0	6	140	12	2.95
	(2.1)	B	-206	206	142	-16	0	16	131	12	-2.91
		C	-193	193	133	-11	-1	12	121	12	-2.99
		D	-253	-506	-349	-131	57	74	-335	-14	3.87
Yano-II -D5^0	$\overline{A}\overline{B}CD$	A	-182	182	125	-3	1	3	114	11	-2.90
	(8.4)	B	-197	197	137	-12	-3	15	124	-12	-2.84
		C	-219	219	151	-10	0	10	139	12	2.94
		D	-155	-309	-212	-108	2	107	-199	-13	3.80
	$\overline{A}B\overline{C}D$	A	-221	221	153	-5	0	5	141	12	-2.90
	(4.8)	B	-261	261	181	-19	9	10	168	12	2.91
		C	-243	243	168	-16	4	12	156	12	-2.84
		D	-178	-356	-245	-119	8	112	-231	-14	3.80
	$A\overline{B}\overline{C}D$	A	-219	219	151	-5	0	5	140	12	2.95
	(0.0)	B	-205	205	143	-16	0	16	130	13	-2.92
		C	-190	190	131	-11	-1	12	119	12	-2.99
		D	-188	-375	-259	-117	12	104	-244	-14	3.84

	BS state (ΔE)[b]		a_{iso}* *(site)*	A_{iso}*	A_{iso}	T_1	T_2	T_3	A_{FC}	A_{PC}	$\rho^{\alpha-\beta}$
Yano-III^0	$\overline{A}\overline{B}CD$	A	-130	130	90	-17	-2	19	90	12	-2.89
	(0.3)	B	-170	170	117	-14	-2	-2	117	12	-2.94
		C	-185	185	128	-8	0	8	128	-12	2.92
		D	-194	-387	-267	-115	23	92	-267	-14	3.89
	$\overline{A}B\overline{C}D$	A	-180	180	124	-21	6	15	124	12	-2.80
	(34.0)	B	-224	224	155	-15	-5	20	155	-12	2.75
		C	-207	207	142	-11	3	8	142	12	-2.90
		D	-231	-461	-318	-124	52	72	-318	-14	3.89
	$A\overline{B}\overline{C}D$	A	-193	193	133	-18	-5	22	133	-12	2.86
	(0.0)	B	-198	198	137	-15	1	14	137	12	-2.90
		C	-180	180	124	-8	0	8	124	12	-2.90
		D	-238	-475	-327	-122	48	73	-327	-14	3.88
exp.											
Kulik[c]		1		193		-18	-18	37			
		2		205		-20	-20	40			
		3		245		-10	-10	20			
		4		295		15	15	-30			
Peloquin[d]		1		245		-13	-13	25			
		2		200		-20	-20	40			
		3		297		-14	-14	27			
		4		217		-17	-17	33			
Charlot[e]		1		186		-5	-2	7			
		2		243		-26	5	20			
		3		257		-32	-17	49			
		4		329		-17	-5	22			

[a]B3LYP/II//B3LYP/SVP results. A_{iso}* is the spin-projected isotropic HFC after scaling by the empirical factor of 1.45 (cf. Computational Details), a_{iso}* is the corresponding scaled site value. The T_i represent the traceless part of the HFC tensor, A_{FC} and A_{PC} the isotropic first-order Fermi-contact and second-order pseudo-contact (spin-orbit) contributions to A_{iso}. $\rho^{\alpha-\beta}$ is the Mulliken spin density at the manganese atom. [b]Spin-coupling pattern of BS states and energy relative to the lowest computed BS state for a given model. [c]Simulation results from ref. [6]. [d]Simulation results from ref. [5]. [e]Simulation results from ref. [7].

much smaller effect on its HFC. In all three spin states, that of the three Mn^{IV} centers which has a spin-up configuration, features the largest A_{iso}*. The large value for Mn_B in the $\overline{A}B\overline{C}D$ state has already been noted above: here Mn_B is surrounded by two Mn^{IV} centers with opposite spin alignment. These variations in the HFCs of different spin configurations may have diagnostic value, but this will require more definite spectra simulations than available to date (see below). We note in passing that structural differences between the different BS spin states are small and probably not responsible for the observed differences in the HFCs.

We turn now to a full comparison of the different models (Table 8.4). For **Ferreira^{+1}**, we see that the a_{iso}* site value for the Mn^{III} center Mn_A is unusually small in all three BS states and thus translates into a very small projected A_{iso}*. While the small HFC may be related to the relatively long distance of the dangler atom Mn_A to the cluster core (see above and Table 8.2), it is interesting that addition of one water molecule to Mn_A (**Ferreira-2^{+1}**) changes the situation completely: except for the energetically disfavored BS state $\bar{A}\bar{B}C\bar{D}$, Mn_B, which is now the Mn^{III} center, exhibits a much more realistic HFC near the expected 300 MHz, and the overall HFC pattern agrees reasonably with the simulation results. Obviously, coordination number plays an important role for the HFCs, as has been found also for mono- and dinuclear complexes.[17]

In its lowest-energy computed BS state $A\bar{B}\bar{C}\bar{D}$, model **Dau^{+1}** provides reasonable but not perfect absolute HFCs, with one value near 350 MHz and three in the range of 200 MHz. The other spin states give results for the Mn^{III} site Mn_A closer to 400 MHz. This holds also fhe highest-energy $\bar{A}B\bar{C}D$ state which, however, would predict one Mn^{IV} HFC near 250 MHz, more consistent with the simulations.

Turning to the polarized-EXAFS-based models, we find that the three original models **Yano-I^0, Yano-II^0**, and **Yano-III^0** all have the Mn^{III} HFC (Mn_D) in the range of 380-510 MHz. Unless we accept spin projection factors for the Mn^{III} ion significantly below 2.0,[5] this appears to high (Table 8.4). The Mn^{IV} HFCs are typically in a more reasonable range, sometimes all near 200 MHz, whereas for some spin-coupling patterns a value in the 250 MHz range is present. Overall, **Yano-I^0** tends to have lower HFCs than the two other models. Moving a water molecule in **Yano-II^0** from Ca to the five-coordinate Mn_A (**Yano-II-A6^0**) changes little, whereas a shift of a water ligand from the six-coordinate Mn^{III} center Mn_D to Mn_A (**Yano-II-D5^0**) changes not only the lowest-energy BS state ($A\bar{B}\bar{C}D$ vs. $\bar{A}\bar{B}CD$) but also reduces the Mn_D HFC somewhat. In fact, for two of the BS states ($\bar{A}\bar{B}CD$, $\bar{A}B\bar{C}D$) rather reasonable HFC patterns are now obtained, whereas for the lowest-energy $A\bar{B}\bar{C}D$ state, the Mn^{III} HFC is on the high side and the Mn^{IV} HFCs appear overall too low (Table 8.4). That is, as for the **Ferreira^{+1}** models above, five-coordinate Mn^{III} has a lower HFC than six-coordinate Mn^{III} (as found also for mono- and some dinuclear complexes[17]), except that for **Ferreira^{+1}** this deteriorated agreement with experiment whereas for the **Yano-II^0** model it overall improves agreement. The effect of protonation of the terminal carboxylato ligand on Mn_A exemplified by **Yano-II^{+1}** is essentially negligible (Table 8.4). We may thus conclude that **Yano-II-D5^0** provides

overall the best agreement with the isotropic ^{55}Mn HFCs from the three simulations. The fact that this holds not for the lowest-energy BS state should probably not be overrated in view of the small energy differences.

Table 8.5. ^{55}Mn nuclear quadrupole couplings [MHz] and asymmetry parameters.

		A		*B*		*C*		*D*	
		$\lvert e^2qQ\rvert$	$\lvert\eta\rvert$	$\lvert e^2qQ\rvert$	$\lvert\eta\rvert$	$\lvert e^2qQ\rvert$	$\lvert\eta\rvert$	$\lvert e^2qQ\rvert$	$\lvert\eta\rvert$
Ferreira^{+1}	$AB\bar{C}\bar{D}$	1.5	0.36	1.7	0.59	0.4	0.76	0.6	0.90
	$A\bar{B}C\bar{D}$	1.5	0.44	1.4	0.51	0.5	0.72	0.7	0.61
	$A\bar{B}\bar{C}D$	1.7	0.38	1.7	0.31	0.4	0.95	0.8	0.63
Ferreira2^{+1}	$AB\bar{C}\bar{D}$	2.1	0.31	0.8	0.99	0.3	0.41	1.2	0.39
	$\bar{A}BC\bar{D}$	2.0	0.36	0.9	0.71	0.4	0.67	1.2	0.32
	$\bar{A}B\bar{C}D$	1.9	0.27	1.0	0.99	0.5	0.55	1.0	0.53
Dau^{+1}	$AB\bar{C}\bar{D}$	2.5	0.40	0.8	0.97	0.8	0.48	0.6	0.85
	$A\bar{B}C\bar{D}$	2.7	0.35	0.9	0.76	0.9	0.37	0.6	0.58
	$A\bar{B}\bar{C}D$	2.7	0.36	1.0	0.98	1.0	0.27	0.5	0.66
Yano-I^{0}	$\bar{A}\bar{B}CD$	3.1	0.65	2.1	0.25	3.9	0.61	0.8	0.38
	$\bar{A}B\bar{C}D$	2.9	0.75	2.1	0.42	4.1	0.57	0.8	0.64
	$A\bar{B}\bar{C}D$	2.9	0.73	2.0	0.53	3.9	0.55	0.8	0.68
Yano-II^{0}	$\bar{A}\bar{B}CD$	3.9	0.54	1.7	0.36	1.8	0.79	1.1	0.31
	$\bar{A}B\bar{C}D$	3.6	0.63	1.9	0.80	1.8	0.61	1.3	0.71
	$A\bar{B}\bar{C}D$	3.6	0.64	1.8	0.88	2.1	0.47	1.3	0.87
Yano-II^{+1}	$\bar{A}\bar{B}CD$	3.4	0.43	2.1	0.29	2.3	0.69	1.5	0.38
	$\bar{A}B\bar{C}D$	3.3	0.41	2.3	0.73	2.4	0.47	1.6	0.77
	$A\bar{B}\bar{C}D$	3.2	0.38	2.1	0.68	2.5	0.46	1.6	0.45
Yano-II-A6^{0}	$\bar{A}\bar{B}CD$	1.7	0.75	2.0	0.42	1.8	0.93	0.9	0.36
	$\bar{A}B\bar{C}D$	1.8	0.43	2.2	0.81	1.8	0.75	1.2	0.69
	$A\bar{B}\bar{C}D$	1.7	0.47	2.1	0.85	2.0	0.58	1.2	0.81
Yano-II-D5^{0}	$\bar{A}\bar{B}CD$	1.6	0.66	2.2	0.04	2.1	0.73	0.3	0.45
	$\bar{A}B\bar{C}D$	1.7	0.35	2.3	0.45	2.0	0.61	0.3	0.81
	$A\bar{B}\bar{C}D$	1.7	0.35	2.3	0.42	2.3	0.48	0.4	0.08
Yano-III^{0}	$\bar{A}\bar{B}CD$	3.8	0.61	1.6	0.57	0.6	0.84	1.2	0.90
	$\bar{A}B\bar{C}D$	3.7	0.59	1.3	0.86	0.6	0.90	1.6	0.53
	$A\bar{B}\bar{C}D$	3.8	0.68	1.4	0.47	0.7	0.96	1.4	0.15

In the spectra simulations, the Mn NQC has either been neglected[7,9] or simulated with relatively small values.[5] Table 8.5 summarizes our computed values for the NQC tensor element $P_{zz} = \dfrac{e^2q_{zz}Q/h}{2I(2I-1)}$ of the various models and BS states. Interestingly, the

Mn^{III} sites exhibit values within a narrower range (0.8-1.7 MHz) than the Mn^{IV} sites (0.3-4.1 MHz). The asymmetry depends also strongly on Mn site, model, and spin configuration. Overall, the values are in the range expected from experience for dinuclear $Mn^{III}Mn^{IV}$ complexes[15,16,75] and assumed in the simulations of Peloquin *et al*. for the OEC.[5]

8.4.4 Histidine ^{14}N EPR Parameters

Previous computations on dinuclear $Mn^{III}Mn^{IV}$ systems suggest that B3LYP without any scaling should provide already reasonable ^{14}N HFCs and NQC parameters. The isotropic nitrogen HFC depends both on SOMO spin delocalization into *s*-type valence orbitals on nitrogen and on spin polarization, two effects that may not necessarily go into the same direction for different bonding situations. In all models, the imidazole is bound to Mn_C (cf. Figures 8.1 – 8.3), which is generally computed to be an Mn^{IV} site. A spin projection factor of +/-1 is thus appropriate. Yeagle *et al*. found that, depending on the projection factors, the observed HFC could be assigned to either an Mn^{III} or an Mn^{IV} site, but the latter required somewhat more unusual intrinsic values.[14]

In Table 8.6 we see that the sign of the computed ^{14}N HFC depends on the spin alignment of Mn_C in a given BS state. That is, due to the dominant spin polarization, A_{iso} is positive when the Mn_C spin is down, negative when it is up. No sign information is available from experiment. The available ESEEM experiments have been simulated by axially symmetrical HFC tensors.[13,14] Yet the anisotropy is so small that it will be difficult to reproduce accurately. We will thus concentrate on A_{iso} and the NQC parameters.

All computed isotropic HFCs (Table 8.6) are too small in absolute value compared to experiment. Not only their sign but also their magnitude features a sizeable dependence on the BS state chosen for analysis (Table 8.6). In previous calculations on dinuclear $Mn^{III}Mn^{IV}$ complexes, somewhat better agreement with experiment for nitrogen nuclei bonded to manganese was found at the same computational level.[17] Yet we cannot exclude that errors in the optimized Mn-N distances affect the HFCs, as the spin polarization is expected to depend on this distance. Distances between a transition metal to a formally neutral ligand like histidiene or imidazole tend to be overestimated by standard DFT calculations. Except for model **Yano-II^{+1}**, this is the case here as well

(Table 8.1 and Tables B1-B8 in Appendix B), with errors up to 0.07-0.10 Å for some models (in particular **Ferreira**$^{+1}$, **Ferreira-1**$^{+1}$, **Dau**$^{+1}$, **Yano-II**^{0}). No overall correlation of the HFCs with these errors is apparent. But within the EXAFS-based **Yano** models, indeed the shortest distances (**Yano-II**$^{+1}$, Table B7) correspond to the largest HFCs, and the longest distances (**Yano-III**^{0}, Table B8) to the lowest HFCs (Table 8.6).

Table 8.6. Comparison of computed ^{14}N HFC and NQC tensors with ESEEM data (in MHz).[a]

	BS state	A_{iso}	T_1	T_2	T_3	P_{zz}	$\|\eta\|$	$\rho^{\alpha-\beta}$
Ferreira^{+1}	$AB\overline{C}\overline{D}$	3.9	-0.2	0.1	0.2	1.98	0.82	0.04
	$A\overline{B}C\overline{D}$	-3.2	-0.4	0.0	0.5	1.97	0.83	-0.04
	$A\overline{B}\overline{C}D$	3.0	-0.5	0.1	0.4	1.98	0.82	0.04
Ferreira2^{+1}	$AB\overline{C}\overline{D}$	4.4	-0.1	0.0	0.1	1.97	0.82	0.05
	$\overline{A}BC\overline{D}$	-4.5	-0.3	0.0	0.3	1.94	0.84	-0.05
	$\overline{A}B\overline{C}D$	2.5	-0.6	0.1	0.5	2.04	0.77	0.03
Dau^{+1}	$AB\overline{C}\overline{D}$	2.0	-0.8	0.2	0.6	-2.27	0.66	0.03
	$A\overline{B}C\overline{D}$	-2.8	-0.4	-0.1	0.5	-2.27	0.66	-0.04
	$A\overline{B}\overline{C}D$	2.6	-0.6	0.1	0.4	-2.26	0.67	0.03
Yano-I^{0}	$\overline{A}\overline{B}CD$	-3.5	-0.3	-0.2	0.5	2.43	0.53	-0.04
	$\overline{A}B\overline{C}D$	3.0	-0.4	0.2	0.2	2.44	0.53	0.04
	$A\overline{B}\overline{C}D$	3.1	-0.6	0.2	0.3	2.44	0.53	0.04
Yano-II^{0}	$\overline{A}\overline{B}CD$	-4.9	-0.2	-0.1	0.4	1.93	0.99	-0.05
	$\overline{A}B\overline{C}D$	3.7	-0.3	0.1	0.2	1.97	0.95	0.04
	$A\overline{B}\overline{C}D$	4.3	-0.4	0.1	0.2	1.93	0.98	0.05
Yano-II^{+1}	$\overline{A}\overline{B}CD$	-5.6	-0.2	-0.1	0.3	1.82	0.65	-0.05
	$\overline{A}B\overline{C}D$	4.1	-0.2	0.1	0.1	1.84	0.70	0.04
	$A\overline{B}\overline{C}D$	5.4	-0.2	0.0	0.2	1.83	0.65	0.05
Yano-II-A6^{0}	$\overline{A}\overline{B}CD$	-4.9	-0.2	-0.1	0.4	1.96	0.95	-0.05
	$\overline{A}B\overline{C}D$	3.8	-0.2	0.1	0.2	1.98	0.93	0.04
	$A\overline{B}\overline{C}D$	4.3	-0.4	0.1	0.2	1.96	0.95	0.05
Yano-II-D5^{0}	$\overline{A}\overline{B}CD$	-4.8	-0.2	-0.2	0.4	1.90	0.99	-0.05
	$\overline{A}B\overline{C}D$	3.3	-0.3	0.1	0.1	1.97	0.93	0.04
	$A\overline{B}\overline{C}D$	4.2	-0.4	0.1	0.2	1.91	0.99	0.05
Yano-III^{0}	$\overline{A}\overline{B}CD$	-2.2	-0.4	-0.3	0.7	-2.65	0.45	-0.03
	$\overline{A}B\overline{C}D$	2.0	-0.5	0.2	0.3	-2.65	0.43	0.03
	$A\overline{B}\overline{C}D$	2.2	-0.7	0.3	0.4	-2.65	0.44	0.03
exp.[b]		7.4	-0.6	-0.6	1. 2	2.3	0.8	
exp.[c]		7.3	-0.5	-0.5	1.0	1.98	0.84	

[a]B3LYP/II//B3LYP/SVP results. See also footnote a in Table 8.4. [b]ESEEM data.[13] [c]ESEEM data.[14]

The nuclear quadrupole coupling constant e^2qQ/h does not offer any discrimination between the models: it is reproduced well essentially by all of them, and it is in a similar range as found for superoxidized dimanganese catalase[75] or for other imidazole imino nitrogen atoms coordinated to metal centers.[76] The asymmetry parameter $|\eta|$ appears to be more sensitive. The experimental value of ca. 0.8 is larger than for dimanganese catalase[75] or other metal-coordinated imidazole ligands.[76] Much too small values are computed for all BS states of models **Yano-I^0** and **Yano-III^0**. Relatively low asymmetry parameters are also obtained for models **Dau^{+1}** and **Yano-II^{+1}**, very large ones for **Yano-II^0** and its derivatives. The differences between the neutral **Yano-II^0** and cationic **Yano-II^{+1}** models for the asymmetry parameter are striking, whereas the shifting of water molecules in **Yano-II^0** (**Yano-II-A6^0** and **Yano-II-D5^0**) has very little effect.

8.5 Conclusions

To be able to relate suggested molecular and electronic structures of the oxygen-evolving Mn_4Ca cluster (OEC) of photosystem II to the large amount of available data from magnetic resonance spectroscopy, the EPR/ENDOR/ESEEM parameters of the S_2 state of the OEC have been calculated for the first time by quantum chemical methods. The prerequisite for this study has been our ability to converge reproducibly the broken-symmetry DFT Kohn-Sham wavefunctions for all low-lying antiferromagnetically coupled S = 1/2 states of the $Mn^{III}(Mn^{IV})_3$ spin system of a wide variety of molecular model structures. Using spin- projection techniques, this allowed the ^{55}Mn hyperfine and nuclear quadrupole coupling tensors, as well as the histidine ^{14}N ESEEM parameters to be evaluated for all models investigated.

Five different model systems based on structural information from X-ray diffraction and polarized EXAFS, and a variety of modifications with altered coordination environment of the Mn and Ca centers, have been studied in detail. The spin-projected ^{55}Mn isotropic hyperfine couplings for the four manganese centers depend characteristically on the structure and spin configuration of the model systems and may therefore be viewed as important diagnostics. So far, a number of models based mainly on the X-ray crystal structures of the Berlin and London groups have been shown to be less likely by their inferior agreement with simulations of ^{55}Mn EPR and ENDOR data. Among the models based predominantly on polarized EXAFS data, one model gave the

best agreement with experiment, provided that the center Mn_D remained only five-coordinate (structure **Yano-II-D5^0**).

So far, the histidine ^{14}N hyperfine and nuclear quadrupole couplings provided less conclusive information. Computed isotropic ^{14}N hyperfine couplings underestimate the experimental values somewhat, most likely in part due to an overestimate of the Mn-N distances in the DFT-optimized structures. The nuclear quadrupole coupling asymmetry parameter appears to be a sensitive measure of the coordination environment of Mn_C and deserves further attention in future work.

The broken-symmetry DFT and spin-projection techniques used here should prove useful for the evaluation of molecular and electronic structure also of the other S states of the Kok cycle of the OEC. Extensions to the S_0 and S_1 states are underway, and applications to further models and different protonations states, as well as to complexes of the OEC with different ligands (ammonia, methanol, azide) may be envisioned. Any model consistent with the structural constraints available from EXAFS or X-ray diffraction may now be evaluated for its agreement between computed and experimental magnetic-resonance data. The main challenges remaining are a) a consistent spin-projection treatment of the spin densities and magnetic-resonance parameters also for bridging ligands, and b) refined spin projections that take into account the influence of zero-field splitting and give access to a more meaningful discussion of the hyperfine anisotropies as well. Once more structural information becomes available, a better modelling of the protein environment will be included by QM/MM methods. Together with improved spectra simulations, quantum chemical methods like those used in this work are expected to shed new light also into the mechanistic details of the intriguing catalytic water oxidation in photosystem II.

Chapter 9

"I could have done it in a much more complicated way" said the Red Queen, immensely proud.

Lewis Carroll

Summary

Photosynthesis is the most fundamental process of life on earth. The biological production of oxygen in plant photosynthesis occurs in photosystem II (PSII). Here two water molecules are coupled in a four-electron oxidation to one O_2 molecule, catalyzed by a tetranuclear manganese complex, known as the oxygen-evolving complex (OEC). In this thesis, density-functional theory (DFT) methods were validated and subsequently employed to study structures, spin-density distributions and EPR parameters of mono-, di-, and tetranuclear complexes with regard to the OEC. The goal was to draw conclusions on the molecular and electronic structure of the OEC.

After a general introduction (Chapter 1), the biological context is summarized in Chapter 2. The methods employed in this thesis are introduced in Chapter 3 (density functional theory) and in Chapter 4 (experimental techniques and calculation of electron paramagnetic resonance parameters).

To acquire experience in the application of modern DFT methods to calculate EPR parameters, validation studies were carried out on mononuclear manganese complexes

(Chapter 5 and 6). Initial work was performed on simple inorganic manganese complexes (Chapter 5), giving special attention to the EPR parameters (g-tensor, ^{1}H, ^{17}O and ^{55}Mn hyperfine coupling constants) of the experimentally well-investigated $[Mn(H_2O)_6]^{2+}$ and $[Mn(H_2O)_6]^{3+}$ complexes. The most suited DFT methods were applied to a series of suitable inorganic mononuclear manganese complexes which should serve as benchmark data for subsequent investigations. Chapter 6 provided method validation for the structurally and spectroscopically (EPR/ENDOR) well-characterized mononuclear manganese site of the saccharide-binding protein concanavalin A to evaluate a) the performance of different DFT exchange-correlation potentials for the calculation of spin-density distributions and metal/ligand hyperfine parameters in biological manganese sites, and b) the validity of the point-dipole approximation in estimating proton positions of coordinated protein residues and water molecules from ENDOR data. The results for simple inorganic complexes and the manganese site in concanavalin A show the same behavior. Isotropic hyperfine couplings on both the metal and the ligand protons are best reproduced when the hybrid functional exhibits about 50% or more exact-exchange admixture. Notably, spin contamination is no problem with larger exact-exchange admixture but even diminishes due to decreased metal-ligand covalency. Spin-orbit contributions to the metal hyperfine tensor have been found to be small for Mn(II) complexes, consistent with the high-spin d^5 electronic characteristics. Anisotropic HFCs are relatively insensitive to the exact-exchange admixture, demonstrating that for ligand atoms they are dominated by the large metal-centered spin density. In the case of concanavalin A, this helps to justify the use of the point-dipole approximation to estimate hydrogen-atom positions from dipolar ^{1}H HFCs determined in ENDOR spectra. The ^{17}O HFCs for the oxygen atoms directly bonded to the manganese center in concanavalin A were predicted based on the investigations in the divalent hexaaqua complex.

In Chapter 7, the EPR parameters of a series of dinuclear manganese(III,IV) complexes with mono(μ-oxo), bis(μ-oxo), (μ-oxo)(μ-carboxylato), bis(μ-oxo)(μ-carboxylato), and (μ-oxo)bis(μ-carboxylato) bridges have been studied by broken-symmetry density functional methods. A main focus has been the influence of the exchange-correlation functional on the computed spin-density distributions and spectroscopic parameters (g-tensors, ^{55}Mn, ^{14}N, and ^{1}H hyperfine coupling tensors, and Heisenberg exchange couplings). The nature of the broken-symmetry state and the origin of its spin contamination have been analyzed by an expansion into restricted determinants, based on paired orbitals. It turned out that the S^2 expectation values near

3.75 obtained at B3LYP level are well in line with the expected seven active orbitals, which include the truly unpaired "SOMO" and three pairs of corresponding magnetic orbitals. Spin-projected g-tensors are generally almost isotropic and exhibit only relatively small deviations from the free-electron value. While the g-tensors are reproduced well by the standard B3LYP functional, their diagnostic value remains low at this point. ^{14}N and ^{1}H hyperfine couplings, ^{55}Mn hyperfine anisotropies, and exchange couplings are well described by hybrid functionals with moderate exact-exchange admixture like B3LYP. The isotropic ^{55}Mn hyperfine couplings require larger exact-exchange admixtures. The error obtained by standard functionals is systematic and it may be remedied to a good approximation by an empirical scaling factor (about 1.45 at B3LYP level). Spin-orbit contributions to the metal hyperfine tensor in these mixed-valence Mn(III)Mn(IV) complexes are not negligible. Standard hybrid functionals like B3LYP with about 20% exact exchange may thus be used with predictive power also for more complicated systems like the oxygen-evolving complex of photosystem II. The influence of terminal and bridging ligands on structure, spin-density distributions, and EPR parameters have been evaluated systematically. Computed hyperfine and g-tensors are not covariant to each other. This information is of importance for spectra simulations and will possibly affect simulation results for the OEC also.

The ultimate goals of this thesis were applications of the validated DFT methods to the tetranuclear manganese cluster of the OEC of PSII to calculate its EPR parameters for the first time. Structure, spin-density distribution, and EPR parameters of some of the most likely suggested Mn_4Ca model clusters for the S_2 state of the OEC have been provided in Chapter 8. For five different models based on X-ray diffraction and polarized-EXAFS studies, and for a variety of modifications derived from these models, ^{55}Mn and ^{14}N hyperfine couplings as well as ^{55}Mn and ^{14}N nuclear quadrupole coupling tensors have been evaluated. This was done explicitly for different spin-coupling patterns of the S = 1/2 ground states, and partly for different distributions of oxidations states of the Mn centers. The calculations confirm a Mn_4(III,IV,IV,IV) situation for all model systems. However, the distribution of these oxidation states depends on the molecular model, in particular on Mn coordination numbers. BS states are in almost all cases below the HS state but exhibit mostly small energy differences between each other, indicating a facile interconversion between the different BS spin configurations. Applying spin-projection techniques and the above mentioned semi-empirical scaling of the Mn hyperfine couplings, computation of the hyperfine and nuclear quadrupole coupling

parameters allowed the direct evaluation of the proposed models against data obtained from the simulation of EPR, ENDOR, and ESEEM spectra. The d^4 Mn(III) ion shows large anisotropy, whereas the Mn(IV) ions have almost isotropic ^{55}Mn HFCs. However, the anisotropic part might suffer more from neglecting the zero-field effects than the isotropic part. The spin configuration influences enormously the hyperfine coupling. If the neighboring manganese atom exhibits an opposite spin alignment, the HFC increases. Furthermore, the coordination number can have a large effect on the HFCs. A higher coordination number and stronger coordination of the ligand increase the isotropic HFC. The spin-projected isotropic ^{14}N HFCs are in all model systems too small compared to the experimental value probably due to an overestimation of the Mn-N_{Im} bond or to the simplified spin-projection scheme. The ^{14}N NQC agree quite well with experimental data for almost all model systems. However, the asymmetry parameter shows differences. Therefore, drawing conclusions from ^{14}N data remains difficult at this point, and the ^{55}Mn hyperfine data appear more diagnostic. The computational evidence disfavors some of the models derived primarily from X-ray diffraction. Among those based on spin-polarized EXAFS data, only a variant with five-fold coordination of Mn_D appears to reproduce the experimental ^{55}Mn hyperfine data well.

In this thesis we have shown that modern density functional methods allow the quantitative prediction of EPR parameters for multinuclear transition metal complexes and for manganese sites in complex biological environments. This opens a wide area of application, in particular regarding the structure elucidation of the tetranuclear manganese complex of photosystem II in its different S states along the Kok cycle. Further work into this direction should improve our knowledge of this fundamental biochemical process.

Zusammenfassung

Im Wasser-oxidierenden Cluster („oxygen-evolving complex“, OEC) des Photosystem II findet sich die primäre Quelle der Sauerstoffproduktion der Erde. Der OEC katalysiert in grünen Pflanzen unter Absorption von Sonnenlicht die Vierelektronen-Oxidation von Wasser zu Sauerstoff in einer zyklischen Sequenz von Oxidationszuständen (Kok-Zyklus). In dieser Arbeit wurden Strukturen, Spindichteverteilungen sowie EPR-Parameter ein-, zwei- und vierkerniger Mangankomplexe, die in Bezug auf den OEC modelliert wurden, mit Hilfe der Dichtefunktionaltheorie (DFT) berechnet. Hauptziel war das Verständnis der molekularen und elektronischen Struktur des vierkernigen Manganclusters des OEC durch direkten Vergleich mit experimentellen EPR-Daten.

Nach einer allgemeinen Einführung (Kapitel 1), wurde der biologische Kontext in Kapitel 2 eingeführt. In den folgenden Kapiteln 3 und 4 wurden die methodischen Hintergründe der EPR-Spektroskopie, der DFT sowie der quantenchemischen Berechnung von EPR-Parametern erörtert.

Kapitel 5 gab einen Einblick in die Validierungen verschiedener DFT-Methoden für die Berechnung der Spindichteverteilungen und EPR-Parameter (insbesondere g-Tensoren und ^{55}Mn, ^{1}H, ^{17}O und ^{14}N Hyperfeintensoren) an geeigneten einkernigen Mangankomplexen. Hierbei standen insbesondere $[Mn(H_2O)_6]^{2+}$ sowie $[Mn(H_2O)_6]^{3+}$ im Vordergrund, welche EPR-spektroskopisch gut charakterisiert sind. In Kapitel 6 wurden unsere Methoden an der Mn-Bindungsstelle des Saccharid-bindenden Proteins Concanavalin A validiert. Die Herausforderung der Berechnungen liegt allgemein in einer korrekten Beschreibung der Spindichte-Verteilung zwischen dem Manganzentrum und den Liganden. Ein Vergleich der berechneten EPR-Parameter mit Hochfeld-EPR-, ENDOR sowie ESEEM-Daten zeigt, dass ein erheblicher Anteil an exaktem Austausch von mindestens 50% notwendig ist, um die isotrope ^{55}Mn Hyperfeinkopplungskonstante korrekt zu reproduzieren, welche aufgrund der schwierig zu beschreibenden Spinpolarisation der Rumpfschalen (2s/3s) negativ ist. Der anisotrope Anteil der ^{55}Mn HFC ist nahezu unabhängig vom Funktional und wird sehr gut wiedergegeben. Für Concanavalin A wurde die Eignung der Punkt-Dipol-Näherung zur Berechnung der Metall-Ligand-Abstände aus gemessenen dipolaren Kopplungen überprüft.

Nachfolgend (Kapitel 7) wurden Berechnungen der EPR-Parameter sowie der Heisenberg-Austauschkopplungskonstanten *J* einer Vielzahl zweikerniger gemischtvalenter Mn(III)Mn(IV)-Komplexe durchgeführt, um die Eignung verschiedener Verfahren zu prüfen. Um reale antiferromagnetisch gekoppelte Zustände mehrkerniger Mangankomplexe mit tiefligenden angeregten Zuständen zu beschreiben, wären Multideterminanten-Ansätze erforderlich. Aufgrund ihres großen Rechenaufwandes bedient man sich stattdessen der Broken-Symmetry DFT (BS-DFT) Methoden, die einen Eindeterminanten-Ansatz verfolgt. Spinprojizierte EPR-Parameter (g-Tensor sowie ^{55}Mn und ^{1}H) sowie *J* wurden systematisch mit experimentellen Daten verglichen. Der g-Tensor, welcher sehr gut durch Berechnungen mit dem B3LYP Funktional wiedergegeben werden kann, ist hierbei in allen untersuchten Komplexen fast isotrop und weicht nur wenig vom g-Wert des freien Elektrons ab. Analog zur Berechnung von EPR-Parametern für einkernige Komplexe wird ein hoher Anteil an exaktem Austausch im Hybridfunktional benötigt, um die ^{55}Mn-Hyperfeinkopplungskonstante zu berechnen. Der systematische Fehler der B3LYP-Ergebnisse zur isotropen ^{55}Mn HFC kann jedoch durch einen zusätzlichen Skalierungsfaktor von 1.45 korrigiert werden. Stickstoff HFCs und *J* können nach Spinprojektion bereits gut mit dem B3LYP-Funktional berechnet werden. Schon kleine Variationen des verbrückenden Liganden führen zu signifikanten Änderungen der ^{55}Mn HFC sowie von *J*. Hingegen üben die terminalen Liganden nur einen geringen Einfluss aus.

Schließlich konnte mit Berechnungen an realistischen vierkernigen Modellsystemen für den OEC begonnen werden (Kapitel 8). Hierbei stand der S_2-Zustand des Kok-Zyklus, welcher im Spinzustand S = 1/2 („multiline signal“ in der EPR) vorliegt, im Vordergrund. Fünf vierkernige Komplexe wurden basierend auf Kristallstrukturanalyse- sowie polarisierten EXAFS-Daten modelliert. Für verschiedene Spinkopplungsmuster des S=1/2-Zustandes wurden nach Spinprojektion die ^{55}Mn und ^{14}N-Hyperfeinkopplungskonstanten sowie die ^{14}N Kernquadrupolkopplungskonstanten ermittelt. Spindichteanalysen bestätigten, dass im S_2-Zustand des Kok-Zyklus eine Oxidationsstufenverteilung von Mn_4(III,IV,IV,IV) vorliegt. Die Spindichteverteilung ihrerseits ist dennoch von Modell zu Modell unterschiedlich und insbesondere von der Koordinationszahl abhängig. Die HS Strukturen sind energetisch weniger stabil als die BS Strukturen, die ihrerseits meist sehr geringe Energiedifferenzen aufweisen. Somit ist eine „Umschaltung“ zwischen verschiedenen BS-Zuständen leicht möglich. Die spinprojizierten ^{55}Mn und ^{14}N HFC wurden mit EPR-, ENDOR- und ESEEM-Daten

verglichen, um die Modellsysteme zu evaluieren. Die d^4 Mn(III) HFC weist stets eine große Anisotropie auf, wohingegen das Mn(IV) Ion eine nahezu isotrope ^{55}Mn HFCs besitzt. Jedoch kann die Vernachlässigung der Nullfeldaufspaltungseffekte in der Spinprojektion einen größeren Einfluss auf den anisotropen Teil als auf den isotropen Teil besitzen, weshalb die anisotropen Daten mit Vorsicht zu behandeln sind. Sowohl die Spinkonfiguration als auch die Koordinationszahl üben einen großen Einfluss auf die ^{55}Mn HFC aus. Die isotrope HFC wird größer, wenn der Spin des benachbarten Manganatoms entgegengesetzt gerichtet ist und wenn die Koordinationszahl und die Stärke der Koordination steigt. Die spinprojizierten isotropen ^{14}N HFCs sind für alle Modellsysteme zu klein. Dies kann sowohl an der Überschätzung der Mn-N_{Im} Bindungslänge liegen oder am vereinfachten Spinprojektionsschema. Hingegen weisen die ^{14}N NQC als auch der Asymmetrieparameter für alle außer einem Modellsystem eine gute Übereinstimmung mit den experimentellen Daten auf. Somit gestalten sich Rückschlüsse von den ^{14}N-Daten auf die Struktur eher schwierig. Zur Evaluierung der Modellsysteme sind demnach insbesondere die ^{55}Mn-Daten von zentraler Bedeutung. Es konnte gezeigt werden, dass diejenigen Modelle, die auf Kristallstrukturanalyse-Daten basieren, eine geringere Übereinstimmung von berechneten und experimentell ermittelten Daten aufweisen. Für die diskutierten Modellsysteme basierend auf polarisierten EXAFS-Daten konnten bei Fünffachkoordination von Mn_D die spektroskopisch ermittelten EPR-Daten reproduziert werden. Damit konnte demonstriert werden, dass die Berechnung von EPR-Parametern für realistische Modelle möglich ist und diagnostischen Wert zur Einschätzung der Tauglichkeit verschiedener Vorschläge zu molekularer und elektronischer Struktur des OEC besitzt.

Es wurde in dieser Arbeit gezeigt, dass moderne Dichtefunktionalmethoden zur Berechnung von EPR Parametern für mehrkernige Übergangsmetallcluster sowie für Manganzentren in komplexer biologischer Umgebung erfolgreich eingesetzt werden können. Dies eröffnet ein weites Gebiet der Anwendung, insbesondere in Zusammenhang mit einer detaillierten Strukturaufklärung des vierkernigen Manganclusters im Photosystem II in seinen verschiedenen S-Zuständen des Kok-Zyklus. Weitere Arbeiten in dieser Richtung sollten zu einem besseren Verständnis dieses fundamentalen biochemischen Prozesses führen.

References

Chapter 1

[1] N. S. Lewis, D. G. Nocera, *Proc. Natl. Acad. Sci.* **2006**, *103*, 15729.
[2] B. Kok, B. Forbush, M. McGloin, *Photochem. Photobiol.* **1970**, *11*, 457. ´
[3] W. Junge, M. Haumann, R. Ahlbrink, A. Mulkidjanian, J. Clausen, *Phil. Trans. Roy. Soc. London B* **2002**, *357*, 1407.
[4] J. Lavergne, W. Junge, *Photosynth. Res.* **1993**, *38*, 279.
[5] E. Schlodder, H. T. Witt, *J. Biol. Chem.* **1999**, *274*, 30387.
[6] H. Dau, M. Haumann, *Coord. Chem. Rev.* **2008**, *252*, 273.
[7] M. Haumann, P. Liebisch, C. Mueller, M. Barra, M. Grabolle, H. Dau, *Science* **2005**, *310*, 1019.
[8] H. Dau, M. Haumann, *Photosynth. Res.* **2007**, *92*, 327.
[9] B. Loll, J. Kern, W. Saenger, A. Zouni, J. Biesiadka, *Nature* **2005**, *438*, 1040.
[10] A. Zouni, H. T. Witt, J. Kern, P. Fromme, N. Krauss, W. Saenger, P. Orth, *Nature* **2001**, *409*, 739.
[11] K. N. Ferreira, T. M. Iverson, K. Maghlaoui, J. Barber, S. Iwata, *Science* **2004**, *303*, 1831.
[12] N. Kamiya, J.-R. Shen, *Proc. Natl. Acad. Sci. U. S. A.* **2003**, *100*, 98.
[13] J. Barber, *Inorg. Chem.* **2008**, *47*, 1700.
[14] J. Yano, V. K. Yachandra, *Inorg. Chem.* **2008**, *47*, 1711.
[15] T. Noguchi, *Coord. Chem. Rev.* **2008**, *252*, 336.
[16] Y. Taguchi, T. Noguchi, *Biochim. Biophy. Acta* **2007**, *1767*, 535.
[17] J. P. Decker, *Manganese Redox Enzymes*, Ed: Pecoraro, **1992**.
[18] R. D. Britt, K. A. Campbell, J. M. Peloquin, M. L. Gilchrist, C. P. Aznar, M. M. Dicus, J. Robblee, J. Messinger, *Biochim. Biophy. Acta* **2004**, *1655*, 158.
[19] A. Haddy, *Photosynth. Res.* **2007**, *92*, 357.
[20] G. C. Dismukes, Y. Siderer, *FEBS Lett.* **1980**, *121*, 78.
[21] G. C. Dismukes, Y. Siderer, *Proc. Natl. Acad. Sci.* **1981**, *78*, 274.
[22] J. L. Casey, K. Sauer, *Biochim. Biophy. Acta* **1984**, *767*, 21.
[23] J. L. Zimmermann, A. W. Rutherford, *Biochim. Biophy. Acta* **1984**, *767*, 160.
[24] J. M. Peloquin, K. A. Campbell, D. W. Randall, M. A. Evanchik, V. L. Pecoraro, W. H. Armstrong, R. D. Britt, *J. Am. Chem. Soc.* **2000**, *122*, 10926.
[25] L. V. Kulik, B. Epel, W. Lubitz, J. Messinger, *J. Am. Chem. Soc.* **2005**, *127*, 2392.
[26] D. W. Randall, B. E. Sturgeon, J. A. Ball, G. A. Lorigan, M. K. Chan, M. P. Klein, W. H. Armstrong, R. D. Britt, *J. Am. Chem. Soc.* **1995**, *117*, 11780.
[27] D. W. Randall, M. K. Chan, W. H. Armstrong, R. D. Britt, *Mol. Phys.* **1998**, *95*, 1283.
[28] G. J. Yeagle, M. L. Gilchrist, Jr., L. M. Walker, R. J. Debus, R. D. Britt, *Phil. Trans. Roy. Soc. B* **2008**, *363*, 1157.
[29] G. J. Yeagle, M. L. Gilchrist, R. M. McCarrick, R. D. Britt, *Inorg. Chem.* **2008**, *47*, 1803.
[30] P. E. M. Siegbahn, *Phil. Trans. Roy. Soc. B* **2008**, *363*, 1221.
[31] P. E. M. Siegbahn, *Chem. Eur. J.* **2008**, *14*, 8290.
[32] E. M. Sproviero, J. A. Gascon, J. P. McEvoy, G. W. Brudvig, V. S. Batista, *J. Am. Chem. Soc.* **2008**, *130*, 6728.
[33] E. M. Sproviero, J. A. Gascon, J. P. McEvoy, G. W. Brudvig, V. S. Batista, *Coord. Chem. Rev.* **2008**, *252*, 395.
[34] P. E. M. Siegbahn, *Inorg. Chem.* **2008**, *47*, 1779.
[35] P. E. M. Siegbahn, *Chem. Eur. J.* **2006**, *12*, 9217.
[36] P. E. M. Siegbahn, M. Lundberg, *Photochem. Photobiol. Sci.* **2005**, *4*, 1035.
[37] L. Noodleman, *Coord. Chem. Rev.* **1995**, *144*, 199.
[38] L. Noodleman, *J. Chem. Phys.* **1981**, *74*, 5737.
[39] G. Blondin, J. J. Girerd, *Chem. Rev.* **1990**, *90*, 1359.
[40] A. Bencini, D. Gatteschi, *EPR of Exchange Coupled Systems*, Springer, **1990**.
[41] S. Schinzel, R. Müller, M. Kaupp, *Theor. Chem. Acc.* **2008**, *120*, 437.

Chapter 2

[1] L. V. Kulik, B. Epel, W. Lubitz, J. Messinger, *J. Am. Chem. Soc.* **2005**, *127*, 2392.
[2] J. M. Peloquin, K. A. Campbell, D. W. Randall, M. A. Evanchik, V. L. Pecoraro, W. H. Armstrong, R. D. Britt, *J. Am. Chem. Soc.* **2000**, *122*, 10926.
[3] J. P. McEvoy, G. W. Brudvig, *Chem. Rev.* **2006**, *106*, 4455.
[4] S. Mukhopadhyay, S. K. Mandal, S. Bhaduri, W. H. Armstrong, *Chem. Rev.* **2004**, *104*, 3981.
[5] R. E. Blankenship, *Molecular Mechanisms of Photosynthesis*, Blackwell Publishers, **2002**.
[6] J. Barber, *Inorg. Chem.* **2008**, *47*, 1700.
[7] W. Kaim, B. Schwederski, *Bioanorganische Chemie*, Teubner, **2004**.
[8] N. S. Lewis, D. G. Nocera, *Proc. Natl. Acad. Sci.* **2006**, *103*, 15729.
[9] B. Kok, B. Forbush, M. McGloin, *Photochem. Photobiol.* **1970**, *11*, 457.
[10] W. Junge, M. Haumann, R. Ahlbrink, A. Mulkidjanian, J. Clausen, *Phil. Trans. Roy. Soc. B* **2002**, *357*, 1407.
[11] J. Lavergne, W. Junge, *Photosynth. Res.* **1993**, *38*, 279.
[12] E. Schlodder, H. T. Witt, *J. Biol. Chem.* **1999**, *274*, 30387.
[13] H. Dau, M. Haumann, *Coord. Chem. Rev.* **2008**, *252*, 273.
[14] M. Haumann, P. Liebisch, C. Mueller, M. Barra, M. Grabolle, H. Dau, *Science* **2005**, *310*, 1019.
[15] H. Dau, M. Haumann, *Photosynth. Res.* **2007**, *92*, 327.
[16] B. Loll, J. Kern, W. Saenger, A. Zouni, J. Biesiadka, *Nature* **2005**, *438*, 1040.
[17] A. Zouni, H. T. Witt, J. Kern, P. Fromme, N. Krauss, W. Saenger, P. Orth, *Nature* **2001**, *409*, 739.
[18] K. N. Ferreira, T. M. Iverson, K. Maghlaoui, J. Barber, S. Iwata, *Science* **2004**, *303*, 1831.
[19] N. Kamiya, J.-R. Shen, *Proc. Natl. Acad. Sci.* **2003**, *100*, 98.
[20] J. Yano, V. K. Yachandra, *Inorg. Chem.* **2008**, *47*, 1711.
[21] T. Noguchi, *Coord. Chem. Rev.* **2008**, *252*, 336.
[22] Y. Taguchi, T. Noguchi, *Biochim. Biophys. Acta* **2007**, *1767*, 535.
[23] J. P. Decker, *Manganese Redox Enzymes*, Ed: Pecoraio, **1992**.
[24] R. D. Britt, K. A. Campbell, J. M. Peloquin, M. L. Gilchrist, C. P. Aznar, M. M. Dicus, J. Robblee, J. Messinger, *Biochim. Biophys. Acta* **2004**, *1655*, 158.
[25] A. Haddy, *Photosynth. Res.* **2007**, *92*, 357.
[26] J. Yano, J. Kern, K.-D. Irrgang, M. J. Latimer, U. Bergmann, P. Glatzel, Y. Pushkar, J. Biesiadka, B. Loll, K. Sauer, J. Messinger, A. Zouni, V. K. Yachandra, *Proc. Natl. Acad. Sci.* **2005**, *102*, 12047.
[27] M. Haumann, M. Grabolle, T. Neisius, H. Dau, *FEBS Letters* **2002**, *512*, 116.
[28] V. K. Yachandra, *Philos. Trans. R. Soc. London B* **2002**, *357*, 1347.
[29] J. Yano, J. Kern, K. Sauer, M. J. Latimer, Y. Pushkar, J. Biesiadka, B. Loll, W. Saenger, J. Messinger, A. Zouni, V. K. Yachandra, *Science* **2006**, *314*, 821.
[30] J. Yano, Y. Pushkar, J. Messinger, U. Bergmann, P. Glatzel, V. K. Yachandra, *AIP Conf. Proc.* **2007**, *882*, 316.
[31] T. A. Roelofs, W. Liang, M. J. Latimer, R. M. Cinco, A. Rompel, J. C. Andrews, K. Sauer, V. K. Yachandra, M. P. Klein, *Proc. Natl. Acad. Sci.* **1996**, *93*, 3335.
[32] J. H. Robblee, J. Messinger, R. M. Cinco, K. L. McFarlane, C. Fernandez, S. A. Pizarro, K. Sauer, V. K. Yachandra, *J. Am. Chem. Soc.* **2002**, *124*, 7459.
[33] M. Haumann, C. Mueller, P. Liebisch, L. Iuzzolino, J. Dittmer, M. Grabolle, T. Neisius, W. Meyer-Klaucke, H. Dau, *Biochemistry* **2005**, *44*, 1894.
[34] V. K. Yachandra, K. Sauer, M. P. Klein, *Chem. Rev.* **1996**, *96*, 2927.
[35] H. Dau, L. Iuzzolino, J. Dittmer, *Biochim. Biophys. Acta* **2001**, *1503*, 24.
[36] J. Yano, Y. Pushkar, P. Glatzel, A. Lewis, K. Sauer, J. Messinger, U. Bergmann, V. Yachandra, *J. Am. Chem. Soc.* **2005**, *127*, 14974.
[37] K. Hasegawa, T.-a. Ono, Y. Inoue, M. Kusunoki, *Bull. Chem. Soc. Jap.* **1999**, *72*, 1013.
[38] V. K. Yachandra, R. D. Guiles, A. E. McDermott, J. L. Cole, R. D. Britt, S. L. Dexheimer, K. Sauer, M. P. Klein, *Biochemistry* **1987**, *26*, 5974.
[39] W. Liang, T. A. Roelofs, R. M. Cinco, A. Rompel, M. J. Latimer, W. O. Yu, K. Sauer, M. P. Klein, V. K. Yachandra, *J. Am. Chem. Soc.* **2000**, *122*, 3399.
[40] T. Kuntzleman, C. F. Yocum, *Biochemistry* **2005**, *44*, 2129.
[41] H. Dau, P. Liebisch, M. Haumann, *Anal. Bioanal. Chem.* **2003**, *376*, 562.
[42] J. Messinger, J. H. Robblee, U. Bergmann, C. Fernandez, P. Glatzel, H. Visser, R. M. Cinco, K. L. McFarlane, E. Bellacchio, S. A. Pizarro, S. P. Cramer, K. Sauer, M. P. Klein, V. K. Yachandra, *J. Am. Chem. Soc.* **2001**, *123*, 7804.
[43] R. D. Britt, J. M. Peloquin, K. A. Campbell, *Annu. Rev. Biophys. Biomol. Struct.* **2000**, *29*, 463.

[44] G. Han, F. M. Ho, K. G. V. Havelius, S. F. Morvaridi, F. Mamedov, S. Styring, *Biochim. Biophys. Acta* **2008**, *1777*, 496.
[45] L. V. Kulik, W. Lubitz, J. Messinger, *Biochemistry* **2005**, *44*, 9368.
[46] L. V. Kulik, B. Epel, W. Lubitz, J. Messinger, *J. Am. Chem. Soc.* **2007**, *129*, 13421.
[47] J. Messinger, J. H. A. Nugent, M. C. W. Evans, *Biochemistry* **1997**, *36*, 11055.
[48] J. Messinger, J. H. Robblee, W. O. Yu, K. Sauer, V. K. Yachandra, M. P. Klein, *J. Am. Chem. Soc.* **1997**, *119*, 11349.
[49] K. A. Ahrling, S. Peterson, S. Styring, *Biochemistry* **1997**, *36*, 13148.
[50] K. A. Campbell, W. Gregor, D. Pham, R. J. Debus, J. M. Peloquin, R. D. Britt, *Book of Abstracts, 216th ACS National Meeting, Boston, August 23-27*, **1998**.
[51] S. L. Dexheimer, M. P. Klein, *J. Am. Chem. Soc.* **1992**, *114*, 2821.
[52] T. Yamauchi, H. Mino, T. Matsukawa, A. Kawamori, T.-A. Ono, *Biochemistry* **1997**, *36*, 7520.
[53] G. C. Dismukes, Y. Siderer, *FEBS Lett.* **1980**, *121*, 78.
[54] G. C. Dismukes, Y. Siderer, *Proc. Natl. Acad. Sci.* **1981**, *78*, 274.
[55] J. L. Casey, K. Sauer, *Biochim. Biophys. Acta* **1984**, *767*, 21.
[56] J. L. Zimmermann, A. W. Rutherford, *Biochim. Biophys. Acta* **1984**, *767*, 160.
[57] T. Matsukawa, H. Mino, D. Yoneda, A. Kawamori, *Biochemistry* **1999**, *38*, 4072.
[58] N. Ioannidis, V. Petrouleas, *Biochemistry* **2000**, *39*, 5246.
[59] N. Ioannidis, V. Petrouleas, *Biochemistry* **2002**, *41*, 9580.
[60] D. Koulougliotis, D. J. Hirsh, G. W. Brudvig, *J. Am. Chem. Soc.* **1992**, *114*, 8322.
[61] Ö. Hansson, R. Aasa, T. Vänngard, *Biophys. J.* **1987**, *51*, 825.
[62] D. H. Kim, R. D. Britt, M. P. Klein, K. Sauer, *J. Am. Chem. Soc.* **1990**, *112*, 9389.
[63] D. W. Randall, B. E. Sturgeon, J. A. Ball, G. A. Lorigan, M. K. Chan, M. P. Klein, W. H. Armstrong, R. D. Britt, *J. Am. Chem. Soc.* **1995**, *117*, 11780.
[64] D. W. Randall, M. K. Chan, W. H. Armstrong, R. D. Britt, *Mol. Phys.* **1998**, *95*, 1283.
[65] G. J. Yeagle, M. L. Gilchrist, R. M. McCarrick, R. D. Britt, *Inorg. Chem.* **2008**, *47*, 1803.
[66] G. J. Yeagle, M. L. Gilchrist, Jr., L. M. Walker, R. J. Debus, R. D. Britt, *Phil. Trans. Roy. Soc. B* **2008**, *363*, 1157.
[67] J.-H. Su, W. Lubitz, J. Messinger, *J. Am. Chem. Soc.* **2008**, *130*, 786.
[68] O. M. Usov, V. M. Grigoryants, R. Tagore, G. W. Brudvig, C. P. Scholes, *J. Am. Chem. Soc.* **2007**, *129*, 11886.
[69] S. H. Kim, W. Gregor, J. M. Peloquin, M. Brynda, R. D. Britt, *J. Am. Chem. Soc.* **2004**, *126*, 7228.
[70] J. M. Peloquin, K. A. Campbell, R. D. Britt, *J. Am. Chem. Soc.* **1998**, *120*, 6840.
[71] K. V. Lakshmi, S. S. Eaton, G. R. Eaton, G. W. Brudvig, *Biochemistry* **1999**, *38*, 12758.
[72] T. Wydrzynski, K. Satoh, *Photosystem II: The Light-Driven Water: Plastoquinone Oxido-Reductase in Photosynthesis*, Springer, **2005**.
[73] F. Rappaport, M. Guergova-Kuras, P. J. Nixon, B. A. Diner, J. Lavergne, *Biochemistry* **2002**, *41*, 8518.
[74] G. T. Babcock, B. A. Barry, R. J. Debus, C. W. Hoganson, M. Atamian, L. McIntosh, I. Sithole, C. F. Yocum, *Biochemistry* **1989**, *28*, 9557.
[75] P. Aedelroth, K. Lindberg, L.-E. Andreasson, *Biochemistry* **1995**, *34*, 9021.
[76] V. L. Pecoraro, M. J. Baldwin, M. T. Caudle, W.-Y. Hsieh, N. A. Law, *Pure Appl. Chem.* **1998**, *70*, 925.
[77] R. I. Cukier, *J. Phys. Chem. B* **2002**, *106*, 1746.
[78] J. S. Vrettos, D. A. Stone, G. W. Brudvig, *Biochemistry* **2001**, *40*, 7937.
[79] K. Olesen, L.-E. Andreasson, *Biochemistry* **2003**, *42*, 2025.
[80] K. Lindberg, L.-E. Andreasson, *Biochemistry* **1996**, *35*, 14259.
[81] M. Haumann, M. Barra, P. Loja, S. Loescher, R. Krivanek, A. Grundmeier, L.-E. Andreasson, H. Dau, *Biochemistry* **2006**, *45*, 13101.
[82] C. F. Yocum, *Coord. Chem. Rev.* **2008**, *252*, 296.
[83] P. E. M. Siegbahn, *Inorg. Chem.* **2008**, *47*, 1779.
[84] P. E. M. Siegbahn, M. Lundberg, *J. Inorg. Biochem.* **2006**, *100*, 1035.
[85] P. E. M. Siegbahn, *Chem. Eur. J.* **2006**, *12*, 9217.
[86] E. M. Sproviero, J. A. Gascon, J. P. McEvoy, G. W. Brudvig, V. S. Batista, *J. Inorg. Biochem.* **2006**, *100*, 786.
[87] E. M. Sproviero, J. A. Gascon, J. P. McEvoy, G. W. Brudvig, V. S. Batista, *Coord. Chem. Rev.* **2008**, *252*, 395.
[88] E. M. Sproviero, J. A. Gascon, J. P. McEvoy, G. W. Brudvig, V. S. Batista, *J. Am. Chem. Soc.* **2008**, *130*, 6728.

[89] E. M. Sproviero, J. A. Gascon, J. P. McEvoy, G. W. Brudvig, V. S. Batista, *J. Am. Chem. Soc.* **2008**, *130*, 3428.

Chapter 3

[1] A. D. Becke, R. M. Dickson, *J. Chem. Phys.* **1990**, *92*, 3610.
[2] T. Ziegler, *Chem. Rev.* **1991**, *91*, 651.
[3] R. G. Parr, W. Yang, *Density-Functional Theory of Atoms and Molecules*, Oxford University Press, **1989**.
[4] W. Koch, M. C. Holthausen, *A Chemist's Guide to Density Functional Theory*, Wiley, **2001**.
[5] D. R. Hartree, *Proc. Camb. Philos. Soc.* **1927**, *24*, 89.
[6] V. Fock, *Z. Phys.* **1930**, *61*, 126.
[7] J. C. Slater, *Phys. Rev.* **1930**, *35*, 210.
[8] G. G. Hall, *Proc. Roy. Soc. A* **1951**, *208*, 328.
[9] C. C. J. Roothaan, *Rev. Mod. Phys.* **1951**, *23*, 69.
[10] P.-O. Löwdin, *Adv. Chem. Phys.* **1959**, *2*, 207.
[11] P. Hohenberg, W. Kohn, *Phys. Rev. B* **1964**, *136*, 864.
[12] W. Kohn, L. J. Sham, *Phys. Rev. A* **1965**, *140*, 1133.
[13] A. V. Arbuznikov, M. Kaupp, *Chem. Phys. Lett.* **2004**, *386*, 8.
[14] A. V. Arbuznikov, M. Kaupp, *Chem. Phys. Lett.* **2004**, *391*, 16.
[15] W. Hieringer, F. Della Sala, A. Görling, *Chem. Phys. Lett.* **2004**, *383*, 115.
[16] A. M. Teale, D. J. Tozer, *Chem. Phys. Lett.* **2004**, *383*, 109.
[17] J. D. Talman, W. F. Shadwick, *Phys. Rev. A* **1976**, *14*, 36.
[18] F. Della Sala, A. Görling, *J. Chem. Phys.* **2001**, *115*, 5718.
[19] O. V. Gritsenko, E. J. Baerends, *Phys. Rev. A* **2001**, *64*, 0425061.
[20] R. T. Sharp, G. K. Horton, *Phys. Rev.* **1953**, *90*, 317.
[21] J. C. Slater, *Phys. Rev.* **1951**, *81*, 385.
[22] D. M. Ceperley, B. J. Alder, *Phys. Rev. Lett.* **1980**, *45*.
[23] S. H. Vosko, L. Wilk, M. Nusair, *Can. J. Phys.* **1980**, *58*, 1200.
[24] J. P. Perdew, Y. Wang, *Phys. Rev. B* **1992**, *45*, 13244.
[25] A. D. Becke, *J. Chem. Phys.* **1986**, *84*, 8524.
[26] J. P. Perdew, Y. Wang, *Phys. Rev. B* **1986**, *33*, 8800.
[27] J. P. Perdew, *Phys. Rev. B* **1986**, *33*, 8822.
[28] A. D. Becke, *Phys. Rev. A* **1988**, *38*, 3098.
[29] C. Lee, W. Yang, R. G. Parr, *Phys. Rev. B* **1988**, *37*, 785.
[30] P. A. M. Dirac, *Proc. Roy. Soc. London A* **1929**, *123*, 714.
[31] J. Tao, J. P. Perdew, V. N. Staroverov, G. E. Scuseria, *Phys. Rev. Lett.* **2003**, *91*, 146401.
[32] A. D. Becke, *J. Chem. Phys.* **1993**, *98*, 5648.
[33] P. J. Stephens, F. J. Devlin, C. F. Chabalowski, M. J. Frisch, *J. Phys. Chem.* **1994**, *98*.
[34] M. Munzarová, P. Kubácek, M. Kaupp, *J. Am. Chem. Soc.* **2000**, *122*, 11900.
[35] M. Munzarová, M. Kaupp, *J. Phys. Chem. A* **1999**, *103*, 9966.
[36] S. Patchkovskii, T. Ziegler, *J. Chem. Phys.* **1999**, *111*, 5730.
[37] E. I. Solomon, R. K. Szilagyi, S. DeBeer George, L. Basumallick, *Chem. Rev.* **2004**, *104*, 419.
[38] C. Remenyi, M. Kaupp, *J. Am. Chem. Soc.* **2005**, *127*, 11399
[39] M. Kaupp, R. Reviakine, O. L. Malkina, A. Arbuznikov, B. Schimmelpfennig, V. G. Malkin, *J. Comp. Chem.* **2002**, *23*, 794.
[40] I. Ciofini, F. Illas, C. Adamo, *J. Chem. Phys.* **2004**, *120*, 3811.
[41] F. Neese, *J. Phys. Chem. Sol.* **2004**, *65*, 781.
[42] L. Noodleman, *J. Chem. Phys.* **1981**, *74*, 5737.
[43] E. Ruiz, *Structure and Bonding* **2004**, *113*, 71.
[44] E. Ruiz, A. Rodriguez-Fortea, J. Cano, S. Alvarez, P. Alemany, *J. Comput. Chem.* **2003**, *24*, 982.
[45] E. Ruiz, J. Cano, S. Alvarez, P. Alemany, *J. Am. Chem. Soc.* **1998**, *120*, 11122.
[46] T. Soda, Y. Kitagawa, T. Onishi, Y. Takano, Y. Shigeta, H. Nagao, Y. Yoshioka, K. Yamaguchi, *Chem. Phys. Lett.* **2000**, *319*, 185.
[47] J. Li, L. Noodleman, D. A. Case, *Inorganic Electronic Structure and Spectroscopy, vol. I*, Eds.: A. B. P. Lever, E.I. Solomon, John Wiley & Sons, New York, p. 661, **1998**.
[48] A. T. Amos, G. G. Hall, *Proc. Roy. Soc. London A* **1961**, *263*, 483.
[49] P.-O. Löwdin, *Rev. Mod. Phys.* **1955**, *97*, 1474.

[50] I. Zilberberg, S. P. Ruzankin, *Chem. Phys. Lett.* **2004**, *394*, 165.
[51] I. Zilberberg, S. P. Ruzankin, S. Malykhin, G. M. Zhidomirov, *Chem. Phys. Lett.* **2004**, *394*, 392.

Chapter 4

[1] J. E. Harriman, *Theoretical Foundations of Electron Spin Resonance*, Academic Press **1978**; J. A. Weil, J. R. Bolton, J. E. Wertz, *Electron Paramagnetic Resonance*, John Wiley & Sons, **1994**.
[2] B. R. McGarvey, *Trans. Met. Chem.* **1966**, *3*, 89.
[3] R. McWeeny, *Spins in Chemistry*, Dover Publications **2004**.
[4] M. Kaupp, M. Buehl, V. G. Malkin, *Calculation of NMR and EPR Parameters: Theory and Applications*, Wiley-VCH, **2004**.
[5] W. Gerlach, O. Stern, *Z. Phys.* **1922**, *9*, 349.
[6] P. A. M. Dirac, *The Principles of Quantum Mechanics*, Clarendon Press, Oxford, **1930**.
[7] M. Munzarová, *PhD Thesis*, Institut für Anorganische Chemie der Universität Stuttgart, **2001**.
[8] A. Szabo, N. S. Ostlund, *Modern Quantum Chemistry: Introduction to Advanced Electronic Structure Theory*, Dover Publications **1996**.
[9] C. J. Cramer, *Essentials of Computational Chemistry: Theories and Models*, John Wiley & Sons **2001**.
[10] M. Kaupp, R. Reviakine, O. L. Malkina, A. V. Arbouznikov, B. Schimmelpfennig, V. G. Malkin, *J. Comp. Chem.* **2002**, *23*, 794.
[11] O. L. Malkina, J. Vaara, B. Schimmelpfennig, M. Munzarová, V. G. Malkin, M. Kaupp, *J. Am. Chem. Soc.* **2000**, *122*, 9206.
[12] F. Neese, *J. Chem. Phys.* **2001**, *115*, 11080.
[13] G. Schreckenbach, T. Ziegler, *J. Phys. Chem. A* **1997**, *101*, 3388.
[14] C. Remenyi, R. Reviakine, A. V. Arbuznikov, J. Vaara, M. Kaupp, *J. Phys. Chem. A* **2004**, *108*, 5026.
[15] A. V. Arbouznikov, J. Vaara, M. Kaupp, *J. Chem. Phys.* **2004**, *120*, 2127.
[16] F. Neese, *J. Chem. Phys.* **2003**, *118*, 3939.
[17] W. Koch, M. C. Holthausen, *A Chemist's Guide to Density Functional Theory*, Wiley, **2001**.
[18] R. H. Sands, W. R. Dunham, *Q. Rev. Biophys.* **1974**, *7*, 443.
[19] K.-O. Schafer, R. Bittl, W. Zweygart, F. Lendzian, G. Haselhorst, T. Weyhermuller, K. Wieghardt, W. Lubitz, *J. Am. Chem. Soc.* **1998**, *120*, 13104.
[20] A. Bencini, D. Gatteschi, *EPR of Exchange Coupled Systems*, Springer, **1990**.
[21] M. Zheng, S. V. Khangulov, G. C. Dismukes, V. V. Barynin, *Inorg. Chem.* **1994**, *33*, 382.
[22] S. Sinnecker, F. Neese, L. Noodleman, W. Lubitz, *J. Am. Chem. Soc.* **2004**, *126*, 2613.
[23] G. Blondin, J. J. Girerd, *Chem. Rev.* **1990**, *90*, 1359.
[24] P. Bertrand, B. Guigliarelli, C. More, *New. J. Chem.* **1991**, *15*, 445.
[25] R. H. Sands, W. R. Dunham, *Q. Rev. Biophys.* **1975**, *7*, 443.
[26] S. Sinnecker, F. Neese, W. Lubitz, *JBIC, J. Biol. Inorg. Chem.* **2005**, *10*, 231.
[27] S. Schinzel, M. Kaupp, *submitted*.
[28] L. V. Kulik, B. Epel, W. Lubitz, J. Messinger, *J. Am. Chem. Soc.* **2005**, *127*, 2392.
[29] J. M. Peloquin, K. A. Campbell, D. W. Randall, M. A. Evanchik, V. L. Pecoraro, W. H. Armstrong, R. D. Britt, *J. Am. Chem. Soc.* **2000**, *122*, 10926.
[30] M.-F. Charlot, A. Boussac, G. Blondin, *Biochim. Biophys. Acta* **2005**, *1708*, 120.

Chapter 5

[1] G. C. Dismukes, *Chem. Rev.* **1996**, *96*, 2909.
[2] W. Kaim, B. Schwederski, *Bioanorganische Chemie*, Teubner Verlag, **2004**.
[3] J. J. R. Frausto da Silva, R. J. P. Williams, *The Biological Chemistry of the Elements. The Inorganic Chemistry of Life*, Clarendon Press, **1991**.
[4] C. W. Bock, A. K. Katz, G. D. Markham, J. P. Glusker, *J. Am. Chem. Soc.* **1999**, *121*, 7360.
[5] E. Zavoiskii, *J. Phys.* **1945**, *9*, 211.
[6] R. Ahlrichs, M. Bär, M. Häser, H. Horn, C. Kölmel, *Chem. Phys. Lett.* **1989**, *162*, 165.
[7] A. D. Becke, *Phys. Rev. A* **1988**, *38*, 3098
[8] J. P. Perdew, *Phys. Rev. B* **1986**, *33*, 8822

[9] A. Schäfer, H. Horn, R. Ahlrichs, *J. Chem. Phys.* **1992**, *97*, 2571.
[10] M. Munzarová, P. Kubácek, M. Kaupp, *J. Am. Chem. Soc.* **2000**, *122*, 11900.
[11] M. Munzarová, M. Kaupp, *J. Phys. Chem. A* **1999**, *103*, 9966.
[12] W. Kutzelnigg, U. Fleischer, M. Schindler, *NMR Basis Principles and Progress, Vol 23*, Eds.: P. Diehl, **1990**.
[13] S. Huzinaga, *Ph. D. thesis*, University of Alberta, Edmonton, **1971**.
[14] P. J. Stephens, F. J. Devlin, C. F. Chabalowski, M. J. Frisch, *J. Phys. Chem.* **1994**, *98*.
[15] A. D. Becke, *J. Chem. Phys.* **1993**, *98*, 5648.
[16] C. Lee, W. Yang, R. G. Parr, *Phys. Rev. B* **1988**, *37*, 785.
[17] V. G. Malkin, O. L. Malkina, R. Reviakine, A. V. Arbouznikov, M. Kaupp, B. Schimmelpfennig, I. Malkin, T. Helgaker, K. Ruud, *MAG-Respect, Version 1.2* **2003**.
[18] B. A. Hess, C. M. Marian, U. Wahlgren, O. Gropen, *Chem. Phys. Lett.* **1996**, *251*, 365.
[19] B. Schimmelpfennig, *Ph.D. thesis*, Stockholms Universitet, **1996**.
[20] S. Mossin, H. O. Sorensen, H. Weihe, J. Glerup, I. Setofte, *Inorg. Chim. Acta* **2005**, *358*, 1096.
[21] S. Patchkovskii, T. Ziegler, *J. Chem. Phys.* **1999**, *111*, 5730.
[22] E. I. Solomon, R. K. Szilagyi, S. DeBeer George, L. Basumallick, *Chem. Rev.* **2004**, *104*, 419.
[23] C. Remenyi, M. Kaupp, *J. Am. Chem. Soc.* **2005**, *127*, 11399
[24] M. Kaupp, R. Reviakine, O. L. Malkina, A. Arbuznikov, B. Schimmelpfennig, V. G. Malkin, *J. Comp. Chem.* **2002**, *23*, 794.
[25] I. Ciofini, F. Illas, C. Adamo, *J. Chem. Phys.* **2004**, *120*, 3811.
[26] C. Remenyi, R. Reviakine, M. Kaupp, *J. Phys. Chem. B* **2007**, *111*, 8290.
[27] X. Tan, M. Bernardo, H. Thomann, C. P. Scholes, *J. Chem. Phys.* **1993**, *98*, 5147.
[28] G. C. Upreti, *J. Magn. Reson.* **1974**, *13*, 336.
[29] V. G. Malkin, O. L. Malkina, M. E. Casida, D. R. Salahub, *J. Am. Chem. Soc.* **1994**, *116*, 5898.
[30] C. Remenyi, R. Reviakine, A. V. Arbuznikov, J. Vaara, M. Kaupp, *J. Phys. Chem. A* **2004**, *108*, 5026
[31] F. Neese, *J. Chem. Phys.* **2003**, *118*, 3939.
[32] D. Baute, D. Goldfarb, *J. Phys. Chem. A* **2005**, *109*.
[33] I. Krivokapic, C. Noble, S. Klitgaard, P. Tregenna-Piggott, H. Weihe, A.-L. Barra, *Angew. Chem. Int. Ed.* **2005**, *44*, 3613.
[34] X. Tan, M. Bernardo, H. Thomann, C. P. Scholes, *J. Chem. Phys.* **1993**, *98*, 5147.

Chapter 6

[1] S. Schinzel, R. Müller, M. Kaupp, *Theor. Chem. Acc.* **2008**, *120*, 437. Tables and Figures were reproduced with permission from Springer.
[2] A. J. Kalb, J. Habash, N. S. Hunter, H. J. Price, J. Raftery, J. R. Helliwell, *Met. Ions Biol. Sys.* **2000**, *37*, 279.
[3] J. Greer, H. W. Kaufman, A. J. Kalb, *J. Mol. Biol.* **1970**, *48*, 365.
[4] J. B. Sumner, S. F. Howell, *J. Bacter.* **1936**, *32*, 227.
[5] M. Shoham, A. J. Kalb, I. Pecht, *Biochemistry* **1973**, *12*, 1914.
[6] W. I. Weis, K. Drickamer, *Annu. Rev. Biochem.* **1996**, *65*, 441.
[7] A. Deacon, T. Gleichmann, A. J. Kalb, H. Price, J. Raftery, G. Bradbrook, J. Yariv, J. R. Helliwell, *J. Chem. Soc., Faraday Trans.* **1997**, *93*, 4305.
[8] E. Meirovitch, Z. Luz, A. J. Kalb, *J. Am. Chem. Soc.* **1974**, *96*, 7542.
[9] E. Meirovitch, Z. Luz, A. J. Kalb, *J. Am. Chem. Soc.* **1974**, *96*, 7538.
[10] P. Manikandan, R. Carmieli, T. Shane, A. J. Kalb, D. Goldfarb, *J. Am. Chem. Soc.* **2000**, *122*, 3488.
[11] H. Metz, J. Kuchler, R. Bottcher, W. Windsch, *Chem. Phys. Lett.* **1982**, *89*, 351.
[12] R. Carmieli, P. Manikandan, A. J. Kalb, D. Goldfarb, *J. Am. Chem. Soc.* **2001**, *123*, 12438.
[13] R. Ahlrichs, M. Bär, M. Häser, H. Horn, C. Kölmel, *Chem. Phys. Lett.* **1989**, *162*, 165.
[14] P. J. Stephens, F. J. Devlin, C. F. Chabalowski, M. J. Frisch, *J. Phys. Chem.* **1994**, *98*.
[15] A. D. Becke, *J. Chem. Phys.* **1993**, *98*, 5648.
[16] A. Schäfer, H. Horn, R. Ahlrichs, *J. Chem. Phys.* **1992**, *97*, 2571.
[17] M. J. Frisch, G. W. Trucks, H. B. Schlegel, G. E. Scuseria, M. A. Robb, J. R. Cheeseman, J. Montgomery, J. A., T. Vreven, K. N. Kudin, J. C. Burant, J. M. Millam, S. S. Iyengar, J. Tomasi, V. Barone, B. Mennucci, M. Cossi, G. Scalmani, N. Rega, G. A. Petersson, H. Nakatsuji, M. Hada, M. Ehara, K. Toyota, R. Fukuda, J. Hasegawa, M. Ishida, T. Nakajima, Y. Honda, O. Kitao, H. Nakai, M. Klene, X. Li, J. E. Knox, H. P. Hratchian, J. B. Cross, V. Bakken, C. Adamo, J. Jaramillo, R. Gomperts, R. E. Stratmann, O. Yazyev, A. J. Austin, R. Cammi, C. Pomelli, J. W. Ochterski, P. Y.

Ayala, K. Morokuma, G. A. Voth, P. Salvador, J. J. Dannenberg, V. G. Zakrzewski, S. Dapprich, A. D. Daniels, M. C. Strain, O. Farkas, D. K. Malick, A. D. Rabuck, K. Raghavachari, J. B. Foresman, J. V. Ortiz, Q. Cui, A. G. Baboul, S. Clifford, J. Cioslowski, B. B. Stefanov, G. Liu, A. Liashenko, P. Piskorz, I. Komaromi, R. L. Martin, D. J. Fox, T. Keith, M. A. Al-Laham, C. Y. Peng, A. Nanayakkara, M. Challacombe, P. M. W. Gill, B. Johnson, W. Chen, M. W. Wong, C. Gonzalez, J. A. Pople, *Gaussian 03, Revision C.02* Gaussian, **2004**.
[18] M. Munzarová, P. Kubácek, M. Kaupp, *J. Am. Chem. Soc.* **2000**, *122*, 11900.
[19] M. Munzarová, M. Kaupp, *J. Phys. Chem. A* **1999**, *103*, 9966.
[20] W. Kutzelnigg, U. Fleischer, M. Schindler, *NMR Basis Principles and Progress, Vol 23*, Eds.: P. Diehl, **1990**.
[21] S. Huzinaga, *Ph. D. thesis*, University of Alberta, Edmonton, **1971**.
[22] A. D. Becke, *Phys. Rev. A* **1988**, *38*, 3098.
[23] J. P. Perdew, *Phys. Rev. B* **1986**, *33*, 8822.
[24] C. Lee, W. Yang, R. G. Parr, *Phys. Rev. B* **1988**, *37*, 785.
[25] V. G. Malkin, O. L. Malkina, R. Reviakine, A. V. Arbouznikov, M. Kaupp, B. Schimmelpfennig, I. Malkin, T. Helgaker, K. Ruud, *MAG-Respect, Version 1.2*, **2003**.
[26] B. A. Hess, C. M. Marian, U. Wahlgren, O. Gropen, *Chem. Phys. Lett.* **1996**, *251*, 365.
[27] B. Schimmelpfennig, *Ph.D. thesis*, Stockholms Universitet, **1996**.
[28] R. Carmieli, P. Manikandan, B. Epel, A. J. Kalb, A. Schnegg, A. Savitsky, K. Moebius, D. Goldfarb, *Biochemistry* **2003**, *42*, 7863.
[29] D. Goldfarb, D. Arieli, *Ann. Rev. Biophys. Biomol. Struct.* **2004**, *33*, 441.
[30] D. Goldfarb, K. V. Narasimhulu, R. Carmieli, *Magn. Reson. Chem.* **2005**, *43*, S40.
[31] S. Patchkovskii, T. Ziegler, *J. Chem. Phys.* **1999**, *111*, 5730.
[32] E. I. Solomon, R. K. Szilagyi, S. DeBeer George, L. Basumallick, *Chem. Rev.* **2004**, *104*, 419.
[33] C. Remenyi, M. Kaupp, *J. Am. Chem. Soc.* **2005**, *127*, 11399.
[34] M. Kaupp, R. Reviakine, O. L. Malkina, A. Arbuznikov, B. Schimmelpfennig, V. G. Malkin, *J. Comp. Chem.* **2002**, *23*, 794.
[35] I. Ciofini, F. Illas, C. Adamo, *J.Chem. Phys.* **2004**, *120*, 3811.
[36] C. Remenyi, R. Reviakine, M. Kaupp, *J. Phys. Chem. B* **2007**, *111*, 8290.
[37] V. G. Malkin, O. L. Malkina, M. E. Casida, D. R. Salahub, *J. Am. Chem. Soc.* **1994**, *116*, 5898.
[38] D. Arieli, T. F. Prisner, M. Hertel, D. Goldfarb, *Phys. Chem. Chem. Phys.* **2004**, *6*, 172.
[39] C. Remenyi, R. Reviakine, A. V. Arbuznikov, J. Vaara, M. Kaupp, *J. Phys. Chem. A* **2004**, *108*, 5026.
[40] F. Neese, *J. Chem. Phys.* **2003**, *118*, 3939.
[41] D. Baute, D. Goldfarb, *J. Phys. Chem. A* **2005**, *109*.
[42] M. L. Munzarová, M. Kaupp, *J. Phys. Chem. B* **2001**, *105*, 12644.
[43] C. Remenyi, M. L. Munzarova, M. Kaupp, *J. Phys. Chem. B* **2005**, *109*, 4227.

Chapter 7

[1] L. Noodleman, *Coord. Chem. Rev.* **1995**, *144*, 199.
[2] L. Noodleman, *J. Chem. Phys.* **1981**, *74*, 5737.
[3] G. Blondin, J. J. Girerd, *Chem. Rev.* **1990**, *90*, 1359.
[4] A. Bencini, D. Gatteschi, *EPR of Exchange Coupled Systems*, Springer, **1990**.
[5] L. Noodleman, E. J. Baerends, *J. Am. Chem. Soc.* **1984**, *106*, 2316.
[6] J. M. Mouesca, L. Noodleman, D. A. Case, B. Lamotte, *Inorg. Chem.* **1995**, *34*, 4347.
[7] S. Sinnecker, F. Neese, L. Noodleman, W. Lubitz, *J. Am. Chem. Soc.* **2004**, *126*, 2613.
[8] S. Sinnecker, F. Neese, W. Lubitz, *J. Biol. Inorg. Chem.* **2005**, *10*, 231.
[9] S. Schinzel, R. Müller, M. Kaupp, *Theor. Chem. Acc.* **2008**, *120*, 437.
[10] E. M. Sproviero, J. A. Gascon, J. P. McEvoy, G. W. Brudvig, V. S. Batista, *J. Inorg. Biochem.* **2006**, *100*, 786.
[11] E. Rudberg, P. Salek, Z. Rinkevicius, H. Aagren, *J. Chem. Theor. Comput.* **2006**, *2*, 981.
[12] T. Soda, Y. Kitagawa, T. Onishi, Y. Takano, Y. Shigeta, H. Nagao, Y. Yoshioka, K. Yamaguchi, *Chem. Phys. Lett.* **2000**, *319*, 185.
[13] R. Ahlrichs, M. Bär, M. Häser, H. Horn, C. Kölmel, *Chem. Phys. Lett.* **1989**, *162*, 165.
[14] V. V. Barynin, M. M. Whittaker, S. V. Antonyuk, V. S. Lamzin, P. M. Harrison, P. J. Artymiuk, J. W. Whittaker, *Structure* **2001**, *9*, 725.
[15] A. D. Becke, *J. Chem. Phys.* **1993**, *98*, 5648.

[16] P. J. Stephens, F. J. Devlin, C. F. Chabalowski, M. J. Frisch, *J. Phys. Chem.* **1994**, *98*.
[17] A. Schäfer, H. Horn, R. Ahlrichs, *J. Chem. Phys.* **1992**, *97*, 2571.
[18] M. Munzarová, M. Kaupp, *J. Phys. Chem. A* **1999**, *103*, 9966.
[19] M. Munzarová, P. Kubácek, M. Kaupp, *J. Am. Chem. Soc.* **2000**, *122*, 11900.
[20] W. Kutzelnigg, U. Fleischer, M. Schindler, *NMR Basis Principles and Progress, Vol 23*, Eds.: P. Diehl, **1990**.
[21] S. Huzinaga, *Ph. D. thesis* **1971**, University of Alberta, Edmonton.
[22] C. Lee, W. Yang, R. G. Parr, *Phys. Rev. B* **1988**, *37*, 785.
[23] V. G. Malkin, O. L. Malkina, R. Reviakine, A. V. Arbouznikov, M. Kaupp, B. Schimmelpfennig, I. Malkin, T. Helgaker, K. Ruud, *MAG-Respect, Version 1.2* **2003**.
[24] B. A. Hess, C. M. Marian, U. Wahlgren, O. Gropen, *Chem. Phys. Lett.* **1996**, *251*, 365.
[25] B. Schimmelpfennig, *Ph.D. thesis*, Stockholms Universitet, **1996**.
[26] I. Zilberberg, S. P. Ruzankin, *Chem. Phys. Lett.* **2004**, *394*, 165.
[27] I. Zilberberg, S. P. Ruzankin, S. Malykhin, G. M. Zhidomirov, *Chem. Phys. Lett.* **2004**, *394*, 392.
[28] M. J. Frisch, G. W. Trucks, H. B. Schlegel, G. E. Scuseria, M. A. Robb, J. R. Cheeseman, J. Montgomery, J. A., T. Vreven, K. N. Kudin, J. C. Burant, J. M. Millam, S. S. Iyengar, J. Tomasi, V. Barone, B. Mennucci, M. Cossi, G. Scalmani, N. Rega, G. A. Petersson, H. Nakatsuji, M. Hada, M. Ehara, K. Toyota, R. Fukuda, J. Hasegawa, M. Ishida, T. Nakajima, Y. Honda, O. Kitao, H. Nakai, M. Klene, X. Li, J. E. Knox, H. P. Hratchian, J. B. Cross, V. Bakken, C. Adamo, J. Jaramillo, R. Gomperts, R. E. Stratmann, O. Yazyev, A. J. Austin, R. Cammi, C. Pomelli, J. W. Ochterski, P. Y. Ayala, K. Morokuma, G. A. Voth, P. Salvador, J. J. Dannenberg, V. G. Zakrzewski, S. Dapprich, A. D. Daniels, M. C. Strain, O. Farkas, D. K. Malick, A. D. Rabuck, K. Raghavachari, J. B. Foresman, J. V. Ortiz, Q. Cui, A. G. Baboul, S. Clifford, J. Cioslowski, B. B. Stefanov, G. Liu, A. Liashenko, P. Piskorz, I. Komaromi, R. L. Martin, D. J. Fox, T. Keith, M. A. Al-Laham, C. Y. Peng, A. Nanayakkara, M. Challacombe, P. M. W. Gill, B. Johnson, W. Chen, M. W. Wong, C. Gonzalez, J. A. Pople, *Gaussian 03, Revision C.02* **2004**, Gaussian.
[29] P. E. M. Siegbahn, *Curr. Opin. Chem. Biol.* **2002**, *6*, 227.
[30] P. E. M. Siegbahn, J. Westerberg, M. Svensson, R. H. Crabtree, *J. Phys. Chem. B* **1998**, *102*, 1615.
[31] M. Pavlov, M. R. A. Blomberg, P. E. M. Siegbahn, *Int. J. Quantum Chem.* **1999**, *73*, 197.
[32] E. Sigfridsson, M. H. M. Olsson, U. Ryde, *Inorg. Chem.* **2001**, *40*, 2509.
[33] O. Horner, E. Anxolabéhère-Mallart, M.-F. Charlot, L. Tchertanov, J. Guilhem, T. A. Mattioli, A. Boussac, J.-J. Girerd, *Inorg. Chem.* **1999**, *38*, 1222.
[34] P. M. Plaksin, R. C. Stoufer, M. Mathew, G. J. Palenik, *J. Am. Chem. Soc.* **1972**, *94*, 2121.
[35] M. Stebler, A. Ludi, H. B. Buergi, *Inorg. Chem.* **1986**, *25*, 4743.
[36] K.-O. Schafer, R. Bittl, W. Zweygart, F. Lendzian, G. Haselhorst, T. Weyhermuller, K. Wieghardt, W. Lubitz, *J. Am. Chem. Soc.* **1998**, *120*, 13104.
[37] K. Wieghardt, U. Bossek, L. Zsolnai, G. Huttner, G. Blondin, J.-J. Girerd, F. Babonneau, *J. Chem. Soc. Chem. Commun.* **1987**, 651.
[38] K. Wieghardt, U. Bossek, J. Bonvoisin, P. Beauvillain, J.-J. Girerd, B. Nuber, J. Weiss, J. Heinze, *Angew. Chem.* **1986**, *98*, 1026.
[39] S. Patchkovskii, T. Ziegler, *J. Chem. Phys.* **1999**, *111*, 5730.
[40] A. T. Amos, G. G. Hall, *Proc. Roy. Soc. Lond.* **1961**, *263*, 483.
[41] I. Rudra, Q. Wu, T. VanVoorhis, *Inorg. Chem.* **2007**, *46*, 10539.
[42] E. Ruiz, J. Cano, S. Alvarez, P. Alemany, *J. Am. Chem. Soc.* **1998**, *120*, 11122.
[43] E. Ruiz, J. Cano, S. Alvarez, P. Alemany, *J. Comput. Chem.* **1999**, *20*, 1391.
[44] E. Ruiz, A. Rodriguez-Fortea, J. Cano, S. Alvarez, P. Alemany, *J. Comput. Chem.* **2003**, *24*, 982.
[45] E. Ruiz, *Chem. Phys. Lett.* **2008**, *460*, 336.
[46] E. Ruiz, A. Rodriguez-Fortea, J. Tercero, T. Cauchy, C. Massobrio, *J. Chem. Phys.* **2005**, *123*, 074102/1.
[47] C. D. Delfs, R. Stranger, *Inorg. Chem.* **2001**, *40*, 3061.
[48] J. E. McGrady, R. Stranger, *J. Am. Chem. Soc.* **1997**, *119*, 8512.
[49] S. Petrie, S. Mukhopadhyay, W. H. Armstrong, R. Stranger, *Phys. Chem. Chem. Phys.* **2004**, *6*, 4871.
[50] T. Soda, Y. Kitagawa, T. Onishi, Y. Takano, Y. Shigeta, H. Nagao, Y. Yoshioka, K. Yamaguchi, *Chem. Phys. Lett.* **2000**, *319*, 223.
[51] R. Caballol, O. Castell, F. Illas, I. d. P. R. Moreira, J. P. Malrieu, *J. Phys. Chem. A* **1997**, *101*, 7860.
[52] E. Ruiz, J. Cirera, S. Alvarez, *Coord. Chem. Rev.* **2005**, *249*, 2649.
[53] E. Ruiz, *Structure and Bonding* **2004**, *113*, 71.
[54] C. D. Delfs, R. Stranger, *Inorg. Chem.* **2000**, *39*, 491.
[55] I. Michaud-Soret, L. Jacquamet, N. Debaecker-Petit, L. Le Pape, V. V. Barynin, J.-M. Latour, *Inorg. Chem.* **1998**, *37*, 3874.

[56] C. Teutloff, K.-O. Schaefer, S. Sinnecker, V. Barynin, R. Bittl, K. Wieghardt, F. Lendzian, W. Lubitz, *Magn. Reson. Chem.* **2005**, *43*, S51.
[57] K. O. Schaefer, R. Bittl, F. Lendzian, V. Barynin, T. Weyhermueller, K. Wieghardt, W. Lubitz, *J. Phys. Chem. B* **2003**, *107*, 1242.
[58] C. Remenyi, R. Reviakine, A. V. Arbuznikov, J. Vaara, M. Kaupp, *J. Phys. Chem. A* **2004**, *108*, 5026.
[59] F. Neese, *J. Chem. Phys.* **2003**, *118*, 3939.
[60] C. Remenyi, R. Reviakine, M. Kaupp, *J. Phys. Chem. B* **2007**, *111*, 8290.
[61] M. Kaupp, H. Bahmann, A. V. Arbuznikov, *J. Chem. Phys.* **2007**, *127*, 194102/1.
[62] H. Bahmann, A. Rodenberg, A. V. Arbuznikov, M. Kaupp, *J. Chem. Phys.* **2007**, *126*, 011103/1.
[63] A. V. Arbuznikov, M. Kaupp, *Chem. Phys. Lett.* **2007**, *440*, 160.
[64] A. V. Arbuznikov, M. Kaupp, *Chem. Phys. Lett.* **2007**, *442*, 496.
[65] A. V. Arbuznikov, M. Kaupp, H. Bahmann, *J. Chem. Phys.* **2006**, *124*, 204102/1.
[66] G. J. Yeagle, M. L. Gilchrist, Jr., L. M. Walker, R. J. Debus, R. D. Britt, *Phil. Trans. Roy. Soc. B* **2008**, *363*, 1157.
[67] G. J. Yeagle, M. L. Gilchrist, R. M. McCarrick, R. D. Britt, *Inorg. Chem.* **2008**, *47*, 1803.
[68] A. Ivancich, V. V. Barynin, J.-L. Zimmermann, *Biochemistry* **1995**, *34*, 6628.
[69] T. L. Stemmler, B. E. Sturgeon, D. W. Randall, R. D. Britt, J. E. Penner-Hahn, *J. Am. Chem. Soc.* **1997**, *119*, 9215.
[70] O. M. Usov, V. M. Grigoryants, R. Tagore, G. W. Brudvig, C. P. Scholes, *J. Am. Chem. Soc.* **2007**, *129*, 11886.
[71] R. D. Britt, *Ph.D. Thesis*, Lawrence Berkeley Laboratory, **1988**.

Chapter 8

[1] G. C. Dismukes, Y. Siderer, *FEBS Lett.* **1980**, *121*, 78.
[2] G. C. Dismukes, Y. Siderer, *Proc. Natl. Acad. Sci.* **1981**, *78*, 274.
[3] J. L. Casey, K. Sauer, *Biochim. Biophys. Acta* **1984**, *767*, 21.
[4] J. L. Zimmermann, A. W. Rutherford, *Biochim. Biophys. Acta* **1984**, *767*, 160.
[5] J. M. Peloquin, K. A. Campbell, D. W. Randall, M. A. Evanchik, V. L. Pecoraro, W. H. Armstrong, R. D. Britt, *J. Am. Chem. Soc.* **2000**, *122*, 10926.
[6] L. V. Kulik, B. Epel, W. Lubitz, J. Messinger, *J. Am. Chem. Soc.* **2005**, *127*, 2392.
[7] M.-F. Charlot, A. Boussac, G. Blondin, *Biochim. Biophys. Acta* **2005**, *1708*, 120.
[8] J. M. Peloquin, R. D. Britt, *Biochim. Biophys. Acta* **2001**, *1503*, 96.
[9] L. V. Kulik, B. Epel, W. Lubitz, J. Messinger, *J. Am. Chem. Soc.* **2007**, *129*, 13421.
[10] D. W. Randall, B. E. Sturgeon, J. A. Ball, G. A. Lorigan, M. K. Chan, M. P. Klein, W. H. Armstrong, R. D. Britt, *J. Am. Chem. Soc.* **1995**, *117*, 11780.
[11] D. W. Randall, M. K. Chan, W. H. Armstrong, R. D. Britt, *Mol. Phys.* **1998**, *95*, 1283.
[12] C. Teutloff, K.-O. Schaefer, S. Sinnecker, V. Barynin, R. Bittl, K. Wieghardt, F. Lendzian, W. Lubitz, *Magn. Reson. Chem.* **2005**, *43*, S51.
[13] G. J. Yeagle, M. L. Gilchrist, Jr., L. M. Walker, R. J. Debus, R. D. Britt, *Phil. Trans. Roy. Soc. B* **2008**, *363*, 1157.
[14] G. J. Yeagle, M. L. Gilchrist, R. M. McCarrick, R. D. Britt, *Inorg. Chem.* **2008**, *47*, 1803.
[15] S. Sinnecker, F. Neese, L. Noodleman, W. Lubitz, *J. Am. Chem. Soc.* **2004**, *126*, 2613.
[16] S. Sinnecker, F. Neese, W. Lubitz, *J. Biol. Inorg. Chem.* **2005**, *10*, 231.
[17] S. Schinzel, M. Kaupp, *submitted*.
[18] P. E. M. Siegbahn, *Phil. Trans. Roy. Soc. B* **2008**, *363*, 1221.
[19] P. E. M. Siegbahn, *Chem. Eur. J.* **2008**, *14*, 8290.
[20] E. M. Sproviero, J. A. Gascon, J. P. McEvoy, G. W. Brudvig, V. S. Batista, *J. Am. Chem. Soc.* **2008**, *130*, 6728.
[21] E. M. Sproviero, J. A. Gascon, J. P. McEvoy, G. W. Brudvig, V. S. Batista, *Coord. Chem. Rev.* **2008**, *252*, 395.
[22] P. E. M. Siegbahn, *Inorg. Chem.* **2008**, *47*, 1779.
[23] P. E. M. Siegbahn, *Chem. Eur. J.* **2006**, *12*, 9217.
[24] P. E. M. Siegbahn, M. Lundberg, *Photochem. Photobiol. Sci.* **2005**, *4*, 1035.
[25] E. M. Sproviero, J. A. Gascon, J. P. McEvoy, G. W. Brudvig, V. S. Batista, *J. Am. Chem. Soc.* **2008**, *130*, 3428.
[26] L. Noodleman, *Coord. Chem. Rev.* **1995**, *144*, 199.

[27] L. Noodleman, *J. Chem. Phys.* **1981**, *74*, 5737.
[28] K. N. Ferreira, T. M. Iverson, K. Maghlaoui, J. Barber, S. Iwata, *Science* **2004**, *303*, 1831.
[29] B. Loll, J. Kern, W. Saenger, A. Zouni, J. Biesiadka, *Nature* **2005**, *438*, 1040.
[30] E. M. Sproviero, J. A. Gascon, J. P. McEvoy, G. W. Brudvig, V. S. Batista, *J. Am. Chem. Soc.* **2008**, *130*, 3428.
[31] J. Yano, J. Kern, K. Sauer, M. J. Latimer, Y. Pushkar, J. Biesiadka, B. Loll, W. Saenger, J. Messinger, A. Zouni, V. K. Yachandra, *Science* **2006**, *314*, 821.
[32] W. Hillier, T. Wydrzynski, *Coord. Chem. Rev.* **2008**, *252*, 306.
[33] J. P. McEvoy, G. W. Brudvig, *Chem. Rev.* **2006**, *106*, 4455.
[34] M. Haumann, M. Barra, P. Loja, S. Loescher, R. Krivanek, A. Grundmeier, L.-E. Andreasson, H. Dau, *Biochemistry* **2006**, *45*, 13101.
[35] C. F. Yocum, *Coord. Chem. Rev.* **2008**, *252*, 296.
[36] H. Dau, A. Grundmeier, P. Loja, M. Haumann, *Phil. Trans. R. Soc. B* **2008**, *363*, 1237.
[37] H. Dau, L. Iuzzolino, J. Dittmer, *Biochim. Biophys. Acta* **2001**, *1503*, 24.
[38] H. Dau, P. Liebisch, M. Haumann, *Anal. Bioanal. Chem.* **2003**, *376*, 562.
[39] M. Haumann, C. Müller, P. Liebisch, L. Iuzzolino, J. Dittmer, M. Grabolle, T. Neisius, W. Meyer-Klaucke, H. Dau, *Biochemistry* **2005**, *44*, 1894.
[40] J. Yano, J. Kern, Y. Pushkar, K. Sauer, P. Glatzel, U. Bergmann, J. Messinger, A. Zouni, V. K. Yachandra, *Phil. Trans. Roy. Soc. B* **2008**, *363*, 1139.
[41] Y. Pushkar, J. Yano, P. Glatzel, J. Messinger, A. Lewis, K. Sauer, U. Bergmann, V. K. Yachandra, *J. Biol. Chem.* **2007**, *282*, 7198.
[42] R. M. Cinco, J. H. Robblee, J. Messinger, C. Fernandez, K. L. M. Holman, K. Sauer, V. K. Yachandra, *Biochemistry* **2004**, *43*, 13271.
[43] J. Yano, V. K. Yachandra, *Inorg. Chem.* **2008**, *47*, 1711.
[44] S. Zein, C. Duboc, W. Lubitz, F. Neese, *Inorg. Chem.* **2008**, *47*, 134.
[45] S. Zein, L. V. Kulik, J. Yano, J. Kern, Y. Pushkar, A. Zouni, V. K. Yachandra, W. Lubitz, F. Neese, J. Messinger, *Phil. Trans. Roy. Soc. B* **2008**, *363*, 1167.
[46] R. Ahlrichs, M. Bär, M. Häser, H. Horn, C. Kölmel, *Chem. Phys. Lett.* **1989**, *162*, 165.
[47] A. D. Becke, *J. Chem. Phys.* **1993**, *98*, 5648.
[48] P. J. Stephens, F. J. Devlin, C. F. Chabalowski, M. J. Frisch, *J. Phys. Chem.* **1994**, *98*.
[49] A. Schäfer, H. Horn, R. Ahlrichs, *J. Chem. Phys.* **1992**, *97*, 2571.
[50] M. J. Frisch, G. W. Trucks, H. B. Schlegel, G. E. Scuseria, M. A. Robb, J. R. Cheeseman, J. Montgomery, J. A., T. Vreven, K. N. Kudin, J. C. Burant, J. M. Millam, S. S. Iyengar, J. Tomasi, V. Barone, B. Mennucci, M. Cossi, G. Scalmani, N. Rega, G. A. Petersson, H. Nakatsuji, M. Hada, M. Ehara, K. Toyota, R. Fukuda, J. Hasegawa, M. Ishida, T. Nakajima, Y. Honda, O. Kitao, H. Nakai, M. Klene, X. Li, J. E. Knox, H. P. Hratchian, J. B. Cross, V. Bakken, C. Adamo, J. Jaramillo, R. Gomperts, R. E. Stratmann, O. Yazyev, A. J. Austin, R. Cammi, C. Pomelli, J. W. Ochterski, P. Y. Ayala, K. Morokuma, G. A. Voth, P. Salvador, J. J. Dannenberg, V. G. Zakrzewski, S. Dapprich, A. D. Daniels, M. C. Strain, O. Farkas, D. K. Malick, A. D. Rabuck, K. Raghavachari, J. B. Foresman, J. V. Ortiz, Q. Cui, A. G. Baboul, S. Clifford, J. Cioslowski, B. B. Stefanov, G. Liu, A. Liashenko, P. Piskorz, I. Komaromi, R. L. Martin, D. J. Fox, T. Keith, M. A. Al-Laham, C. Y. Peng, A. Nanayakkara, M. Challacombe, P. M. W. Gill, B. Johnson, W. Chen, M. W. Wong, C. Gonzalez, J. A. Pople, *Gaussian 03, Revision C.02*, Gaussian, **2004**.
[51] M. Munzarová, M. Kaupp, *J. Phys. Chem. A* **1999**, *103*, 9966.
[52] M. Munzarová, P. Kubácek, M. Kaupp, *J. Am. Chem. Soc.* **2000**, *122*, 11900.
[53] W. Kutzelnigg, U. Fleischer, M. Schindler, *NMR Basis Principles and Progress, Vol 23*, Eds.: P. Diehl, **1990**.
[54] S. Huzinaga, *Ph. D. thesis*, University of Alberta, Edmonton, **1971**.
[55] S. Schinzel, R. Müller, M. Kaupp, *Theor. Chem. Acc.* **2008**, *120*, 437.
[56] V. G. Malkin, O. L. Malkina, R. Reviakine, A. V. Arbouznikov, M. Kaupp, B. Schimmelpfennig, I. Malkin, T. Helgaker, K. Ruud, *MAG-Respect, Version 1.2* **2003**.
[57] B. A. Hess, C. M. Marian, U. Wahlgren, O. Gropen, *Chem. Phys. Lett.* **1996**, *251*, 365.
[58] B. Schimmelpfennig, *Ph.D. thesis*, Stockholms Universitet, **1996**.
[59] A. T. Amos, G. G. Hall, *Proc. Roy. Soc. London A* **1961**, *263*, 483.
[60] I. Zilberberg, S. P. Ruzankin, S. Malykhin, G. M. Zhidomirov, *Chem. Phys. Lett.* **2004**, *394*, 392.
[61] I. Zilberberg, S. P. Ruzankin, *Chem. Phys. Lett.* **2004**, *394*, 165.
[62] P. E. M. Siegbahn, J. Westerberg, M. Svensson, R. H. Crabtree, *J. Phys. Chem. B* **1998**, *102*, 1615.
[63] P. E. M. Siegbahn, *Curr. Opin. Chem. Biol.* **2002**, *6*, 227.
[64] E. Sigfridsson, M. H. M. Olsson, U. Ryde, *Inorg. Chem.* **2001**, *40*, 2509.
[65] M. Pavlov, M. R. A. Blomberg, P. E. M. Siegbahn, *Int. J. Quant. Chem.* **1999**, *73*, 197.

[66] J. Messinger, *Phys. Chem. Chem. Phys.* **2004**, *6*, 4764.
[67] J. Messinger, J. H. Robblee, U. Bergmann, C. Fernandez, P. Glatzel, H. Visser, R. M. Cinco, K. L. McFarlane, E. Bellacchio, S. A. Pizarro, S. P. Cramer, K. Sauer, M. P. Klein, V. K. Yachandra, *J. Am. Chem. Soc.* **2001**, *123*, 7804.
[68] K. A. Ahrling, P. J. Smith, R. J. Pace, *J. Am. Chem. Soc.* **1998**, *120*, 13202.
[69] Ö. Hansson, R. Aasa, T. Vänngard, *Biophys. J.* **1987**, *51*, 825.
[70] L. V. Kulik, W. Lubitz, J. Messinger, *Biochemistry* **2005**, *44*, 9368.
[71] G. A. Lorigan, R. D. Britt, *Biochemistry* **1994**, *33*, 12072.
[72] G. A. Lorigan, R. D. Britt, *Photosynth. Res.* **2001**, *66*, 189.
[73] H. Dau, M. Haumann, *Coord. Chem. Rev.* **2008**, *252*, 273.
[74] J. Yano, Y. Pushkar, J. Messinger, U. Bergmann, P. Glatzel, V. K. Yachandra, *AIP Conf. Proc.* **2007**, *882*, 316.
[75] K. O. Schaefer, R. Bittl, F. Lendzian, V. Barynin, T. Weyhermueller, K. Wieghardt, W. Lubitz, *J. Phys. Chem. B* **2003**, *107*, 1242.
[76] C. I. H. Ashby, C. P. Cheng, E. N. Duesler, T. L. Brown, *J. Am. Chem. Soc.* **1978**, *100*, 6063.

Appendix A

Table A1. Influence of the terminal ligand on interatomic distances (in Å) in (μ-O)$_2$ bridged model complexes.[a]

		Mn-Mn	*Mn^{III}-O1*	*Mn^{III}-O2*	*Mn^{IV}-O1*	*Mn^{IV}-O2*
$[(NH_3)_4Mn(\mu\text{-}O)_2Mn(NH_3)_4]^{3+}$	HS	2.769	1.897	1.897	1.776	1.776
	BS	2.776	1.891	1.888	1.765	1.784
$[(dab)_2Mn(\mu\text{-}O)_2Mn(dab)_2]^{3+}$	HS	2.727	1.888	1.888	1.758	1.758
	BS	2.734	1.875	1.875	1.751	1.751
$[(bipy)_2Mn(\mu\text{-}O)_2Mn(bipy)_2]^{3+}$	HS	2.761	1.898	1.899	1.779	1.779
	BS	2.761	1.883	1.894	1.772	1.767
	Exp.[a]	2.716	1.853	1.856	1.784	1.784
$[(phen)_2Mn(\mu\text{-}O)_2Mn(phen)_2]^{3+}$	HS	2.754	1.897	1.897	1.777	1.777
	BS	2.755	1.886	1.885	1.767	1.767
	Exp.[b]	2.748	1.802	1.802	1.798	1.798

[a]X-ray studies taken from ref. [1]. [b]X-ray studies taken from ref. [2].

Table A2. Influence of the bridge on interatomic distances (in Å) in tacn model complexes.[a]

		Mn-Mn	*Mn^{III}-O1*	*Mn^{III}-O2a*	*Mn^{III}-O3a*	*Mn^{IV}-O1*	*Mn^{IV}-O2b*	*Mn^{IV}-O3b*
$[(tacn)(H_20)Mn_2(\mu\text{-}O)(H_2O)(tacn)]^{5+}$	HS	3.835	2.113	-	-	1.730	-	-
	BS	3.801	2.086	-	-	1.724	-	-
$[(tacn)(H_2O)Mn_2(\mu\text{-}O)_2(tacn)]^{3+}$	HS	2.720	1.883	1.876	-	1.785	1.786	-
	BS	2.713	1.872	1.866	-	1.778	1.778	-
$[tacnMn(\mu\text{-}O)(\mu\text{-}OOAc)Mnmtacn]^{4+}$	HS	3.404	1.89	1.928	-	1.766	1.913	-
	BS	3.422	1.958	1.934	-	1.709	1.908	-
$[(tacn)Mn_2(\mu\text{-}O)_2(\mu\text{-}OAc)(tacn)]^{2+}$	HS	2.663	1.883	1.878	2.224	1.784	1.785	1.92
	BS	2.645	1.873	1.866	2.224	1.778	1.779	1.922
	Exp.[a]	2.588	1.817	1.808	2.079	1.817	1.808	2.079
$[tacnMn(\mu\text{-}O)(\mu\text{-}OOAc)_2Mntacn]^{3+}$	HS	3.198	1.867	2.111	2.058	1.772	1.906	1.915
	BS	3.210	1.843	2.116	2.061	1.759	1.908	1.917
	Exp.[b]	3.230	1.826	1.999	1.948	1.814	1.951	2.000

[a]X-ray studies from ref. [3], the mixed-valent cation possesses crystallographically imposed C_2 symmetry.
[b]X-ray studies from ref. [4].

Table A3. Influence of terminal ligand on Mulliken atomic spin densities and S^2 expectation values of HS and BS states of $(\mu\text{-O})_2$ bridged complexes.[a]

	Mn^{III}	Mn^{IV}	*O1*	*O2*	$\langle S^2 \rangle$
$[(NH_3)_4Mn(\mu\text{-O})_2Mn(NH_3)_4]^{3+}$	3.97	-2.76	-0.19	-0.19	3.77
$[(dab)_2Mn(\mu\text{-O})_2Mn(dab)_2]^{3+}$	3.93	-2.60	-0.23	-0.23	3.75
$[(bipy)_2Mn(\mu\text{-O})_2Mn(bipy)_2]^{3+}$	3.95	-2.69	-0.21	-0.21	3.77
$[(phen)_2Mn(\mu\text{-O})_2Mn(phen)_2]^{3+}$	3.95	-2.69	-0.21	-0.21	3.77

[a]B3LYP single-point calculation with 9s7p4d basis for Mn and IGLO-II basis for the ligand atoms.

Table A4. Influence of the bridge on Mulliken atomic spin densities and S^2 expectation values of the BS state of tacn-based complexes.[a]

	Mn^{III}	Mn^{IV}	*O1*	*O2a*	*O3a*	*O2b*	*O3b*	$\langle S^2 \rangle$
$[(tacn)(H_20)Mn_2(\mu\text{-O})(H_2O)(tacn)]^{5+}$	4.22	-3.26	-0.09	-	-	-	-	4.08
$[(tacn)(H_2O)Mn_2(\mu\text{-O})_2(tacn)]^{3+}$	3.91	-2.77	-0.16	-0.15	-	-	-	3.77
$[tacnMn(\mu\text{-O})(\mu\text{-OAc})Mnmtacn]^{4+}$	4.02	-3.15	-0.07	-0.03	-	0.02	-	3.91
$[(tacn)Mn_2(\mu\text{-O})_2(\mu\text{-OAc})(tacn)]^{2+}$	3.88	-2.74	-0.16	-0.14	0.02	-	0.04	3.76
$[tacnMn(\mu\text{-O})(\mu\text{-OAc})_2Mntacn]^{3+}$	3.93	-2.94	-0.18	0.01	-0.01	0.03	0.03	3.81

[a]B3LYP single-point calculation with 9s7p4d basis for Mn and IGLO-II basis for the ligand atoms.

Table A5. Expansion coefficients and set of restricted determinants for the PO-based expansion of the unrestricted BS determinant of $[(bipy)_2Mn(\mu\text{-}O)_2Mn(bipy)_2]^{3+}$.[a]

C_i		D_i[*paired orbital*]	C_i		D_i[*paired orbital*]
C_0	$0.668 \cdot 10^{-2}$	D_0	C_3	$-0.302 \cdot 10^{-1}$	D_3([191,201],[194,198], [195,197])
C_1	$-0.108 \cdot 10^{-2}$	D_1([191,201]	C_2	$0.592 \cdot 10^{-2}$	D_2([191,201],[195,197])
C_2	$0.311 \cdot 10^{-3}$	D_2([191,201],[192,200])	C_1	$-0.191 \cdot 10^{-2}$	D_1([192,200])
C_2	$0.523 \cdot 10^{-2}$	D_2([191,201],[193,199])	C_2	$0.925 \cdot 10^{-2}$	D_2([192,200],[193,199])
C_2	$0.553 \cdot 10^{-2}$	D_2([191,201],[194,198])	C_3	$-0.471 \cdot 10^{-1}$	D_3([192,200],[193,199], [194,198])
C_2	$0.592 \cdot 10^{-2}$	D_2([191,201],[195,197])	C_4	0.257	D_4([192,200],[193,199], [194,198], [195,197])
C_3	$0.150 \cdot 10^{-2}$	D_3([191,201],[192,200], [193,199])	C_3	$-0.505 \cdot 10^{-1}$	D_3([192,200],[193,199], [195,197])
C_4	$0.766 \cdot 10^{-2}$	D_4([191,201],[192,200], [193,199], [194,198])	C_2	$0.978 \cdot 10^{-2}$	D_2([192,200],[194,198])
C_5	$-0.418 \cdot 10^{-1}$	D_5([191,201],[192,200], [193,199], [194,198], [195,197])	C_3	$-0.533 \cdot 10^{-1}$	D_3([192,200],[194,198], [195,197])
C_4	$0.821 \cdot 10^{-2}$	D_4([191,201],[192,200], [193,199], [195,197])	C_2	$0.104 \cdot 10^{-1}$	D_2([192,200],[195,197])
C_3	$-0.158 \cdot 10^{-2}$	D_3([191,201],[192,200], [194,198])	C_1	$-0.322 \cdot 10^{-1}$	D_1([193,199])
C_4	$0.86 \cdot 10^{-2}$	D_4([191,201],[192,200], [194,198], [195,197])	C_2	0.164	D_2([193,199],[194,198])
C_3	$0.170 \cdot 10^{-2}$	D_3([191,201],[192,200], [195,197])	C_3	-0.896	D_3([193,199],[194,198], [195,197])
C_2	$0.523 \cdot 10^{-2}$	D_2([191,201],[193,199])	C_2	0.175	D_2([193,199],[195,197])
C_3	$-0.266 \cdot 10^{-1}$	D_3([191,201],[193,199], [194,198])	C_1	$-0.340 \cdot 10^{-1}$	D_1([194,198])
C_4	0.145	D_4([191,201],[193,199], [194,198], [195,197])	C_2	0.185	D_2([194,198],[195,197])
C_3	$-0.285 \cdot 10^{-1}$	D_3([191,201],[193,199], [195,197])	C_1	$-0.364 \cdot 10^{-1}$	D_1([195,197])
C_2	$0.553 \cdot 10^{-2}$	D2([191,201],[194,198])			

Sum $(i \cdot [C_i^2])$	$\langle S^2 \rangle_{unrestricted} - \langle S^2 \rangle_{exact}$	$\langle S^2 \rangle_{unrestricted}$
2.99	3.02	3.77

[a]B3LYP results. Cf. eq. (3.37).

Table A6. Dependence of Heisenberg exchange coupling constant J (in cm^{-1}) of $[(bipy)_2Mn(\mu\text{-}O)_2Mn(bipy)_2]^{3+}$ on the functional.[a]

	Noodleman		**Yamaguchi**		**Ruiz**[b]	
	SVP	*EPR*	*SVP*	*EPR*	*SVP*	*EPR*
BLYP	-	-272	-	-263	-	-136
B3LYP	-141	-136	-140	-134	-71	-68
BHLYP	-	-71	-	-71	-	-36
B60LYP	-	-50	-	-50	-	-25
B70LYP	-	-34	-	-33	-	-17
B80LYP	-	-26	-	-25	-	-13
B90LYP	-	-74	-	-73	-	-37
Exp.[c]		-148				

[a]SVP: E_{bs} and E_{hs} from optimized structures (B3LYP/SVP) in broken-symmetry and high-spin state, respectively. EPR: SP calculations (B3LYP/9s7p4d for Mn and IGLO-II for N,O,H,C.) at the B3LYP/SVP optimized structures. [b]Evaluation of J using the BS DFT formula from eq. (3.35).[5-7] [c]Experimental J value from ref. [2].

Table A7. Influence of terminal ligand set on Heisenberg exchange coupling constant J (in cm^{-1}) in $(\mu\text{-}O)_2$ bridged complexes.[a]

	Noodleman		**Yamaguchi**		**Exp.**[b]
	SVP	*EPR*	*SVP*	*EPR*	
$[(NH_3)_4Mn(\mu\text{-}O)_2Mn(NH_3)_4]^{3+}$	-132	-122	-131	-121	
$[(dab)_2Mn(\mu\text{-}O)_2Mn(dab)_2]^{3+}$	-154	-145	-153	-144	
$[(bipy)_2Mn(\mu\text{-}O)_2Mn(bipy)_2]^{3+}$	-141	-136	-140	-134	-148
$[(phen)_2Mn(\mu\text{-}O)_2Mn(phen)_2]^{3+}$	-142	-136	-141	-135	-148

[a]SVP: E_{bs} and E_{hs} from optimized structures (B3LYP/SVP) in broken-symmetry and high-spin state, respectively. EPR: SP calculations (B3LYP/9s7p4d for Mn and IGLO-II for N,O,H,C.) at the B3LYP/SVP optimized structures [b]Experimental J value from ref. [2].

Table A8. Dependence of individual contributions (eqs. (4.39,4.40,4.43)) to the g-tensor of **2-(μ-O)$_2$** on functional.[a]

		g_{iso}	g_{11}	g_{22}	g_{33}
BLYP	g_{HS}	2.0006	1.9980	2.0017	2.0021
	g_{BS}	1.9995	1.9762	2.0096	2.0126
	g_1 [Mn^{III}]	1.9972	1.9903	2.0002	2.0010
	g_2 [Mn^{IV}]	1.9952	1.9975	1.9939	1.9943
	g	2.0001	1.9889	2.0050	2.0065
B3LYP	g_{HS}	1.9988	1.9961	2.0000	2.0005
	g_{BS}	1.9995	1.9762	2.0096	2.0126
	g_1 [Mn^{III}]	1.9989	1.9936	2.0012	2.0020
	g_2 [Mn^{IV}]	1.9987	1.9994	1.9983	1.9984
	g	1.9991	1.9878	2.0040	2.0055
BHLYP	g_{HS}	1.9963	1.9934	1.9975	1.9981
	g_{BS}	2.0030	1.9685	2.0193	2.0213
	g_1 [Mn^{III}]	1.9972	1.9903	2.0002	2.0010
	g_2 [Mn^{IV}]	1.9952	1.9975	1.9939	1.9943
	g	1.9991	1.9830	2.0066	2.0078
B-60LYP	g_{HS}	1.9958	1.9927	1.9970	1.9976
	g_{BS}	2.0014	1.9607	2.0205	2.0231
	g_1 [Mn^{III}]	1.9965	1.9887	2.0000	2.0008
	g_2 [Mn^{IV}]	1.9948	1.9980	1.9931	1.9934
	g	1.9981	1.9794	2.0068	2.0082
B-70LYP	g_{HS}	1.9953	1.9919	1.9968	1.9973
	g_{BS}	1.9974	1.9491	2.0193	2.0238
	g_1 [Mn^{III}]	1.9956	1.9865	1.9996	2.0006
	g_2 [Mn^{IV}]	1.9950	1.9990	1.9930	1.9929
	g	1.9962	1.9741	2.0062	2.0083
B-80LYP	g_{HS}	1.9949	1.9909	1.9967	1.9971
	g_{BS}	1.9932	1.9370	2.0168	2.0258
	g_1 [Mn^{III}]	1.9947	1.9841	1.9992	2.0006
	g_2 [Mn^{IV}]	1.9952	1.9998	1.9934	1.9923
	g	1.9942	1.9684	2.0051	2.0090
B-90LYP	g_{HS}	1.9945	1.9895	1.9969	1.9972
	g_{BS}	2.0013	1.9497	1.9970	2.0571
	g_1 [Mn^{III}]	1.9954	1.9846	1.9969	2.0047
	g_2 [Mn^{IV}]	1.9934	1.9962	1.9969	1.9872
	g	1.9940	1.9677	2.0052	2.0091

Table A9. ^{14}N Hyperfine and nuclear quadrupole couplings (in MHz).[a]

			a_{iso} *(site)*	A_{iso}	T_1	T_2	T_3	$\lvert e^2qQ\rvert$	$\lvert\eta\rvert$	$\rho^{\alpha-\beta}$
2-(μ-O)$_2$	Mn^{III}	N1	7.3	14.6	-2.0	-1.7	3.7	3.83	0.07	0.027
		N2	0.3	0.6	-0.9	-0.6	1.5	3.09	0.07	-0.029
	Mn^{IV}	N3	-2.5	2.5	-0.5	0.0	0.5	2.28	0.30	0.044
		N4	-2.9	1.9	-0.4	0.1	0.2	2.91	0.09	0.034
	Exp.[b]			2.8				2.3		
	Exp.[c]			9.5				2.9		
3-(μ-O)$_2$	Mn^{III}	N1	6.4	12.8	-1.9	-1.7	3.6	3.81	0.07	0.026
		N2	0.2	0.3	-1.0	-0.6	1.8	3.04	0.09	-0.029
	Mn^{IV}	N3	-2.5	2.5	-0.6	0.0	0.6	2.21	0.31	0.046
		N4	-1.9	1.9	-0.4	0.2	0.3	2.87	0.11	0.035
	Exp.[c]			9.7				3.0		
4-(μ-O)$_2$(μ-OAc)	Mn^{III}	N1	-1.3	-2.5	-0.4	-0.2	0.6	3.89	0.23	-0.038
		N2	-0.6	-1.2	-0.6	-0.5	1.1	3.98	0.22	-0.029
		N3	5.4	10.8	-2.4	-2.2	4.5	5.45	0.09	0.041
	Mn^{IV}	N4	-1.4	1.4	-0.2	0.1	0.1	3.77	0.25	0.032
		N5	-1.5	1.5	-0.2	0.0	0.1	3.72	0.30	0.037
		N6	-1.4	1.4	-0.3	-0.2	0.5	3.68	0.09	0.045
	Exp.[c]			9.7				3.0		
5-(μ-O)$_2$(μ-OAc)	Mn^{III}	N1	-0.8	-1.6	-0.5	-0.3	0.8	3.93	0.23	-0.035
		N2	-0.9	-1.8	-0.5	-0.3	0.8	3.86	0.22	-0.037
		N3	5.9	11.7	-2.2	-2.1	4.4	4.89	0.15	0.044
	Mn^{IV}	N4	-1.5	1.5	-0.1	0.0	0.1	3.75	0.26	0.035
		N5	-1.7	1.7	-0.1	0.0	0.1	2.36	0.27	0.039
		N6	-1.0	1.0	-0.1	-0.1	0.2	3.32	1.0	0.042
	Exp.[c]			9.6				2.20		
Mn-cat	Mn^{III}	N1	-2.4	-4.7	-0.8	-0.5	1.3	2.63	0.53	-0.038
	Mn^{IV}	N2	-2.7	2.7	-0.5	0.2	0.3	2.64	0.51	0.032
	Exp.[d]			|2.45|				2.34	0.51	

[a]B3LYP results. A_{iso} is the total isotropic value, T_i represent the traceless part of the full **A** tensor, $|e^2QC|$ denote the electric quadrupole coupling and $|\eta|$ the asymmetry parameter. $\rho^{\alpha-\beta}$ represents the Mulliken spin density at the nitrogen atom. [b]ENDOR studies from ref. [8]. [c]ENDOR studies from ref. [9]. [d]ESEEM studies from ref. [10].

Table A10. ^{1}H Hyperfine couplings (in MHz) of $[(bipy)_2Mn(\mu\text{-}O)_2Mn(bipy)_2]^{3+}$.[a]

	Mn^{III}						**Mn^{IV}**				
	A_{iso}	T_1	T_2	T_3	$\rho^{\alpha-\beta}$		A_{iso}	T_1	T_2	T_3	$\rho^{\alpha-\beta}$
H1	1.2	-6.7	-2.1	8.8	0.001	H9	1.2	-6.2	-0.2	6.4	0.000
H2	0.5	-1.0	-0.5	1.5	0.001	H10	-0.2	-0.8	-0.1	0.9	0.000
H3	-0.1	-0.6	-0.4	1.0	0.000	H11	0.3	-0.5	0.1	0.4	0.000
H4	0.5	-0.9	-0.7	1.6	0.001	H12	0.4	-0.7	0.2	0.5	0.001
H5	0.0	-0.9	-0.7	1.6	0.000	H13	0.2	-0.6	0.3	0.4	0.000
H6	-0.4	-0.6	-0.5	1.1	0.000	H14	0.1	-0.4	0.2	0.2	0.000
H7	0.2	-0.9	-0.7	1.5	0.000	H15	0.0	-0.6	0.2	0.3	0.000
H8	-0.3	-4.8	-3.6	8.4	0.000	H16	0.6	-3.4	1.5	1.9	0.001
Exp.[b]		-5.1	-4.4	9.8				*-3.4*	1.2	2.4	
		-6.2	-3.4	9.8				*-1.2*	*-1.2*	2.4	
		-7.9	-1.2	9.8				*-0.4*	*-1.2*	1.2	
		-7.9	-1.2	7.9				*-0.4*	*-0.4*	1.2	

[a]B3LYP results. A_{iso} is the total isotropic value, T_i represent the traceless part of the full **A** tensor. $\rho^{\alpha-\beta}$ represents the Mulliken spin density at the hydrogen atom [b]ENDOR studies, error ±0.02 MHz; the isotropic part A_{iso} of the experimental tensor is smaller than 0.5 MHz in all cases, from ref. [9].

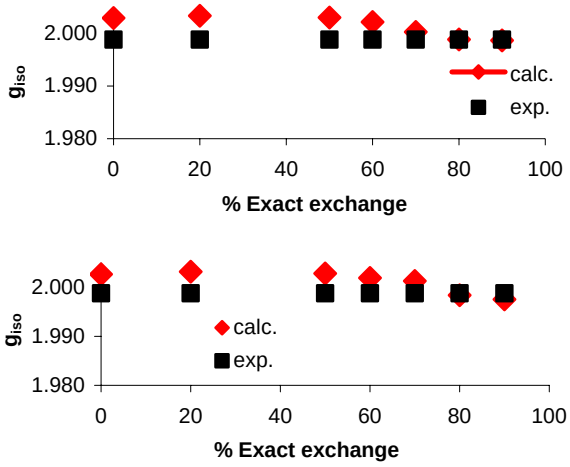

Figure A1. Dependence of g_{iso} on the amount of exact-exchange admixture for **Mn-cat**. The figure on the top shows the g_{iso} values on the structure optimized in the BS state. The figure on the bow shows the g_{iso} values on the X-ray structure.

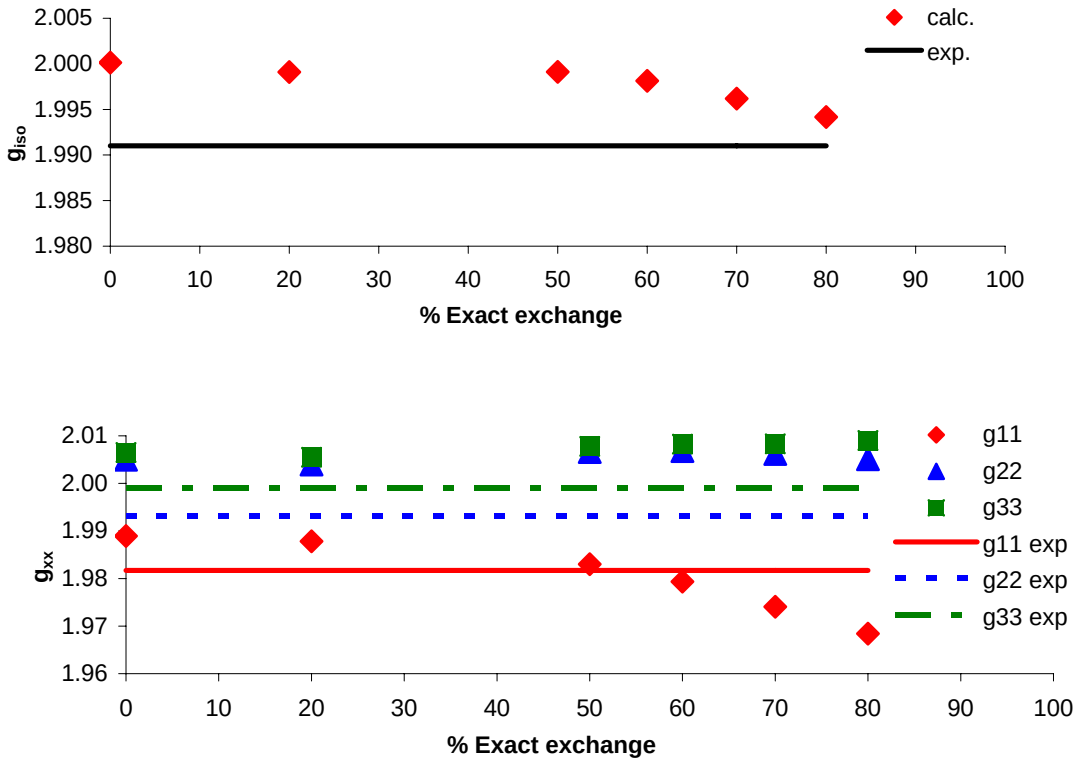

Figure A2. Dependence of g_{iso}, as well as g_{11}, g_{22}, and g_{33} for **2-(μ-O)$_2$** on the amount of exact-exchange admixture. Experimental values taken from ref. [11].

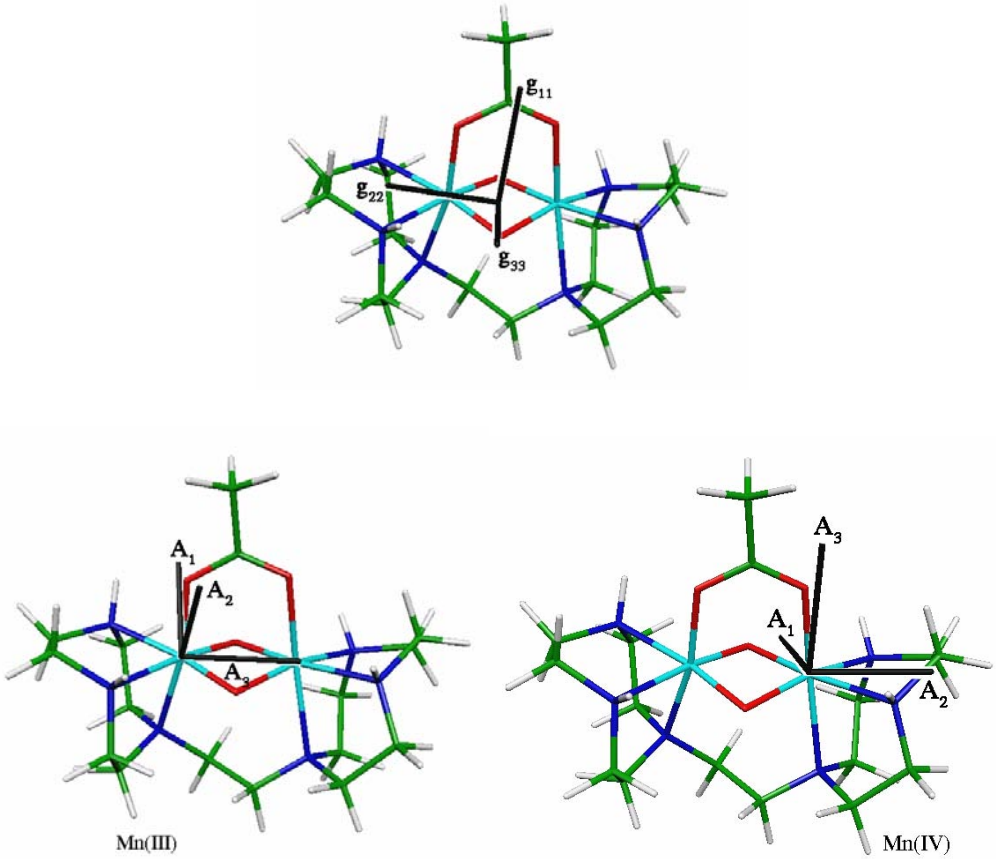

Figure A3. Orientation of g-tensor and manganese hyperfine tensors of $[(dtne)Mn(\mu\text{-}O)_2(\mu\text{-}OAc)Mn]^{2+}$ (B3LYP results).

References – Appendix A

[1] P. M. Plaksin, R. C. Stoufer, M. Mathew, G. J. Palenik, *J. Am. Chem. Soc.* **1972**, *94*, 2121.
[2] M. Stebler, A. Ludi, H. B. Buergi, *Inorg. Chem.* **1986**, *25*, 4743.
[3] K. Wieghardt, U. Bossek, L. Zsolnai, G. Huttner, G. Blondin, J.-J. Girerd, F. Babonneau, *J. Chem. Soc. Chem. Commun.* **1987**, 651.
[4] K. Wieghardt, U. Bossek, J. Bonvoisin, P. Beauvillain, J.-J. Girerd, B. Nuber, J. Weiss, J. Heinze, *Angew. Chem.* **1986**, *98*, 1026.
[5] E. Ruiz, *Structure and Bonding* **2004**, *113*, 71.
[6] E. Ruiz, A. Rodriguez-Fortea, J. Cano, S. Alvarez, P. Alemany, *J. Comput. Chem.* **2003**, *24*, 982.
[7] E. Ruiz, J. Cano, S. Alvarez, P. Alemany, *J. Am. Chem. Soc.* **1998**, *120*, 11122.
[8] R. D. Britt, *Ph.D. Thesis*, Lawrence Berkeley Laboratory, **1988**.
[9] K.-O. Schafer, R. Bittl, W. Zweygart, F. Lendzian, G. Haselhorst, T. Weyhermuller, K. Wieghardt, W. Lubitz, *J. Am. Chem. Soc.* **1998**, *120*, 13104.
[10] A. Ivancich, V. V. Barynin, J.-L. Zimmermann, *Biochemistry* **1995**, *34*, 6628.
[11] C. Teutloff, K.-O. Schaefer, S. Sinnecker, V. Barynin, R. Bittl, K. Wieghardt, F. Lendzian, W. Lubitz, *Magn. Reson. Chem.* **2005**, *43*, S51.

Appendix B

Table B1. Distances [Å] and relative stabilites [kJ/mol] of the HS and different BS states for **Ferreira**$^{+1}$.

	*A*BCD (HS)	*A*B$\overline{\text{C}}\overline{\text{D}}$	*A*$\overline{\text{B}}$C$\overline{\text{D}}$	*A*$\overline{\text{B}}\overline{\text{C}}$D	X-ray[a]
Mn_A-Mn_B	3.731	3.735	3.710	3.728	3.226
Mn_A-Mn_C	3.751	3.735	3.781	3.760	3.245
Mn_A-Mn_D	5.387	5.391	5.404	5.403	5.124
Mn_B-Mn_C	2.775	2.760	2.759	2.763	2.722
Mn_B-Mn_D	2.794	2.799	2.795	2.797	2.677
Mn_C-Mn_D	2.830	2.824	2.835	2.834	2.657
Ca-Mn_A	5.082	5.074	5.090	5.084	3.951
Ca-Mn_B	5.342	5.339	5.306	5.315	3.371
Ca-Mn_C	3.996	3.988	3.983	3.981	3.393
Ca-Mn_D	3.926	3.922	3.911	3.906	3.344
Mn_C-N_{Im}	2.175	2.085	2.084	2.082	2.015
ΔE_{rel} [b]	75.6	8.6	5.4	0.0	-
$\langle S^2 \rangle$ [b]	49.38	6.92	6.91	6.88	-

[a] X-ray structure at 3.5 Å from Ref. [1]. [b]B3LYP/II//B3LYP/SVP results for relative energies and $\langle S^2 \rangle$, see Computational Details.

Table B2. Distances [Å] and relative stabilites [kJ/mol] of the HS and different BS states for **Ferreira-2**$^{+1}$.

	A*B*CD (HS)	A*B*$\overline{\text{C}}\overline{\text{D}}$	$\overline{\text{A}}$*B*C$\overline{\text{D}}$	$\overline{\text{A}}$*B*$\overline{\text{C}}$D	X-ray[a]
Mn_A-Mn_B	3.666	3.652	3.639	3.638	3.226
Mn_A-Mn_C	3.465	3.464	3.461	3.461	3.245
Mn_A-Mn_D	5.118	5.122	5.113	5.118	5.124
Mn_B-Mn_C	2.918	2.893	2.914	2.900	2.722
Mn_B-Mn_D	2.800	2.798	2.799	2.797	2.677
Mn_C-Mn_D	2.846	2.839	2.852	2.852	2.657
Ca-Mn_A	4.958	4.962	4.964	4.960	3.951
Ca-Mn_B	5.457	5.447	5.443	5.436	3.371
Ca-Mn_C	3.954	3.951	3.944	3.957	3.393
Ca-Mn_D	3.866	3.869	3.862	3.865	3.344
Mn_C-N_{Im}	2.099	2.089	2.086	2.096	2.015
ΔE_{rel} [b]	11.9	7.9	0.0	23.7	-
$\langle S^2 \rangle$ [b]	49.01	6.95	6.89	6.88	-

[a] X-ray structure at 3.5 Å from Ref. [1]. [b]See footnote b of Table B1.

Table B3. Distances [Å] and relative stabilites [kJ/mol] of the HS and different BS states for **Dau**$^{+1}$.

	*A*BC*D* (HS)	*A*B$\bar{C}\bar{D}$	*A*$\bar{B}$C$\bar{D}$	*A*$\bar{B}\bar{C}$D
Mn_A-Mn_B	2.874	2.888	2.883	2.899
Mn_A-Mn_C	4.113	4.133	4.115	4.139
Mn_A-Mn_D	5.157	5.173	5.161	5.191
Mn_B-Mn_C	2.904	2.904	2.910	2.894
Mn_B-Mn_D	2.782	2.783	2.782	2.779
Mn_C-Mn_D	2.753	2.752	2.755	2.757
Ca-Mn_A	3.473	3.481	3.474	3.486
Ca-Mn_B	3.284	3.273	3.277	3.266
Ca-Mn_C	3.324	3.319	3.316	3.308
Ca-Mn_D	3.286	3.277	3.275	3.284
Mn_C-N_{Im}	2.087	2.088	2.087	2.086
ΔE_{rel} [a]	-9.2	0.0	10.2	11.5
$<S^2>$[a]	48.98	6.93	6.92	6.89

[a]See footnote b of Table B1.

Table B4. Distances [Å] and relative stabilites [kJ/mol] of the HS and different BS states for **Yano-I**^{0}.

	ABC*D* (HS)	$\bar{A}\bar{B}$C*D*	$\bar{A}$B$\bar{C}$*D*	A$\bar{B}\bar{C}$*D*	exp.[a]
Mn_A-Mn_B	2.714	2.716	2.706	2.707	2.729
Mn_A-Mn_C	4.993	5.002	5.005	4.996	4.738
Mn_A-Mn_D	5.186	5.229	5.193	5.216	4.936
Mn_B-Mn_C	2.708	2.710	2.715	2.706	2.703
Mn_B-Mn_D	4.140	4.176	4.140	4.173	3.260
Mn_C-Mn_D	2.821	2.835	2.831	2.850	2.809
Ca-Mn_A	3.307	3.305	3.307	3.304	5.039
Ca-Mn_B	3.406	3.394	3.402	3.393	3.397
Ca-Mn_C	4.311	4.283	4.315	4.283	4.942
Ca-Mn_D	3.198	3.240	3.194	3.195	3.400
Mn_C-N_{Im}	2.052	2.053	2.052	2.053	-
ΔE_{rel} [b]	4.4	1.7	0.0	2.9	-
$<S^2>$[b]	48.94	6.94	6.89	6.90	-

[a]Structure I of polarized EXAFS study from Ref. [2]. [b]See footnote b of Table B1.

Table B5. Distances [Å] and relative stabilites [kJ/mol] of the HS and different BS states for **Yano-II-A6^0**.

	ABC*D* (HS)	$\overline{A}\overline{B}$C*D*	$\overline{A}$B$\overline{C}$*D*	A$\overline{B}\overline{C}$*D*	exp.[a]
Mn_A-Mn_B	2.704	2.706	2.706	2.707	2.721
Mn_A-Mn_C	4.734	4.740	4.742	4.732	4.956
Mn_A-Mn_D	5.361	5.362	5.350	5.333	5.495
Mn_B-Mn_C	2.782	2.782	2.790	2.780	2.700
Mn_B-Mn_D	3.472	3.462	3.463	3.440	3.285
Mn_C-Mn_D	2.829	2.829	2.817	2.815	2.804
Ca-Mn_A	3.130	3.131	3.130	3.127	3.607
Ca-Mn_B	3.478	3.476	3.498	3.495	3.398
Ca-Mn_C	4.517	4.527	4.538	4.535	4.364
Ca-Mn_D	3.564	3.573	3.577	3.571	3.395
Mn_C-N_{Im}	2.033	2.032	2.033	2.031	-
ΔE_{rel}[b]	15.8	0.0	0.9	2.1	-
$<S^2>$[b]	48.94	6.95	6.92	6.94	-

[a]Structure IIa of polarized EXAFS study from Ref. [2]. [b]See footnote b of Table B1.

Table B6. Distances [Å] and relative stabilites [kJ/mol] of the HS and different BS states for **Yano-II-D5^0**.

	ABC*D* (HS)	$\overline{A}\overline{B}$C*D*	$\overline{A}$B$\overline{C}$*D*	A$\overline{B}\overline{C}$*D*	exp.[a]
Mn_A-Mn_B	2.704	2.708	2.706	2.708	2.721
Mn_A-Mn_C	4.811	4.817	4.821	4.810	4.956
Mn_A-Mn_D	5.350	5.348	5.355	5.338	5.495
Mn_B-Mn_C	2.774	2.773	2.779	2.770	2.700
Mn_B-Mn_D	3.399	3.386	3.406	3.382	3.285
Mn_C-Mn_D	2.808	2.809	2.806	2.805	2.804
Ca-Mn_A	3.170	3.167	3.168	3.167	3.607
Ca-Mn_B	3.518	3.515	3.529	3.522	3.398
Ca-Mn_C	4.592	4.606	4.607	4.603	4.364
Ca-Mn_D	3.615	3.624	3.630	3.619	3.395
Mn_C-N_{Im}	2.033	2.032	2.035	2.031	-
ΔE_{rel}[b]	8.0	8.4	4.8	0.0	-
$<S^2>$[b]	48.95	6.87	6.84	6.93	-

[a]Structure IIa of polarized EXAFS study from Ref. [2]. [b]See footnote b of Table B1.

Table B7. Distances [Å] and relative stabilites [kJ/mol] of the HS and different BS states for **Yano-II^{+1}**.

	ABC*D* (HS)	A$\bar{B}\bar{C}$*D*	$\bar{A}$B$\bar{C}$*D*	$\bar{A}\bar{B}$C*D*	exp.[a]
Mn_A-Mn_B	2.709	2.716	2.714	2.711	2.721
Mn_A-Mn_C	4.828	4.828	4.835	4.834	4.956
Mn_A-Mn_D	5.404	5.386	5.402	5.401	5.495
Mn_B-Mn_C	2.790	2.786	2.796	2.792	2.700
Mn_B-Mn_D	3.505	3.479	3.501	3.491	3.285
Mn_C-Mn_D	2.862	2.853	2.855	2.860	2.804
Ca-Mn_A	3.113	3.111	3.115	3.111	3.607
Ca-Mn_B	3.368	3.374	3.374	3.363	3.398
Ca-Mn_C	4.264	4.270	4.266	4.274	4.364
Ca-Mn_D	3.429	3.426	3.429	3.435	3.395
Mn_C-N_{Im}	2.009	2.006	2.009	2.008	-
ΔE_{rel}[b]	1.7	0.0	7.8	1.7	-
$<S^2>$[b]	48.96	6.96	6.84	6.89	-

[a]Structure IIa of polarized EXAFS study from Ref. [2]. [b]See footnote b of Table B1.

Table B8. Distances [Å] and relative stabilites [kJ/mol] of the HS and different BS states for **Yano-III^{0}**.

	ABC*D* (HS)	A$\bar{B}\bar{C}$*D*	$\bar{A}$B$\bar{C}$*D*	$\bar{A}\bar{B}$C*D*	exp.[a]
Mn_A-Mn_B	2.717	2.718	2.720	2.718	2.721
Mn_A-Mn_C	5.143	5.154	5.162	5.142	4.970
Mn_A-Mn_D	5.525	5.481	5.500	5.514	5.456
Mn_B-Mn_C	2.787	2.788	2.793	2.783	2.720
Mn_B-Mn_D	3.733	3.677	3.700	3.717	3.251
Mn_C-Mn_D	2.846	2.826	2.827	2.844	2.804
Ca-Mn_A	3.725	3.730	3.731	3.718	4.375
Ca-Mn_B	3.360	3.363	3.362	3.357	3.732
Ca-Mn_C	3.362	3.384	3.383	3.368	3.401
Ca-Mn_D	3.413	3.408	3.408	3.417	3.403
Mn_C-N_{Im}	2.123	2.117	2.115	2.121	-
ΔE_{rel}[b]	1.1	0.0	34.0	0.3	-
$<S^2>$[b]	48.97	6.88	6.80	6.92	-

[a]Structure III of polarized EXAFS study from Ref. [2]. [b]See footnote b of Table B1.

Table B9. Relative stabilities [kJ/mol] of the HS and different BS states all EXAFS-based models **Yano** with identical atomic composition.

	ABC*D* (HS)	$\overline{A}\overline{B}$C*D*	$\overline{A}$B$\overline{C}$*D*	A$\overline{B}\overline{C}$*D*
Yano-I^0	4.4	1.7	0.0	2.9
Yano-II^0	61.1	46.3	46.8	48.3
Yano-II-A6^0	45.9	30.1	31.1	33.2
Yano-II-D5^0	39.2	39.6	36.0	31.2
Yano-III^0	55.7	55.0	88.7	54.6

Table B10. Dependence of NO occupation numbers and PO overlaps for **Yano-II-D5^0** on different BS states.[a]

NO number	$\overline{A}\overline{B}C\mathit{D}$	$\overline{A}B\overline{C}\mathit{D}$	$A\overline{B}\overline{C}\mathit{D}$
198	1.989 (0.989)	1.988 (0.988)	1.988 (0.988)
199	1.987 (0.987)	1.986 (0.986)	1.985 (0.985)
200	1.986 (0.986)	1.985 (0.985)	1.984 (0.984)
201	1.986 (0.986)	1.984 (0.984)	1.982 (0.982)
202	1.983 (0.983)	1.983 (0.983)	1.981 (0.981)
203	1.983 (0.983)	1.980 (0.980)	1.978 (0.978)
204	1.979 (0.979)	1.979 (0.979)	1.977 (0.977)
205	1.201 (0.201)	1.212 (0.212)	1.212 (0.212)
206	1.167 (0.167)	1.171 (0.171)	1.171 (0.171)
207	1.069 (0.069)	1.113 (0.113)	1.113 (0.113)
208	1.028 (0.028)	1.061 (0.061)	1.061 (0.061)
209	1.011 (0.011)	1.027 (0.027)	1.027 (0.027)
210	1.000 (0.000)	1.010 (0.010)	1.010 (0.010)
211	1.000 (SOMO)	1.000 (SOMO)	1.000 (SOMO)
212	0.998 (0.002)	0.979 (0.021)	0.990 (0.010)
213	0.989 (0.011)	0.965 (0.035)	0.973 (0.027)
214	0.972 (0.028)	0.923 (0.077)	0.938 (0.062)
215	0.931 (0.069)	0.887 (0.113)	0.886 (0.114)
216	0.833 (0.167)	0.826 (0.174)	0.828 (0.172)
217	0.792 (0.208)	0.739 (0.260)	0.787 (0.212)
218	0.020 (0.980)	0.021 (0.979)	0.023 (0.977)
219	0.017 (0.983)	0.019 (0.981)	0.022 (0.978)
220	0.017 (0.983)	0.017 (0.983)	0.018 (0.981)
221	0.014 (0.986)	0.016 (0.984)	0.017 (0.983)
222	0.014 (0.986)	0.015 (0.985)	0.015 (0.985)
223	0.013 (0.987)	0.013 (0.987)	0.015 (0.985)
224	0.010 (0.990)	0.012 (0.988)	0.012 (0.988)

[a]See Figures B1 – B3 for the thirteen magnetic NOs 205-217.

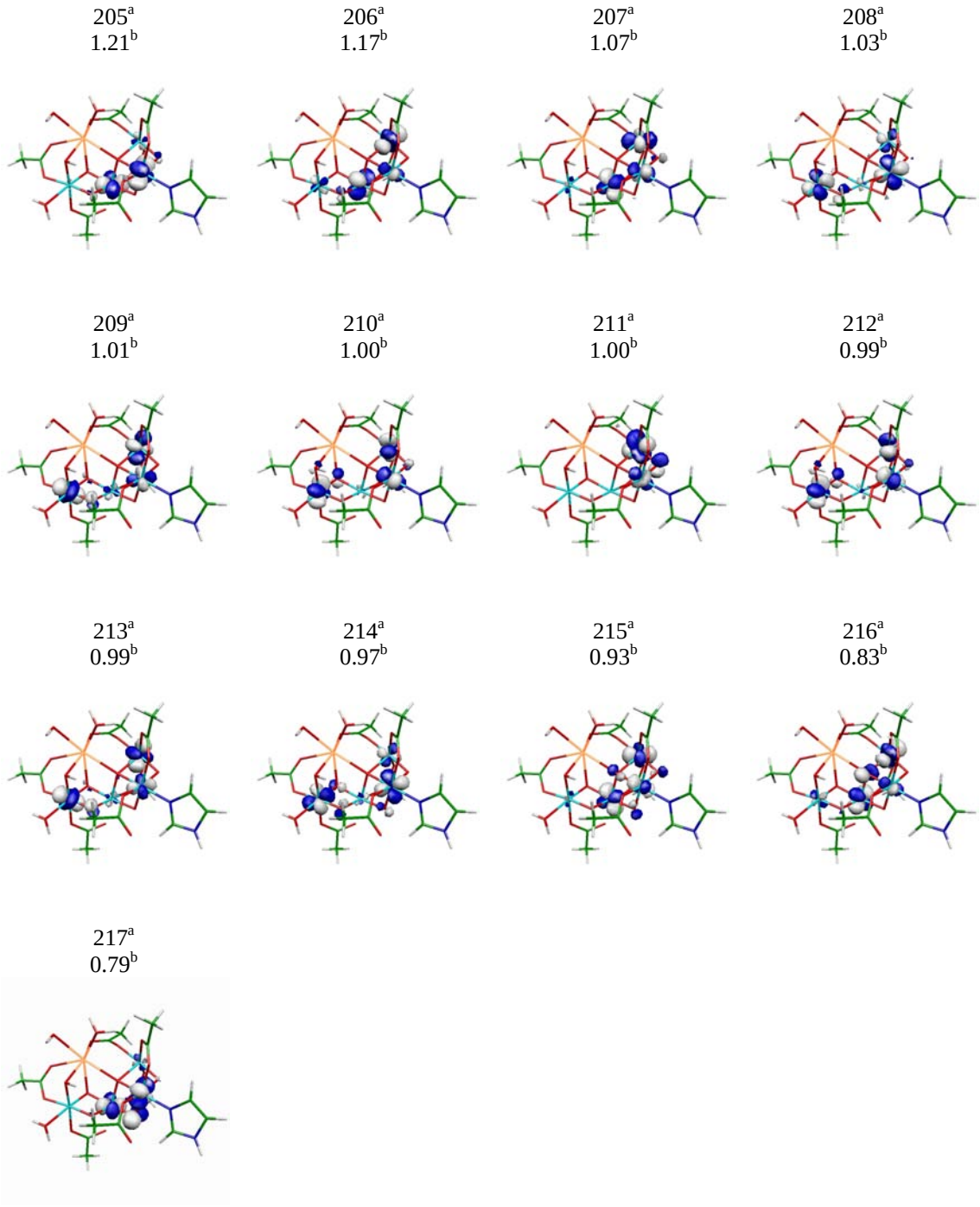

Figure B1. Active (magnetic) NO's for **Yano-II-D5^{0}** ($\overline{A}\overline{B}CD$) (isosurfaces ±0.05 a.u.). [a]Orbital Number. [b]NO occupation number.

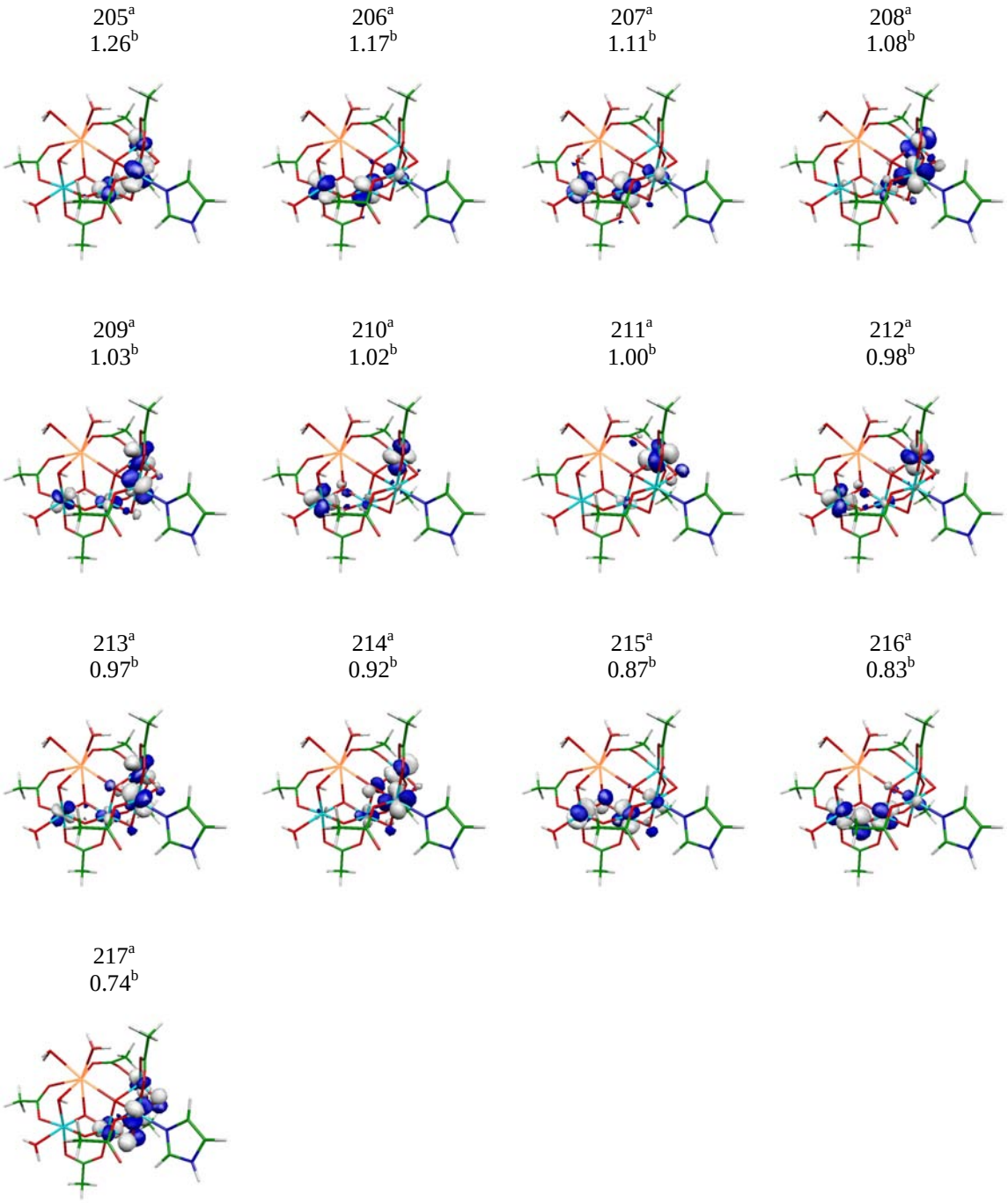

Figure B2. Active (magnetic) NO's for **Yano-II-D5^{0}** ($\overline{A}B\overline{C}D$) (isosurfaces ±0.05 a.u.). [a]Orbital Number. [b]NO occupation number.

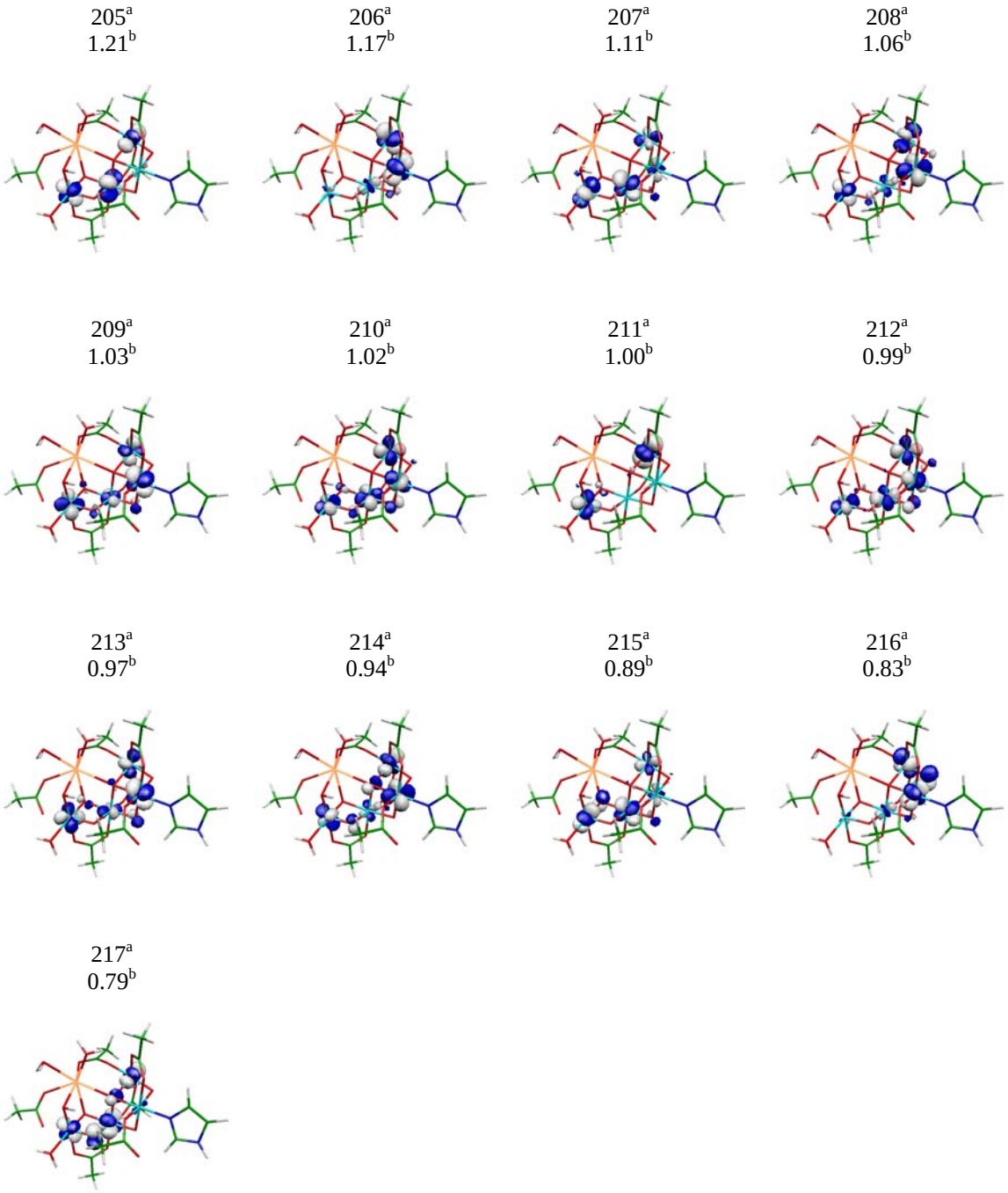

Figure B3. Active (magnetic) NO's for **Yano-II-D5^0** ($A\overline{B}\overline{C}D$) (isosurfaces ±0.05 a.u.). [a]Orbital Number. [b]NO occupation number.

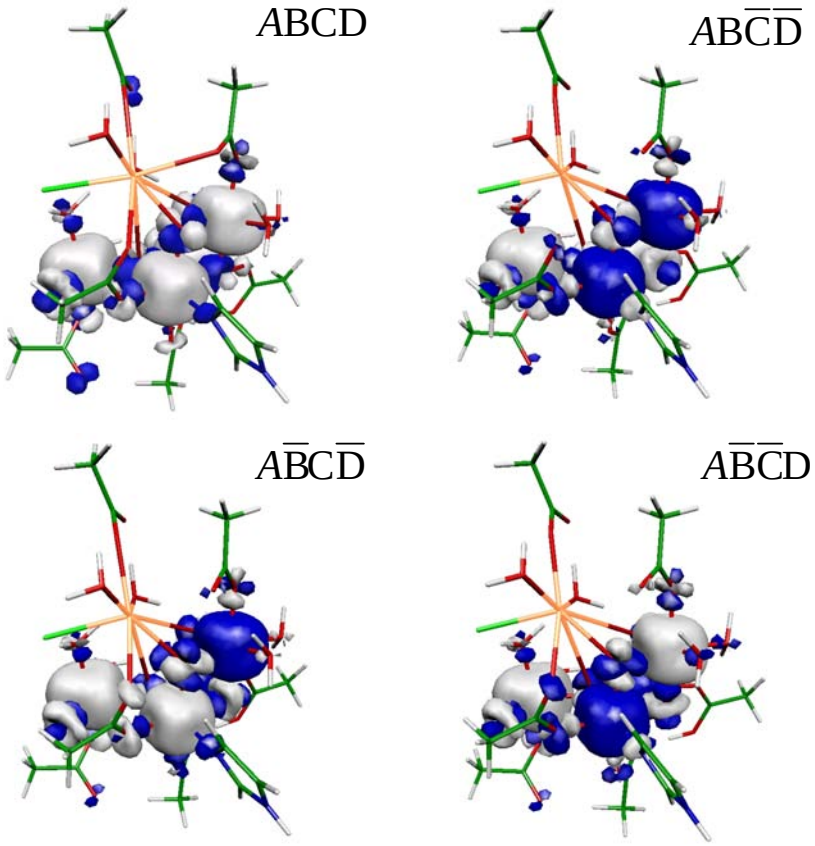

Figure B4. Spin-density plots of **Ferreira**$^{+1}$. Isosurfaces ± 0.003 a.u.

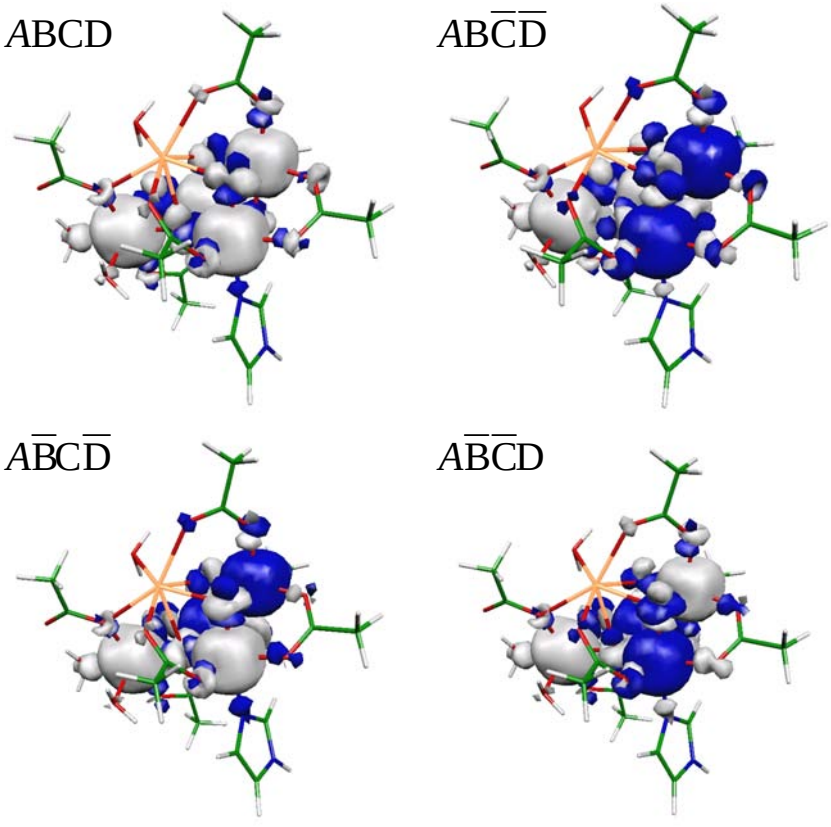

Figure B5. Spin-density plots of **Dau**$^{+1}$. Isosurfaces ± 0.003 a.u.

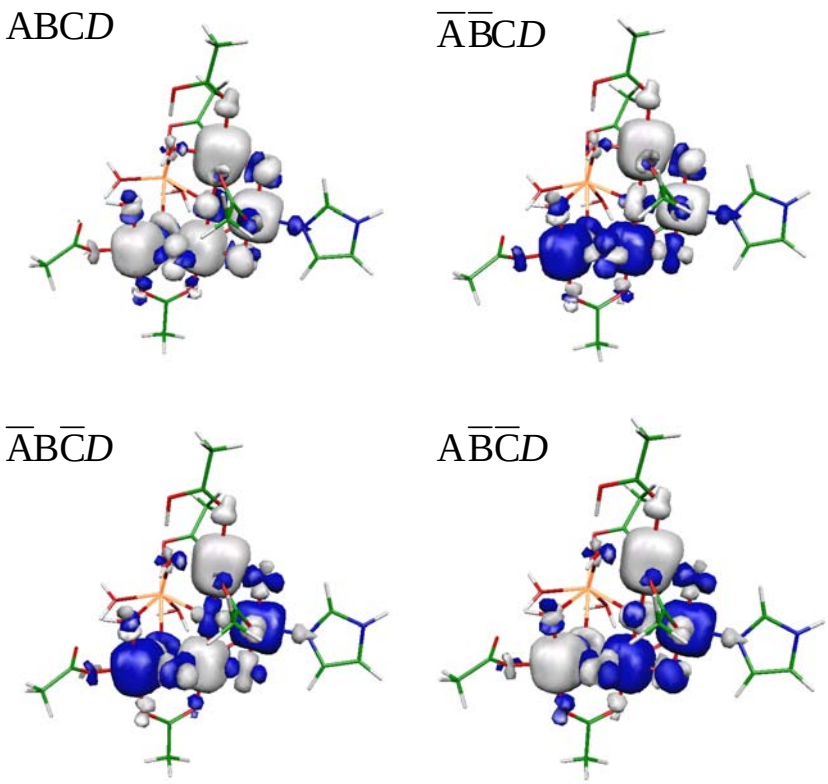

Figure B6. Spin-density plots of **Yano-I^0**. Isosurfaces ± 0.003 a.u.

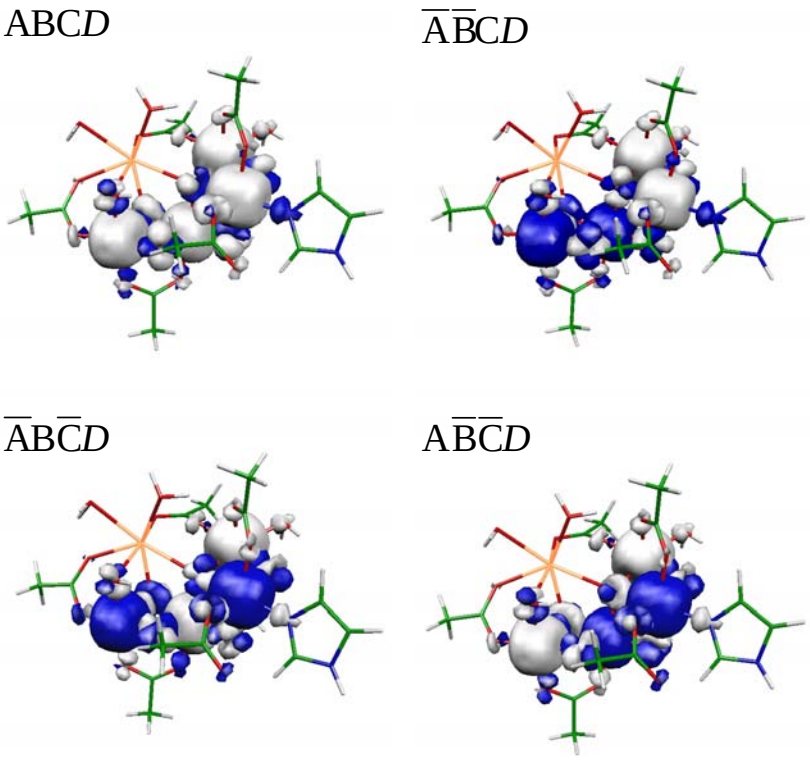

Figure B7. Spin-density plots of **Yano-II^0**. Isosurfaces ± 0.003 a.u.

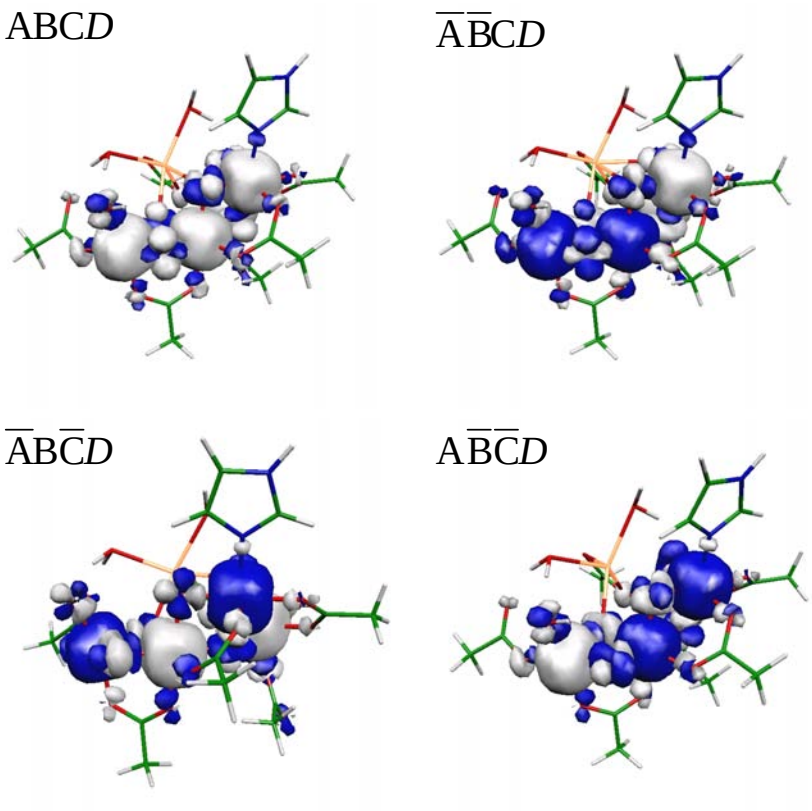

Figure B8. Spin-density plots of **Yano-III^0**. Isosurfaces ± 0.003 a.u.

References – Appendix B

[1] K. N. Ferreira, T. M. Iverson, K. Maghlaoui, J. Barber, S. Iwata, *Science* **2004**, *303*, 1831.
[2] J. Yano, J. Kern, K. Sauer, M. J. Latimer, Y. Pushkar, J. Biesiadka, B. Loll, W. Saenger, J. Messinger, A. Zouni, V. K. Yachandra, *Science* **2006**, *314*, 821.

List of Publications

Publications

Structural and Electronic Analysis of Lanthanide Complexes: Reactivity May Not Necessarily Be Independent of the Identity of the Lanthanide Atom - A DFT Study, S. Schinzel, M. Bindl, M. Visseaux, H. Chermette, *J. Phys. Chem. A* **2006**, *110*, 11324–11331.

Evaluation of the Carbene Hydride Mechanism in the Carbon-Carbon Bond Formation Process of Alkane Metathesis through a DFT Study, S. Schinzel, H. Chermette, C. Copéret, J.-M. Basset, *J. Am. Chem. Soc.* **2008**, *130*, 7984–7987.

Structure and electron paramagnetic resonance parameters of the manganese site of concanavalin A studied by density functional methods, S. Schinzel, R. Müller, M. Kaupp, *Theor. Chem. Acc.* **2008**, *120*, 437–445.

Synthesis, Reactivity, and Electronic Structure of [n]Vanadoarenophanes: An Experimental and Theoretical Study, H. Braunschweig, M. Kaupp, C. J. Adams, T. Kupfer, K. Radacki, S. Schinzel, *J. Am. Chem. Soc.* **2008**, *130*, 11376–11393.

Synthesis and Structure of a Ferrocenylboron Dication, H. Braunschweig, M. Kaupp, C. Lambert, D. Nowak, K. Radacki, S. Schinzel, K. Uttinger, *Inorg. Chem.* **2008**, *47*, 7456–7458.

Synthesis, Crystal Structure, EPR and DFT studies, and Redox Properties of [2]Tetramethyl-disilacobaltocenophane, H. Braunschweig, F. Breher, M. Kaupp, M. Groß, T. Kupfer, D. Nied, K. Radacki, S. Schinzel, *Organometallics* **2008**, *27*, 6427–6433.

Validation of Broken-Symmetry Density Functional Methods for the Calculation of Electron Paramagnetic Resonance Parameters of Dinuclear Mixed-Valence $Mn^{IV}Mn^{III}$ Complexes, S. Schinzel, M. Kaupp, *submitted*.

On the Structure of the Oxygen-Evolving Complex of Photosystem II: Density Functional Calculations on Electron Paramagnetic Resonance Parameters of the S_2 State, S. Schinzel, J. Schraut, M. Kaupp, *submitted*.

Posters

Alkane metathesis on silica-supported tantalum hydride: a DFT study, S. Schinzel, H. Chermette, C. Copéret, J. M. Basset, *11th International Conference on the Applications of Density Functional Theory (DFT) in Chemistry and Physics*, Genf (Switzerland), **2005**.

Density-Functional Studies of the Electron Paramagnetic Resonance Parameters of Mononuclear Manganese Complexes, S. Schinzel, C. Remenyi, R. Reviakine, M. Kaupp, *42nd Symposium for Theoretical Chemistry*, Berlin (Germany), **2006**.

Structural and electronic analysis of lanthanide complexes: f orbitals may be not just spectators and reactivity may not necessarily be independent of the identity of the lanthanide atom; a DFT study, H. Chermette, S. Schinzel, M. Visseaux, *43nd Symposium for Theoretical Chemistry*, Saarbrücken (Germany), **2007**.

Density-Functional Study of Electronic Structure and EPR Parameters of Biologically Relevant Manganese Complexes, S. Schinzel, M. Kaupp, *European Summer School in Quantum Chemistry*, Torre Normanna (Italy), **2007**; *43nd Symposium for Theoretical Chemistry*, Saarbrücken (Germany), **2007**.

Quantenchemische Berechnungen zu EPR-Parametern von zweikernigen gemischtvalenten Modellsystemen in Hinblick auf den vierkernigen Mangancluster des Photosystems II, S. Schinzel, M. Kaupp, *Chemie-Symposium der Studierenden Mainfrankens*, Würzburg (Germany), **2007**.

Density-Functional Study of Electronic Structure and EPR Parameters of Biologically Relevant Dinuclear Manganese Complexes, S. Schinzel, M. Kaupp, *10th Young Scientists Conference on Chemistry*, Rostock (Germany), **2008**.

Das Photosystem II: Aufklärung der Struktur des vierkernigen Manganclusters mittels quantenchemischer Berechnungen von EPR-Parametern, S. Schinzel, M. Kaupp, *Chemie-Symposium der Studierenden Mainfrankens*, Würzburg (Germany), **2008**.

Oral Presentations

Quantum chemical investigations of EPR parameters of dinuclear manganese compounds, *Workshop on Modern Methods in Quantum Chemistry*, Mariapfarr (Austria), **2008**.

Density-Functional Study of Electronic Structure and EPR Parameters of Biologically Relevant Multinuclear Manganese Complexes, *7th European Conference on Computational Chemistry*, San Servolo (Italy), **2008**.

Acknowledgment

First of all, I would like to thank *Prof. Dr. Martin Kaupp* for the challenging research subject. I really enjoyed it to work on this extremely fascinating topic. Martin has always been available to answer my questions and to fruitful discussions. Furthermore, I am really grateful to him that he gave me the possibilities to participate at interesting conferences and to attend the EPR spectroscopy workgroups of Prof. Dr. T. Prisner (Goethe Universität, Frankfurt am Main/Germany) and of Prof. Dr. R. David Britt (University of California, Davis/USA). Above all I thank him that he always provided confidence in me.

In addition, I wish to thank my whole workgroup:

- *Dr. Alexei Arbuznikov*. He was always open for questions on DFT.
- *Dr. James Asher*. He teached me in CPMD and in English.
- *Hilke Bahmann*. She accompanied me during the whole PhD time. Thanks for the nice time and the enormous amount of discussions (about DFT, equations, and especially about everything else).
- *Kathrin Götz*. We had a really nice time (hot and cold) not only in 415. Thank you for always looking after my localized plants, converting X-ray structures, correcting my talks and my thesis, and especially for all the motivating words.
- *Dr. Christian Remenyi*. He introduced me in this nice subject and gave useful hints even when he was chef editor.
- *Manuel Renz*. My personal EndNote and Typo3-Manual, as well as “formatting” expert. I had really a nice time in 415, also with his calculator.
- *Robert Müller* and *Dr. Roman Reviakine*. Without their computational support on MAG and Linux in general, I could never have done my PhD thesis (especially Robert for “frag”).
- *Dr. Sebastian Riedel*. He introduced my already during my F-Praktikum to Gaussian. Even in Helsinki, Canada, and Freiburg, he was always available for my questions.
- *Johannes Schraut*. I am so happy that he continues with this extremely beautiful research project. I really enjoyed the work with you on the PSII. Good luck!
- *Dr. Alexander Patrakov*, *Dr. Sylwia Kacprzak* and *Dr. Irina Malkin*.
- The whole *Malkin family* (including *Michal, Stano, Elena* and *Peter*). They have always brought some fresh new ideas from Bratislava to Würzburg.

- *Robert Müller*, *Sandra Sänze*, *Julia Gath*, *Juliane Köhler*, *Johannes Buback*, *Katharina Wagner*, *Bartosz Zarzycki*, *Christoph S. W. Fischer*, *Johannes Schraut*, *Michael Steinbauer*, and *Marius Silaghi*. It was really a pleasure for me that they spent their F- or "Schnupper"-Praktika with me. Some of them, I like to thank for their nice account names, and my workgroup, for accepting my calculations carried out "incognito"!

Furthermore, I thank all the people of the chemistry department, which supported during my PhD studies with chemical discussions and with coffee. Here, I only want to list some of them.

- *Dr. Krzysztof Radacki*. All types of questions, concerning computational support, programs, and anything else, were always extensively answered.
- *Rainer Sigritz*, *Manuela Gross*, and *Dr. Thomas Kupfer*. It was a pleasure for me to calculate their compounds.
- *Dr. Rian Dewhurst*. Thanks for the useful comments on my English.
- *Steffi Sparka*. Not only the organization of the chemistry lab course for physicists succeeded perfectly.
- *Dr. Katharina Uttinger*, *Markus Fischer*, *Dr. Stefan Metz*, *Gerd Gröger*, *Anatoly Patrakov*, and *Dr. Nele Welter*. They inspired my work through intensive conversations.
- *Martin Bindl*. Fortunately, the MPI in Mülheim an der Ruhr has access to more journals than the university of Würzburg.

Special thanks to *all of my friends*, who are not listed here and who have given me so much inspiration, preferable to Rosita, Peter, and Roland. Last but not least, I am grateful to *my parents* and *my sister Stefanie*, who have always supported me, especially with nice e-mails.

Furthermore, I would like to thank *Prof. Dr. T. Prisner* (Goethe Universität, Frankfurt am Main/Germany) and of *Prof. Dr. R. David Britt* (University of California, Davis/USA) and their workgroups for giving me the possibility to get to know some technical aspects of EPR spectroscopy.

Finally, I am grateful to the *Fonds der Chemischen Industrie* for a scholarship.